THE UNIVERSITY OF MANITOBA

THREE DIMENSIONAL MOTION OF A BURIED TUNNEL IN AN INFINITE MEDIUM

BY

KONG-FAN CHOW

A thesis

SUBMITTED TO THE FACULTY OF GRADUATE STUDIES

IN PARTIAL FULFILLMENT OF THE REQUIREMENTS FOR THE DEGREE OF

MASTER OF SCIENCE IN CIVIL ENGINEERING

WINNIPEG, MANITOBA

JANUARY, 1985

THREE DIMENSIONAL MOTION OF A BURIED TUNNEL IN AN INFINITE MEDIUM

BY

KONG-FAN CHOW

A thesis submitted to the Faculty of Graduate Studies of
the University of Manitoba in partial fulfillment of the requirements
of the degree of

MASTER OF SCIENCE

ABSTRACT

Dynamic amplification of stresses and displacements induced in a buried tunnel have been studied. In this thesis a three dimensional non-axisymmetric motion of a tunnel of general shape buried in an infinite medium caused by longitudinal and polarized shear waves is examined in detail here. The changes in the response due to different ground properties ,changes in incident angles and wave frequencies are carefully examined. It is found that the response depends very much on the wave frequency and angle of incidence. And the stresses induced on the tunnel are larger when the surrounding soil is soft.

ACKNOWLEDGEMENTS

The author wishes to express his most sincere appreciation to his advisor, Dr. A.H. Shah, for his extensive guidance, encouragement and assistance throughout this thesis work. Without all the help he offered, the thesis work would have not been possible.

Special appreciation goes to Dr. J.I. Glanville and Dr. L. Shafai for their careful reading of the thesis and their invaluable suggestions.

Finally, the author like to mention that this thesis work was made possible under the Research Grant No. A7988 sponsored by the Natural Sciences and Engineering Research Council of Canada.

TABLE OF CONTENTS

LIST OF TABLES

LIST OF FIGURES

CHAPTER 1 INTRODUCTION

1.1 PREFACE

Earthquakes and explosions generate two types of body waves that travel through the interior of the elastic earth. One of them is a compressive wave and the other is a shear wave. In seismology they are referred to as P and S waves, respectively. The displacement field in the P wave is parallel to the direction of propagation of the wave. The S wave has a displacement field polarized in the plane perpendicular to the direction of propagation. The S wave can be furthur decomposed into SH and SV waves. They produce the displacement fields parallel to the horizontal and vertical directions, respectively. The scattering theory of elastic waves by circular cylindrical inclusions and flaws embedded in an infinite homogeneous isotropic solid has been studied extensively.

A review of the past works on the subject of scattering and diffraction of incident plane waves on buried pipelines reveals that very little attention has been paid to the full interaction problem between the pipe and its surrounding ground. For instance, Nelson and Weidlinger [1] and Wang and O'Rourke [2] have studied the propagation of plane compressional and shear elastic waves in an infinite homogeneous isotropic elastic medium containing an infinitely long embedded tunnels or pipelines. However, these studies are based on the assumption that the pipelines or tunnels closely follow the ground's motion and that no soil-pipe interaction takes place. The propagation of free harmonic waves in an infinitely long circular cylinder has been investigated, under the restriction of axial symmetry of motion by McFadden [3] and Herrmann and Mirsky [4]. The theory for the scattering of plane elastic waves by a circular cylindrical obstacle in a solid medium was formulated by White [5]. He derived systems of boundary-condition equations whose unknowns are coefficients in infinite-series expansions of potential functions representing the scattered waves. Among all these studies, most investigators treated the pipe as a beam on elastic foundation [1,2] or model the pipe as a set of spring-mass system [1]. Besides this simplified modeling, a shell model is also used to represent the pipe [6,7]. Again the interaction of the host medium with the embedded shell has not been taken into considerations. The governing equations for the wave motion of the surrounding medium have not been solved simultaneously with the equations of motion of the shell. A departure to this is made by the work of Hindy and Novak [8] who attempted to include the effect of the interaction of the shell with its surrounding ground. They approximated the resistance given to the shell by the surrounding ground to be that of a rigid cylinder in simple harmonic motion. However, their investigation is limited to only a two-dimensional motion study of the buried pipelines or tunnels. Also works by Pao and Mow [9], Zienkiewicz, Kelly and Bittess [10], Underwood and

Geers [11] are limited to plane-strain investigation. Apart from these, Chakraborty [12] modeled the pipe as a thin circular cylindrical shell and using Flugge's bending theory of shell [13], developed an analysis of three-dimensional motion of a shell in an infinite medium. However, these analysis is restricted to solve only one type of scatterer after formulation, and the surrounding medium is limited to isotropic and homogeneous.

Various mathmatical techniques have been developed to solve the wave scattering problem. Among all these techniques, two methods are widely used; namely the separation of variables and numerical solution of integral equation. However, most of these mathmatical techniques are also restricted to solve only one scatterer. To overcome this deficiency, Datta and Shah et al [14-16] have proposed another approach to solve this problem. In this alternate approach, media inhomogeneities (pipeline, tunnel, etc.) are enclosed in a closed contour. The interior region is represented by suitable finite elements. In the exterior region the solution is expressed in a complete expansion in outgoing and incoming waves [17]. The hybrid finite element and eigenfunction expansion technique (FEEET) suggested by Datta et al [17] is furthur extented by the author from a plane-strain to a three-dimensional motion analysis of a buried tunnel and the results are presented in this thesis.

1.2 OBJECTIVE AND SCOPE

A combined analytical and finite element method is presented for studying diffraction of elastic waves by a buried tunnel in an infinite medium for three-dimensional motion. The method consists of dividing the infinite space into two regions; an interior bounded region containing the tunnel and exterior unbounded region. The interior region is represented by finite elements and wave function expansion is used to represent the field in the exterior homogeneous isotropic medium.

In this thesis, Chapter II will present an analytical exact solution method to solve a circular cavity inclusion for scattering of waves, and results obtained by this method are to be compared with the FEEET method mentioned in Chapter III to ensure the accuracy of the combined finite element and wave function expansion method. The FEEET method is then used to investigate the three-dimensional scattering of longitudinal and shear waves by a buried tunnel in an infinite medium. Finally, Chapter IV gives the discussions of various parameters such as the wave number, the wave incident angle and the properties of the surrounding material which affect the performance of the buried tunnel.

CHAPTER 2

2.1 GENERAL THEORY

It is assumed that the pipe is infinite in extent, and embedded in an infinite homogeneous isotropic medium as shown in Fig. 1a.

The governing equation of motion for an isotropic elastic medium in invariant form is

$$\mu \underset{\sim}{\nabla}^2 \vec{u} + (\lambda + \mu) \underset{\sim}{\nabla} (\underset{\sim}{\nabla} \cdot \vec{u}) = \rho \ddot{\vec{u}} \tag{2.1}$$

where λ and μ are Lame's constants and ρ the mass density, and ∇ is the usual del operator. The solution to equation (2.1) can be written in the form

$$\vec{u} = \underset{\sim}{\nabla} \phi + \underset{\sim}{\nabla} \Lambda (\underset{\sim}{e}_z \psi) + \frac{1}{k_s} \underset{\sim}{\nabla} \Lambda \underset{\sim}{\nabla} \Lambda (\underset{\sim}{e}_z \chi) \tag{2.2}$$

where ϕ is the longitudinal wave potential for P wave, and ψ, χ are the shear wave potentials for SV and SH waves, respectively; $\underset{\sim}{e}_z$ is a unit vector in z direction and the constant k_s is defined later. Substituting eqn (2.2) into eqn (2.1) the potentials ϕ, ψ, and χ satisfy the wave equations

$$\begin{aligned} V_p^2 \ \nabla^2 \phi &= \ddot{\phi} , \\ V_s^2 \ \nabla^2 \psi &= \ddot{\psi} , \\ V_s^2 \ \nabla^2 \chi &= \ddot{\chi} , \end{aligned} \tag{2.3}$$

where

$$\begin{aligned} V_p &= [(\lambda + 2\mu)/\rho]^{\frac{1}{2}} \\ \text{and} \quad V_s &= [\lambda/\rho]^{\frac{1}{2}} \end{aligned} \tag{2.4}$$

are the dilational and shear wave velocities, respectively.

For harmonic motion, the displacement potentials ϕ, ψ, and χ can be expressed for "nth" harmonic as

$$\phi = f(r)e^{in\theta} \; e^{i(\xi z-\omega t)},$$
$$\psi = g_3(r)e^{in\theta} \; e^{i(\xi z-\omega t)}, \tag{2.5}$$
$$\chi = g_1(r)e^{in\theta} \; e^{i(\xi z-\omega t)},$$

where ω is the circular frequency, and ξ is related to the wave number of the dilational and shear waves as

$$\xi = k_p \sin \theta_o \text{ , (for dilational wave)}$$
$$\xi = k_s \sin \psi_o \quad \text{(for shear wave)} \tag{2.6}$$

In eqn (2.6) $k_p = \frac{\omega}{V_p}$, $k_s = \frac{\omega}{V_s}$, θ_o and ψ_o are the incident angles of the dilational and shear waves in the x-z plane, respectively, as shown in Figure 1a.

For a bounded region the total solutions for $f(r)$, $g_1(r)$ and $g_3(r)$ can be written as

$$f(r) = A \; Z_n (\alpha_A r) + B \; W_n(\alpha_A r),$$
$$g_1(r) = A_1 \; Z_n (\beta_A r) + B_1 \; W_n(\beta_A r), \tag{2.7}$$
$$g_3(r) = A_3 \; Z_n (\beta_A r) + B_3 \; W_n(\beta_A r)$$

in which A, A_1, A_3, B, B_1, B_3 are unknown constants. Eqn (2.7) is given in terms of the Bessel functions J and Y, or the modified Bessel functions I and K of the arguments $\alpha_A r = |\alpha r|$ and $\beta_A r = |\beta r|$, depending whether α and β are real or imaginary. For brevity, Z denotes a J or I function and W denotes a Y or K function. α and β are defined as

$$\alpha^2 = \frac{\omega^2}{V_p^2} - \xi^2 ,$$
$$\beta^2 = \frac{\omega^2}{V_s^2} - \xi^2 \tag{2.8}$$

For an unbounded region the scattered solutions for $f(r)$, $g_1(r)$ and $g_3(r)$ can be written in terms of the outgoing waves satisfying the radiation conditions as

$$\begin{aligned} f(r) &= C\, H_n\,(\alpha_A r), \\ g_1(r) &= C_1\, H_n\,(\beta_A r), \\ g_3(r) &= C_3\, H_n\,(\beta_A r). \end{aligned} \tag{2.9}$$

where C, C_1, C_3 are unknown constants.

In polar coordinates the displacement components u_r, u_θ, u_z and the stresses σ_{rr}, $\sigma_{r\theta}$, σ_{rz} and $\sigma_{\theta\theta}$ are given as

$$\begin{aligned} u_r &= \frac{\partial\phi}{\partial r} + \frac{1}{r}\frac{\partial\psi}{\partial\theta} + \frac{1}{k_s}\frac{\partial^2\chi}{\partial r\partial z}, \\ u_\theta &= \frac{1}{r}\frac{\partial\phi}{\partial r} - \frac{\partial\psi}{\partial r} + \frac{1}{k_s}\frac{\partial^2\chi}{\partial\theta\partial z}, \\ u_z &= \frac{\partial\phi}{\partial z} + \frac{1}{k_s}\left(\frac{\partial^2\chi}{\partial z^2} + k_s^2\,\chi\right) \end{aligned} \tag{2.10}$$

and

$$\begin{aligned} \sigma_{rr} &= \lambda\left(\frac{\partial u_r}{\partial r} + \frac{u_r}{r} + \frac{1}{r}\frac{\partial u_\theta}{\partial\theta} + \frac{\partial u_z}{\partial Z}\right) + 2\mu\frac{\partial u_r}{\partial r}, \\ \sigma_{r\theta} &= \mu\left(\frac{\partial u_\theta}{\partial r} - \frac{u_\theta}{r} + \frac{1}{r}\frac{\partial u_r}{\partial\theta}\right), \\ \sigma_{rz} &= \mu\left(\frac{\partial u_r}{\partial z} + \frac{\partial u_z}{\partial r}\right), \\ \sigma_{\theta\theta} &= \lambda\left(\frac{\partial u_r}{\partial r} + \frac{1}{r}\frac{\partial u_\theta}{\partial\theta} + \frac{u_r}{r} + \frac{\partial u_z}{\partial z}\right) + 2\mu\left(\frac{1}{r}\frac{\partial u_\theta}{\partial\theta} + \frac{u_r}{r}\right). \end{aligned} \tag{2.11}$$

For convenience, the surrounding elastic medium and the pipe will be denoted by region 1 and 2, respectively. In the sequel the material constants of regions R_1 and R_2 will be designated by subscripts 1 and 2, respectively.

2.2 ANALYTICAL TECHNIQUE

2.2.1 Region R_2

Using equations (2.5), (2.7), (2.10) and (2.11) the total displacement and stress fields in Region 2 can be written as

$$\frac{u_r^{(2)}}{e^{i\psi}} = A\,u_{r_1} + B\,u_{r_2} + A_1\,u_{r_3} + B_1\,u_{r_4} + A_3\,u_{r_5} + B_3\,u_{r_6}\,,$$

$$\frac{u_\theta^{(2)}}{e^{i\psi}} = A\,u_{t_1} + B\,u_{t_2} + A_1\,u_{t_3} + B_1\,u_{t_4} + A_3\,u_{t_5} + B_3\,u_{t_6}\,,$$

$$\frac{u_z^{(2)}}{e^{i\psi}} = A\,u_{z_1} + B\,u_{z_2} + A_1\,u_{z_3} + B_1\,u_{z_4} + A_3\,u_{z_5} + B_3\,u_{z_6} \tag{2.12}$$

and

$$\frac{\sigma_{rr}^{(2)}}{e^{i\psi}\,\mu_2} = A\,S_{r_1} + B\,S_{r_2} + A_1\,S_{r_3} + B_1\,S_{r_4} + A_3\,S_{r_5} + B_3\,S_{r_6}\,,$$

$$\frac{\sigma_{r\theta}^{(2)}}{e^{i\psi}\,\mu_2} = A\,S_{rt_1} + B\,S_{rt_2} + A_1\,S_{rt_3} + B_1\,S_{rt_4} + A_3\,S_{rt_5} + B_3\,S_{rt_6}\,,$$

$$\frac{\sigma_{rz}^{(2)}}{e^{i\psi}\,\mu_2} = A\,S_{rz_1} + B\,S_{rz_2} + A_1\,S_{rz_3} + B_1\,S_{rz_4} + A_3\,S_{rz_5} + B_3\,S_{rz_6}\,,$$

$$\frac{\sigma_{\theta\theta}^{(2)}}{e^{i\psi}\,\mu_2} = A\,S_{tt_1} + B\,S_{tt_2} + A_1\,S_{tt_3} + B_1\,S_{tt_4} + A_3\,S_{tt_5} + B_3\,S_{tt_6} \tag{2.13}$$

where $\psi = \eta\theta + \xi z$ and expressions for u_{r_i}, u_{t_i}, u_{z_i}, S_{r_i}, $S_{r_{t_i}}$, $S_{r_{z_i}}$ and S_{tt_i} $(i = 1, 2, ..6)$ are listed in Appendix 1.

2.2.2 Region R_1

Since it is assumed that the seismic sources are outside the pipe, the interaction of the incident seismic disturbance $\vec{u}^{(i)}$ with the pipe will give rise to scattered wave, $\vec{u}^{(s)}$. It may be noted that both $\vec{u}^{(i)}$ and $\vec{u}^{(s)}$ will satisfy eqn (2.1). Thus the total field, $\vec{u}$ in the ground is written as

$$\vec{u}^{(1)} = \vec{u}^{(i)} + \vec{u}^{(s)} \tag{2.14}$$

2.2.3 Scattered Field

Substituting eqn (2.9) into eqn (2.10) and (2.11), the scattered displacement and stress components are obtained as the following:

$$\frac{u_r^{(s)}}{e^{i\psi}} = C\, D_{r_1} + C_1\, D_{r_2} + C_3\, D_r 3 \,,$$

$$\frac{u_\theta^{(s)}}{e^{i\psi}} = C\, D_{t_1} + C_1\, D_{t_2} + C_3\, D_{t_3} \,,$$

$$\frac{u_z^{(s)}}{e^{i\psi}} = C\, D_{z_1} + C_1\, D_{z_2} + C_3\, D_{z_3} \,, \tag{2.15}$$

and

$$\frac{\sigma_{rr}^{(s)}}{\mu_1 e^{i\psi}} = C\, E_{r_1} + C_1\, E_{r_2} + C_3\, E_{r_3} \,,$$

$$\frac{\sigma_{r\theta}^{(s)}}{\mu_1 e^{i\psi}} = C\, E_{rt_1} + C_1\, E_{rt_2} + C_3\, E_{rt_3} \,,$$

$$\frac{\sigma_{rz}^{(s)}}{\mu_1 e^{i\psi}} = C\, E_{rz_1} + C_1\, E_{rz_2} + C_3\, E_{rz_3} \,,$$

$$\frac{\sigma_{\theta\theta}^{(s)}}{\mu_1 e^{i\psi}} = C\, E_{tt_1} + C_1\, E_{tt_2} + C_3\, E_{tt_3} \,, \tag{2.16}$$

in which D_{r_i}, D_{t_i}, D_{z_i} and E_{r_i}, E_{rt_i}, E_{rz_i}, E_{tt_i} (i = 1, 2, 3) are are listed in Appendix 1.

2.2.4 Incident Waves

As before the displacement field $\vec{u}^{(i)}$ can be expressed in terms of three potentials $\phi^{(i)}$, $\psi^{(i)}$ and $\chi^{(i)}$ as

$$\vec{u}^{(i)} = \nabla \phi^{(i)} + \underset{\sim}{\nabla} \wedge (\underset{\sim}{e}_z \psi^{(i)}) + \frac{1}{k_s} \underset{\sim}{\nabla} \wedge \underset{\sim}{\nabla} \wedge (\underset{\sim}{e}_z \chi^{(i)}) \tag{2.17}$$

If the incident wave is a P wave, then only $\phi^{(i)}$ exists in eqn (2.17) and the other two potentials $\psi^{(i)}$ and $\chi^{(i)}$ will not exist. It follows that $\phi^{(i)}$ and $\chi^{(i)}$ will vanish in eqn (2.17) for incident SV wave, and similarly only $\chi^{(i)}$ will exist in eqn (2.17) and the two other potentials will vanish if the incident wave is SH wave.

Suppose that the incident disturbance is a longitudinal wave given by

$$\vec{u}^{(i)} = \nabla \phi^{(i)} \tag{2.18}$$

in which

$$\phi^{(i)} = \sum_{n=-\infty}^{\infty} J_n (\alpha_1 r) e^{in\theta} e^{i\xi z} e^{i\omega t} \tag{2.19}$$

this wave represents a propagation vector making an angle θ_o with the x-axis in the x-z plane, with wave length $\lambda = k_{p_1} \cos \theta_o$, and apparent wave speed $C = \frac{\omega}{\lambda}$ along the pipe. Substituting eqn (2.19) into eqns (2.10) and (2.11), one can write the components of the incident displacement and stress fields for the dilational P wave, which are given in Appendix 1. Similarly, knowing $\psi^{(i)}$ and $\chi^{(i)}$ for shear SV and SH waves, the corresponding components of the incident displacement and stress fields can be found and are listed in Appendix 1. Note that for the dilational P wave as given in eqn (2.19), ξ and k_{p_1} are related as indicated in the relation $\xi = k_{p_1} \sin \theta_o$, and similarly for SV and SH waves $\xi = k_{s_1} \sin \psi_o$.

2.3 SOLUTIONS

Boundary conditions are applied for the purpose of determining the unknown constants A, A_1, A_3, B, B_1, B_3 and C, C_1, C_3.

(Refer to the pipe geometry in figure 1b)

At r = b, the condition of continuity requires that the total displacement in region 2 be equal to the sum of the incident and scattered displacement in region 1. Transposing the scattered displacement on the same side as the total displacement in the equation, one can write

$$\begin{aligned} u_r^{(2)}(b) - u_r^{(s)}(b) &= u_r^{(i)}(b) , \\ u_\theta^{(2)}(b) - u_\theta^{(s)}(b) &= u_\theta^{(i)}(b) , \\ u_z^{(2)}(b) - u_z^{(s)}(b) &= u_z^{(i)}(b) . \end{aligned} \tag{2.20a}$$

Similarly for the stress field

$$\begin{aligned} \sigma_{rr}^{(2)}(b) - \sigma_{rr}^{(s)}(b) &= \sigma_{rr}^{(i)} , \\ \sigma_{r\theta}^{(2)}(b) - \sigma_{r\theta}^{(s)}(b) &= \sigma_{r\theta}^{(i)} , \\ \sigma_{rz}^{(2)}(b) - \sigma_{rz}^{(s)}(b) &= \sigma_{rz}^{(i)} . \end{aligned} \tag{2.20b}$$

At r = a, the traction-free boundary implies that

$$\begin{aligned} \sigma_{rr}^{(2)}(a) &= 0 , \\ \sigma_{r\theta}^{(2)}(a) &= 0 , \\ \sigma_{rz}^{(2)}(a) &= 0 . \end{aligned} \tag{2.20c}$$

From nine equations (2.20a), (2.20b) and (2.20c), for each harmonic "n" the corresponding constants < $A_n, B_n, A_{1n}, B_{1n}, B_{3n}, C_n, C_{1n}, C_{3n}$, > can be solved accordingly.

2.3.1 Cavity Inclusion

For the case of cavity of radius "a", the pertinent boundary conditions are given as

$$\sigma_{rr}^{(s)}(a) + \sigma_{rr}^{(i)}(a) = 0 \quad ,$$

$$\sigma_{r\theta}^{(s)}(a) + \sigma_{r\theta}^{(i)}(a) = 0 \quad ,$$

$$\sigma_{rz}^{(s)}(a) + \sigma_{rz}^{(i)}(a) = 0 \quad . \qquad (2.21)$$

from which for each harmonic "n" corresponding constants < C_n, C_{1n}, C_{3n} > can be obtained.

CHAPTER 3

3.1 HYBRID FINITE ELEMENT AND EIGENFUNCTION EXPANSION TECHNIQUE (FEEET)

3.1.1 Numerical-Analytical Technique

Dynamic amplifications of stresses and displacements in the wall of an infinitely long continous tunnel embedded in an elastic medium is studied here. A combined finite element and eigenfunction expansion technique is used for this purpose. In this numerical technique, it is assumed that the media inhomogenities are enclosed inside region R_2 by closed contour B as shown in figure 2. This interior region is subdivided into finite elements having N_I interior nodes and N_B boundary nodes. The closed contour B separates two different regions, interior region R_2 is the media of the inhomogenities containing the tunnel, and exterior region R_1 is an infinite region assumed to be isotropic and homogeneous.

(i) Exterior Region (Wave function expansion)

In the exterior region R_1, the displacement field $\vec{u}^{(1)}$ is composed of two parts as mentioned before

$$\vec{u}^{(1)} = \vec{u}^{(i)} + \vec{u}^{(s)} \tag{3.1}$$

where $\vec{u}^{(i)}$ is the incident field displacement and $\vec{u}^{(s)}$ is from the contribution of the scattered waves.

The displacement and stress components for P, SV or SH fields are given in cartesian coordinates in Appendix 2. For the scattered field evaluating the equation (2.15) at N_B nodes on the boundary B, the scattered nodal displacement vector $\{\vec{q}_r^{(s)}\}$ can be written in terms of generalized coordinates {a} as

$$\{\vec{q}^{(s)}_{r_B}\} = \left[G_{r\theta}\right] \{a\} \tag{3.2}$$

where $\{\vec{q}^{(s)}_{r_B}\} = \{u^{(s)}_{r_B}, u^{(s)}_{\theta_B}, u^{(s)}_{z_B}\}^T$

$\{a\} = \{C_i, C_{1_i}, C_{3_i}\}^T$ for $i = 1, 2, \ldots, NB$

and the superscript T represents transpose, the complex matrix $[G_{r\theta}]$ is composed of the known functions in the scattered displacement field and can be found in Appendix 2. Since $\{\vec{q}^{(s)}_{r_B}\}$ is evaluated in (r, θ, z) coordinates a transformation matrix [T] as defined in Appendix 2 is needed. The element components T_i of the transformation matrix is given by

$$[T_i] = \begin{bmatrix} \cos\theta_i & \sin\theta_i & 0 \\ -\sin\theta_i & \cos\theta_i & 0 \\ 0 & 0 & 1 \end{bmatrix} \tag{3.3}$$

Using the transformation matrix the nodal displacement vector $\{\vec{q}^{(s)}_{x_B}\}$ in cartesian coordinates can be written as

$$\{\vec{q}^{(s)}_{x_B}\} = [T]^T\{\vec{q}^{(s)}_{r_B}\}^T = [T]^T [G_{r\theta}] \{a\} = [G_{xy}] \{a\} \tag{3.4}$$

where $$[G_{xy}] = [T]^T [G_{r\theta}] \tag{3.5}$$

and the components of $\{\vec{q}^{(S)}_{x_B}\}$ in cartesian coordinates is given by

$$\{\vec{q}^{(s)}_{x_B}\} = \{u^{(s)}_{x_B}, u^{(s)}_{y_B}, u^{(s)}_{z_B}\}^T .$$

Again using the strain-displacement and stress-strain relations, the scattered stress fields are found in matrix notation as

$$\{ \vec{\sigma}^{(s)}_{r_B} \} = [F_{r\theta}] \{a\} \tag{3.6}$$

where $\{ \vec{\sigma}^{(s)}_{r_B} \} = \{\sigma^{(s)}_{rr}, \sigma^{(s)}_{r\theta}, \sigma^{(s)}_{rz}\}^T$

and the complex matrix $[F_{r\theta}]$ which is composed of the known functions in the scattered stress fields is defined in Appendix 2. It is reminded that both $\{\sigma^{(s)}_{r_B}\}$ and $[F_{r\theta}]$ are in polar coordinates.

Substituting eqn (3.4) into eqn (3.6), we get

$$\{ \vec{\sigma}^{(s)}_{r_B} \} = [F_{r\theta}] [G_{r\theta}]^{-1} \{\vec{q}^{(s)}_{r_B}\} \quad . \tag{3.7}$$

It is seen from eqn (3.7) that if the final equations are to be solved in terms of the nodal displacements the complex matrix $[G_{r\theta}]$ has to be inverted. For the purpose of avoiding the inversion an alternate approach is used in which the equations are solved in terms of the generalized coordinates $\{a\}$. To do this, the virtual work done on the boundary B has to be found and written as

$$\delta\Pi = \int_B \{ \delta \vec{q}^{*\,(1)}_{r_B} \}^T \{ \vec{\sigma}^{(1)}_{r_B}\} \, d\Gamma \tag{3.8}$$

where the superscript * indicates complex conjugate,

and
$$\vec{q}^{(1)}_{r_B} = \vec{q}^{(s)}_{r_B} + \vec{q}^{(i)}_{r_B} \; ,$$
$$\vec{\sigma}^{(1)}_{r_B} = \vec{\sigma}^{(s)}_{r_B} + \vec{\sigma}^{(i)}_{r_B} \tag{3.9}$$

Noting $\delta \vec{q}^{(1)}_{r_B} = \delta \vec{q}^{(s)}_{r_B}$

and substituting $\{\vec{q}^{(s)}_{r_B}\}$ and $\{ \vec{\sigma}^{(s)}_{r_B}\}$ from eqn (3.4) and (3.7) into eqn (3.8), the virtual work can be written as

$$\delta\Pi = \{ \delta a^* \}^T \{ \vec{P}_B^{(1)} \} \tag{3.10}$$

in which $\{ \vec{P}_B^{(1)} \}$ is the generalized interaction force between R_1 and R_2 and is given by

$$\{ \vec{P}_B^{(1)} \} = [R] \{ a \} + \{ \vec{P}_B^{(i)} \} \tag{3.11}$$

in which $[R] = \int_B [G^*_{r\theta}]^T [F_{r\theta}] \, d\Gamma$

and $\{ \vec{P}_B^{(i)} \} = \int_B [G^*_{r\theta}]^T \{ \vec{\sigma}_{r_B}^{(i)} \} d\Gamma$.

For numerical evaluation, [R] and $\{\vec{P}_B^{(i)}\}$ in eqn (3.11) are approximated as

$$[R] = R_B \, \Delta\theta \, [G^*_{r\theta}]^T [F_{r\theta}]$$

and

$$\{ \vec{P}_B^{(i)} \} = R_B \, \Delta\theta \, [G^*_{r\theta}]^T \{ \vec{\sigma}_{r_B}^{(i)} \} \tag{3.12}$$

where R_B is the radius of the circular boundary contour B, $\Delta\Theta = 2\Pi/NB$.

(ii) <u>Interior Region (Finite Element Method)</u>

Figure 2 shows the geometry of the tunnel. The bounded region R_2 is contained within the boundary B, within the region R_2 is the tunnel and the non-homogeneity. The interior region R_2 is further sub-divided into finite elements as shown in Fig. 3. This finite element mesh is having $N_I + N_B$ nodes, where N_I and N_B are the numbers of interior nodes and nodes on circular boundary contour B, respectively.

The displacement fields within each element is expressed in terms of the shape functions $[N_j]$ and the nodal displacement value $\{q_j^e\}$ as

$$\{ \vec{u}^e \} = [N] \quad \{q_j^e\} \tag{3.13}$$

the subscript j refers to the node position for an element, some internal (subscripted I) and some on the boundary B (subscripted B).

If an element has 'n' number of nodes, then

$$[N] = \left[\begin{array}{ccc|ccc|ccc|ccc} N_1 & 0 & 0 & N_2 & 0 & 0 & . & . & . & N_n & 0 & 0 \\ 0 & N_1 & 0 & 0 & N_2 & 0 & . & . & . & 0 & N_n & 0 \\ 0 & 0 & N_1 & 0 & 0 & N_2 & . & . & . & 0 & 0 & N_n \end{array}\right] . \tag{3.14}$$

The strain within an element related to the displacement field $\{\vec{u}^e\}$ is given by

$$\begin{aligned} \{\vec{\varepsilon}^e\} &= [L]\ [N]\ \{\vec{u}^e\} \\ &= [B]\ \{\vec{u}^e\} \end{aligned} \tag{3.15}$$

where [L] is an operator matrix

$$[L] = \begin{bmatrix} \partial/\partial x & 0 & 0 \\ 0 & \partial/\partial y & 0 \\ 0 & 0 & i\xi \\ 0 & i\xi & \partial/\partial y \\ i\xi & 0 & \partial/\partial x \\ \partial/\partial y & \partial/\partial x & 0 \end{bmatrix},$$

and

$$[B] = [L]\ [N]. \tag{3.16}$$

In order to determine the elemental impedance matrix, the first step is to obtain the elemental stiffness matrix. The internal potential energy of an element is given by

$$V^e_{pot} = \frac{1}{2} \int\int\int [\{\vec{q}^{*e}\}^T\ [B^*]\ [D]\ [B]\ \{\vec{q}^e\}\ dx\ dy\ dz \tag{3.17}$$

For the purpose of eliminating the integration over the z-direction, it can be shown that if one takes the integration over one wavelength Λ_z, eqn (3.17) will become

$$\frac{V^e_{pot}}{\Lambda_z} = \frac{1}{2} \{\vec{q}^{*e}\}^T \left[\int\int [B^*]^T [D]\ [B]\ \ dx\ dy \ \right] \{\vec{q}^e\} \tag{3.18}$$

For an isotropic material [D] is a 6x6 matrix given by

$$[D] = \begin{bmatrix} D_1 & D_2 & D_2 & 0 & 0 & 0 \\ D_2 & D_1 & D_2 & 0 & 0 & 0 \\ D_2 & D_2 & D_1 & 0 & 0 & 0 \\ 0 & 0 & 0 & D_3 & 0 & 0 \\ 0 & 0 & 0 & 0 & D_3 & 0 \\ 0 & 0 & 0 & 0 & 0 & D_3 \end{bmatrix} \tag{3.19}$$

where $D_1 = \lambda_e + 2\mu_e$, $D_2 = \lambda_e$, and $D_3 = \mu_e$.

Taking variation, the stiffness matrix of an element is obtained from eqn (3.18) as

$$[k^e] = \int\int [B^*]^T\ [D]\ [B]\ dx\ dy \quad . \tag{3.20}$$

It may be noted that $[k^e]$ is a Hermitian matrix. For reference, a 3x3 matrix $[Q_{ij}]$ defined as

$$[Q_{ij}] = [B^*_i]^T\ [D]\ [B_j] \tag{3.21}$$

is given in Appendix 2.

When each $[k^e]$ is assembled to form the global stiffness matrix, the global stiffness matrix will be a complex matrix and will occupy large storage space in computer operations. Therefore, in order to save storage space, a manipulation has been done on $[Q_{ij}]$ to transform it into a real symmetric matrix and detail is included in Appendix 2.

The next task is to determine the elemental mass matrix so that a final elemental impedance matrix can be formed. To do this, the kinetic energy of an element is given as

$$\frac{T^e_{kin}}{\Lambda_z} = \frac{\rho_\omega 2}{2} \{\vec{q}^{*e}\}^T \left[\int\int [N]^T [N] \, dx \, dy \right] \{\vec{q}^e\} \tag{3.22}$$

From equation (3.22) the elemental mass matrix is written as

$$[m^e] = \int\int [N]^T \, [N] \, dx \, dy \tag{3.23}$$

Since the elemental stiffness matrix and the elemental mass matrix are known from eqn (3.20) and eqn (3.23), the elemental impedance matrix S_{II}, S_{IB}, S_{BI} and S_{BB} can be defined as

$$[S^e_{PQ}] = \int\int_{R_e} [B^*_p]^T \, [D] \, [B_Q] - \rho_e \, \omega^2 \, [N_p]^T \, [N_Q] \; dx \, dy \tag{3.24}$$

From [14] the appropriate functional for minimization in the region R_2 can be written as

$$F = \vec{q}^{*T}_{x_I} S_{II} \vec{q}_{x_I} + \vec{q}^{*T}_{x_I} S_{IB} \vec{q}_{x_B} + \vec{q}^{*T}_{x_B} S_{BI} \vec{q}_{x_I} + \vec{q}^{*T}_{x_B} S_{BB} \vec{q}_{x_B} \tag{3.25}$$

in which the continuity across the boundary B,

$$\vec{q}_{x_B} = \vec{q}^{(2)}_{x_B} = q^{(1)}_{x_B} = \vec{q}^{(s)}_{x_B} + \vec{q}^{(i)}_{x_B} \tag{3.26}$$

is used and $\vec{q}^{(2)}_{x_I}$ is denoted as $\vec{q}_{x_I}$.

3.2 NUMERICAL SOLUTION

In order to solve the nodal displacement vector, substituting (3.26) into eqn (3.25) and minimizing the functional F, one obtain in matrix notation

$$\begin{bmatrix} S_{II} & S_{IB} \, G_{xy} \\ G^{*T}_{xy} \, S_{BI} & G^{*T}_{xy} \, S_{BB} \, G_{xy} \end{bmatrix} \begin{Bmatrix} \vec{q}_{x_I} \\ \{a\} \end{Bmatrix} = \begin{Bmatrix} -S_{IB} \, \vec{q}^{(i)}_{x_B} \\ -G^{*T}_{xy} \, S_{BB} \, \vec{q}^{(i)}_{x_B} + \vec{P}^{(1)}_B \end{Bmatrix} . \tag{3.27}$$

It can be seen from eqn (3.27) that the first equation can be written as

$$\vec{q}_{x_I} = -S_{II}^{-1} [S_{IB} G_{xy} \{a\} + S_{IB} \vec{q}^{(i)}_{x_B}]. \tag{3.28}$$

subsituting eqn (3.11) and (3.28) into the second equation of (3.27), one obtain

$$[G^{*T}_{xy} (S_{BB} - S_{BI} S_{II}^{-1} S_{IB}) G_{xy} - R] \{ a \} =$$
$$- G^{*T}_{xy} (S_{BB} - S_{BI}^{-1} S_{II}^{-1} S_{IB}) \vec{q}^{(i)}_{x_B} + \vec{P}^{(i)}_B \tag{3.29}$$

Once eqn (3.29) is solved for the generalized coordinates $\{a\}$, the exterior and interior displacements can be calculated from eqn (3.4) and eqn (3.28), respectively. As the displacements for all $N_I + N_B$ nodes are known, the stress at each node can be solved accordingly.

CHAPTER 4

4.1 Numerial Results and Discussion

The object of this work is to analyse the motion of the shell excited by an incident seismic wave. Dynamic stresses, axial and hoop stresses, in the tunnel and the wall displacements are calculated when the tunnel is excited by plane longitudinal P wave and polarized shear SV and SH waves. The incident potentials $\phi^{(i)}$, $\psi^{(i)}$ and $\chi^{i)}$ representing these waves are given in Appendix 1. To obtain the dynamic amplification factor, the results for the displacements and stresses presented are normalized with respect to the maximum displacement and stress amplitudes of the incident waves respectively.

The numerical results presented here are for a concrete tunnel of thickness to radius ratio (T/A) = 0.2. The material properties of concrete used here are

$\rho \cong$ mass density = 2.24×10^3 kg/m^3 ,

E $\cong$ Young's modulus = 1.6×10^{10} N/m^2 ,

$\sigma \cong$ Poisson's ration = 0.2.

To show the dependence of the displacements and stresses on the material properties of the tunnel and the ground two representative cases have been considered here. In the first problem considered the tunnel is surrounded by a soft soil and in the second problem the tunnel is surrounded by rock material, these will be referred as Case I and Case II, respectively. The material properties of soft soil and rock considered here are given in Table 1.

TABLE 1

Material Properties of Soft Soil and Rock

Material Properties / Case	I Soft Soil	II Rock
ρ kg/m^3	$2.665 * 10^3$	$2.665 * 10^3$
E N/m^2	$6.9 * 10^8$	$7.567 * 10^9$
σ	0.45	0.25

Before we present the results for the tunnel, we would like to check the accuracy of our finite element method (FEEET). For this purpose, a cylindrical cavity inclusion of radius = a is analyzed by the exact solution (analytical method) and the finite element method (approximate solution). Results from these two methods at point P shown in the insert in Table 2 are presented in tabular forms for comparison. From Tables 2-7 we show the comparison between the predictions for the displacement and stress amplitudes by analytical and finite element methods for a circular cavity. It can be seen that the displacements and stresses agree quite well up to $k_2a = 2.0$. Here and in sequel k_2 implies $k_2 = k_{s_1}$, i.e. shear wave number of the host material. In the following numerical results for the tunnel are presented for k_2a less than 1.06.

(i) <u>Incident P-Wave</u>

First we will discuss the numerical results for incident P-wave. Figures 4-12 show the polar plots of results for incident longitudinal waves when the tunnel is embedded in a homogeneous soft soil referred to as Case I. The stresses and displacements are normalized with respect to the corresponding maximum free field stresses and displacements. In all figures the normalization factors are denoted by NF. It is seen from Fig. 4-6 that the axial stress amplification increases as the incident angle increases. As the incident angle becomes almost parallel the axis of the tunnel, the amplification reaches a maximum for the lowest frequency (or k_2a). Note that although the maximum amplification occurring at the lowest k_2a, it is not surprising that the axial stress amplitude increases with frequencies. It is also found that for small incident angle (Fig. 4) the axial stress amplification initially increases with k_2a and then decreases to the lower amplification value at the larger k_2a. But for the large incident angle, the amplification simply decreases with increasing k_2a (Fig. 6). As for the hoop stress, it is interesting to note that the normalized hoop stresses have a rather constant value irrespective of the incident angle. However, it is noted that the hoop stress amplification decreases with increasing k_2a for all incident angles. Figures 7-9 show the polar plottings for the axial displacement. It is found that the real part and the imaginary part of the axial displacement behave quite differently. The distribution of the real part has maximum value occurs at the lower portion of the tunnel for small incident angle. But the distribution becomes almost uniform around the tunnel as the incident angle increases to 85°. It should be noted that the imaginary part of the axial displacement has a rather uniform distribution around the tunnel irrespective of the shape of the tunnel and the incident angle. Figures 7-8 show that the changes in frequency do not affect the amplification of the imaginary part when incident angle is small. However it shows clearly in Fig. 9 that the amplification of the imaginary part decreases with increasing frequency. As for the real part, the amplification simply increases with frequency. Note that there is a maximum occurring at $\theta = 46.3°$ or $133.7°$ (Fig. 7), this maximum disappears as the incident angle increased to 85° (Fig. 9). Figures 10-12 show the changes in the shear stress σ_{rz} with frequency for different incident angles. It is found that the real and imaginary part behave differently. For incident angles 5° and 30°, the real part amplification of the shear stress decreases with increasing frequency while for 85° incidence (Fig. 12), the real part amplification increases with frequency. The imaginary part just behaves the other way round, first it increases with frequency for 5° incidence but decreases with frequency for 85° incidence. It should be noted that both the real and the imaginary part have maximum occurring at $\theta = 46.3$ or $133.7°$, but the maximum of the real part shifts to $\theta = 90°$ as the incident angle increased to 85° (Fig. 12).

Similar polar plottings are shown in Figs. 13-21 for the case when the tunnel is embedded in rock material which is referred to as Case II. It is found that the amplification of the axial stress and the hoop stress both decrease with frequency for all three incident angles. Howerver, it is noted from Fig. 14, the axial stress amplification of the upper arch top of the tunnel does not decrease with frequency, but rather increases as frequency increases. One more interesting point to be noted is that there is a pronounced maximum axial stress occurring at $\theta = 46.3°$ or $133.7°$ for 5° and 30° incidence. As noted earlier this maximum almost disappears when the incident angle is 85° (Fig. 15), in which there is an almost even axial stress amplification distribution around the tunnel. Figures 16-18 show that the maximum real part of the axial displacement occurring at $\theta = 270°$ (at the top of the tunnel) first increaes with increasing k_2a but then decreases after reaching the maximum. As for the imaginary part, the displacement distribution gets more and more even around the tunnel as the incident angle increases. From Figs. 19-20 it is noted that for the shear stress σ_{rz} the maximum amplification for the real part occurring at $\theta = 46.3°$ or $133.7°$ remains almost the same value irrespective of the changes in frequency. The real part amplification decreases with increasing frequency. The imaginary part of σ_{rz} has the maximum amplification at the same point on the tunnel as the real part, but this maximum first increases and then decreases with increasing frequency for small incident angles (Fig. 19-20). However, this maximum amplification monotonically decreases with increasing frequency for large incident angle (Fig. 21).

Figures 22-33 show the variations of the maximum axial stress, hoop stress, axial displacement and the shear stress σ_{rz} with incident angles for Case I and Case II. For each stress or displacement, only the results are presented for one small and one large wave number. From Figs. 22-23, it is seen that the hoop stress is much larger than the axial stress for all angles of incidence for Case I. However, this is not true in Case II when the tunnel is embedded in rock. Figures 24-25 show that for small incident angles, the hoop stress is greater than the axial stress, however, at an incident angle around 50°-55°, both stresses have equal value but after this point the hoop stress begins to have smaller values than the axial stress. It is found that the axial stress somewhat increases with increasing incident angle. But the hoop stress remains rather constant irrespective of the incident angle in

Case I. As in Case II, the hoop stress decreases with increasing incident angle. Figures 26-29 show the variation of the maximum real and imaginary part of the axial displacement with incident angle. For Case I and Case II the maximum of the imaginary part occurs at the larger incident angle which is almost parallel to the tunnel axis. It is found that for both cases, the maximum of the real part is very flat at low frequency but becomes very pronounced at high frequency. Note that the maximum does not occur at the largest incident angle but on some moderate incident angles depending on the frequency. Figures 30-33 show the variation of maximum shear stress $|\sigma_{rz}|$ with incident angle. It is found that the amplitude of the shear stress is smaller than the two other major stresses (the hoop stress and the axial stress) for all frequencies. It is noted that the imaginary part increases with increasing incident angle and has a maximum occurring at the larger incident angle in Case I. However, in Case II the imaginary part has a rather small and constant value at low frequency. At high frequency it first increases with increasing incident angles but then drops very slowly after reaching a maximum at a moderate incident angle. The variation of the real part is comparatively simple, it initially increases with increasing incident angle and then drops after the maximum. For both cases it should be noted that the maximum occurs at around 45° incidence for all frequencies.

For comparison purposes, stress and displacement results from Case I and Case II are plotted and compared in Figs. 34-45. Note that the circular frequency in the soft soil and the rock considered here is the same. And for the same wave speed the values of k_2a are different for the soft soil and rock. Figure 34-37 show the comparison between axial stress and hoop stress. It is found that the stress amplification factor for Case I is greater than that for Case II both for axial stress and hoop stress. It is also found that the axial stress and hoop stress induced on the tunnel wall when the wave is travelling in soft soil is much greater than those when wave is travelling in rock. Figures 38-41 show the comparison between the axial displacement. Not unexpectedly for small incident angle (i.e. wave is propagating almost perpendicular to tunnel axis) the amplitude of the real and imaginary part of the axial displacement in Case I is greater than those in Case II. However, the amplfication factor in Case II may be greater than that of Case I as in Fig. 38. Surprisingly, when wave is travelling at an incident angle almost parallel the tunnel axis the situation is reversed, both the amplitude and the amplfiication factor for the real and imaginary part in Case II is greater than those in Case I. Figures 42-45 show the comparison between the shear stress $|\sigma_{rz}|$. Obviously the shear stress in Case I is much greater than that in Case II, this agrees to what we have found from Figs. 38-41 for axial stress and hoop stress. This suggests that it is always true that stresses induced in the tunnel wall is much greater when the tunnel is embedded in soft soil than in rock. As for the axial displacement, the situation depends very much on the incident angle. It is observed that when the incident angle is small, the axial displacement for Case I is greater. As the incident angle is increased to almost parallel the tunnel axis, the axial displacement for Case II is dominantly greater.

(ii) Incident SV-Wave

Similar to P-wave set of plottings for SV-wave are given for discussion. Figures 46-54 show the polar plots of results for Case I. As opposed to the P-wave case Figs. 46-48 show that the axial stress amplification for SV-wave decreases as the incident angle increases. Unlike the P-wave where the maximum axial stress amplification occurring at the largest incident angle (85°) for the lowest frequency, in the SV-wave case the maximum amplification instead reaches a maximum at the lowest incident angle (5°) but also for the lowest frequency. One more thing in contrast to the P-wave case is that at small incident angle, the stress distribution is far more uniform around the tunnel wall than the uneven stress distribution at large incident angle. It is also found that the axial stress amplification decreases with increasing frequency. As for the hoop stress, it is noted that both the stress amplification and the stress amplitude decreases with increasing incident angle. Note that there is a pronounced maximum occurs at $\theta = 46.3°$ or $133.7°$ for all incident angles. Figures 49-51 show the polar plots for the real and imaginary part of the axial displacement. It is interesting to note that the maximum amplfication for the real part found at the top of the tunnel ($\theta = 270°$) at small or moderate incident angles shifted abruptly to $\theta = 46.3°$ or $133.7°$ at large incident angle. It is found that the real part amplification decreases with increasing frequency at large incident angle but increases with frequency at small incident angle. As for the imaginary part it is found that the distribution is rather uniform at small and moderate incident angles for low frequency (Fig. 49-50). Note that the amplification factor decreases with increasing frequency. Figures 52-54 show the similar plottings for σ_{rz}. For the real part, the interesting thing noticed is that the stress distribution for the moderate incident angle is quite different from the other incident angles. First the maximum stress occurred at the top of the tunnel at the moderate incident angle (30°), while for 5° and 85° incident angles the maximum occur at $\theta = 46.3°$ or 133.7°. Furthermore, the stress amplification somewhat decreass with increasing frequency for 5° and 85° incidences but for 30° incidence it is noted that the amplification on the upper portion of the tunnel increases with frequency. Note that the amplification is largest at 30° incidence. Like the real part, the behavior of the stress amplification of the imaginary part for the moderate incident angle is different from the other incident angles. Note that the maximum stress occurs at the top of the tunnel at 5° and 85° incidences, but shifted to $\theta = 46.3°$ or 133.7° at 30° incidence. It is found that the imaginary part amplification increases with increasing incident angle.

Similar plottings for Case II are presented in Figs. 55-63. It is interesting to find that the behavior for the axial stress and hoop stress at 5° incidence is somewhat identical to that at 30° incidence both for the amplification and the stress distribution. Note that the maximum axial stress occurs at the top of the tunnel for 5° and 30° incidences but shifted to the bottom of the tunnel for 85° incidence. It is also found that the maximum hoop stress at $\theta = 0°$ or 180° at 5° and 30° incidence moved downward to a point near $\theta = 46.3°$ or 133.7° at 85° incidence. From Figs. 58-60, it is noted that the maximum of the real part of the axial displacement at the top of the tunnel first increases and then decreases with increasing frequency for small incident angle. However, the maximum occurs at the bottom of the tunnel and monotonicaly decreases with increasing frequency for large incident angle. The stress distribution of the imaginary part is somewhat symmetric about x-axis for 5° and 30° incidence. However at 85° incidence the distribution is rather even around irrespective of the shape of the tunnel. Note that the amplification is largest at the largest angle of incidence. From Figs. 61-63 it is found that the real part of the shear stress σ_{rz} has maximum at $\theta = 46.3°$ or 133.7° for all incident angles. Note that for the largest incident angle, the maximum amplification remains a rather constant value irrespective of the changes in frequency. It is found that for the imaginary part, the maximum occurs at the top of the tunnel for large angle of incidence, while for small angle of incidence the maximum occurs at $\theta = 46.3°$ or 133.7°.

Variations of the maximum stresses and displacement with incident angle for Case I and Case II for SV-waves are shown in Figs. 64-75. It is seen from Figs. 64-75 that for SV-wave the axial stress is much larger than the hoop stress for all incident angles in Case I. Note that the maximum for both the axial stress and hoop stress occur at moderate incident angles. However the behavior in Case II is not as simple as in Case I as seen in Figs. 66-67. For small frequency (k_2a) the axial stress is smaller than the hoop stress for all incident angles. But for large frequency at incident angles 35°-75° (approx.) the hoop stress in turn is larger than the axial stress. Figures 68-71 show the variaton of maximum real and imaginary part of the axial displacement with incident angle. For both cases it is found that the maximum of the imaginary part occurs at the smallest incident angle for all frequencies. The imaginary part somewhat decreases with increasing incident angle, except there is a sudden drop at 35° incident for Case II at high frequency (Fig. 71). It is found that in Case I for small frequency, the real part has some very small and constant values irrespective of the incident angles. At high frequency a very pronounced maximum is found at 10° (approx.) incidence, and after this point the real part decreases with increasing incident angle at a moderate rate. For Case II, the real part initially decreases with increasing incident angle but then increases after reaching a minimum around 60°-70° incidence for both frequencies. Figures 72-75 show the variation of the maximum shear stress $|\sigma_{rz}|$ with incident angle. Again as found in the P-wave case, the shear stress is much smaller than the hoop stress and the axial stress. It is interesting to note that for small frequency the real part of the shear stress behave similarly for Case I and Case II. In both cases a very obvious minimum is found around 45° incident angle. However for large frequency it is noted that a very contrast situation appears, the maximum of the real part occurs at the smallest incident angle in Case I while in Case II the maximum occurs at the largest incident angle. For the imaginary part it should be noted that at high frequency for both cases, initially a maximum starts at the smallest incident angle and then begins to drop slowly as incident angle increases. However at an angle around 60° a second maximum occurs but with a smaller amplitude than the first maximum.

Comparison plottings for results from Case I and Case II are shown in Figs. 76-87. Observations made in P-wave case that the stress (hoop stress, axial stress and the shear stress σ_{rz}) amplitudes in Case I are much larger than those in Case II, apply to SV-wave case also. Again the astonishing axial displacement behavior observed in P-wave can also be found in SV-wave (Fig. 80-83). It is found that at the small incident angle the amplitude for both the real and imaginary part in Case I is much larger than those in Case II. However at the incident angle almost parallel to the axis of the tunnel, both the amplification and amplitude of the real and imaginary part in Case II is dramatically greater than those in Case I.

(iii) Incident SH Wave

Finally we will discuss the numerical results for incident SH-wave. Figures 88-96 show the polar plots of results for stresses and displacement induced by an incident SH-wave in Case I. From Figs. 88-90 it is found that the axial stress amplification somewhat decreases with increasing frequency for all angle of incidence, except for 85° incidence (Fig. 90) where the amplification initially increases a little and then decreases with the increasing frequency. Note that at 5° incidence there are two very pronounced maxima of approximately equal amplitude at θ = 46.3° or 133.7° and at θ = 62.2° or 117.8°. These maxima begin to become less pronounced as the incident angle increases and finally disappear at the largest incident angle. It should be noted that there are also two maxima hoop stress induced on the tunnel wall, however these maxima remain very pronounced for the 5° and 30° incident angle and there is still one of the maxima remaining at θ = 32° or 148.° as the incident angle increased to 85°. It should be noted in Figs. 91-93 that the normalization factor NF for the axial displacement is not shown because the incident free field axial displacement for SH-wave does not exist. The amplitude of the real part of the axial displacement increases with frequency for all incident angles. It is found that there are two maxima of equal amplitude (approx.) at the upper portion of the tunnel at $\theta = 228.7°$ or $311.3°$ and at the lower portion of the tunnel at $\theta = 138.8°$ or $41.2°$. The maximum at the lower portion of the tunnel begins to have smaller amplitude than the maximum at the upper portion as the incident angle increases. It is noted that the imaginary part of the axial displacement increases with frequency at small incident angle but decreases with increasing frequency at the largest incident angle. Figures 94-96 show the polar plots for the shear stress σ_{rz}. It is interesting to note that the amplification factors of the real part are approximately equal at 5° and 30° incident angle for all frequencies, especially at the upper portion of the tunnel. Note that the maximum of the real part somewhat decreases with increasing frequency for all incident angles. The imaginary part behaves similarly where the amplifications are nearly identical at 5° and 30° incidence. It is also found that the amplification simply decreases with increasing frequency for all incident angles.

Similar polar plots for Case II are shown in Figs. 97-105. It is surprising to find that the stress distribution of the axial stress on the flat bottom surface on the lower portion of the tunnel fluctuates drastically at small incident angle (Fig. 97) which do not happen in P or SV wave cases. It is found that the stress value fluctuates up and down rapidly along the bottom surface of the tunnel, but as the incident angle increased to 85° the stress distribution becomes a lot more "smooth" (Fig. 99). Note the very large amplification at 85° incidence, this is because the maximum incident free field axial stress is a very small value. Again the hoop stress distribution and the amplification for 5° incidence resembles those of 30° incidence irrespecitve of the change in incident angle. This somehow gives us an idea that the hoop stress is not very sensitive to the change in incident angle at small angles. Figures 100-102 show the polar plots for the axial displacement. The behavior of the real and imaginary part is comparatively simple, their amplification increases with frequency at all incident angles. Figures 103-105 show that the maximum amplification for the real part of σ_{rz} occurs at the lowest frequency for small incident angles. Note less than unity amplification for the imaginary part for 5°, 30° and 85° incident angles, which implies there is a reduction of the incident free field which subsequently induced on the tunnel wall.

Variations of the various stresses and the axial displacement with incident angle are shown in Figs. 106-117. From Figs. 106-107 it is found that the hoop stress is larger than the axial stress for small angles of incidence in Case I. The axial stress begins to have larger value at a certain incident angle depending on frequency, and remains to have larger value thereafter. As for Case II, the hoop stress has dominantly larger value than the axial stress for small frequency (Fig. 108). However for high frequency the axial stress in turn has larger value at large incident angles as in Fig. 109. Note that the hoop stress decreases with increasing incident angle for all frequencies in both cases. It should also be noted that the axial stress in Case II rises to a fairly stable value after 45° (approx.) incident angle. FIgures 110-111 show that the real part of the axial displacement has insignificant small values for small frequency but suddenly rises to a dominantly larger value than the imaginary part for high frequency in Case I. Note that the real and imaginary part has maximum at largest incident angle for small frequency while for large frequency the maximum occurs around moderate incident angles. As for Case II the real part of the axial displacement has smaller value than the imaginary part for small and large frequency (Fig. 112-113). It is interesting to find that the real part has three approximately equal amplitude minima occurring at 5°, 45° and 85° incident angles. Figures 114-117 show that the real part of the shear stress $|\sigma_{rz}|$ has some insignificant values for small frequency in both cases, and as for the imaginary part it keeps on increasing steadily with incident angle. For large frequency it is found that the real part has maximum occurring at moderate incident angles for both cases. While the imaginary part also has maximum at moderate incident angles in Case I but with maximum occurring at the largest incident angle in Case II.

Results for SH-wave similar to those of P-wave and SV-wave are found in Figs. 118-129 for comparison purpose of Case I and Case II. However, it is found that only the imaginary part of the axial displacement in Case II is greater than that in Case I at 85° incident angle. While the real part (distribution above the x-axis) at the same incident angle behaves the same way as the stresses do, i.e. values in Case I is larger than those in Case II.

REFERENCES

1. I. Nelson and P Weidlinger, "Dynamic Seismic Analysis of Long Segmented Lifeline", Journal of Pressure Vessel Technology, Vol. 101, 1979, pp.10-19.

2. L. R. L. Wang and M. O'Rourke, "State of the Art of Buried Lifeline Earthquake Engineering", Proceedings of the Current State of Lifeline Earthquake Engineering, ASCE, Los Angles, Califonia.

3. J. A. McFadden, "Radial Vibrations of Thick-Walled Hollow Cylinders", Journal of Acoustical Society of America, Vol. 26, 1954, pp.714-715.

4. G. Herrmann and I. Mirsky, "Three Dimensional and Shell-Theory Analysis of Axially Symmetric Motions of Cylinders", Trans. Am. Soc. Mech. Engrs., Paper n56-APM-32, June, 1956.

5. P. M. White, "Elastic Wave Scattering at a Cylindrical Discontinuity in a Solid", Journal of Acoustical Society of America, Vol. 30, 1958, pp.771-785.

6. Muleski, G. E., Ariman, T., and Aumen, C. F., "A Shell Model of a Buried Pipe in a Seismic Environment", J. Pressure Vessel Tech., Trans. ASME, Vol. 101, 1979, pp.44-50.

7. Muleski, G. E. and Ariman, T., "Improved Seismic Input and Soil Models and Quasi-Static Approximations in Buried Pipe", Earthquake Behavior and Safety of Oil and Gas Storage Facilities, Buried Pipelines and Equipment, Ed. T. Ariman, PVP-Vol. 77, ASME, New York, 1983, pp.202-208.

8. Hindy, A. and Novak, M., "Earthquake Response of Underground Pipelines", Earth. Engg. Str. Dyn., Vol. 7, 1979 ,pp.451-476.

9. Y. H. Pao and C. C. Mow, The Diffraction of Elastic Waves and Dynamic Stress Concentration, Crane and Russak, New York, 1973.

10. O. C. Zienkiewicz, D. W. Kelly and P. Bittess, "The Sommerfeld (Radiation) Condition on Infinite Domains and Its Modeling in Numerical Procedures", in Lecture Note in Mathmatics, Vol. 704, Eds. R. Glowinski and J. L. Lyons, Springer-Verlag, Berlin, pp.169-203, 1979.

11. P. Underwood and T. J. Geers, "Doubly Asymptotic, Boundary Element Analysis of Dynamic Soil-Structure Interaction", International Journal of Solids and Structures, Vol. 17, 1981, pp,687-697.

12. Tapesh Chakraborty, "Forced Vibrations of Continuous Pipeline Due to Propagating Seismic Loads", M. Sc. Thesis, University of Colorado, 1983.

13. S. K. Datta, A. H. Shah and N. El-Akily, "Dynamic Analysis of Embedded Pipelines", in Siesmic Risk Analysis and Its Application to Reliability Based Design of Lifeline Systems, Proceedings of Review Meeting of U. S.-Japan Cooperative Research, Honolulu, Hawaii, 1981, pp.143-172.

14. A. H. Shah, K. C. Wong and S. K. Datta "Single and Multiple Scattering of Elastic Waves in Two Dimensions", Journal of Acoustical Society of America, Vol. 74, n3, Sept. 1983, pp.1033-1043.

15. A. H. Shah, S. K. Datta, K. C. Wong and P. M. O'Leary, "Dynamic Amplification of Displacements and Stresses Around Buried Pipelines and Tunnels", ed. S. K. Datta, AMD-Vol. 60, ASME, New York, 1984, pp.147-162.

16. S. K. Datta, K. C. Wong, and A. H. Shah, "Dynamic Amplification of Stresses and Displacemments Induced in a Buried Pipe in a Semi-infinite Medium", Journal of Engineering Mechanics of A. S. C. E., Vol. 110, n10, Oct. 1984, pp.1451-1466.

17. Datta, S. K., Wong, K. C., and Shah, A. H., "Dynamic Stresses and Displacements Around Cylindrical Cavities of Arbitrary Shape", submitted for publication.

APPENDICES

APPENDIX 1

APPENDIX 1

Expressions for functions u_{r_i}, u_{t_i}, u_{z_i}, S_{r_i}, S_{rt_i}, S_{rz_i}, and S_{tt_i} (i=1,2,...,6) appearing in eqn (2.12) and (2.13) are given as

$$u_{r_1} = [\frac{n}{r} J_n (\alpha_2 r) - \alpha_2 J_{n+1} (\alpha_2 r)]$$

$$u_{r_2} = [\frac{n}{r} Y_n (\alpha_2 r) - \alpha_2 Y_{n+1} (\alpha_2 r)]$$

$$u_{r_3} = \frac{i\xi}{k_{s_2}} [\frac{n}{r} J_n(\beta_2 r) - \beta_2 J_{n+1} (\beta_2 r)]$$

$$u_{r_4} = \frac{i\xi}{k_{s_2}} [\frac{n}{r} Y_n (\beta_2 r) - \beta_2 Y_{n+1} (\beta_2 r)]$$

$$u_{r_5} = [\frac{in}{r} J_n (\beta_2 r)]$$

$$u_{r_6} = [\frac{in}{r} Y_n (\beta_2 r)]$$

$$u_{t_1} = [\frac{in}{r} J_n (\alpha_2 r)]$$

$$u_{t_2} = [\frac{in}{r} Y_n (\beta_2 r)]$$

$$u_{t_3} = [\frac{-n\xi}{k_{s_2} r} J_n (\beta_2 r)]$$

$$u_{t_4} = [\frac{-n\xi}{k_{s_2} r} Y_n (\beta_2 r)]$$

$$u_{t_5} = [\beta_2 J_{n+1} (\beta_2 r) - \frac{n}{r} J_n (\beta_2 r)]$$

$$u_{t_6} = [\ \beta_2 Y_{n+1}\ (\beta_2 r) - \frac{n}{r} Y_n\ (\beta_2 r)\ ]$$

$$u_{z_1} = [\ i\xi J_n\ (\alpha_2 r)\ ]$$

$$u_{z_2} = [\ i\xi Y_n\ (\alpha_2 r)\ ]$$

$$u_{z_3} = [\ \frac{\beta_2^2}{k_{s_2}} J_n\ (\beta_2 r)\ ]$$

$$u_{z_4} = [\ \frac{\beta_2^2}{k_{s_2}} Y_n\ (\beta_2 r)\ ]$$

$$u_{z_5} = u_{z_6} = 0$$

$$S_{r_1} = [\ \frac{2n(n-1)}{r^2} - (\beta_2^2 - \xi^2)\ ]\ J_n\ (\alpha_2 r) + \frac{2\alpha_2}{r} J_{n+1}\ (\alpha_2 r)$$

$$S_{r_2} = [\ \frac{2n(n-1)}{r^2} - (\beta_2^2 - \xi^2)\ ]\ Y_n\ (\alpha_2 r) + \frac{2\alpha_2}{r} Y_{n+1}\ (\alpha_2 r)$$

$$S_{r_3} = \frac{2i\xi}{k_{s_2}} [\ (\frac{n(n-1)}{r^2} - \beta_2^2)\ J_n(\beta_2 r) + \frac{\beta_2}{r} J_{n+1}\ (\beta_2 r)\ ]$$

$$S_{r_4} = \frac{2i\xi}{k_{s_2}} [\ (\frac{n(n-1)}{r^2} - \beta_2^2)\ Y_n(\beta_2 r) + \frac{\beta_2}{r} Y_{n+1}\ (\beta_2 r)\ ]$$

$$S_{r_5} = \frac{2in}{r} [\ -\beta_2 J_{n+1}\ (\beta_2 r) + \frac{(n-1)}{r} J_n\ (\beta_2 r)\ ]$$

$$S_{r_6} = \frac{2in}{r} [\ -\beta_2 Y_{n+1}\ (\beta_2 r) + \frac{(n-1)}{r} Y_n\ (\beta_2 r)\ ]$$

$$S_{rt_1} = \frac{2in}{r} \left[-\alpha_2 J_{n+1} (\alpha_2 r) + \frac{(n-1)}{r} J_n (\alpha_2 r) \right]$$

$$S_{rt_2} = \frac{2in}{r} \left[-\alpha_2 Y_{n+1} (\alpha_2 r) + \frac{(n-1)}{r} Y_n (\alpha_2 r) \right]$$

$$S_{rt_3} = - \frac{2n\xi}{k_{s_2} r} \left[\frac{(n-1)}{r} J_n (\beta_2 r) - \beta_2 J_{n+1} (\beta_2 r) \right]$$

$$S_{rt_4} = - \frac{2n\xi}{k_{s_2} r} \left[\frac{(n-1)}{r} J_n (\beta_2 r) - \beta_2 Y_{n+1} (\beta_2 r) \right]$$

$$S_{rt_5} = - \left[\frac{2n(n-1)}{r^2} - \beta_2^2 \right] J_n (\beta_2 r) - \frac{2\beta_2}{r} J_{n+1} (\beta_2 r)$$

$$S_{rt_6} = - \left[\frac{2n(n-1)}{r^2} - \beta_2^2 \right] Y_n (\beta_2 r) - \frac{2\beta_2}{r} Y_{n+1} (\beta_2 r)$$

$$S_{rz_1} = - 2i\xi \left[\alpha_2 J_{n+1} (\alpha_2 r) - \frac{n}{r} J_n (\alpha_2 r) \right]$$

$$S_{rz_2} = - 2i\xi \left[\alpha_2 Y_{n+1} (\alpha_2 r) - \frac{n}{r} Y_n (\alpha_2 r) \right]$$

$$S_{rz_3} = \frac{1}{k_{s_2}} (\beta_2^2 - \xi^2) \left[\frac{n}{r} J_n (\beta_2 r) - \beta_2 J_{n+1} (\beta_2 r) \right]$$

$$S_{rz_4} = \frac{1}{k_{s_2}} (\beta_2^2 - \xi^2) \left[\frac{n}{r} Y_n (\beta_2 r) - \beta_2 Y_{n+1} (\beta_2 r) \right]$$

$$S_{rz_5} = \left[\frac{-n\xi}{r} J_n (\beta_2 r) \right]$$

$$S_{rz_6} = \left[\frac{-n\xi}{r} Y_n (\beta_2 r) \right]$$

$$S_{tt_1} = [\ 2\alpha_2^2 + \xi^2 - \beta_2^2 - \frac{2n(n-1)}{r^2}\ ]\ J_n\ (\alpha_2 r) - \frac{2\alpha_2}{r} J_{n+1}\ (\alpha_2 r)$$

$$S_{tt_2} = [\ 2\alpha_2^2 + \xi^2 - \beta_2^2 - \frac{2n(n-1)}{r^2}\ ]\ Y_n\ (\alpha_2 r) - \frac{2\alpha_2}{r} Y_{n+1}\ (\alpha_2 r)$$

$$S_{tt_3} = - \frac{2i\xi}{k_{s_2} r}\ [\ \frac{n(n-1)}{r} J_n\ (\beta_2 r) + \beta_2 J_{n+1}\ (\beta_2 r)\ ]$$

$$S_{tt_4} = - \frac{2i\xi}{k_{s_2} r}\ [\ \frac{n(n-1)}{r} Y_n\ (\beta_2 r) + \beta_2 Y_{n+1}\ (\beta_2 r)\ ]$$

$$S_{tt_5} = \frac{2in}{r}\ [\ \beta_2 J_{n+1}\ (\beta_2 r) - \frac{(n-1)}{r} J_n\ (\beta_2 r)\ ]$$

$$S_{tt_6} = \frac{2in}{r}\ [\ \beta_2 Y_{n+1}\ (\beta_2 r) - \frac{(n-1)}{r} Y_n\ (\beta_2 r)\ ]$$

REGION R_1

The expressions for functions D_{r_i}, D_{t_i}, D_{z_i}, E_{r_i}, E_{rt_i}, E_{rz_i} and E_{tt_i} (i=1,2,3) appearing in eqns (2.15) and (2.16) are written as

Scattered Field

$$D_{r_1} = [\ \frac{n}{r} H_n\ (\alpha_1 r) - \alpha_1 H_{n+1}\ (\alpha_1 r)\ ]$$

$$D_{r_2} = \frac{i\xi}{k_{s_1}}\ [\ \frac{n}{r} H_n\ (\beta_1 r) - \beta_1 H_{n+1}\ (\beta_1 r)\ ]$$

$$D_{r_3} = [\ \frac{in}{r} H_n\ (\beta_1 r)\ ]$$

$$D_{t_1} = \left[\frac{in}{r} H_n \; (\alpha_1 r) \right]$$

$$D_{t_2} = \left[- \frac{n \; \xi}{k_{s_1} r} H_n \; (\beta_1 r) \right]$$

$$D_{t_3} = \left[\beta_1 H_{n+1} \; (\beta_1 r) - \frac{n}{r} H_n \; (\beta_1 r) \right]$$

$$D_{z_1} = \left[i\xi H_n \; (\alpha_1 r) \right]$$

$$D_{z_2} = \left[\frac{\beta_1^2}{k_{s_1}} H_n \; (\beta_1 r) \right]$$

$$D_{z_3} = 0$$

$$E_{r_1} = \left[\frac{2n(n-1)}{r^2} - (\beta_1^2 - \xi^2) \right] H_n \; (\alpha_1 r) + \frac{2\alpha_1}{r} H_{n+1} \; (\alpha_1 r)$$

$$E_{r_2} = \frac{2i\xi}{k_{s_1}} \left[\left(\frac{n(n-1)}{r^2} - \beta_1^2\right) H_n \; (\beta_1 r) + \frac{\beta_1}{r} H_{n+1} \; (\beta_1 r) \right]$$

$$E_{r_3} = \frac{2in}{r} \left[- \beta_1 H_{n+1} \; (\beta_1 r) + \frac{(n-1)}{r} H_n \; (\beta_1 r) \right]$$

$$E_{rt_1} = -2i\xi \left[\alpha_1 H_{n+1} \; (\alpha_1 r) - \frac{n}{r} H_n \; (\alpha_1 r) \right]$$

$$E_{rt_2} = - \frac{2n\xi}{k_{s_1} r} \left[\frac{(n-1)}{r} H_n \; (\beta_1 r) - \beta_1 H_{n+1} \; (\beta_1 r) \right]$$

$$E_{rt_3} = - \left[\frac{2n(n-1)}{r^2} - \beta_1^2 \right] H_n \; (\beta_1 r) - \frac{2\beta_1}{r} H_{n+1} \; (\beta_1 r)$$

$$E_{rz_1} = -2i\xi \left[\alpha_1 H_{n+1} \; (\alpha_1 r) - \frac{n}{r} H_n \; (\alpha_1 r) \right]$$

$$E_{rz_2} = \frac{1}{k_{s_1}} (\beta_1^2 - \xi^2) [\frac{n}{r} H_n (\beta_1 r) - \beta_1 H_{n+1} (\beta_1 r)]$$

$$E_{rz_3} = [- \frac{n\xi}{r} H_n (\beta_1 r)]$$

$$E_{tt_1} = [(2\alpha_1^2 + \xi^2 + \beta_1^2) H_n (\alpha_1 r) - \frac{2\alpha_1}{r} H_{n+1} (\alpha_1 r)]$$

$$E_{tt_2} = - \frac{2i\xi}{k_{s_1} r} [\frac{n(n-1)}{r} H_n (\beta_1 r) + \beta_1 H_{n+1} (\beta_1 r)]$$

$$E_{tt_3} = \frac{2in}{r} [\beta_1 H_{n+1} (\beta_1 r) - \frac{(n-1)}{r} H_n (\beta_1 r)]$$

Incident Field

For each type of dilatational P wave and shear SV and SH waves, corresponding components of displacement and stress fields are listed.

1) Incident P Wave

For P-Wave $\phi^{(i)} = J_n (\alpha_1 r) e^{in\theta} e^{i\xi z} e^{-i\omega t}$

$$u_r^{(i)} = [\frac{n}{r} J_n (\alpha_2 r) - \alpha_2 J_{n+1} (\alpha_2 r)] e^{i\psi}$$

$$u_\theta^{(i)} = [\frac{in}{r} J_n (\alpha_1 r)] e^{i\psi}$$

$$u_z^{(i)} = [i\xi J_n(\alpha_1 r)] e^{i\psi}$$

$$\frac{\sigma_{rr}^{(i)}}{\mu_1} = \{[\frac{2n(n-1)}{r^2} - (\beta_1^2 - \xi^2)] J_n (\alpha_1 r) + \frac{2\alpha_1}{r} J_{n+1} (\alpha_1 r)\} e^{i\psi}$$

$$\frac{\sigma_{r\theta}^{(i)}}{\mu_1} = \{ \frac{2in}{r} [-\alpha_1 J_{n+1} (\alpha_1 r) + \frac{(n-1)}{r} J_n (\alpha_1 r)]\} e^{i\psi}$$

$$\frac{\sigma_{rz}^{(i)}}{\mu_1} = \{ -2i\xi [\alpha_1 J_{n+1} (\alpha_1 r) - \frac{n}{r} J_n (\alpha_1 r)] e^{i\psi}$$

$$\frac{\sigma_{\theta\theta}^{(i)}}{\mu_1} = \{(2\alpha_1^2 + \xi^2 - \beta_1^2 - \frac{2n(n-1)}{r^2}) J_n (\alpha_1 r) - \frac{2\alpha_1}{r} J_{n+1} (\alpha_1 r)\} e^{i\psi}$$

2) Incident SV-Wave

$$\text{For SV-Wave} \quad \chi^{(i)} = -\frac{i}{\cos\psi_0} J_n\,(\beta_1 r)\; e^{in\theta} e^{i\xi z} e^{-i\omega t}$$

$$u_r^{(i)} = -\frac{i}{\cos\psi_0}\left\{ \frac{i\xi}{k_{s_1}} \left[\frac{n}{r} J_n\,(\beta_1 r) - \beta_1 J_{n+1}(\beta_1 r) \right]\right\} e^{i\psi}$$

$$u_\theta^{(i)} = -\frac{i}{\cos\psi_0}\left[-\frac{n\xi}{k_{s_1} r} J_n\,(\beta_1 r) \right] e^{i\psi}$$

$$u_z^{(i)} = -\frac{i}{\cos\psi_0}\left[\frac{\beta_1^2}{k_{s_1}} J_n\,(\beta_1 r) \right] e^{i\psi}$$

$$\frac{\sigma_{rr}^{(i)}}{\mu_1} = -\frac{i}{\cos\psi_0}\left\{ \frac{2i\xi}{k_{s_1}} \left[\left(\frac{n(n-1)}{r^2} - \beta_1^2 \right) J_n\,(\beta_1 r) + \frac{\beta_1}{r} J_{n+1}\,(\beta_1 r) \right]\right\} e^{i\psi}$$

$$\frac{\sigma_{rz}^{(i)}}{\mu_1} = -\frac{i}{\cos\psi_0}\left\{ \frac{1}{k_{s_1}} (\beta_1^2 - \xi^2) \left[\frac{n}{r} J_n(\beta_1 r) - \beta_1 J_{n+1}\,(\beta_1 r) \right]\right\} e^{i\psi}$$

$$\frac{\sigma_{\theta\theta}^{(i)}}{\mu_1} = -\frac{i}{\cos\psi_0}\left\{ -\frac{2i\xi}{k_{s_1} r} \left[\frac{n(n-1)}{r} J_n\,(\beta_1 r) + \beta_1 J_{n+1}\,(\beta_1 r) \right]\right\} e^{i\psi}$$

3) Incident SH-Wave

$$\text{For SH-Wave} \quad \psi^{(i)} = -\frac{i}{\cos\psi_0} J_n\,(\beta_1 r)\; e^{in\theta} e^{i\xi z} e^{-i\omega t}$$

$$u_r^{(i)} = -\frac{i}{\cos\psi_0}\left[\frac{in}{r} J_n\,(\beta_1 r) \right] e^{i\psi}$$

$$u_\theta^{(i)} = -\frac{i}{\cos\psi_0}\left[\beta_1 J_{n+1}\,(\beta_1 r) - \frac{n}{r} J_n(\beta_1 r) \right] e^{i\psi}$$

$$u_z^{(i)} = 0$$

$$\frac{\sigma_{rr}^{(i)}}{\mu_1} = -\frac{i}{\cos\psi_0}\left\{ \frac{2in}{r} \left[-\beta_1 J_{n+1}\,(\beta_1 r) + \frac{(n-1)}{r} J_n\,(\beta_1 r) \right]\right\} e^{i\psi}$$

$$\frac{\sigma_{r\theta}^{(i)}}{\mu_1} = - \frac{i}{\cos\psi_0} \{ - [\frac{2n(n-1)}{r^2} - \beta_1^2] J_n (\beta_1 r) - \frac{2\beta_1}{r} J_{n+1} (\beta_1 r) \} e^{i\psi}$$

$$\frac{\sigma_{rz}^{(i)}}{\mu_1} = - \frac{i}{\cos\psi_0} [- \frac{n\xi}{r} J_n (\beta_1 r)] e^{i\psi}$$

$$\frac{\sigma_{\theta\theta}^{(i)}}{\mu_1} = - \frac{i}{\cos\psi_0} \{ \frac{2in}{r} [\beta_1 J_{n+1} (\beta_1 r) - \frac{(n-1)}{r} J_n (\beta_1 r)] \} e^{i\psi}$$

Note that in all the expressions in this Appendix, summation sign is omitted. For the purpose of numerical solution, the limit of the summation in all the expressions is taken from $n = -(\frac{m}{2} - 1)$ to $\frac{m}{2}$. In which 'm' is the total number of terms taken for evaluation.

APPENDIX 2

APPENDIX 2

Incident Field

For each type of wave corresponding components of displacement and stress fields are listed in cartesian coordinates.

i) Incident P Wave

$$\phi^{(i)} = e^{i(\xi z + \alpha_1 y)}$$

$$u_x^{(i)} = 0$$

$$u_y^{(i)} = i\,\alpha_1\, e^{i(\xi z + \alpha_1 y)}$$

$$u_z^{(i)} = i\,\xi\, e^{i(\xi z + \alpha_1 y)}$$

$$\frac{\sigma_{xx}^{(i)}}{\mu_1} = -\lambda_1^* k_{p_1}^2\, e^{i(\xi z + \alpha_1 y)}$$

$$\frac{\sigma_{yy}^{(i)}}{\mu_1} = -(\lambda_1^* k_{p_1}^2 + 2\,\alpha_1^2) e^{i(\xi z + \alpha_1 y)}$$

$$\frac{\sigma_{zz}^{(i)}}{\mu_1} = -(\lambda_1^* k_{p_1}^2 + 2\,\xi^2) e^{i(\xi z + \alpha_1 y)}$$

$$\frac{\sigma_{yz}^{(i)}}{\mu_1} = -2\,\xi\alpha_1 e^{i(\xi z + \alpha_1 y)}$$

$$\sigma_{xy}^{(i)} = \sigma_{xz}^{(i)} = 0$$

in which λ_1 is normalized by μ_1 such that

$$\lambda_1^* = \frac{\lambda_1}{\mu_1}$$

ii) Incident SV Wave

$$\chi^{(i)} = e^{i\xi z} e^{i\beta_1 y}$$

$$u_x^{(i)} = 0$$

$$u_y^{(i)} = i\ \xi\ e^{i(\xi z + \beta_1 y)}$$

$$u_z^{(i)} = -\ i\ \beta_1 e^{i(\xi z + \beta_1 y)}$$

$$\sigma_{xx}^{(i)} = 0$$

$$\frac{\sigma_{yy}^{(i)}}{\mu_1} = -\ 2\ \xi\ \beta_1\ e^{i(\xi z + \beta_1 y)}$$

$$\frac{\sigma_{zz}^{(i)}}{\mu_1} = 2\ \xi\ \beta_1\ e^{i(\xi z + \beta_1 y)}$$

$$\frac{\sigma_{yz}^{(i)}}{\mu_1} = (\beta_1^2 - \xi^2)\ e^{i(\xi z + \beta_1 y)}$$

$$\sigma_{xy}^{(i)} = \sigma_{xz}^{(i)} = 0$$

iii) Incident SH Wave

$$\psi^{(i)} = e^{i\xi z}\ e^{i\beta_1 y}$$

$$u_x^{(i)} = k_{s_1}\ e^{i(\xi z + \beta_1 y)}$$

$$u_y^{(i)} = 0$$

$$u_z^{(i)} = 0$$

$$\sigma_{xx}^{(i)} = \sigma_{yy}^{(i)} = \sigma_{zz}^{(i)} = \sigma_{yz}^{(i)} = 0$$

$$\frac{\sigma_{xy}^{(i)}}{\mu_1} = i\ k_{s_1}\ \beta_1\ e^{i(\xi z + \beta_1 y)}$$

$$\frac{\sigma_{xz}^{(i)}}{\mu_1} = i\ \xi\ k_{s_1}\ e^{i(\xi z + \beta_1 y)}$$

Matrix definition

The matrix $[G_{r\theta}]$ from eqn. (3.2) is made up by known functions for the scattered displacement fields which evaluated at the boundary and can be defined as

$$
[\,G_{r\theta}\,]_{r=b} = \left[\begin{array}{ccc}
\{Dr_{1_n}^{(\theta_1)}\}^T & \{Dr_{2_n}^{(\theta_1)}\}^T & \{Dr_{3_n}^{(\theta_1)}\}^T \\
\{Dr_{1_n}^{(\theta_2)}\}^T & \{Dr_{2_n}^{(\theta_2)}\}^T & \{Dr_{3_n}^{(\theta_2)}\}^T \\
\vdots & \vdots & \vdots \\
\{Dr_{1_n}^{(\theta_{NB})}\}^T & \{Dr_{2_n}^{(\theta_{NB})}\}^T & \{Dr_{3_n}^{(\theta_{NB})}\}^T \\
\hline
\{Dt_{1_n}^{(\theta_1)}\}^T & \{Dt_{2_n}^{(\theta_1)}\}^T & \{Dt_{3_n}^{(\theta_1)}\}^T \\
\{Dt_{1_n}^{(\theta_2)}\}^T & \{Dt_{2_n}^{(\theta_2)}\}^T & \{Dt_{3_n}^{(\theta_2)}\}^T \\
\vdots & \vdots & \vdots \\
\{Dt_{1_n}^{(\theta_{NB})}\}^T & \{Dt_{2_n}^{(\theta_{NB})}\}^T & \{Dt_{3_n}^{(\theta_{NB})}\}^T \\
\hline
\{Dz_{1_n}^{(\theta_1)}\}^T & \{Dz_{2_n}^{(\theta_1)}\}^T & \{Dz_{3_n}^{(\theta_1)}\}^T \\
\{Dz_{1_n}^{(\theta_2)}\}^T & \{Dz_{2_n}^{(\theta_2)}\}^T & \{Dz_{3_n}^{(\theta_2)}\}^T \\
\vdots & \vdots & \vdots \\
\{Dz_{1_n}^{(\theta_{NB})}\}^T & \{Dz_{2_n}^{(\theta_{NB})}\}^T & \{Dz_{3_n}^{(\theta_{NB})}\}^T
\end{array}\right]
$$

where θ_j is the angle of the j^{th} node on the boundary.

The size of the transformation matrix [T] depends on the number of nodes taken on boundary B. For the purpose of illustration, assume that the total number of boundary nodes = 4, then the size of [T] will be 12x12, and can be written as

$$[T]^T = \left[\begin{array}{ccc|ccc|ccc|ccc}
\cos\theta_1 & \sin\theta_1 & 0 & 0 & 0 & 0 & 0 & 0 & 0 & 0 & 0 & 0 \\
0 & 0 & 0 & \cos\theta_2 & \sin\theta_2 & 0 & 0 & 0 & 0 & 0 & 0 & 0 \\
0 & 0 & 0 & 0 & 0 & 0 & \cos\theta_3 & \sin\theta_3 & 0 & 0 & 0 & 0 \\
0 & 0 & 0 & 0 & 0 & 0 & 0 & 0 & 0 & \cos\theta_4 & \sin\theta_4 & 0 \\
\hdashline
-\sin\theta_1 & \cos\theta_1 & 0 & 0 & 0 & 0 & 0 & 0 & 0 & 0 & 0 & 0 \\
0 & 0 & 0 & -\sin\theta_2 & \cos\theta_2 & 0 & 0 & 0 & 0 & 0 & 0 & 0 \\
0 & 0 & 0 & 0 & 0 & 0 & -\sin\theta_3 & \cos\theta_3 & 0 & 0 & 0 & 0 \\
0 & 0 & 0 & 0 & 0 & 0 & 0 & 0 & 0 & -\sin\theta_4 & \cos\theta_4 & 0 \\
\hdashline
0 & 0 & 1 & 0 & 0 & 0 & 0 & 0 & 0 & 0 & 0 & 0 \\
0 & 0 & 0 & 0 & 0 & 1 & 0 & 0 & 0 & 0 & 0 & 0 \\
0 & 0 & 0 & 0 & 0 & 0 & 0 & 0 & 1 & 0 & 0 & 0 \\
0 & 0 & 0 & 0 & 0 & 0 & 0 & 0 & 0 & 0 & 0 & 1
\end{array}\right]_{12\times 12}$$

Matrix $[F_{r\theta}]$ is composed of the known terms from the scattered stress fields, as from eqn (3.6) which evaluated at the boundary.

$$
[\,F_{r\theta}\,]_{r=b} = \left[\begin{array}{ccc}
\{Er_{1_n}(\theta_1)\}^T & \{Er_{2_n}(\theta_1)\}^T & \{Er_{3_n}(\theta_1)\}^T \\
\vdots & \vdots & \vdots \\
\{Er_{1_n}(\theta_{N_B})\}^T & \{Er_{2_n}(\theta_{N_B})\}^T & \{Er_{3_n}(\theta_{N_B})\}^T \\
\hline
\{Ert_{1_n}(\theta_1)\}^T & \{Ert_{2_n}(\theta_1)\}^T & \{Ert_{3_n}(\theta_1)\}^T \\
\vdots & \vdots & \vdots \\
\{Ert_{1_n}(\theta_{N_B})\}^T & \{Ert_{2_n}(\theta_{N_B})\}^T & \{Ert_{3_n}(\theta_{N_B})\}^T \\
\hline
\{Ez_{1_n}(\theta_1)\}^T & \{Ez_{2_n}(\theta_1)\}^T & \{Ez_{3_n}(\theta_1)\}^T \\
\vdots & \vdots & \vdots \\
\{Erz_{1_n}(\theta_{NB})\}^T & \{Erz_{2_n}(\theta_{NB})\}^T & \{Erz_{3_n}(\theta_{NB})\}^T
\end{array}\right]
$$

Matrix [Q_{ij}]

Matrix [Q_{ij}] = [B_i^*]^T [D] [B_j] can be written as

$$
[Q_{ij}] = \left[\begin{array}{c:c:c}
\begin{gathered} D_1 N_{i,x} + D_3 \xi^2 N_i N_j + \\ D_3 N_{i,y} N_{j,y} \end{gathered} & D_2 N_{i,x} N_{j,y} + D_3 N_{i,y} N_{j,x} & D_2 \hat{\imath} \xi N_{i,x} N_j - D_3 \hat{\imath} \xi N_i N_{j,x} \\ \hdashline
\begin{gathered} D_2 N_{i,y} N_{j,x} + \\ D_3 N_{i,x} N_{j,y} \end{gathered} & \begin{gathered} D_1 N_{i,y} N_{j,y} + D_3 \xi^2 N_i N_j + \\ D_3 N_{i,x} N_{j,x} \end{gathered} & D_2 \hat{\imath} \xi N_{i,y} N_j - D_3 \hat{\imath} \xi N_i N_{j,y} \\ \hdashline
\begin{gathered} -D_2 \hat{\imath} \xi N_i N_{j,x} + \\ D_3 \hat{\imath} \xi N_{i,x} N_j \end{gathered} & -D_2 \hat{\imath} \xi N_i N_{j,y} + D_3 \hat{\imath} \xi N_{i,y} N_j & \begin{gathered} D_1 \xi^2 N_i N_j + D_3 N_{i,y} N_{j,y} + \\ D_3 N_{i,x} N_{j,x} \end{gathered}
\end{array}\right]
$$

which is Hermitian, and $\hat{\imath} = \sqrt{-1}$,

$$
N_{i,x} = \frac{\partial N_i(x,y)}{\partial x} \quad ; \quad N_{i,y} = \frac{\partial N_i(x,y)}{\partial y}
$$

Transformation Process

Since

$$
\begin{aligned}
[\ Q_{ij}\ ] &= [\ B_i^*\ ]^T\ [\ D\ ]\ [\ B_j\ ] \\
&= [\ B_i^*\ ]^T [\ Q_j\ ]
\end{aligned}
$$

$$[\,B_i^*\,]^T = \begin{bmatrix} N_{i,x} & 0 & 0 & 0 & -\hat{\imath}\xi N_i & N_{i,y} \\ 0 & N_{i,y} & 0 & -\hat{\imath}\xi N_i & 0 & N_{i,x} \\ 0 & 0 & -\hat{\imath}\xi N_i & N_{i,y} & N_{i,x} & 0 \end{bmatrix}$$

$$[\,Q_j\,] = \begin{bmatrix} D_1 N_{j,x} & D_2 N_{j,y} & D_2 \hat{\imath}\xi N_j \\ D_2 N_{j,x} & D_1 N_{j,y} & D_2 \hat{\imath}\xi N_j \\ D_2 N_{j,x} & D_2 N_{j,y} & D_1 \hat{\imath}\xi N_j \\ 0 & D_3 \hat{\imath}\xi N_j & D_3 N_{j,y} \\ D_3 \hat{\imath}\xi N_j & 0 & D_3 N_{j,x} \\ D_3 N_{j,y} & D_3 N_{j,x} & 0 \end{bmatrix}$$

Then divide every third column of $[\,B_i^*\,]^T$ and $[\,Q_j\,]$ by $\sqrt{-1}$, and the multiply again each third row by $\sqrt{-1}$, this will yield

$$[\,\overline{B}_i^*\,]^T = \begin{bmatrix} N_{i,x} & 0 & 0 & 0 & -\hat{\imath}\xi N_i & N_{i,y} \\ 0 & N_{i,y} & 0 & -\hat{\imath}\xi N_i & 0 & N_{i,x} \\ 0 & 0 & \xi N_i & \hat{\imath} N_{i,y} & \hat{\imath} N_{i,x} & 0 \end{bmatrix}$$

$$
[\,\overline{Q}_j\,] = \begin{bmatrix} D_1N_{j,x} & D_2N_{j,y} & D_2\xi N_j \\ D_2N_{j,x} & D_1N_{j,y} & D_2\xi N_j \\ D_2N_{j,x} & D_2N_{j,y} & D_1\xi N_j \\ 0 & D_3\hat{1}\xi N_j & -D_3\hat{1}N_{j,y} \\ D_3\hat{1}\xi N_j & 0 & -D_3\hat{1}N_{j,x} \\ D_3N_{j,y} & D_3N_{j,x} & 0 \end{bmatrix}
$$

in which the upper bar means transformed matrix.

And $[\,\overline{Q}_{ij}\,] = [\,\overline{B}_i^*\,]^T\,[\,\overline{Q}_j\,]$

where $[\,\overline{Q}_{ij}\,]$ is a symmetric real matrix and is written as

$$
[\,\overline{Q}_{ij}\,] = \begin{bmatrix} D_1N_{i,x}+D_3\xi^2N_iN_j+ D_3N_{i,y}N_{j,y} & D_2N_{i,x}N_{j,y}+D_3N_{i,y}N_{j,x} & D_2\xi N_{i,x}N_j-D_3\xi N_iN_{j,x} \\ & D_1N_{i,y}N_{j,y}+D_3\xi^2N_iN_j+ D_3N_{i,x}N_{j,x} & D_2\xi N_{i,y}N_j-D_3\xi N_iN_{j,y} \\ \text{SYMMETRY} & & D_1\xi^2N_iN_j+D_3N_{i,y}N_{j,y}+ D_3N_{i,x}N_{j,x} \end{bmatrix}
$$

A P P E N D I X 3

TABLES

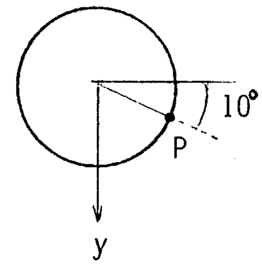

k_2a	FEM-36 Nodes UR	FEM-36 Nodes UZ	ANL-36 Terms UR	ANL-36 Terms UZ
0.1	0.299(-1)	0.261(-2)	0.299(-1)	0.261(-2)
0.2	0.616(-1)	0.519(-2)	0.617(-1)	0.519(-2)
0.4	0.138	0.103(-1)	0.139	0.103(-1)
0.6	0.241	0.159(-1)	0.244	0.159(-1)
0.8	0.354	0.227(-1)	0.362	0.226(-1)
1.2	0.467	0.339(-1)	0.484	0.339(-1)
1.6	0.517	0.398(-1)	0.544	0.399(-1)
2.0	0.589	0.461(-1)	0.627	0.463(-1)

k_2a	FEM-36 Nodes STT	FEM-36 Nodes SZZ	ANL-36 Terms STT	ANL-36 Terms SZZ
0.1	0.152(-1)	0.693(-2)	0.150(-1)	0.678(-2)
0.2	0.633(-1)	0.289(-1)	0.626(-1)	0.283(-1)
0.4	0.288	0.132	0.285	0.129
0.6	0.759	0.346	0.751	0.339
0.8	1.48	0.673	1.46	0.659
1.2	2.70	1.23	2.68	1.21
1.6	3.66	1.66	3.66	1.65
2.0	4.94	2.23	4.99	2.25

Table 2 : Comparison of displacements and stresses for P-Wave, Incident angle = 5

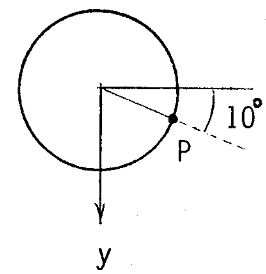

k_2a	FEM-36 Nodes UR	UZ	ANL-36 Terms UR	UZ
0.1	0.859(-2)	0.994(-1)	0.859(-2)	0.994(-1)
0.2	0.173(-1)	0.199	0.173(-1)	0.199
0.4	0.356(-1)	0.396	0.358(-1)	0.397
0.6	0.552(-1)	0.577	0.557(-1)	0.582
0.8	0.738(-1)	0.724	0.751(-1)	0.735
1.2	0.959(-1)	0.953	0.100	0.985
1.6	0.111	1.13	0.120	1.19
2.0	0.124	1.23	0.141	1.34

k_2a	FEM-36 Nodes STT	SZZ	ANL-36 Terms STT	SZZ
0.1	0.162(-2)	0.331(-2)	0.154(-2)	0.321(-2)
0.2	0.659(-2)	0.133(-1)	0.625(-2)	0.129(-1)
0.4	0.262(-1)	0.531(-1)	0.248(-1)	0.513(-1)
0.6	0.519(-1)	0.114	0.484(-1)	0.110
0.8	0.647(-1)	0.183	0.582(-1)	0.175
1.2	0.102	0.281	0.947(-1)	0.254
1.6	0.198	0.583	0.181	0.542
2.0	0.299	0.852	0.248	0.779

Table 3 : Comparison of displacements and stresses for SV-Wave, Incident angle = 5

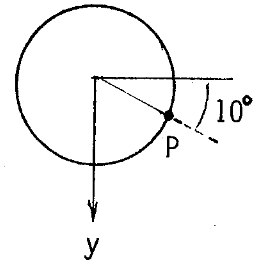

k_2a	FEM-36 Nodes UR	UZ	ANL-36 Terms UR	UZ
0.1	0.175(-1)	0.153(-3)	0.175(-1)	0.155(-3)
0.2	0.355(-1)	0.643(-3)	0.355(-1)	0.653(-3)
0.4	0.746(-1)	0.287(-2)	0.750(-1)	0.292(-2)
0.6	0.117	0.700(-2)	0.118	0.716(-2)
0.8	0.159	0.130(-1)	0.163	0.134(-1)
1.2	0.260	0.304(-1)	0.275	0.318(-1)
1.6	0.393	0.546(-1)	0.435	0.584(-1)
2.0	0.544	0.812(-1)	0.636	0.893(-1)

k_2a	FEM-36 Nodes STT	SZZ	ANL-36 Terms STT	SZZ
0.1	0.143(-1)	0.674(-2)	0.138(-1)	0.621(-2)
0.2	0.585(-1)	0.276(-1)	0.566(-1)	0.255(-1)
0.4	0.248	0.117	0.240	0.108
0.6	0.579	0.274	0.562	0.252
0.8	1.03	0.490	1.00	0.451
1.2	2.33	1.11	2.26	1.02
1.6	4.13	1.99	4.03	1.80
2.0	6.18	3.04	6.07	2.71

Table 4 : Comparison of displacements and stresses for SH-Wave, Incident angle = 5

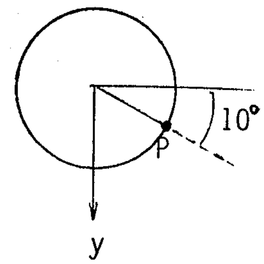

k_2a	FEM-36 Nodes UR	UZ	ANL-36 Terms UR	UZ
0.1	0.483(-2)	0.260(-1)	0.493(-2)	0.260(-1)
0.2	0.177(-1)	0.521(-1)	0.184(-1)	0.522(-1)
0.4	0.777(-1)	0.110	0.828(-1)	0.112
0.6	0.206	0.191	0.208	0.197
0.8	0.403	0.298	0.440	0.306
1.2	0.608	0.389	0.667	0.389
1.6	0.617	0.392	0.669	0.387
2.0	0.632	0.409	0.675	0.404

k_2a	FEM-36 Nodes STT	SZZ	ANL-36 Terms STT	SZZ
0.1	0.183(-1)	0.103(-1)	0.180(-1)	0.101(-1)
0.2	0.760(-1)	0.427(-1)	0.748(-1)	0.416(-1)
0.4	0.345	0.191	0.340	0.186
0.6	0.909	0.498	0.892	0.484
0.8	1.76	0.963	1.72	0.928
1.2	2.64	1.47	2.49	1.35
1.6	2.69	1.56	2.36	1.34
2.0	2.80	1.71	2.21	1.37

Table 5 : Comparison of displacements and stresses for P-Wave, Incident angle = 60

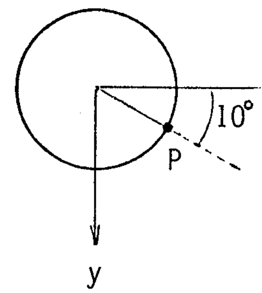

k_2a	FEM-36 Nodes UR	UZ	ANL-36 Terms UR	UZ
0.1	0.851(-1)	0.509(-1)	0.851(-1)	0.509(-1)
0.2	0.170	0.105	0.170	0.105
0.4	0.339	0.228	0.340	0.228
0.6	0.512	0.369	0.515	0.368
0.8	0.682	0.514	0.689	0.513
1.2	0.939	0.731	0.960	0.730
1.6	1.08	0.815	1.13	0.816
2.0	1.24	0.860	1.32	0.867

k_2a	FEM-36 Nodes STT	SZZ	ANL-36 Terms STT	SZZ
0.1	0.820(-2)	0.168(-1)	0.778(-2)	0.163(-1)
0.2	0.342(-1)	0.695(-1)	0.325(-1)	0.674(-1)
0.4	0.153	0.303	0.145	0.294
0.6	0.386	0.741	0.368	0.718
0.8	0.757	1.40	0.720	1.35
1.2	1.84	3.10	1.74	2.97
1.6	3.22	4.87	3.01	4.62
2.0	5.13	6.94	4.77	6.47

Table 6 : Comparison of displacements and stresses for SV-Wave, Incident angle = 60

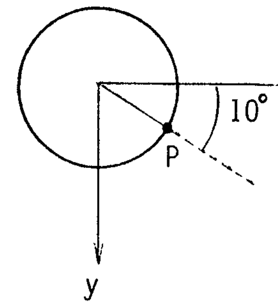

k_2a	FEM-36 Nodes UR	FEM-36 Nodes UZ	ANL-36 Terms UR	ANL-36 Terms UZ
0.1	0.174(-1)	0.145(-2)	0.174(-1)	0.147(-2)
0.2	0.348(-1)	0.556(-2)	0.349(-1)	0.565(-2)
0.4	0.718(-1)	0.201(-1)	0.720(-1)	0.204(-1)
0.6	0.114	0.406(-1)	0.115	0.413(-1)
0.8	0.163	0.648(-1)	0.165	0.659(-1)
1.2	0.272	0.115	0.279	0.117
1.6	0.388	0.163	0.403	0.165
2.0	0.548	0.209	0.580	0.212

k_2a	FEM-36 Nodes STT	FEM-36 Nodes SZZ	ANL-36 Terms STT	ANL-36 Terms SZZ
0.1	0.716(-2)	0.339(-2)	0.693(-2)	0.313(-2)
0.2	0.294(-1)	0.141(-1)	0.285(-1)	0.130(-1)
0.4	0.127	0.613(-1)	0.123	0.567(-1)
0.6	0.312	0.149	0.302	0.138
0.8	0.601	0.279	0.581	0.257
1.2	1.46	0.627	1.40	0.564
1.6	2.61	1.08	2.50	0.944
2.0	4.33	1.80	4.13	1.54

Table 7 : Comparison of displacements and stresses for SH-Wave, Incident angle = 60

A P P E N D I X 4

FIGURES

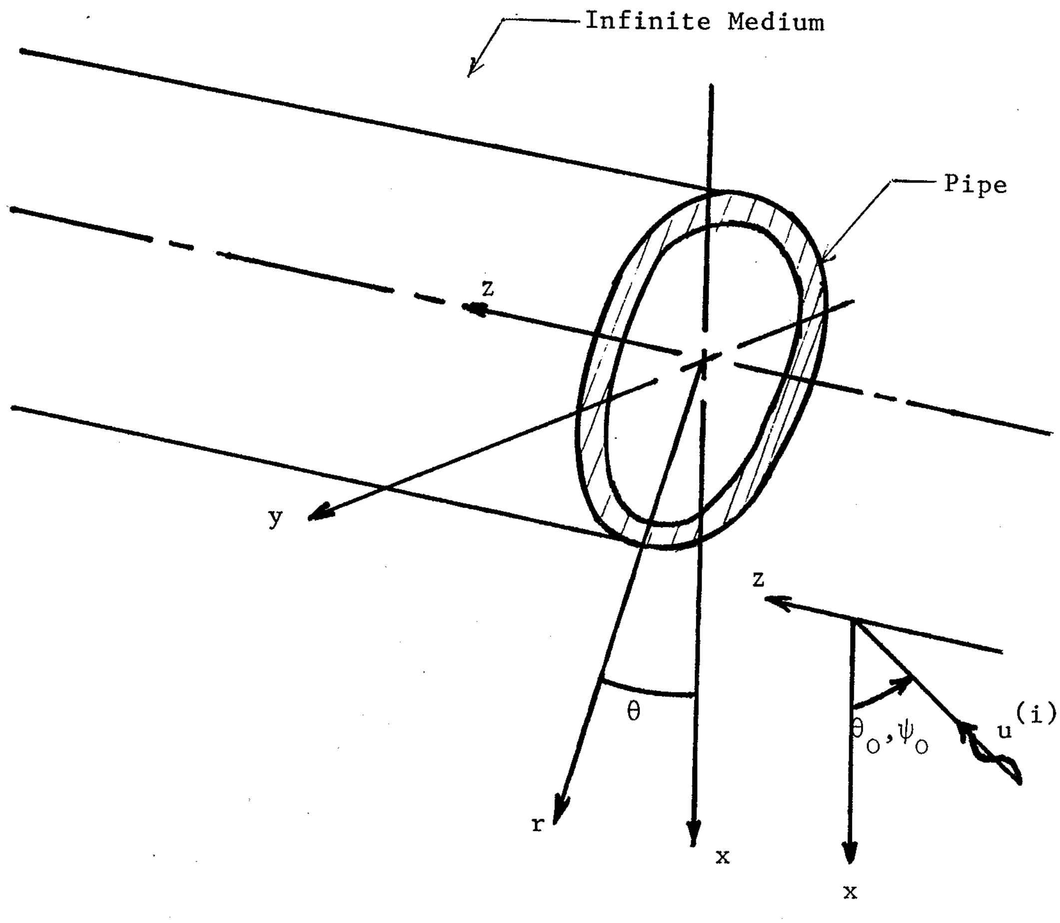

Fig. 1a Geometry of the Pipe for Analytical work

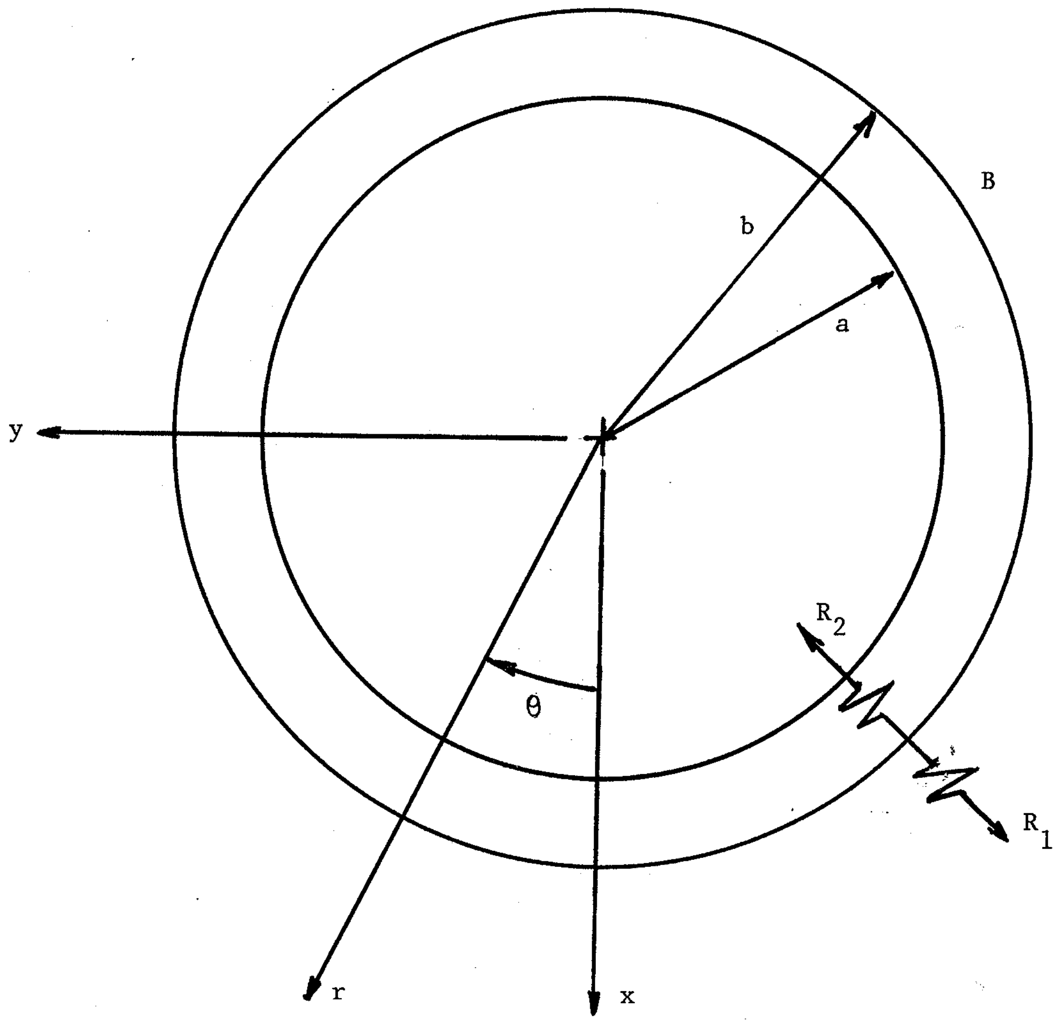

Fig. 1b Geometry of the Pipe for Analytical Work (end view)

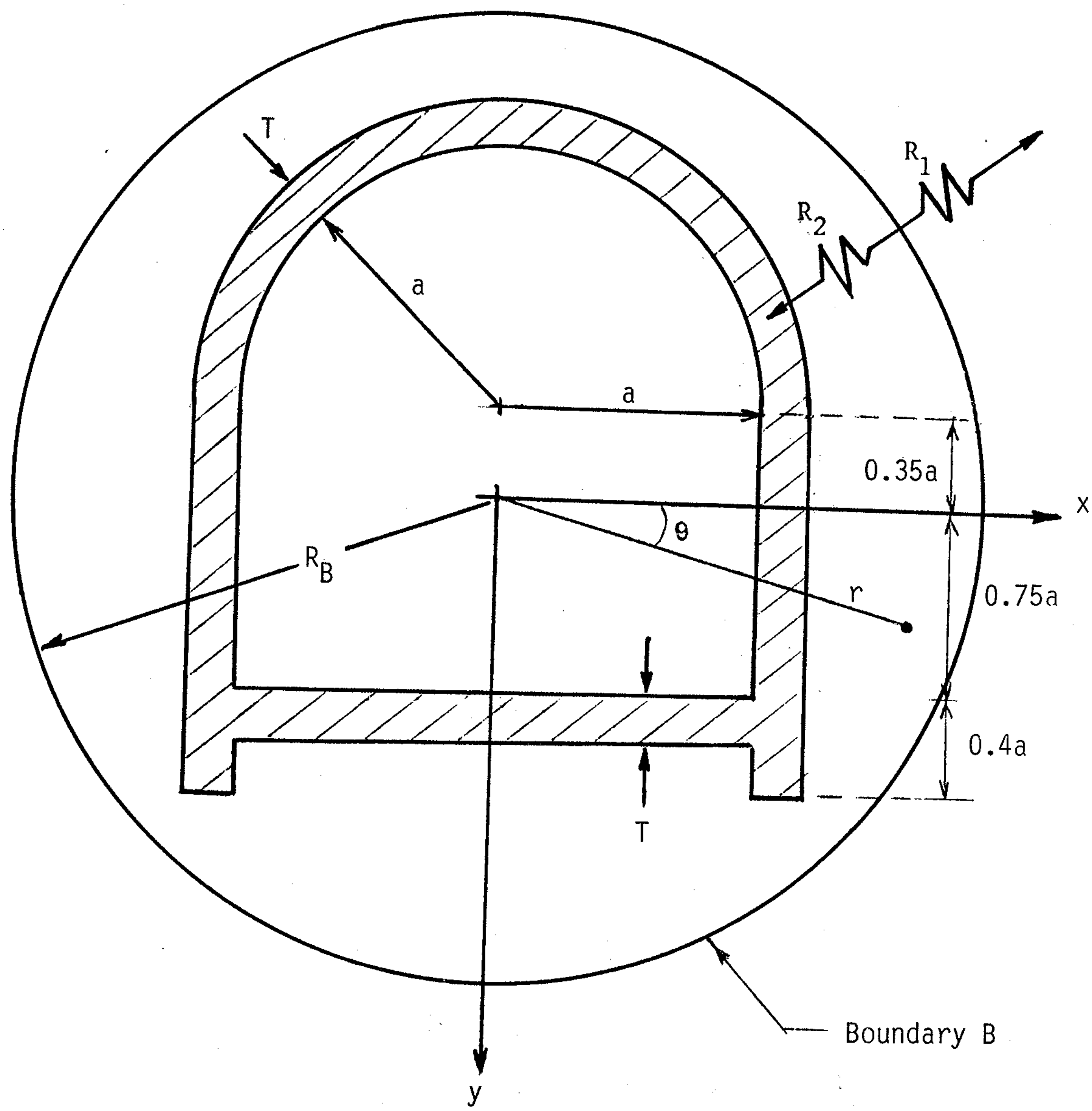

Fig. 2 Geometry of Tunnel for FEEET method

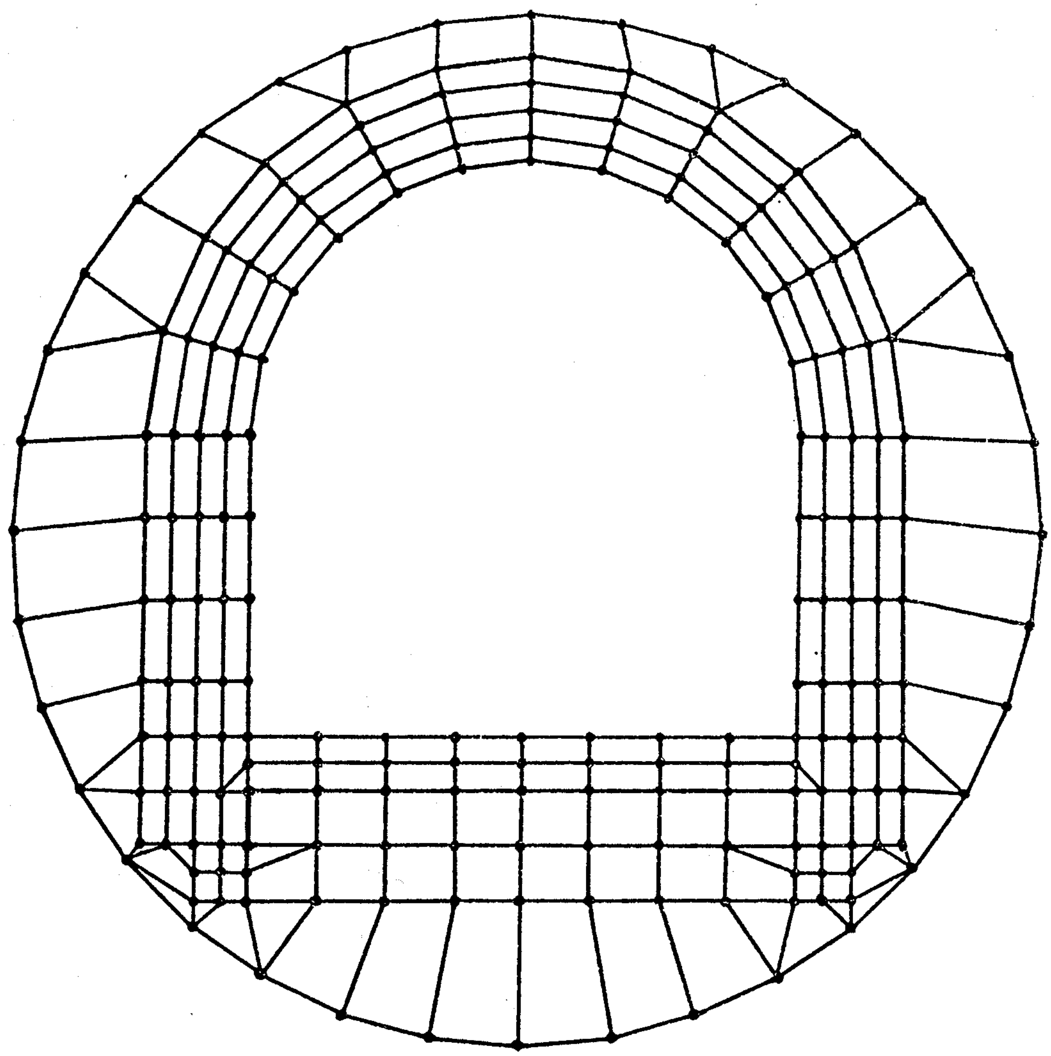

Fig. 3 Finite element grid for the Tunnel

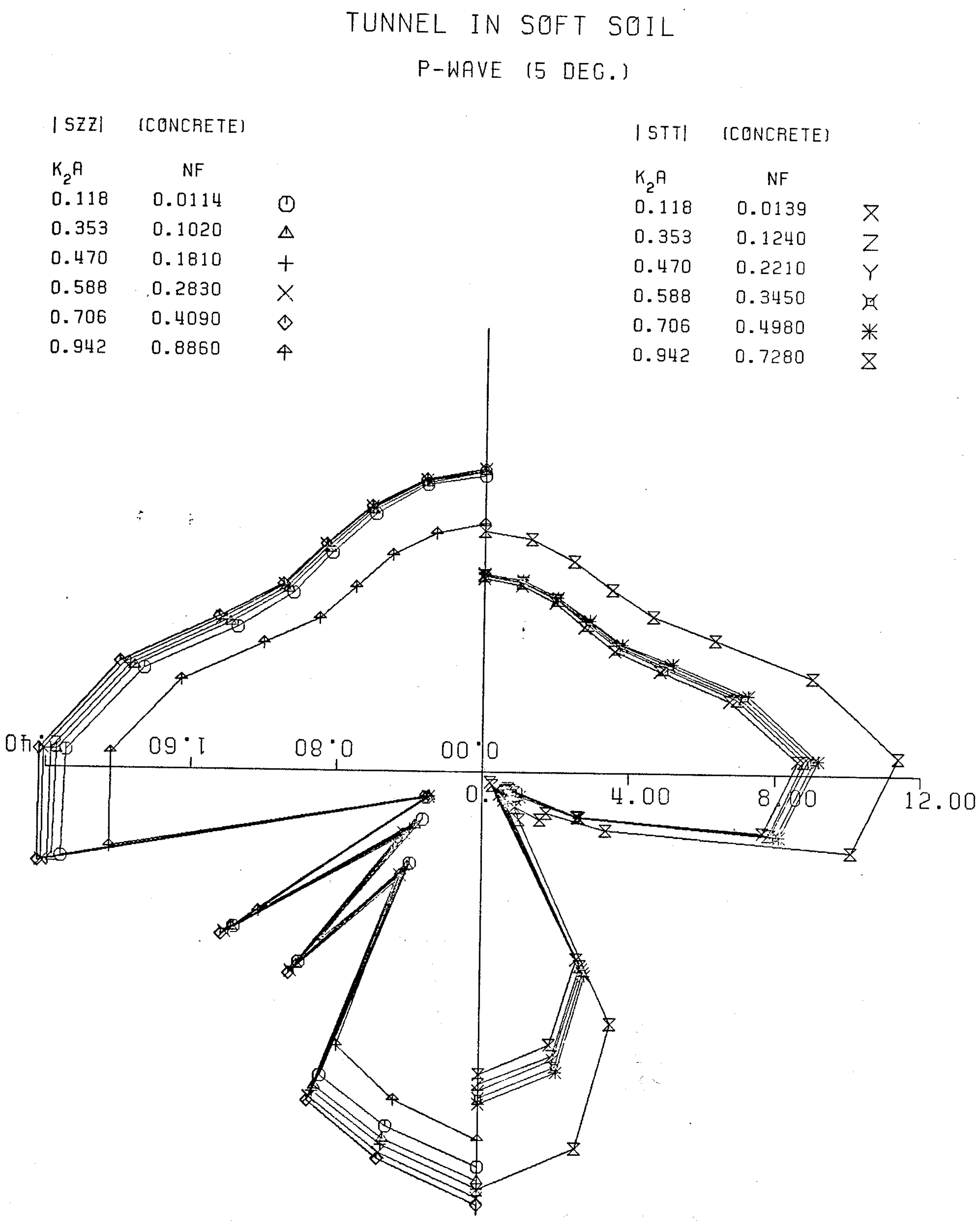

Fig. 4 Normalized axial stress and hoop stress in tunnel wall vs frequency for P-Wave when the incident angle = 5° (Case I)

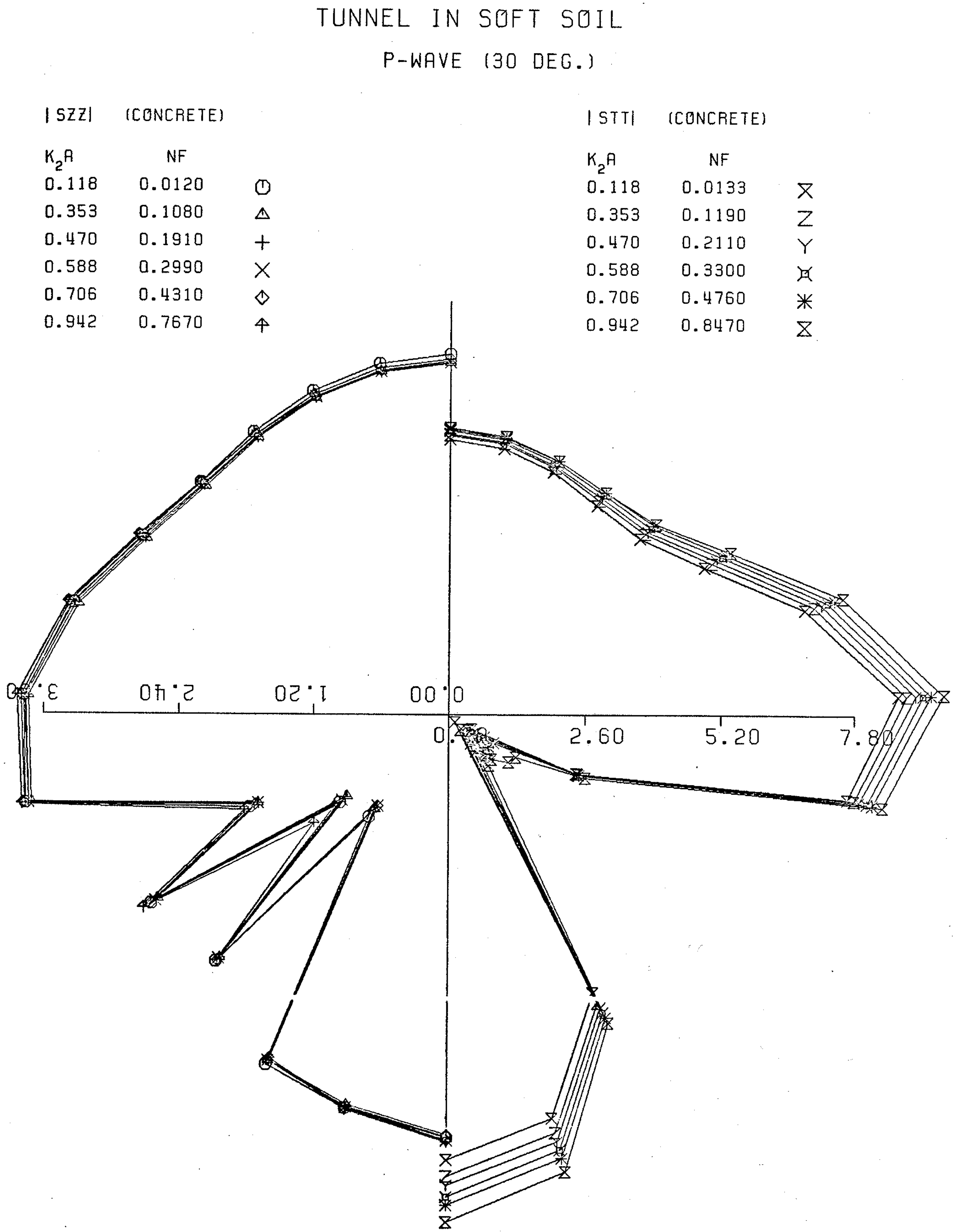

Fig. 5 Normalized axial stress and hoop stress in tunnel wall vs frequency for P-Wave when the incident angle = 30° (Case I)

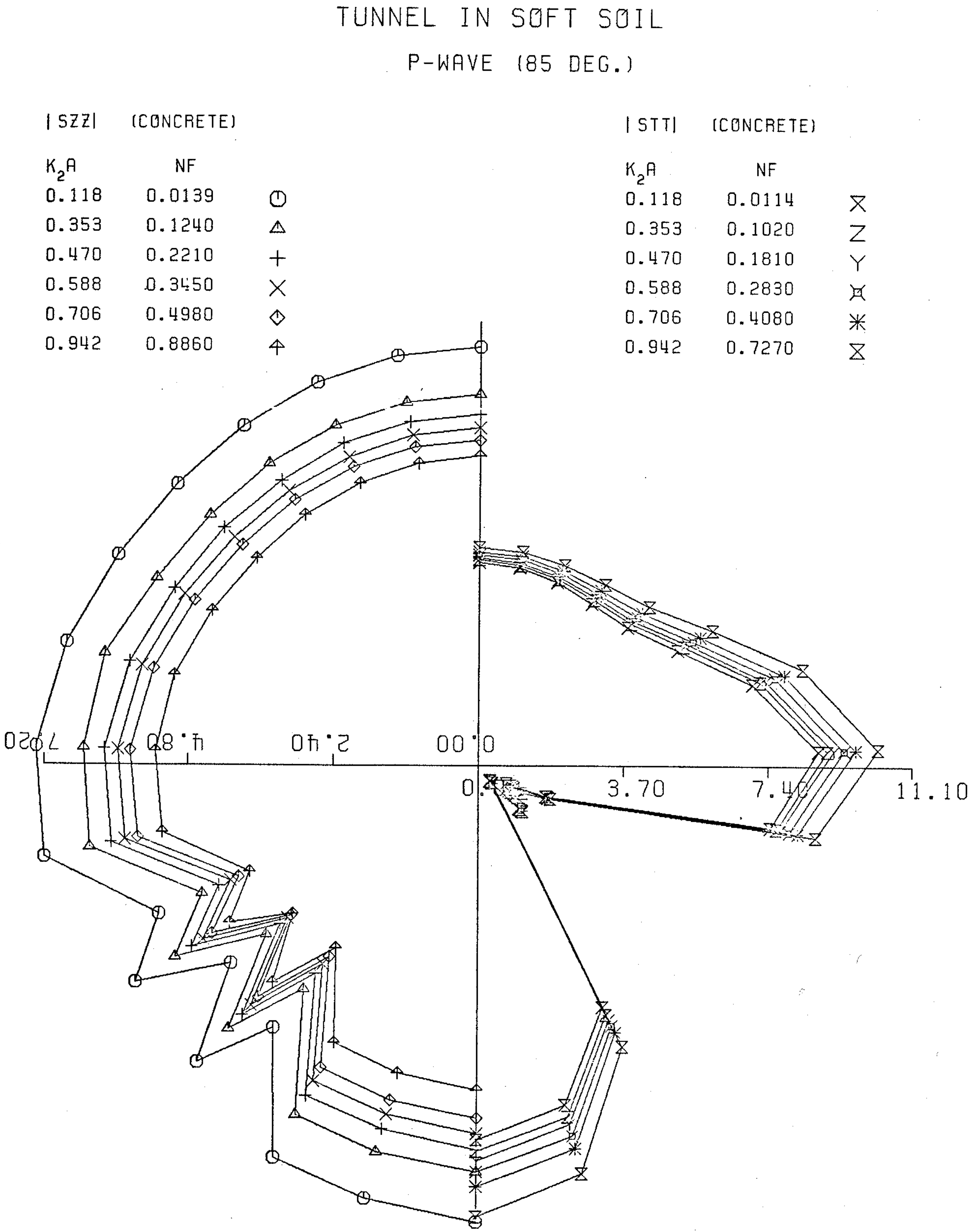

Fig. 6 Normalized axial stress and hoop stress in tunnel wall vs frequency for P-Wave when the incident angle = 85° (Case I)

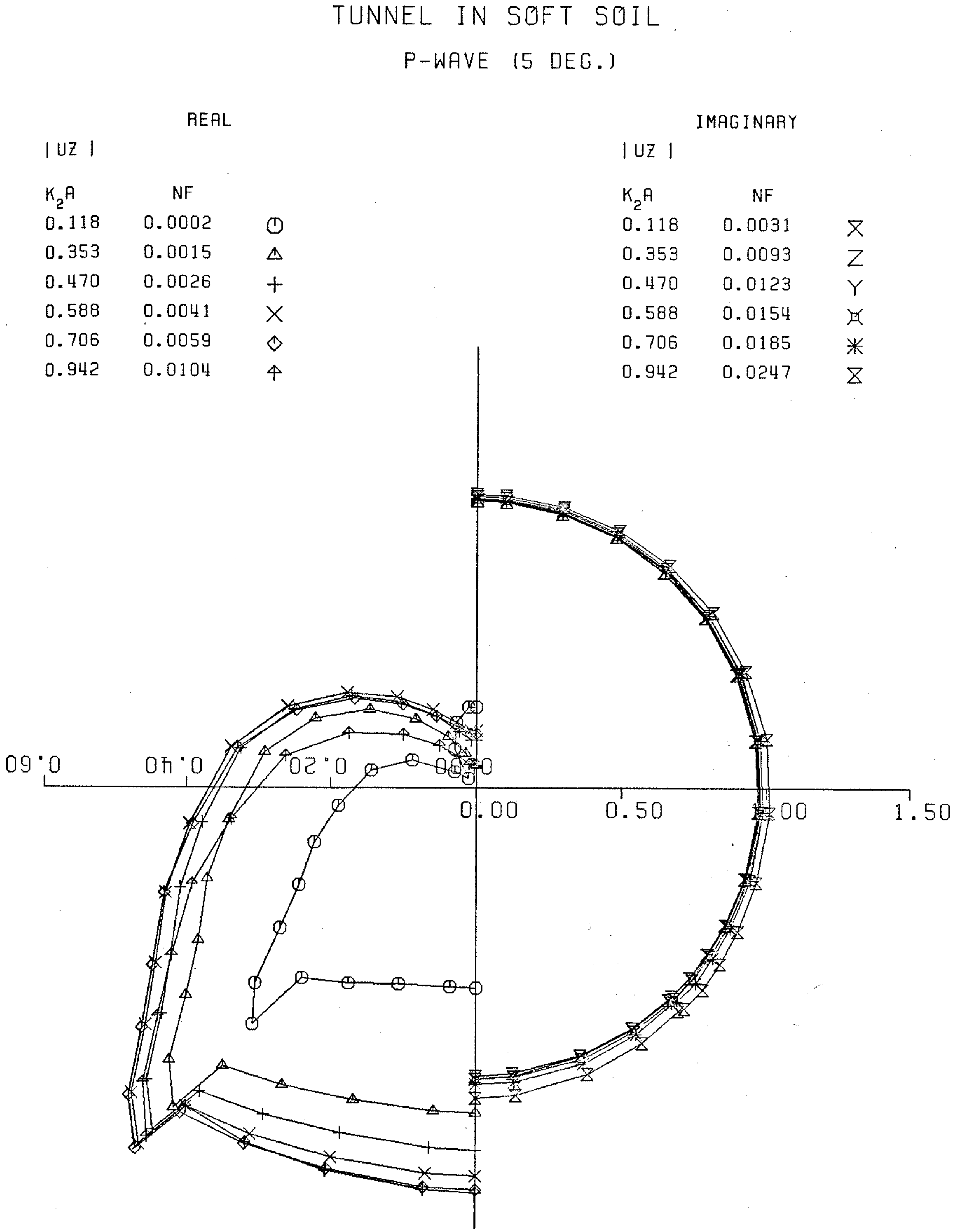

Fig. 7 Normalized real and imaginary part of axial displacement vs frequency for P-Wave when the incident angle = 5° (Case I)

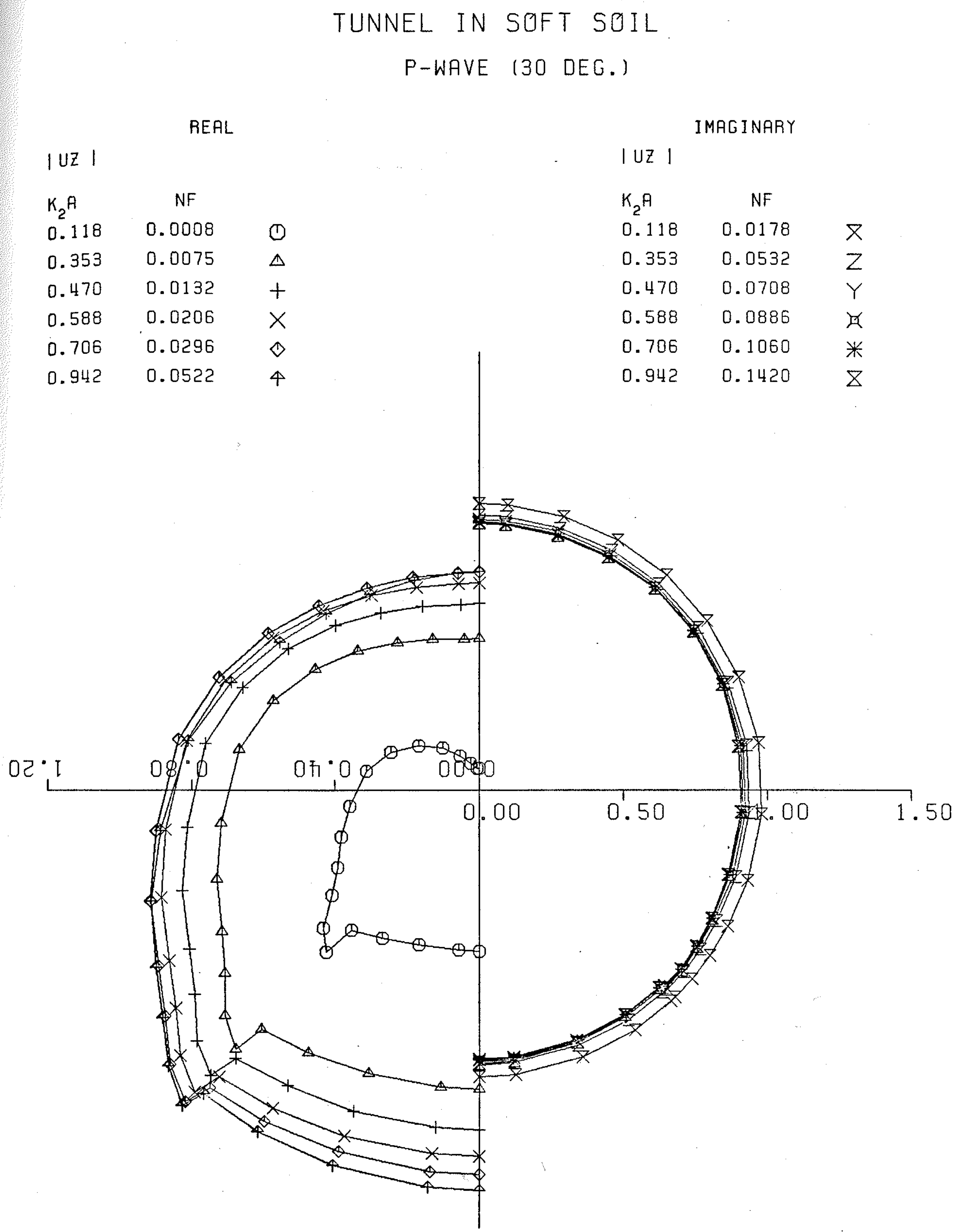

Fig. 8 Normalized real and imaginary part of axial displacement vs frequency for P-Wave when the incident angle = 30° (Case I)

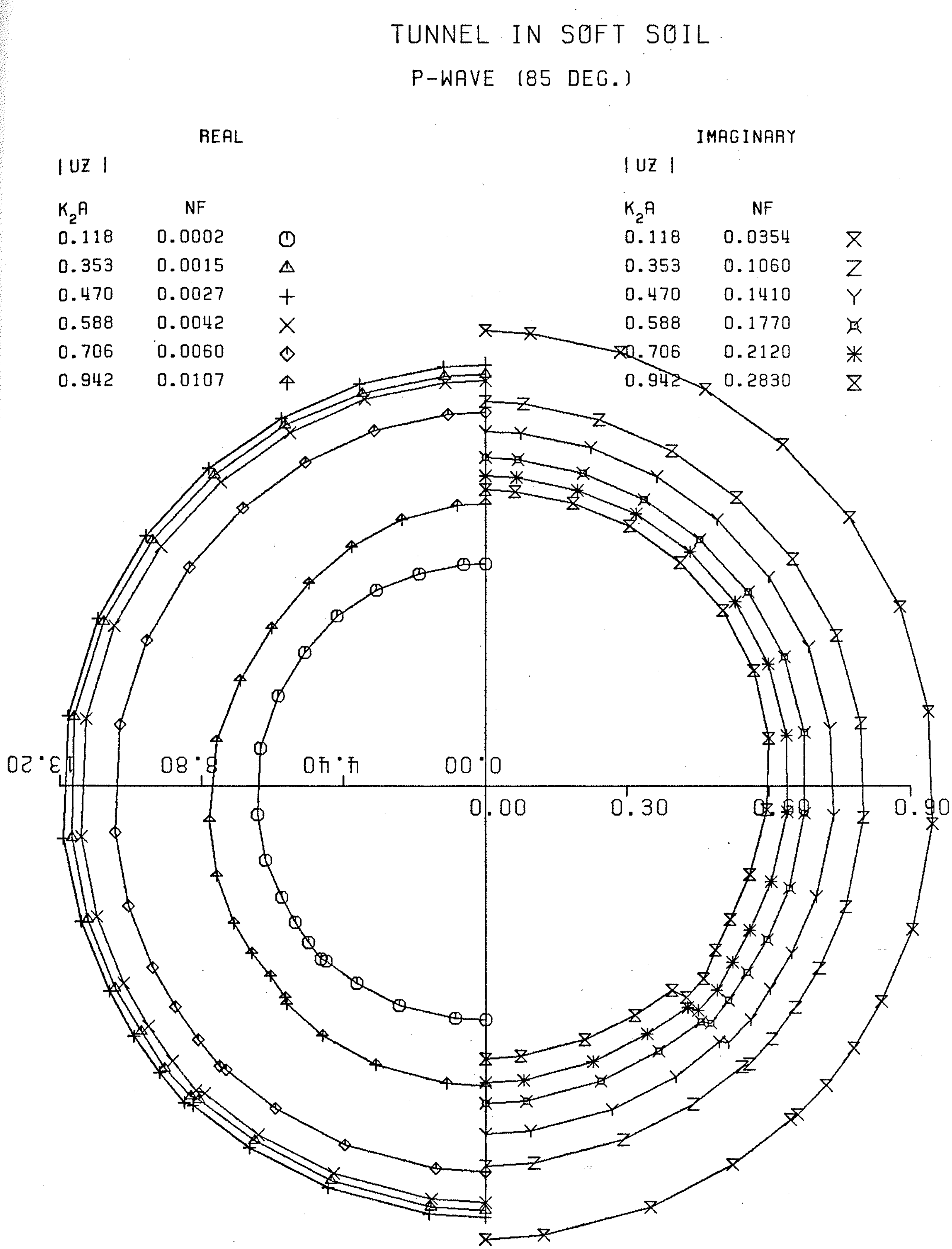

Fig. 9 Normalized real and imaginary part of axial displacement vs frequency for P-Wave when the incident angle = 85° (Case I)

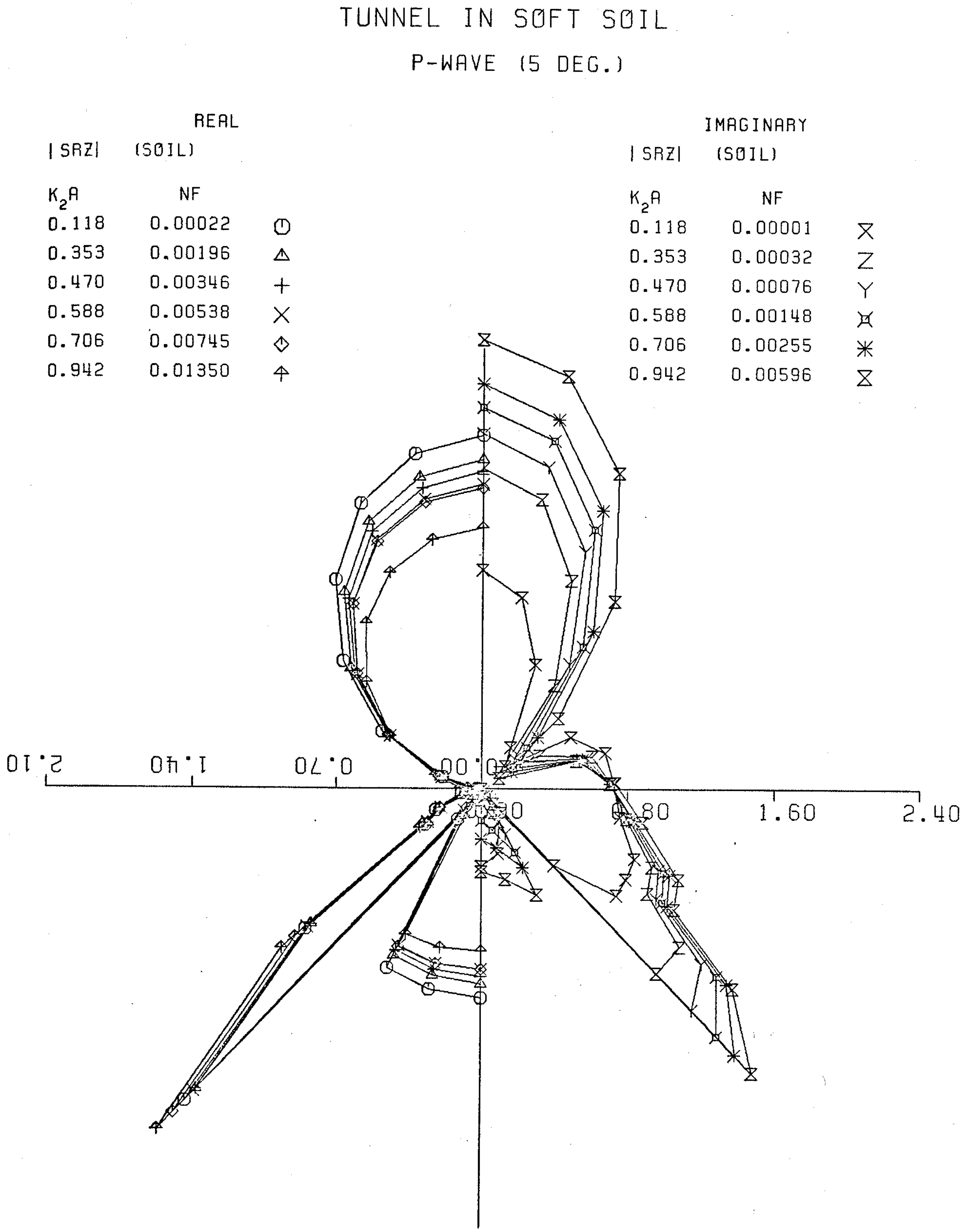

Fig. 10 Normalized real and imaginary part of shear stress SRZ in soil vs frequency for P-Wave when the incident angle = 5° (Case I)

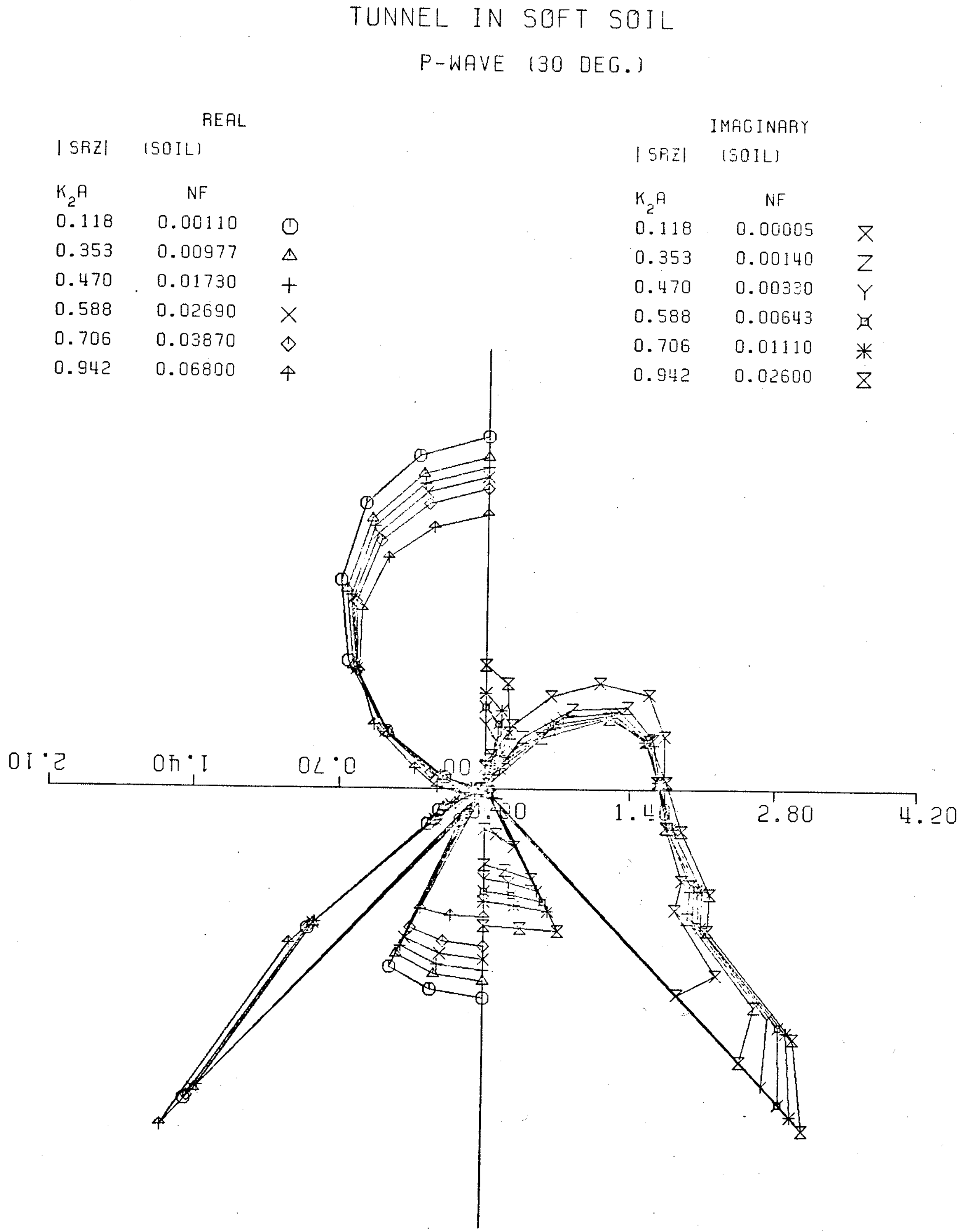

Fig. 11 Normalized real and imaginary part of shear stress SRZ in soil vs frequency for P-Wave when the incident angle = 30° (Case I)

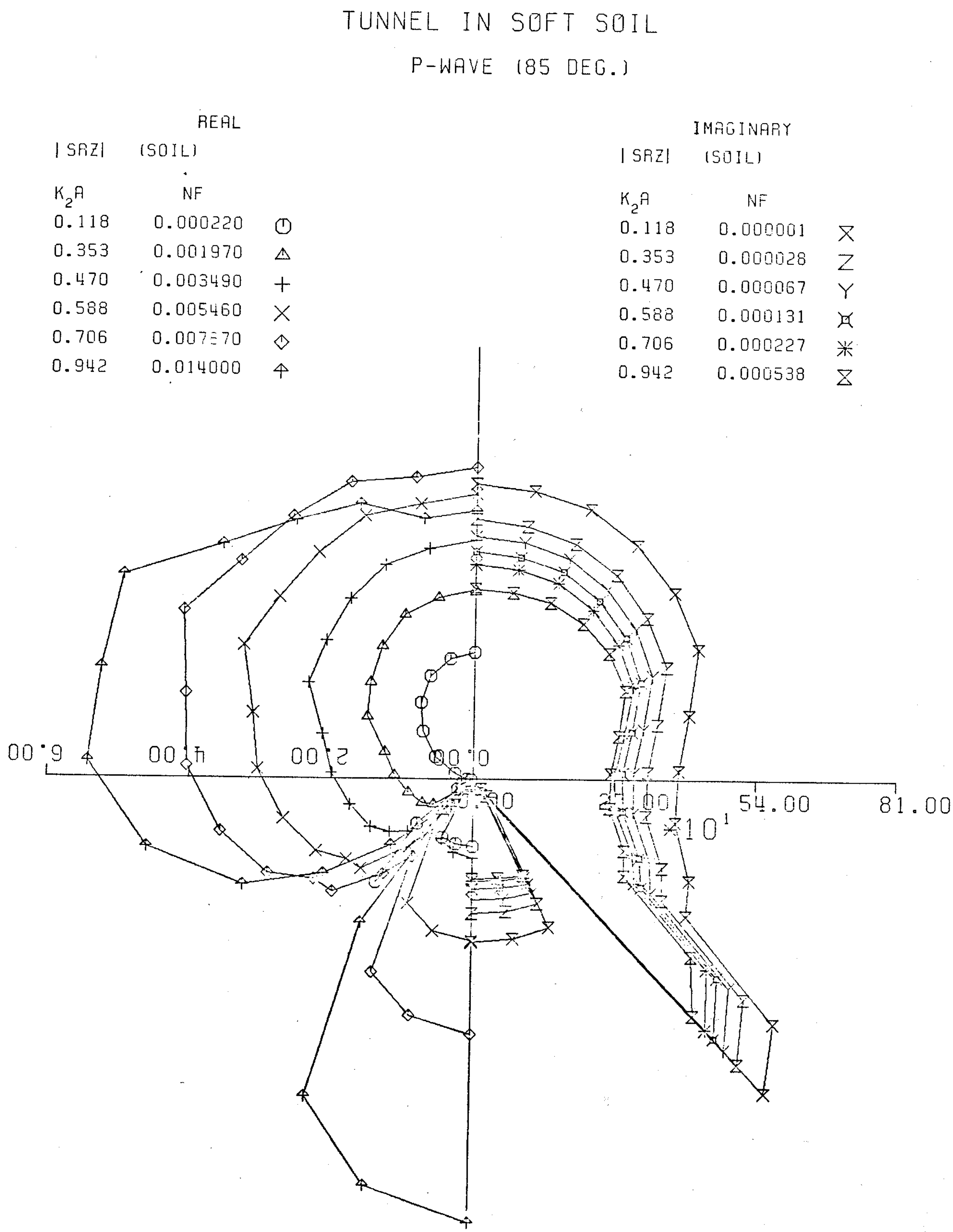

Fig. 12 Normalized real and imaginary part of shear stress SRZ in soil vs frequency for P-Wave when the incident angle = 85° (Case I)

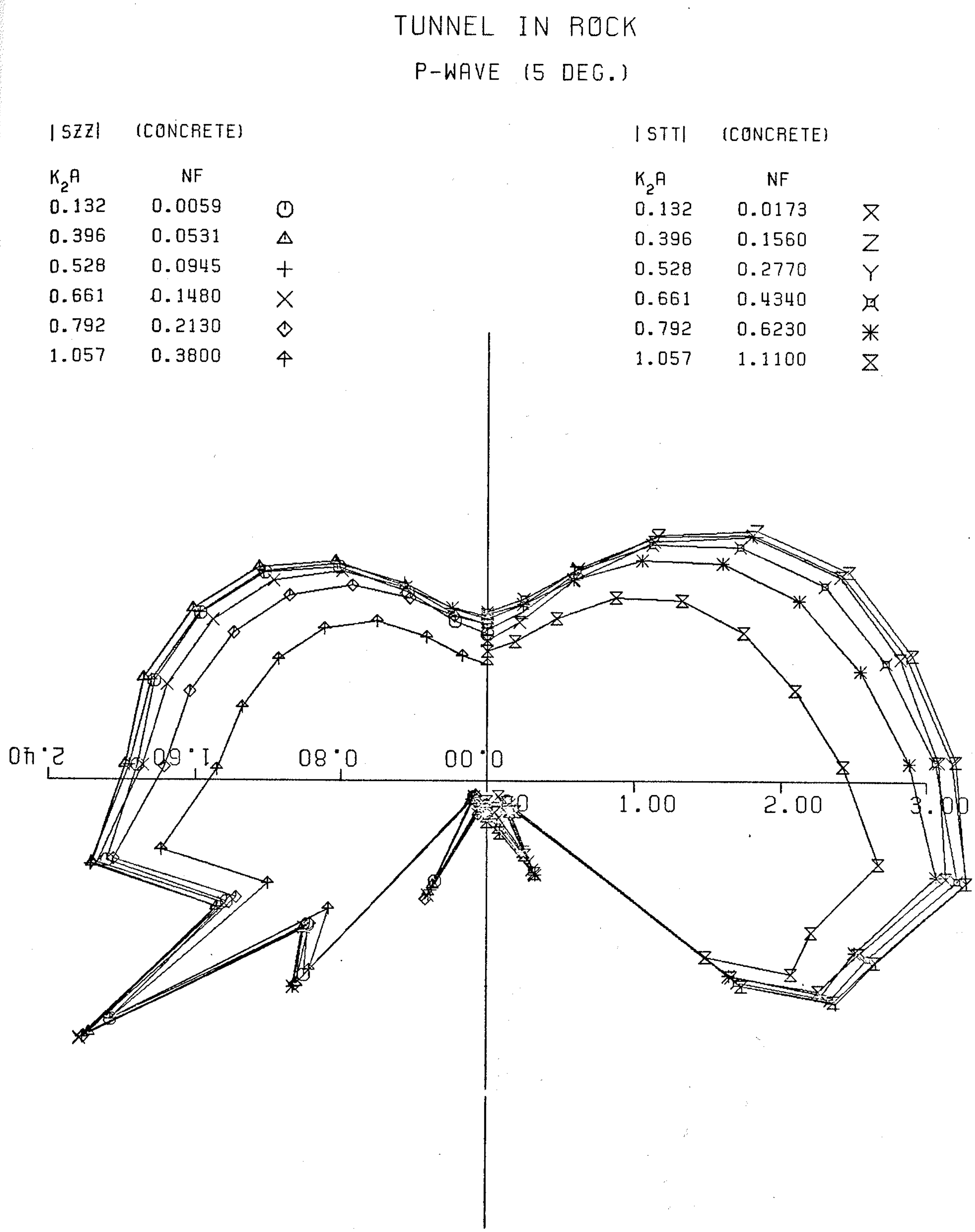

Fig. 13 Normalized axial stress and hoop stress in tunnel wall vs frequency for P-Wave when the incident angle = 5°(Case II)

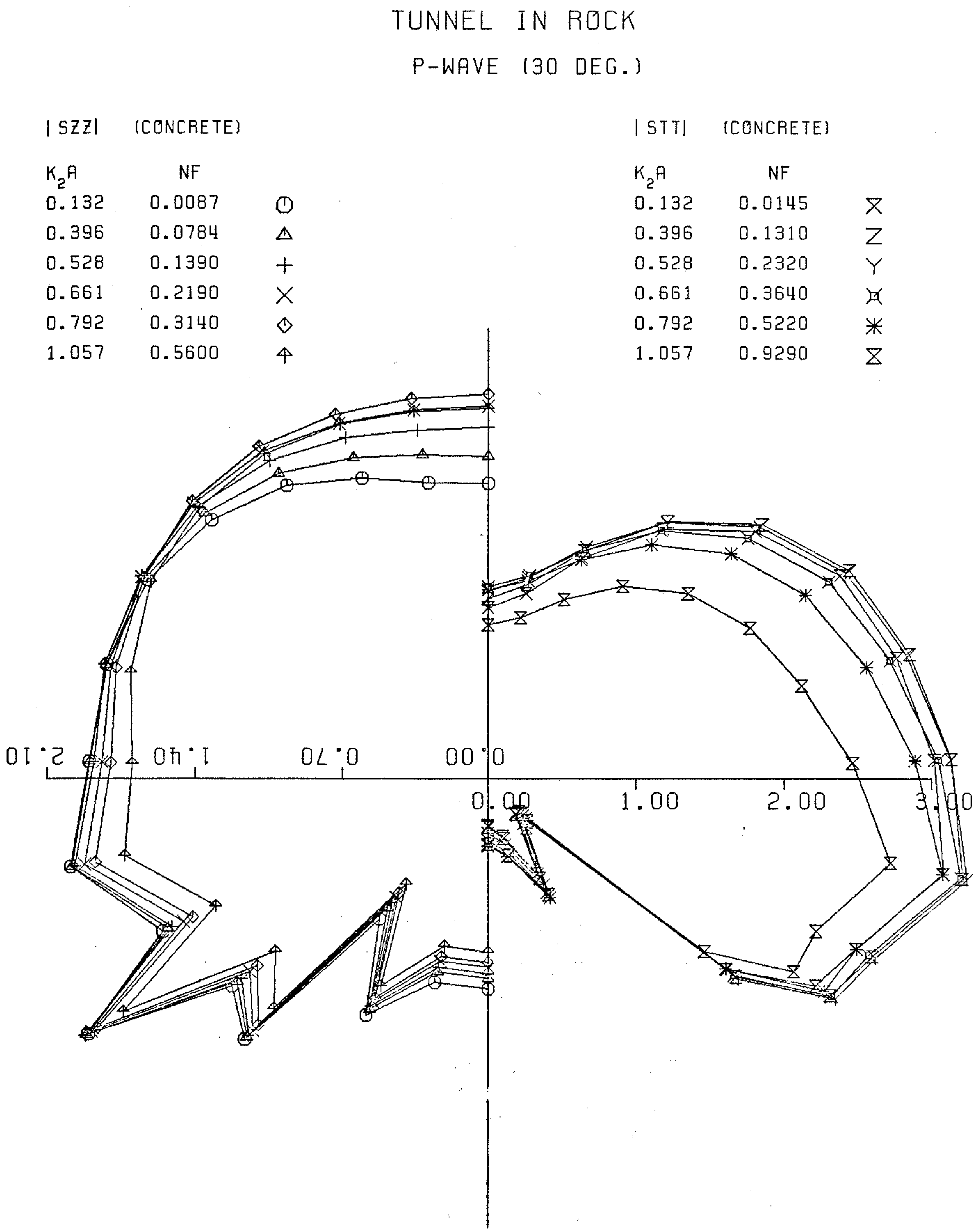

Fig. 14 Normalized axial stress and hoop stress in tunnel wall vs frequency for P-Wave when the incident angle = 30° (Case II)

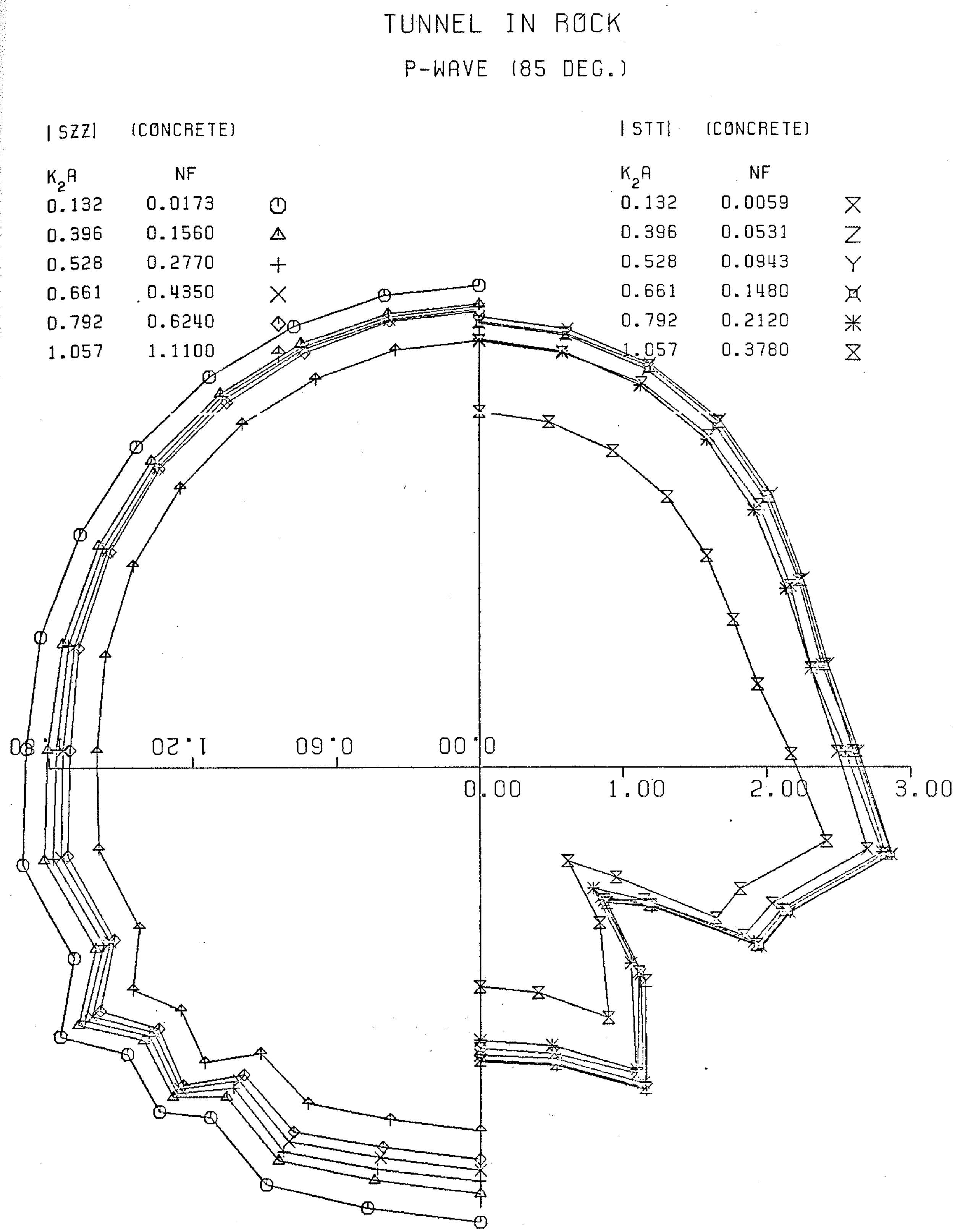

Fig. 15 Normalized axial stress and hoop stress in tunnel wall vs frequency for P-Wave when the incident angle = 85° (Case II)

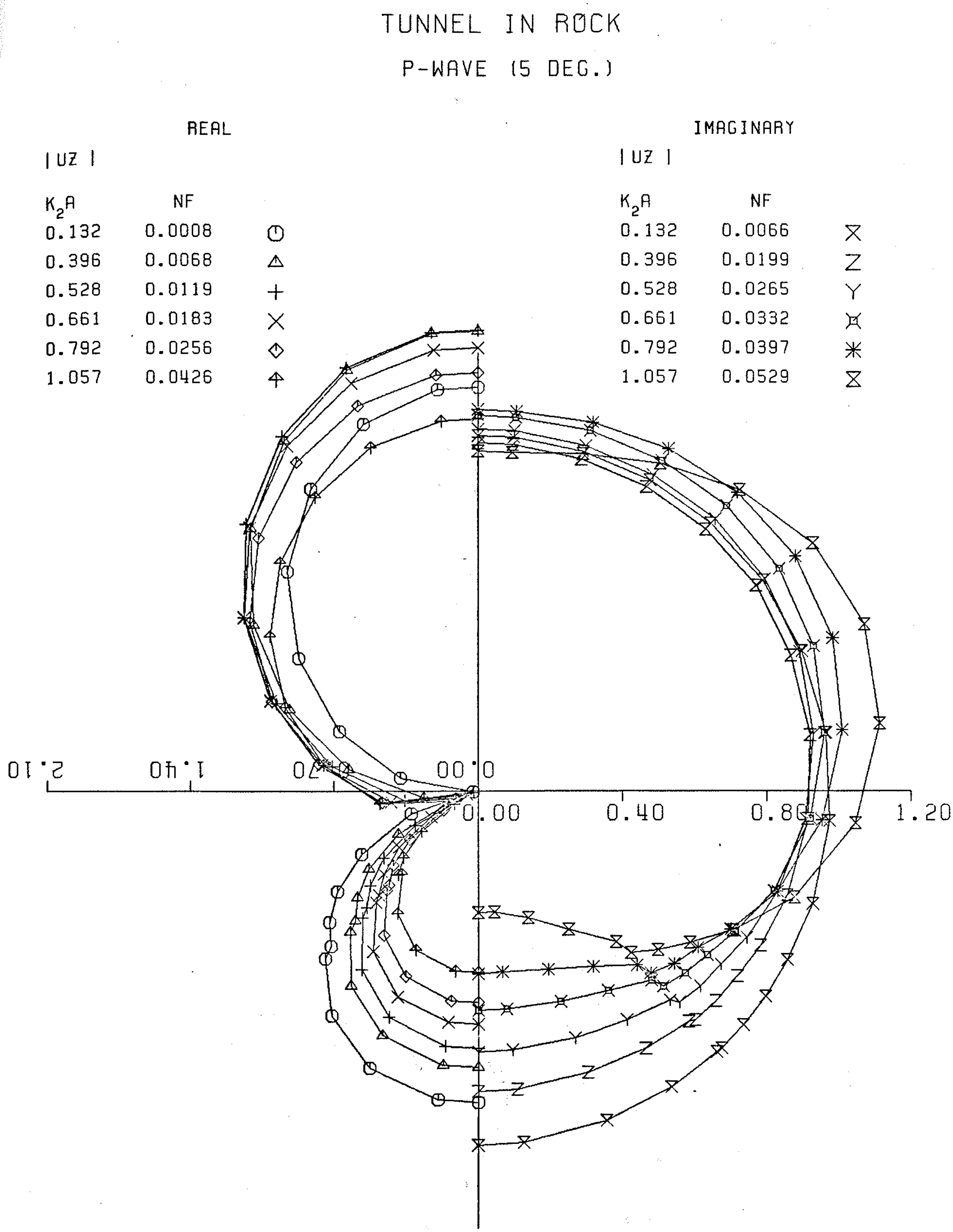

Fig. 16 Normalized real and imaginary part of axial displacement vs frequency for P-Wave when the incident angle = 5° (Case II)

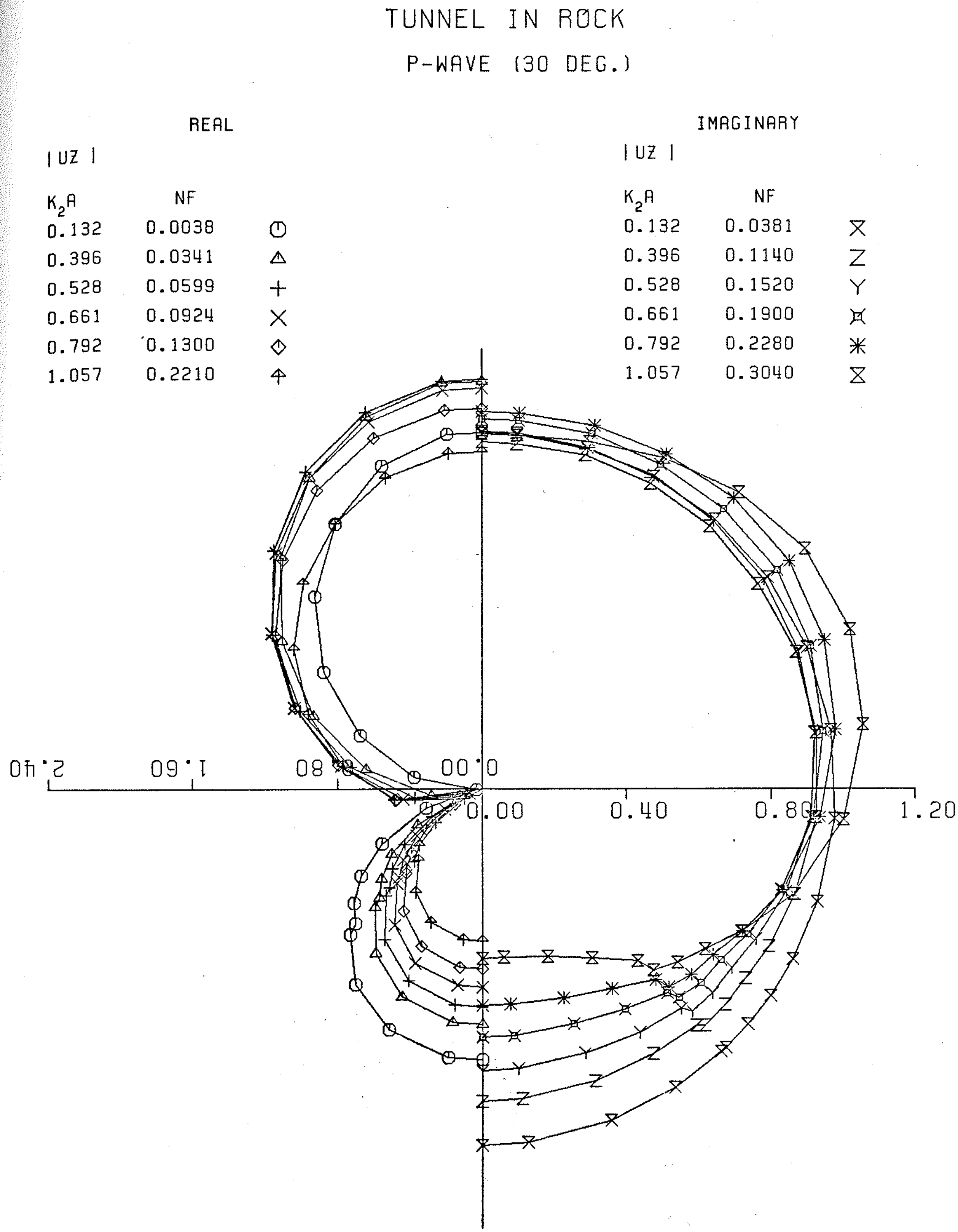

Fig. 17 Normalized real and imaginary part of axial displacement vs frequency for P-Wave when the incident angle = 30°(Case II)

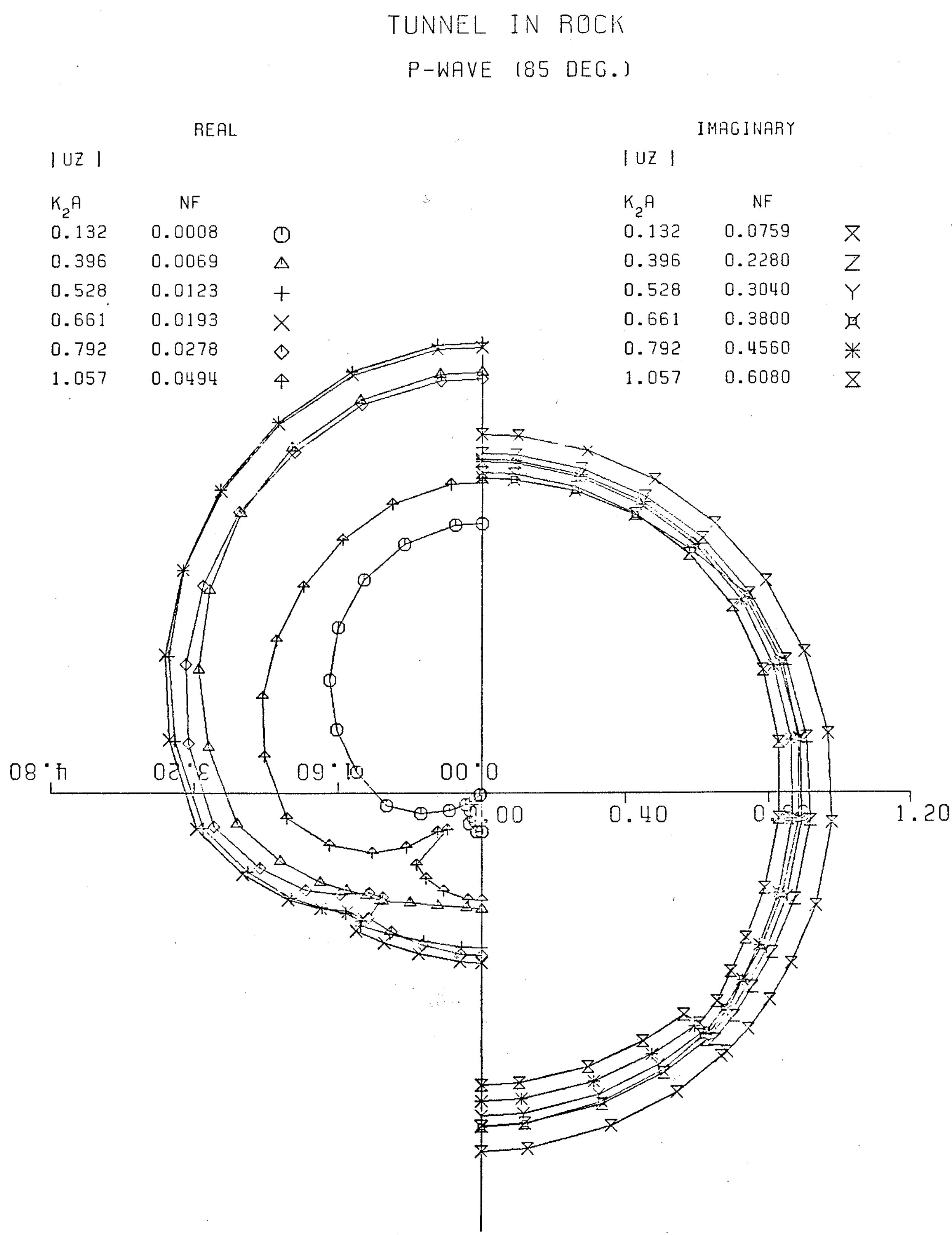

Fig. 18 Normalized real and imaginary part of axial displacement vs frequency for P-Wave when the incident angle = 85° (Case II)

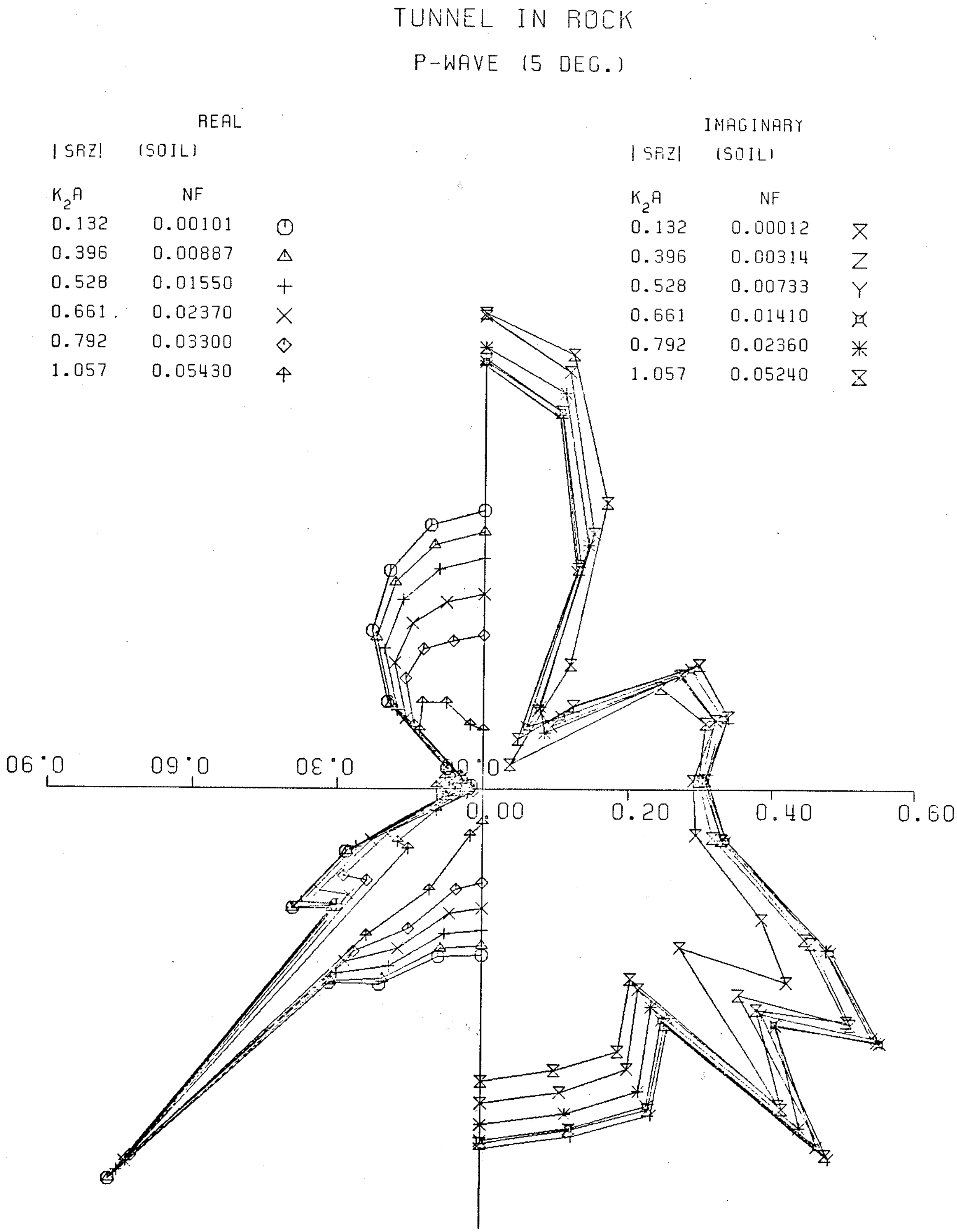

Fig. 19 Normalized real and imaginary part of shear stress SRZ in soil vs frequency for P-Wave when the incident angle = 5° (Case II)

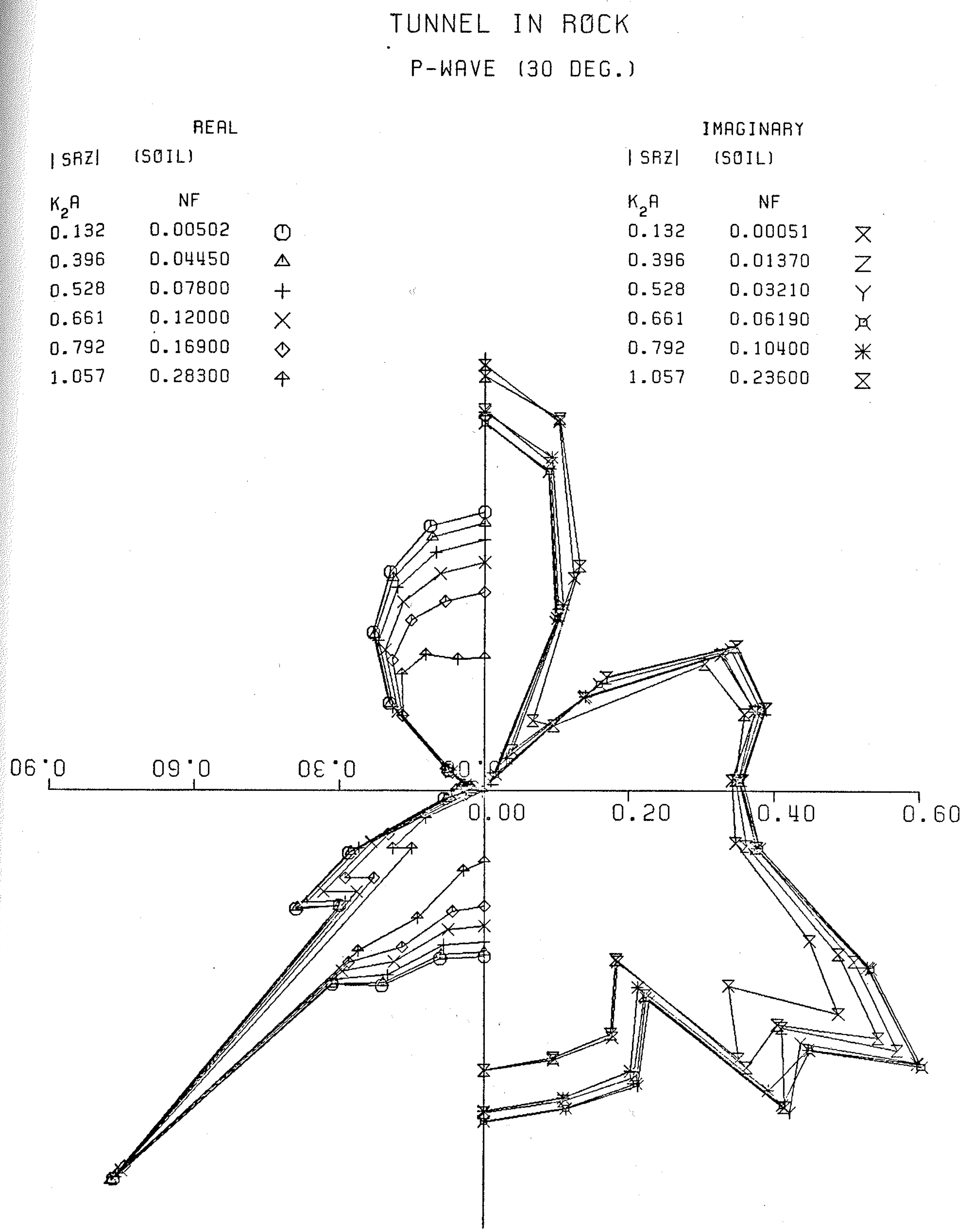

Fig. 20 Normalized real and imaginary part of shear stress SRZ in soil vs frequency for P-Wave when the incident angle = 30° (Case II)

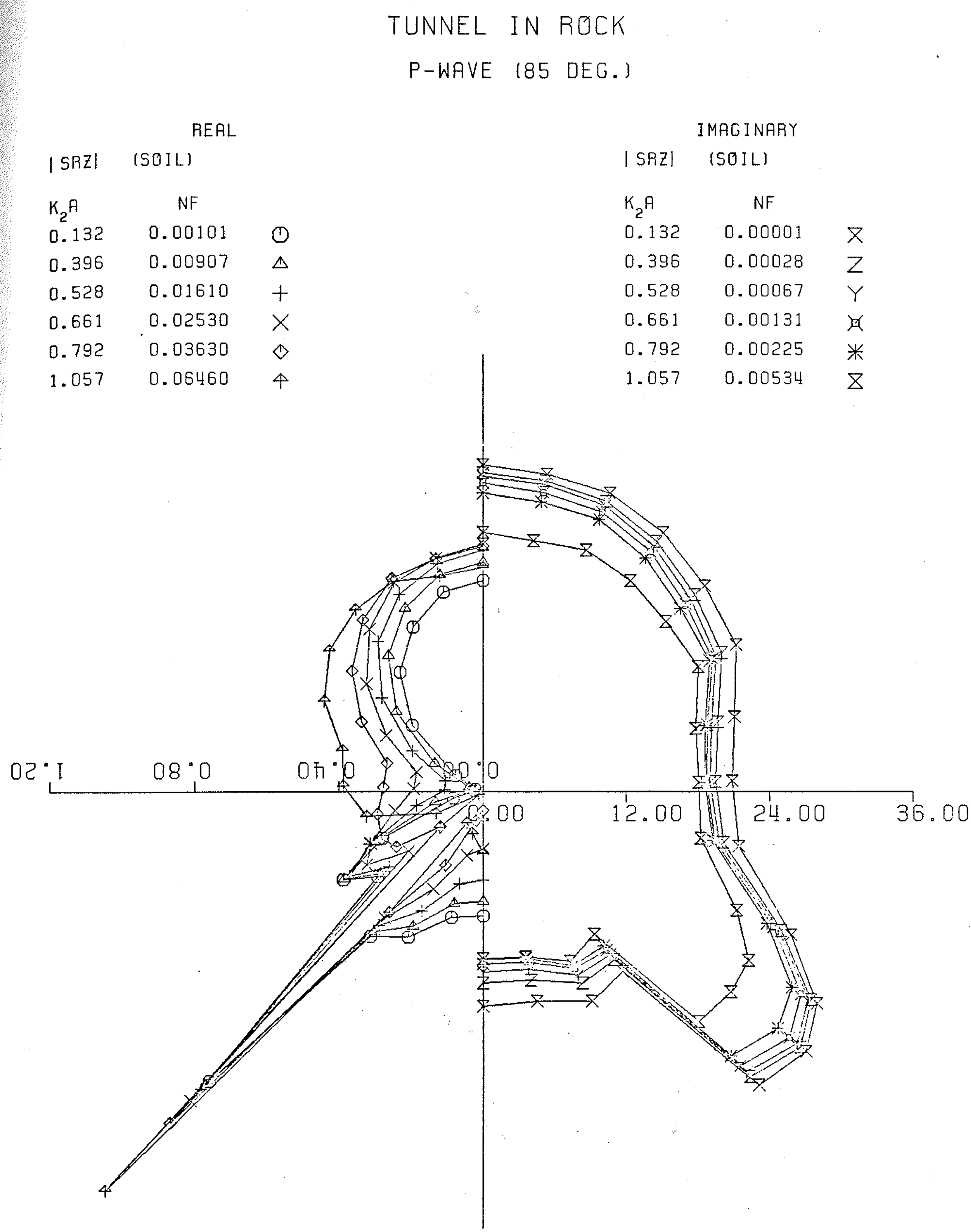

Fig. 21 Normalized real and imaginary part of shear stress SRZ in soil vs frequency for P-Wave when the incident angle = 85°(Case II)

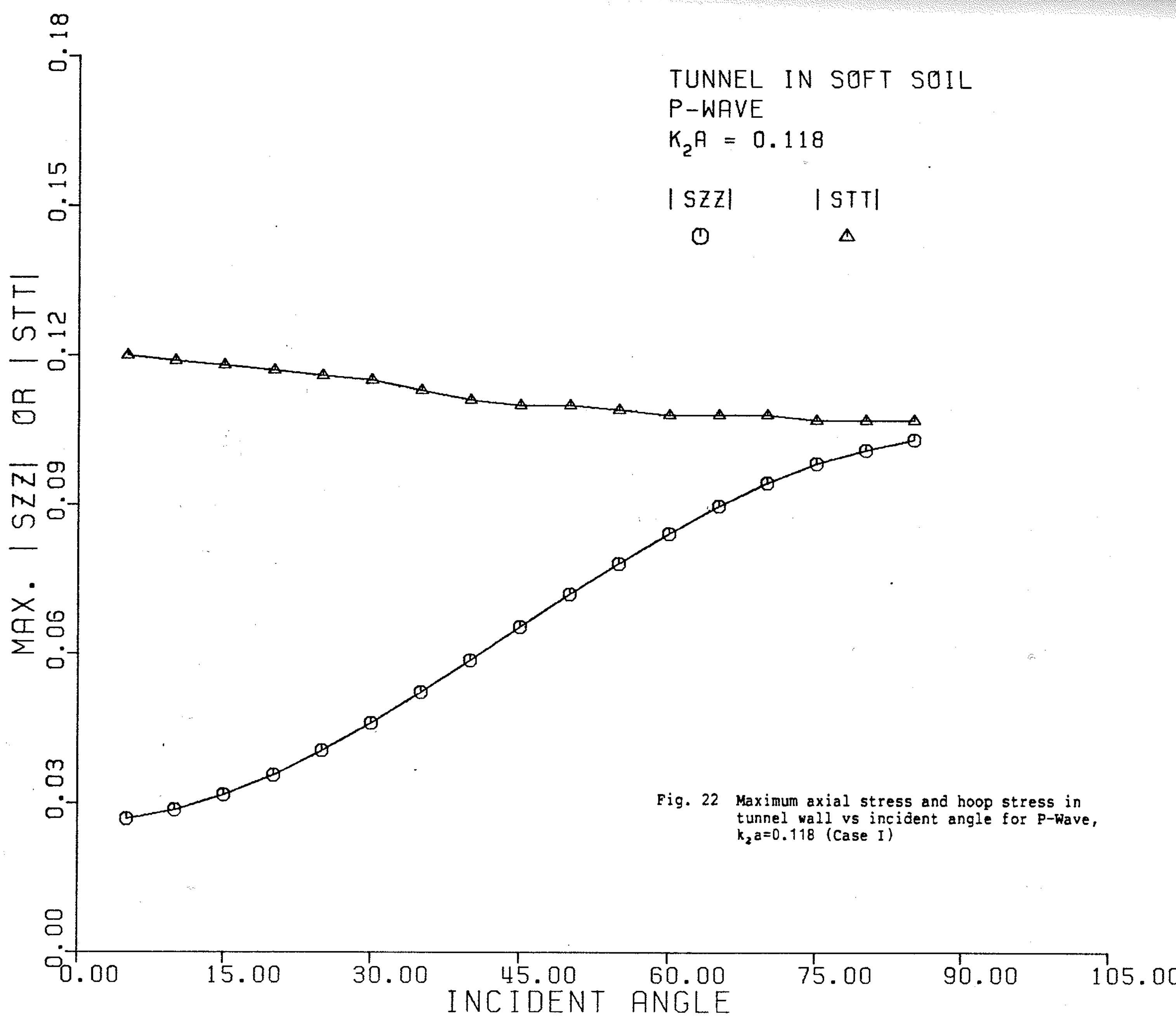

Fig. 22 Maximum axial stress and hoop stress in tunnel wall vs incident angle for P-Wave, k_2a=0.118 (Case I)

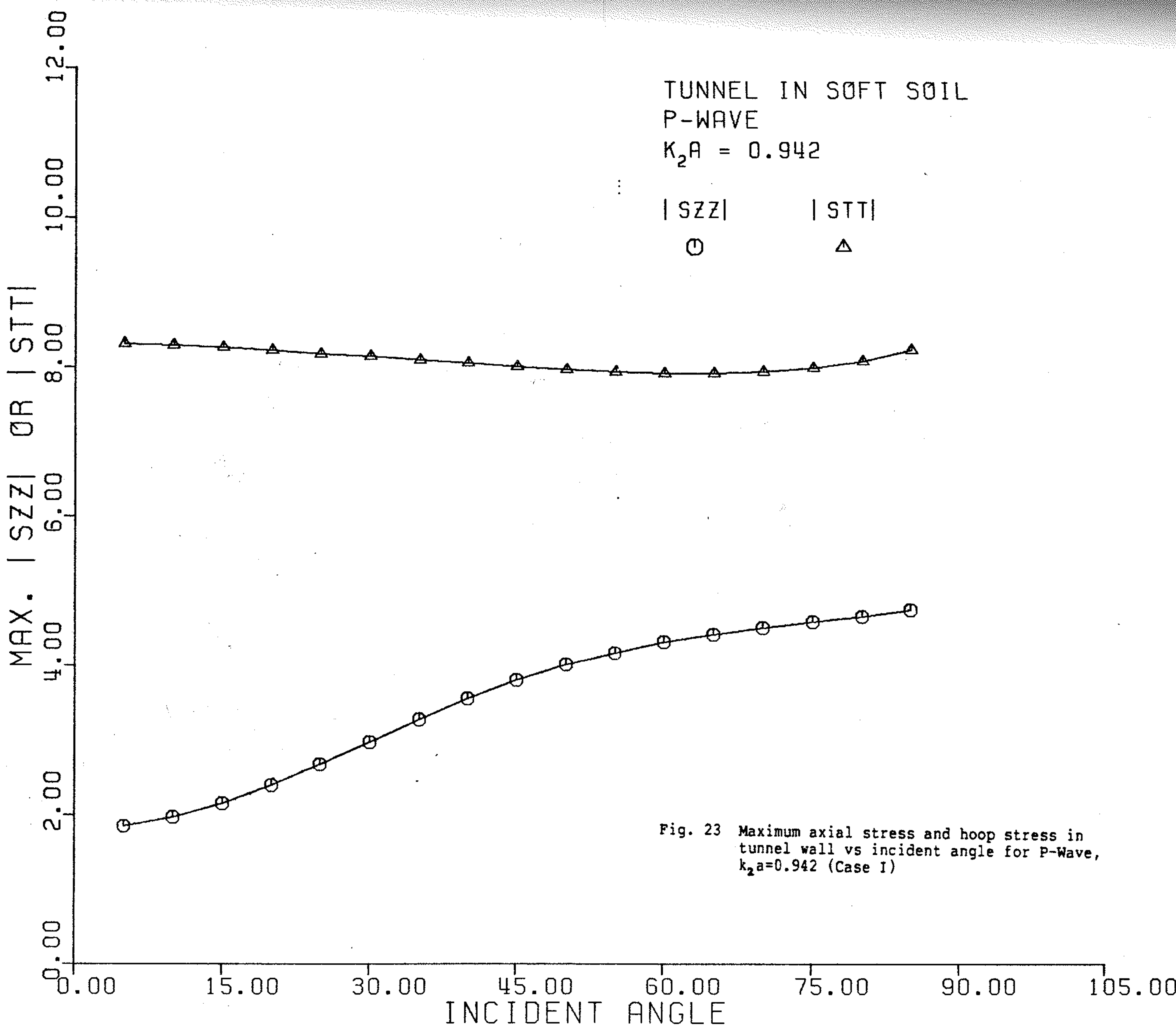

Fig. 23 Maximum axial stress and hoop stress in tunnel wall vs incident angle for P-Wave, k_2a=0.942 (Case I)

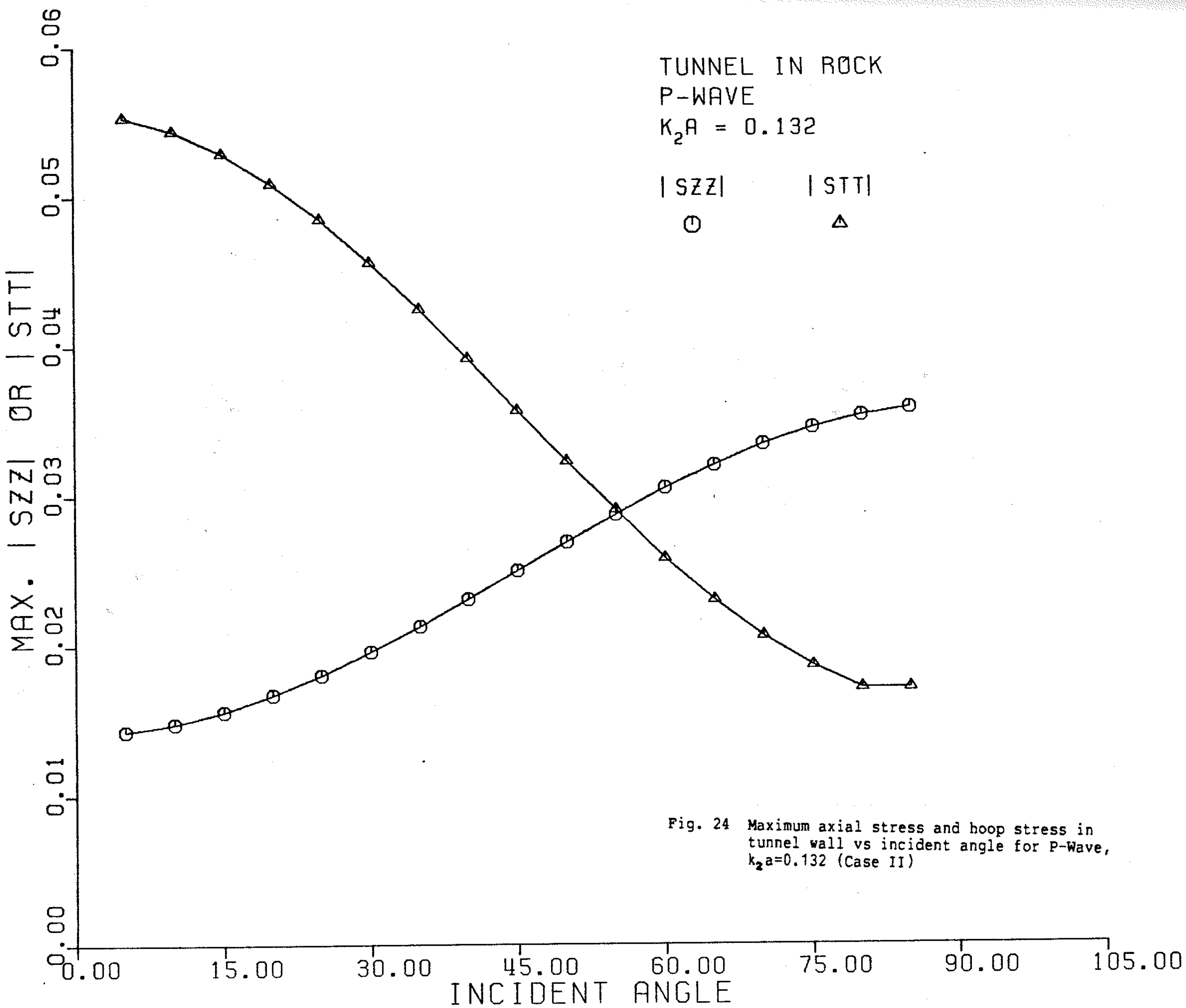

Fig. 24 Maximum axial stress and hoop stress in tunnel wall vs incident angle for P-Wave, $k_2a=0.132$ (Case II)

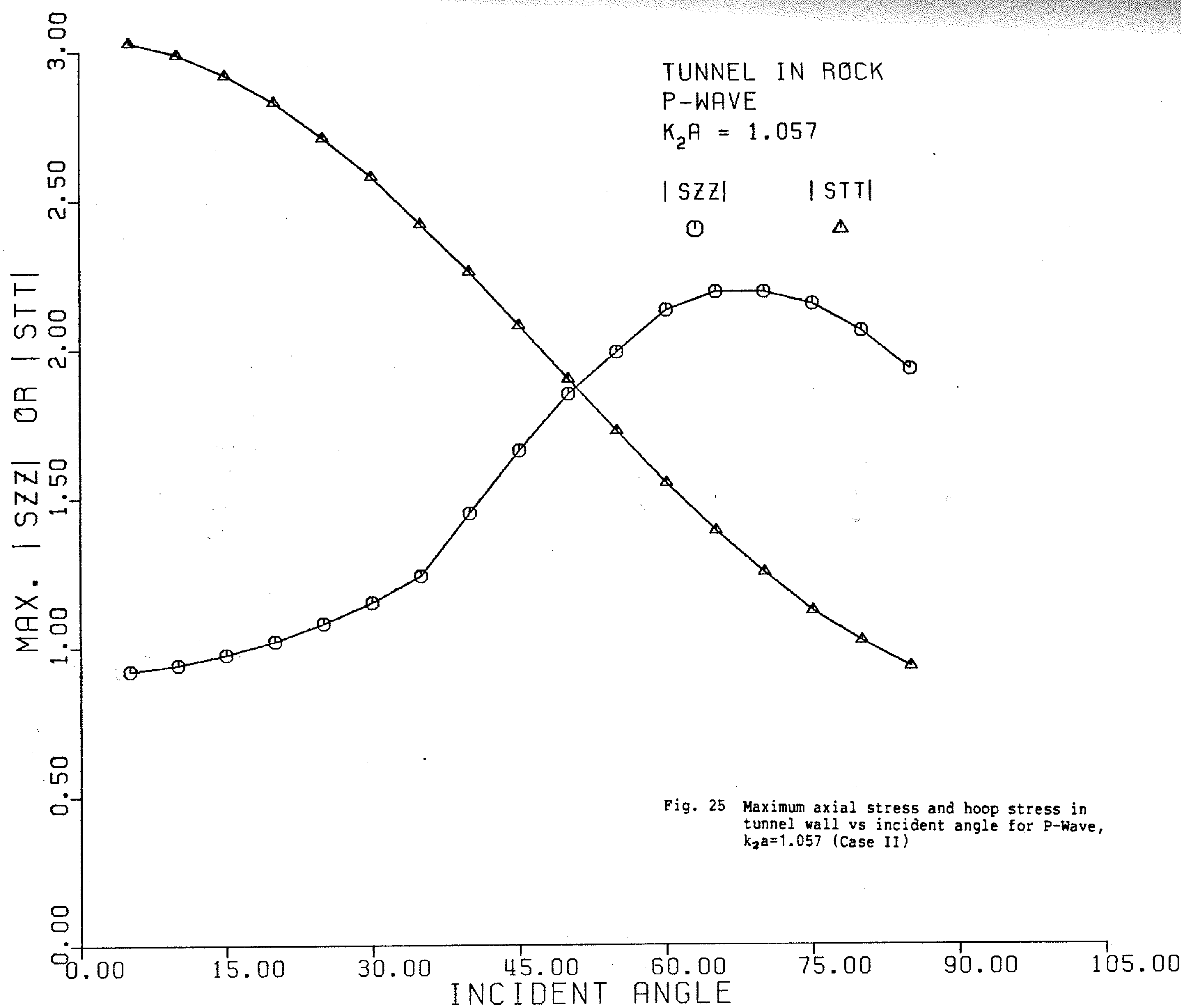

Fig. 25 Maximum axial stress and hoop stress in tunnel wall vs incident angle for P-Wave, k_2a=1.057 (Case II)

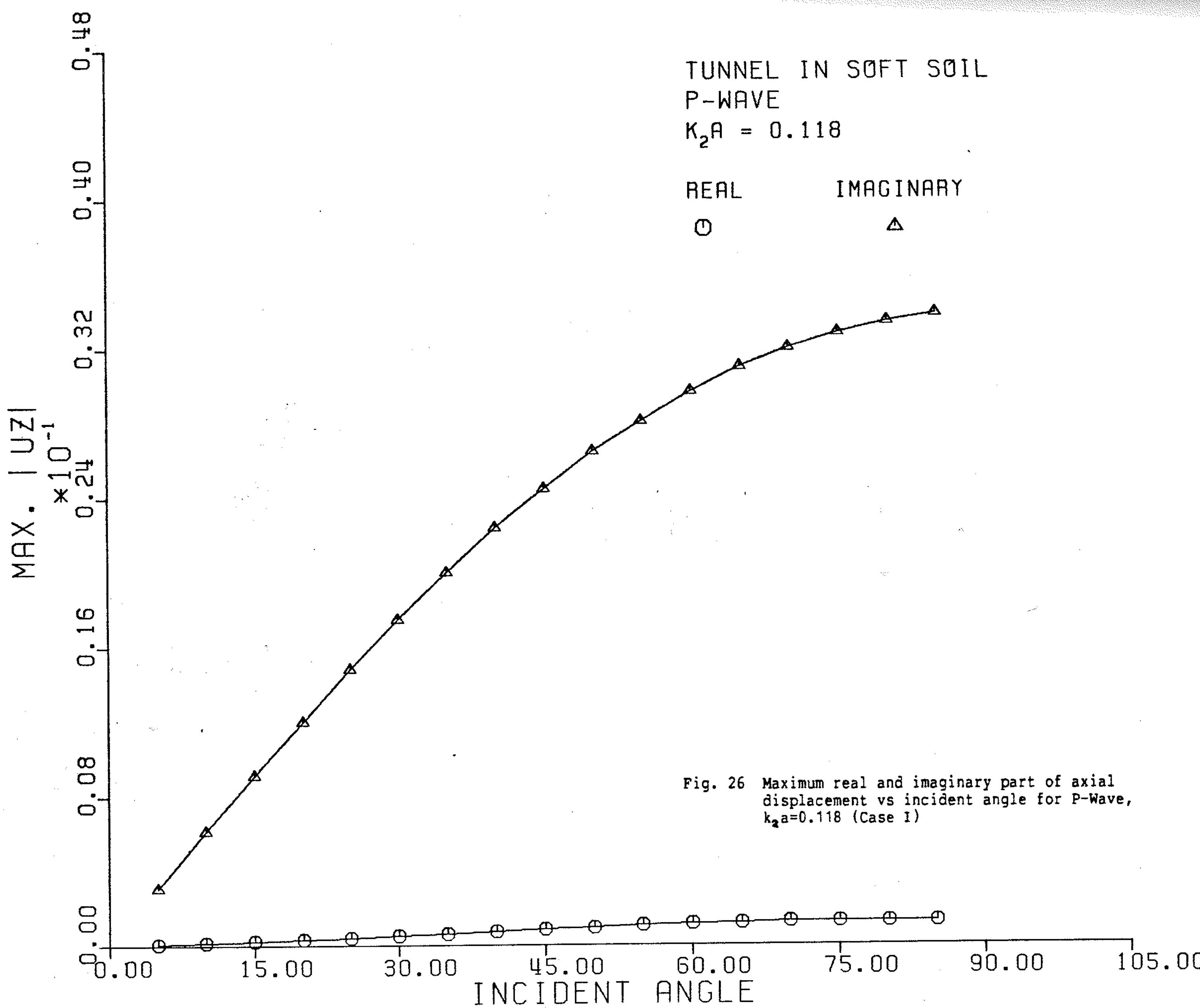

Fig. 26 Maximum real and imaginary part of axial displacement vs incident angle for P-Wave, $k_2a=0.118$ (Case I)

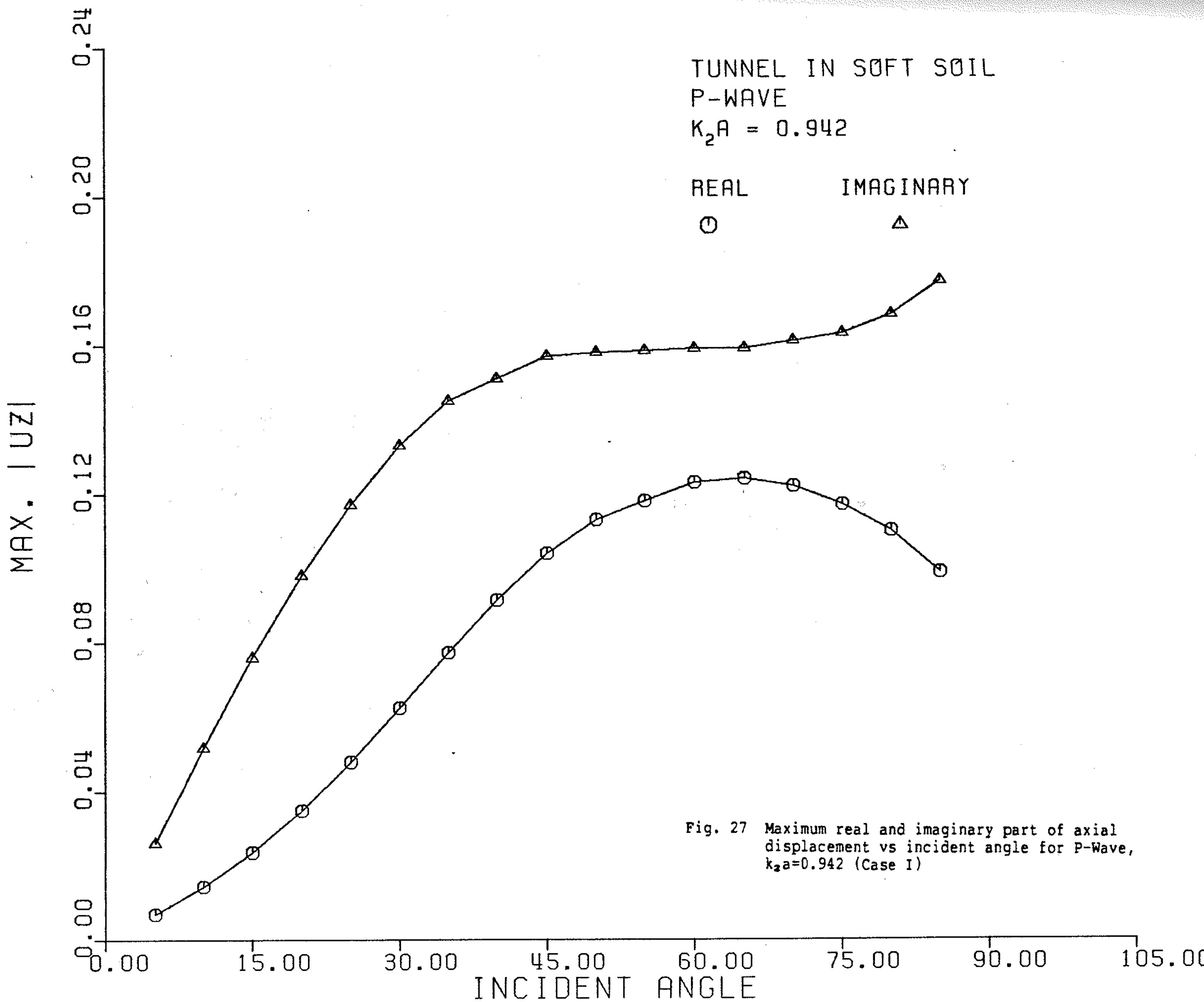

Fig. 27 Maximum real and imaginary part of axial displacement vs incident angle for P-Wave, $k_2a=0.942$ (Case I)

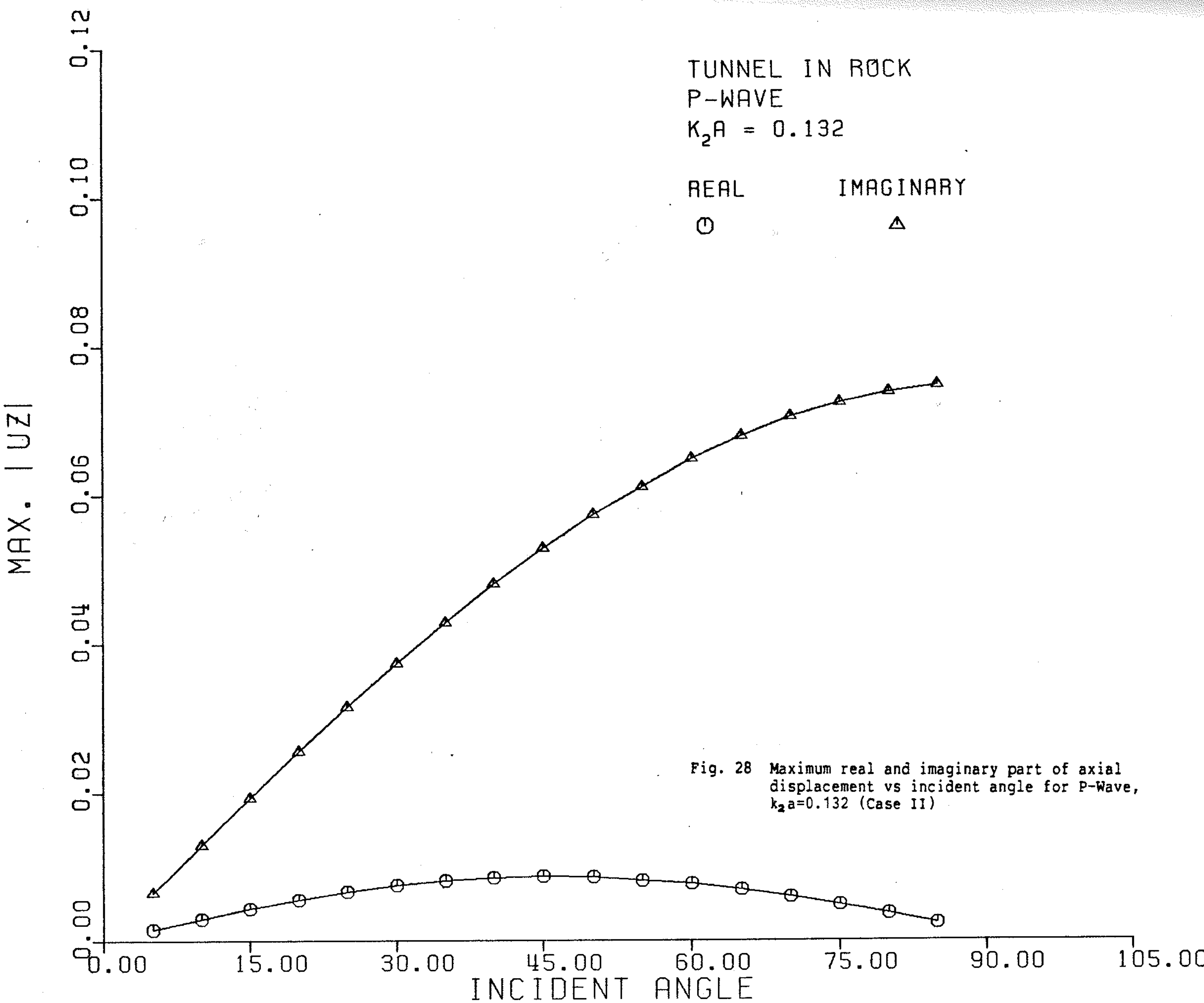

Fig. 28 Maximum real and imaginary part of axial displacement vs incident angle for P-Wave, $k_2a=0.132$ (Case II)

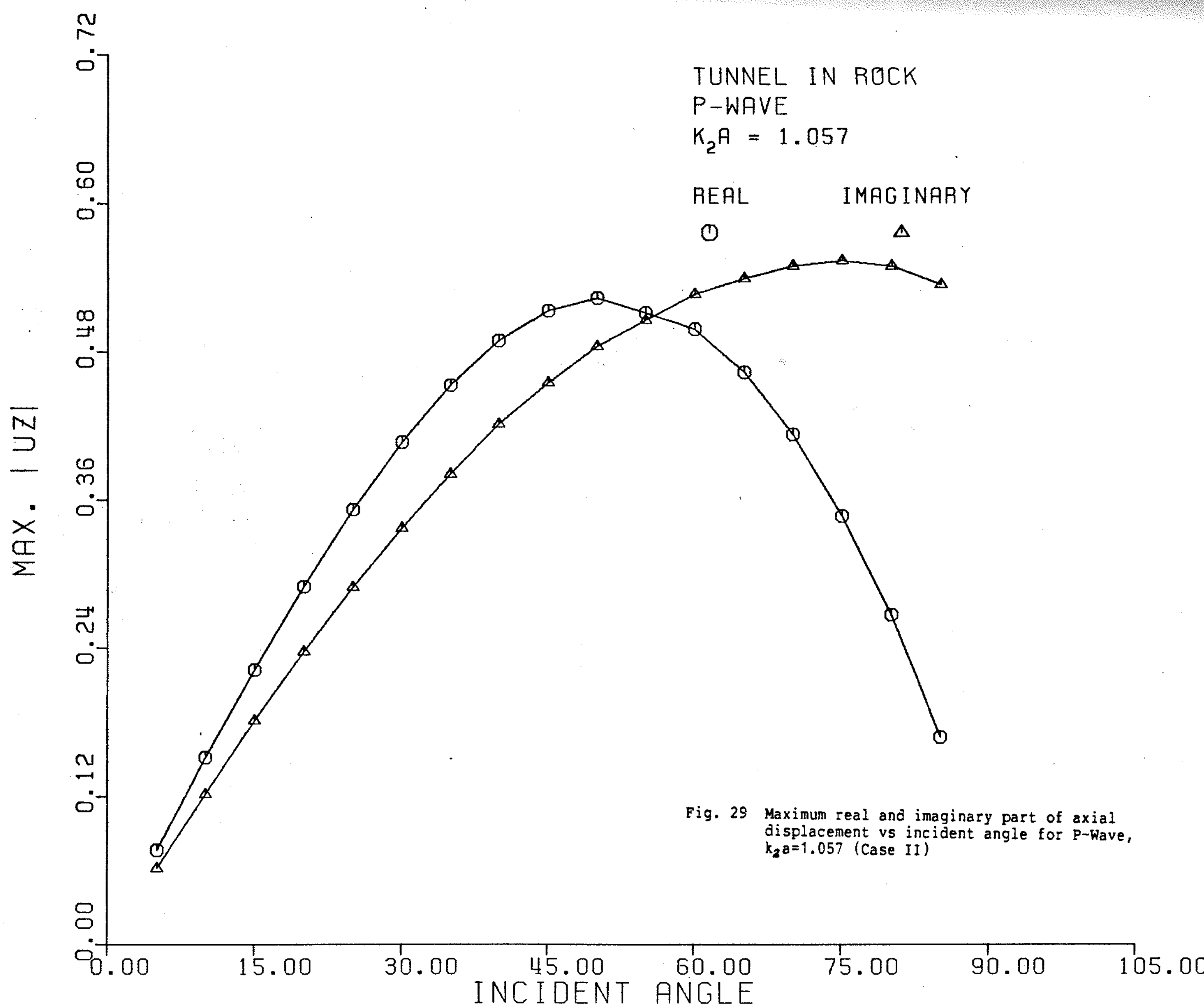

Fig. 29 Maximum real and imaginary part of axial displacement vs incident angle for P-Wave, k_2a=1.057 (Case II)

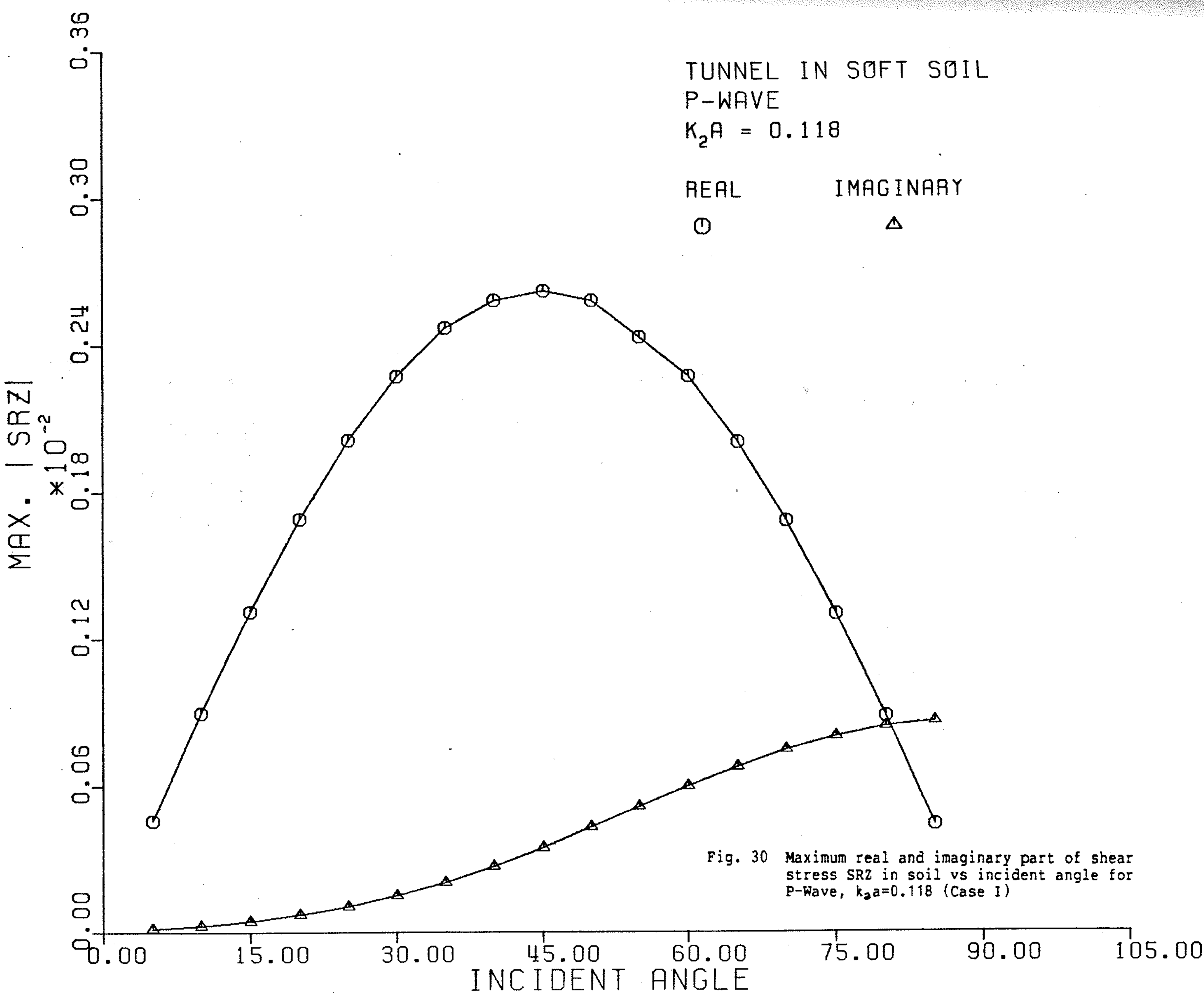

Fig. 30 Maximum real and imaginary part of shear stress SRZ in soil vs incident angle for P-Wave, k_2a=0.118 (Case I)

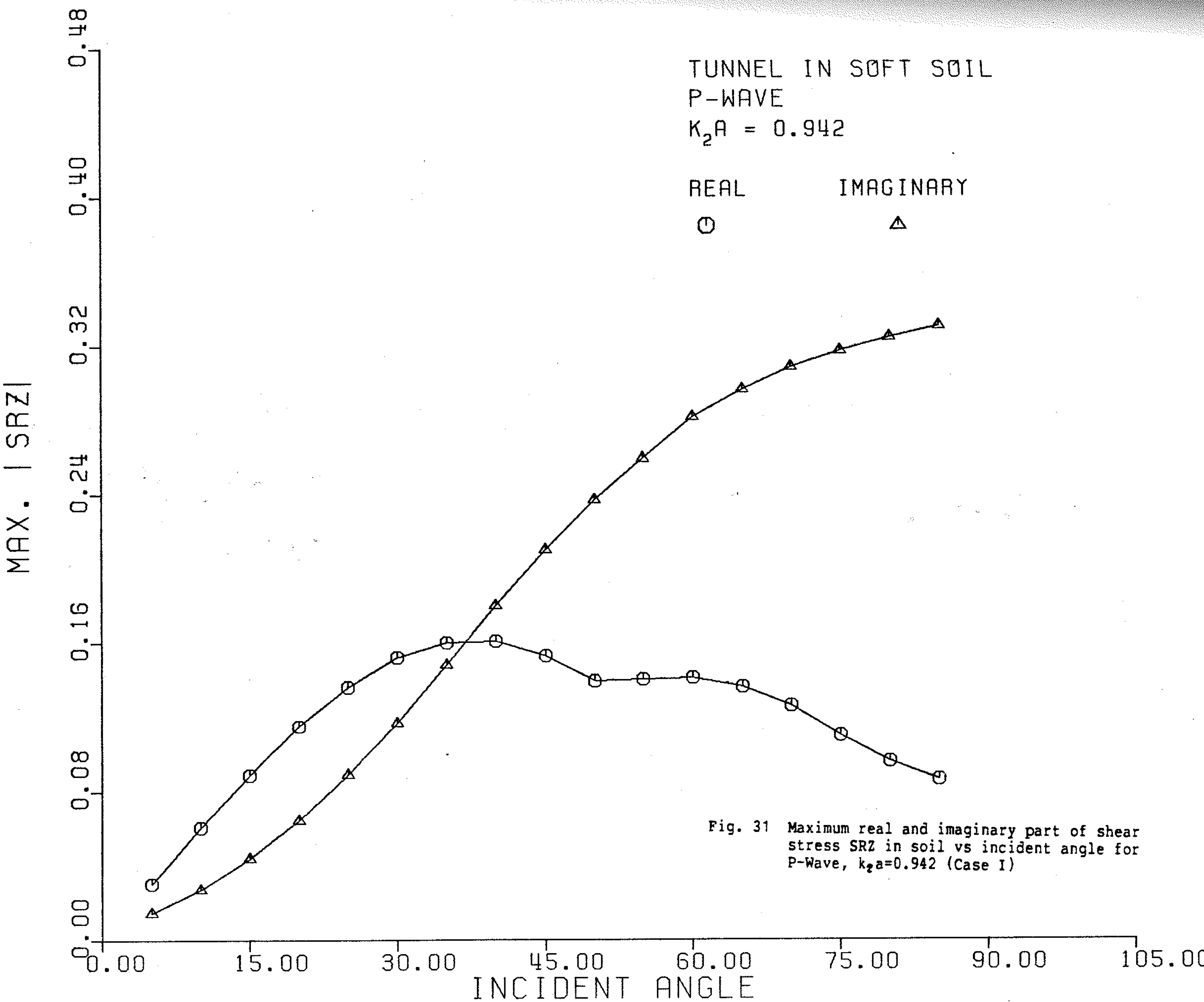

Fig. 31 Maximum real and imaginary part of shear stress SRZ in soil vs incident angle for P-Wave, k_2a=0.942 (Case I)

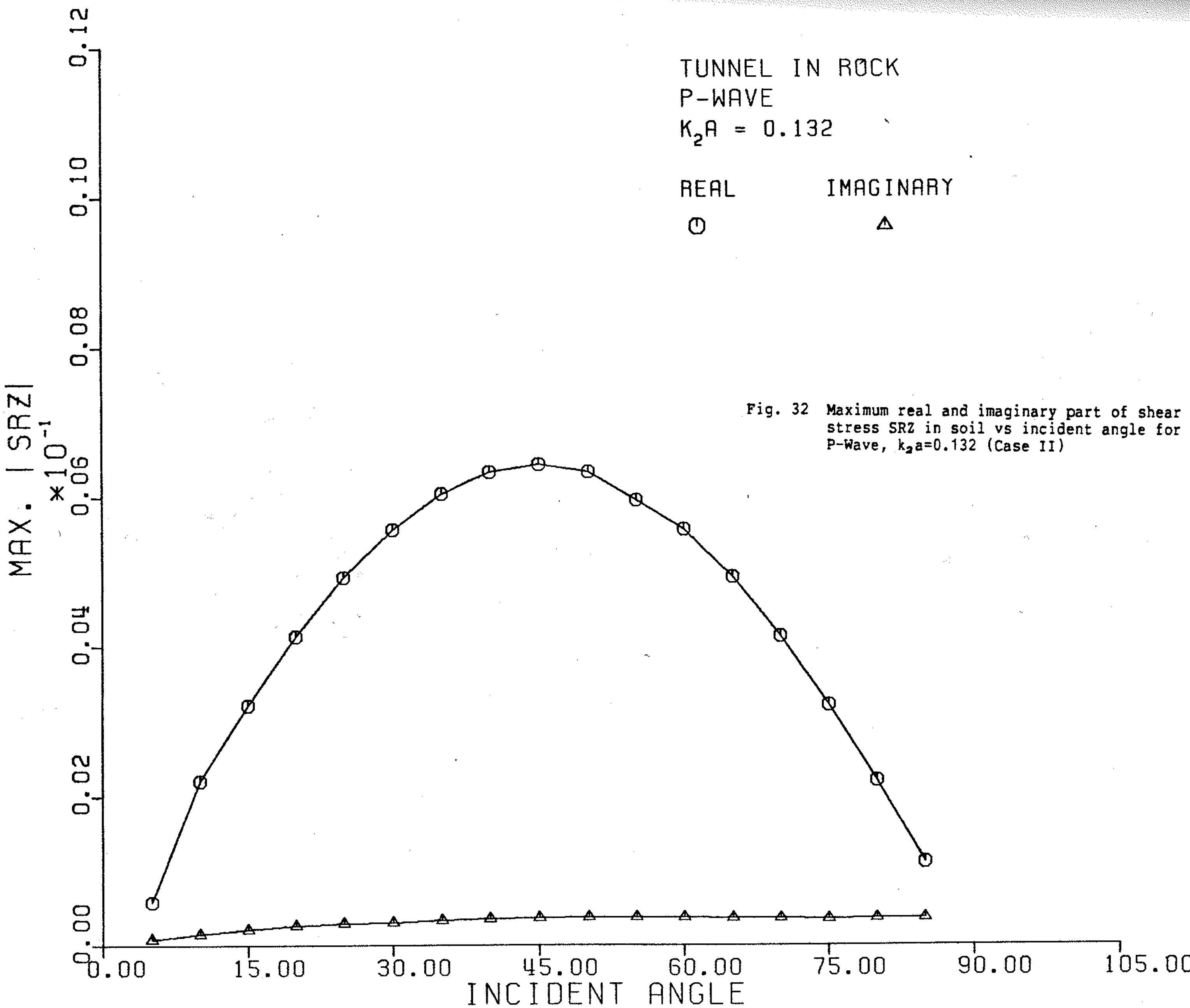

Fig. 32 Maximum real and imaginary part of shear stress SRZ in soil vs incident angle for P-Wave, $k_2a=0.132$ (Case II)

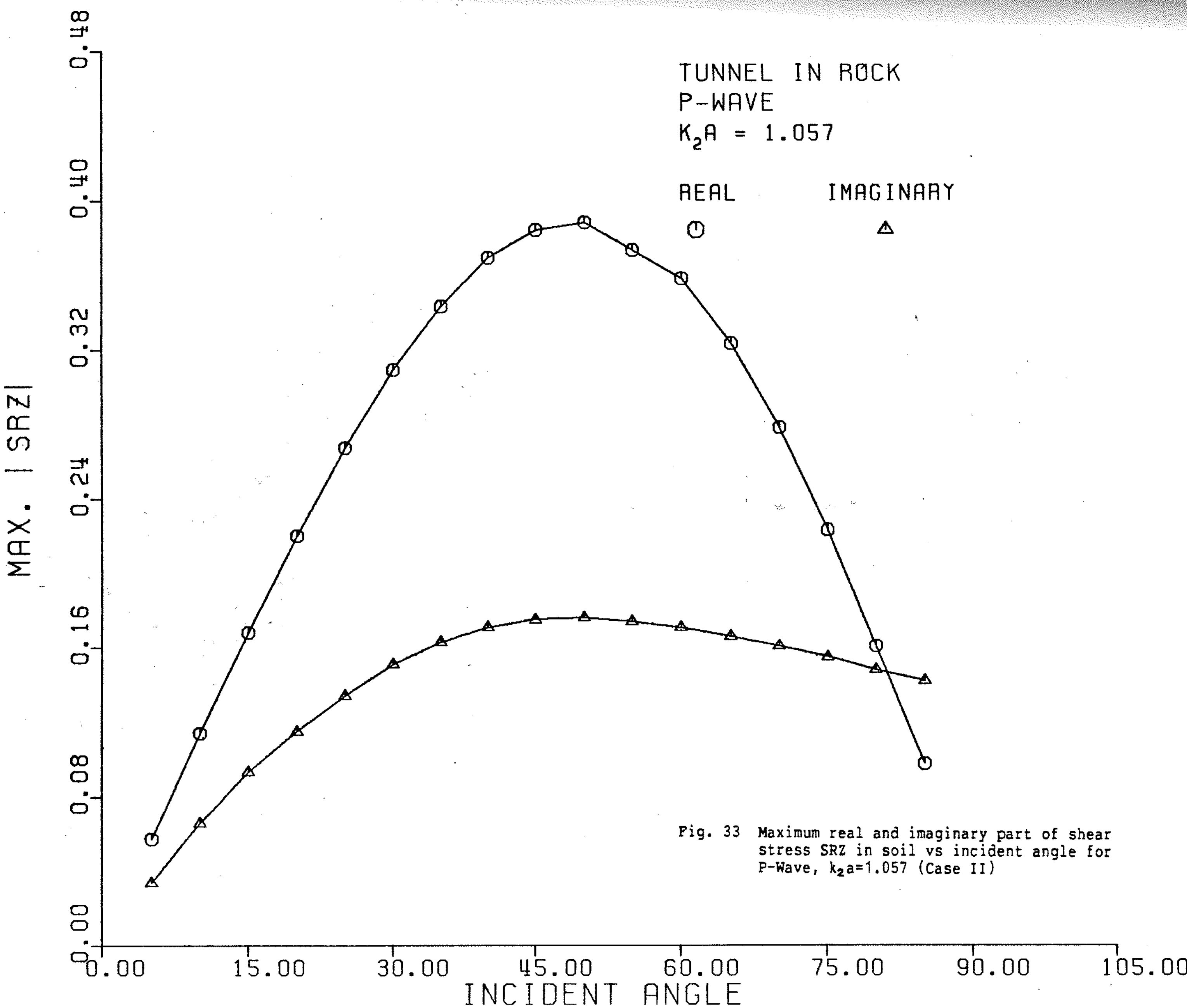

Fig. 33 Maximum real and imaginary part of shear stress SRZ in soil vs incident angle for P-Wave, $k_2a=1.057$ (Case II)

P-WAVE (5 DEG.)
SZZ (CONCRETE)

TUNNEL IN ROCK			TUNNEL IN SOFT SOIL		
$\frac{WA}{2\pi}$ (M/SEC)		NF	$\frac{WA}{2\pi}$ (M/SEC)		NF
89.50	+	0.094	89.50	⊕	2.920
134.33	×	0.213	134.33	△	6.600

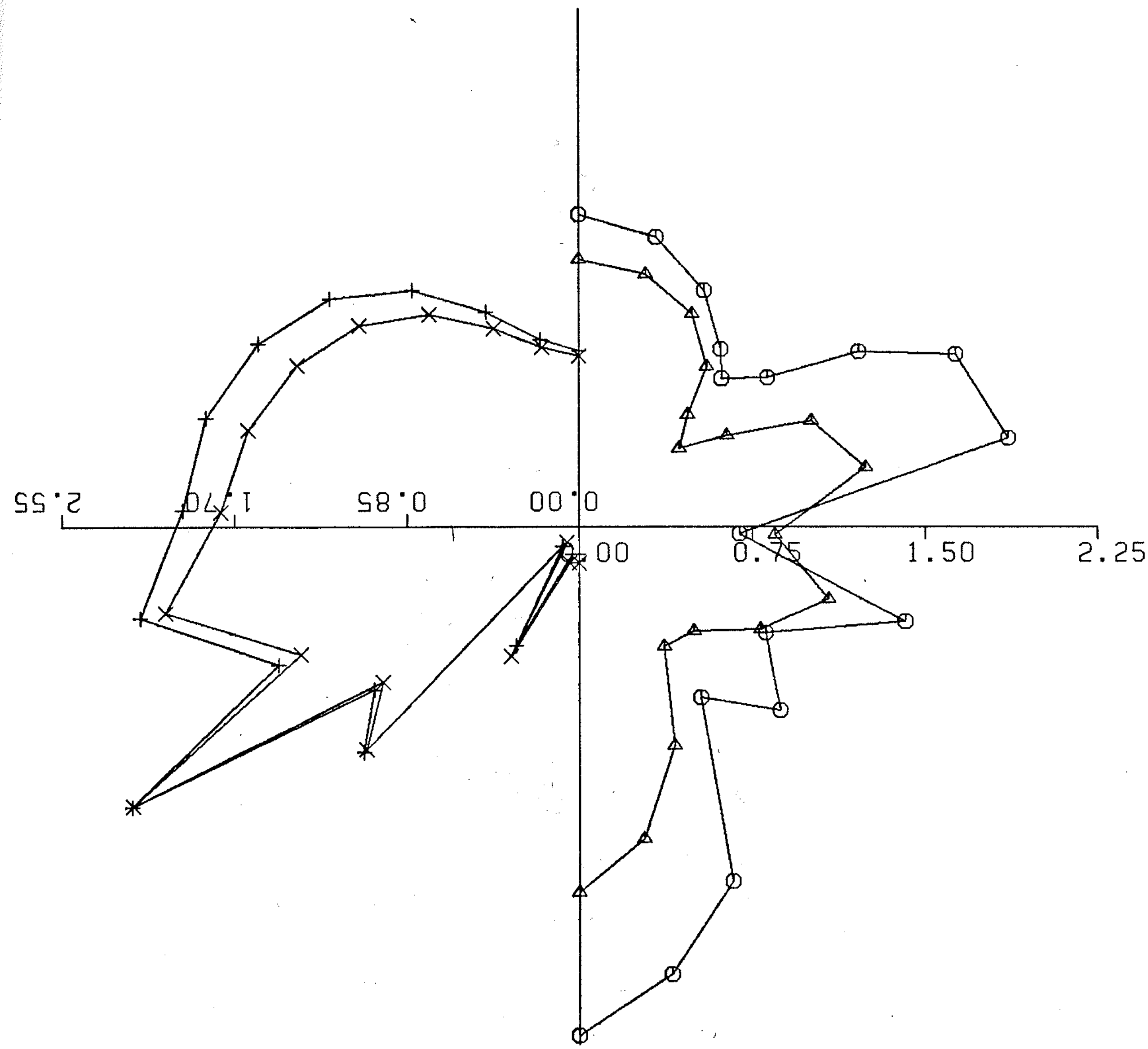

Fig. 34 Comparison between Case I and Case II for normalized axial stress in tunnel wall for P-Wave, incident angle = 5°

P-WAVE (85 DEG.)
SZZ (CONCRETE)

TUNNEL IN ROCK

$\frac{\omega A}{2\pi}$ (M/SEC)		NF
89.50	+	0.277
134.33	×	0.624

TUNNEL IN SOFT SOIL

$\frac{\omega A}{2\pi}$ (M/SEC)		NF
89.50	○	3.540
134.33	△	7.970

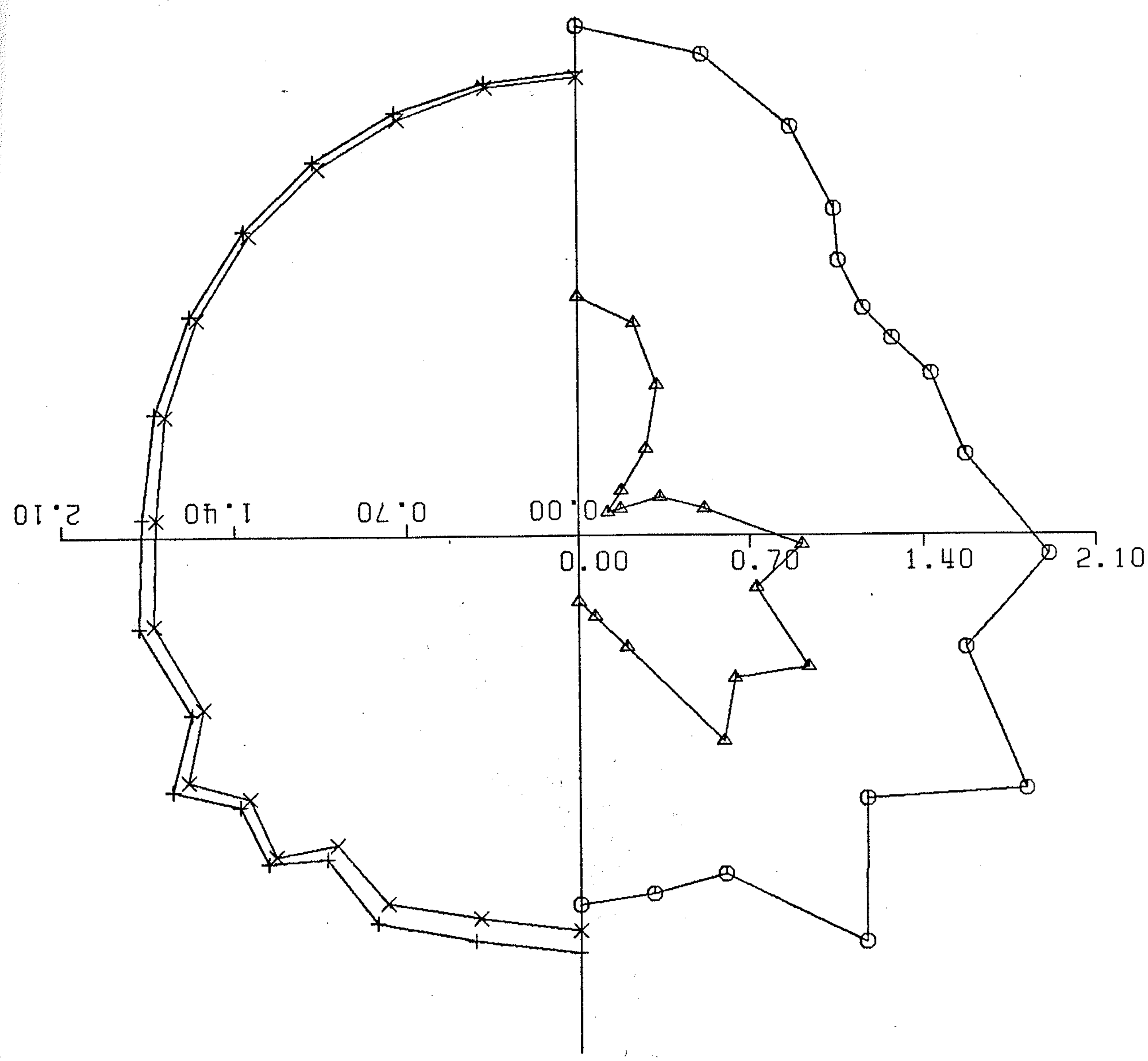

Fig. 35 Comparison between Case I and Case II for normalized axial stress in tunnel wall for P-Wave, incident angle = 85°

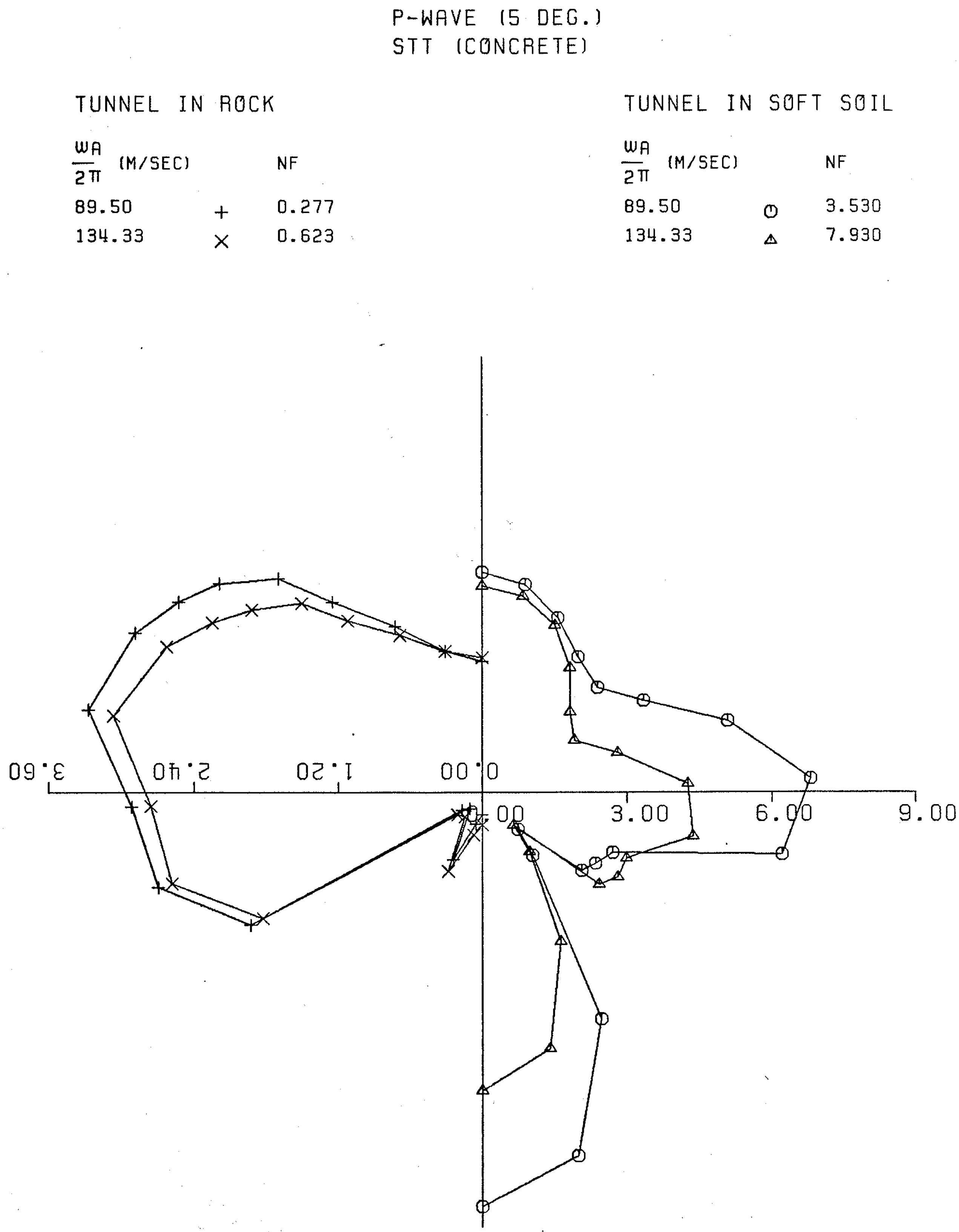

Fig. 36 Comparison between Case I and Case II for normalized hoop stress in tunnel wall for P-Wave, incident angle = 5°

P-WAVE (85 DEG.)
STT (CONCRETE)

TUNNEL IN ROCK			TUNNEL IN SOFT SOIL		
$\frac{WA}{2\pi}$ (M/SEC)		NF	$\frac{WA}{2\pi}$ (M/SEC)		NF
89.50	+	0.094	89.50	○	2.910
134.33	×	0.212	134.33	△	6.540

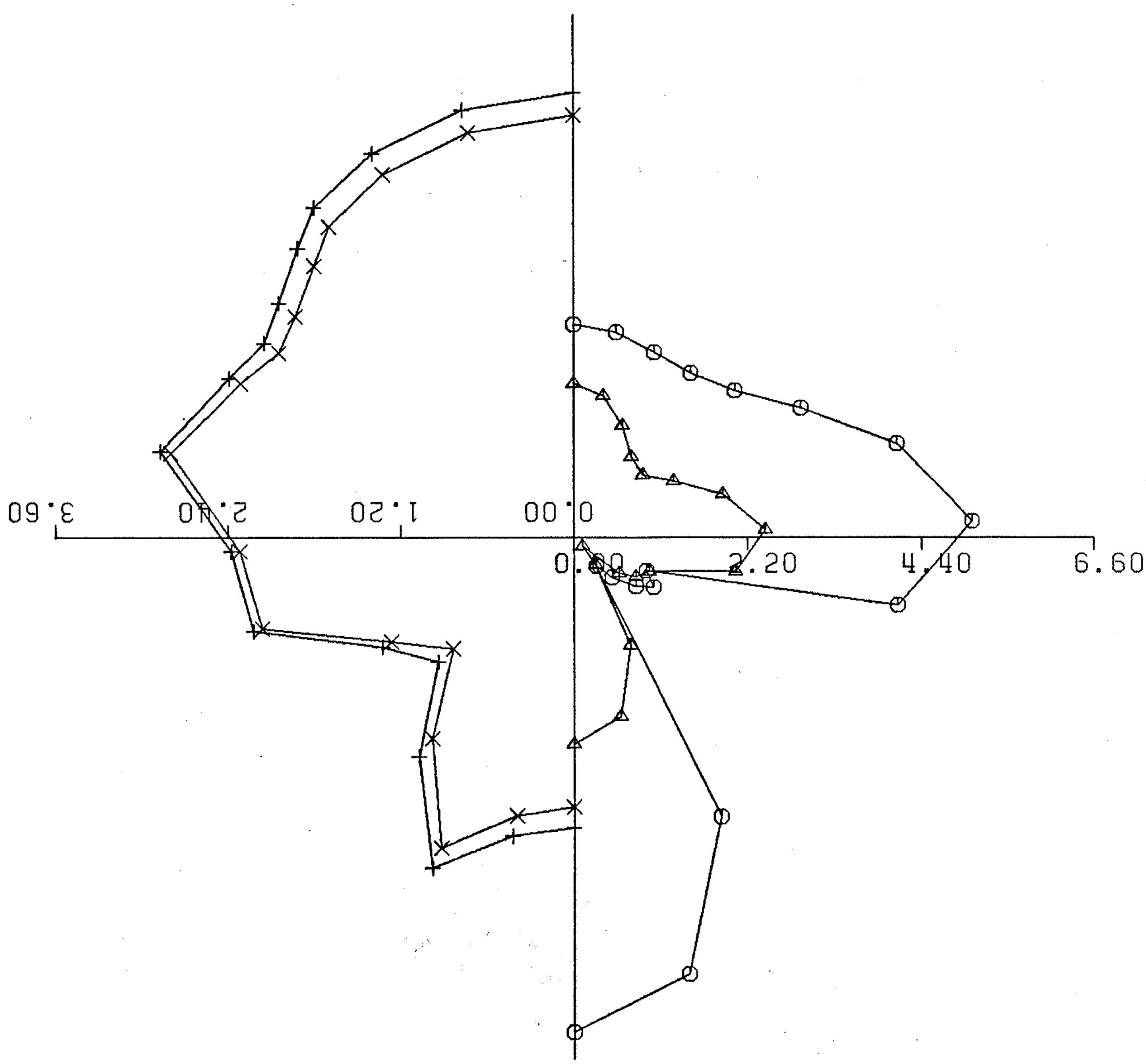

Fig. 37 Comparison between Case I and Case II for normalized hoop stress in tunnel wall for P-Wave, incident angle = 85°

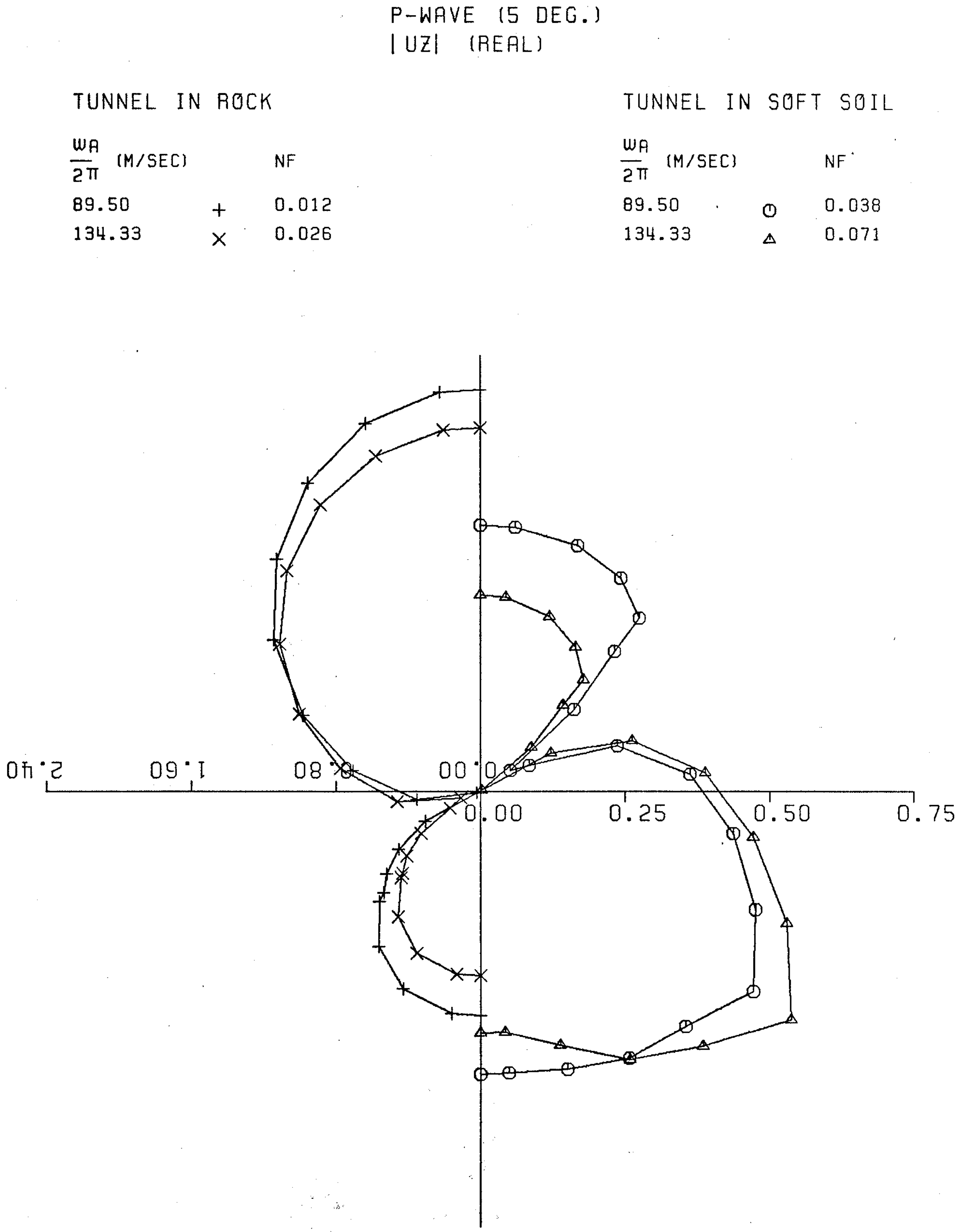

Fig. 38 Comparison between Case I and Case II for normalized real part of axial displacement for P-Wave, incident angle = 5°

P-WAVE (85 DEG.)
|UZ| (REAL)

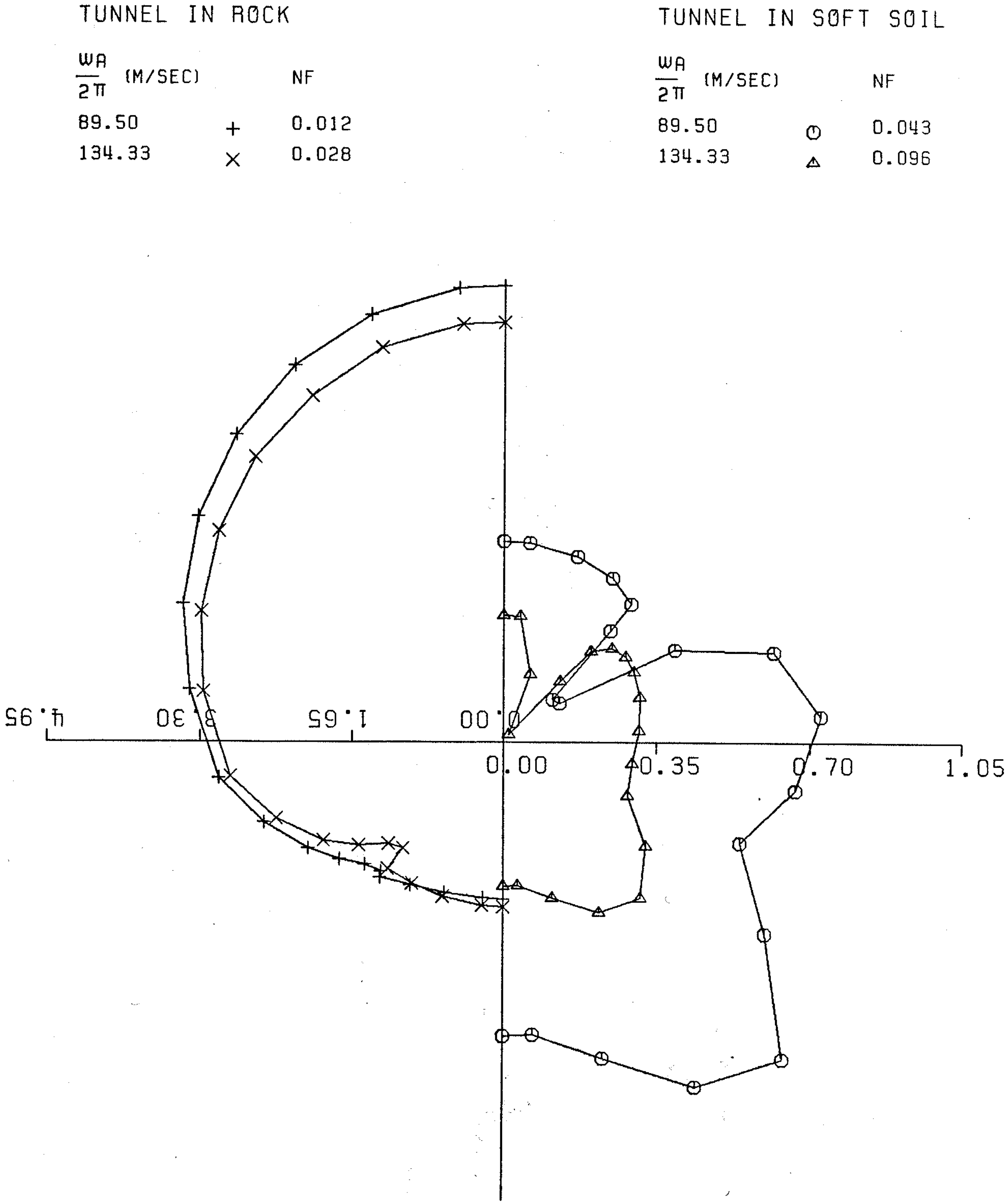

Fig. 39 Comparison between Case I and Case II for normalized real part of axial displacement for P-Wave, incident angle = 85°

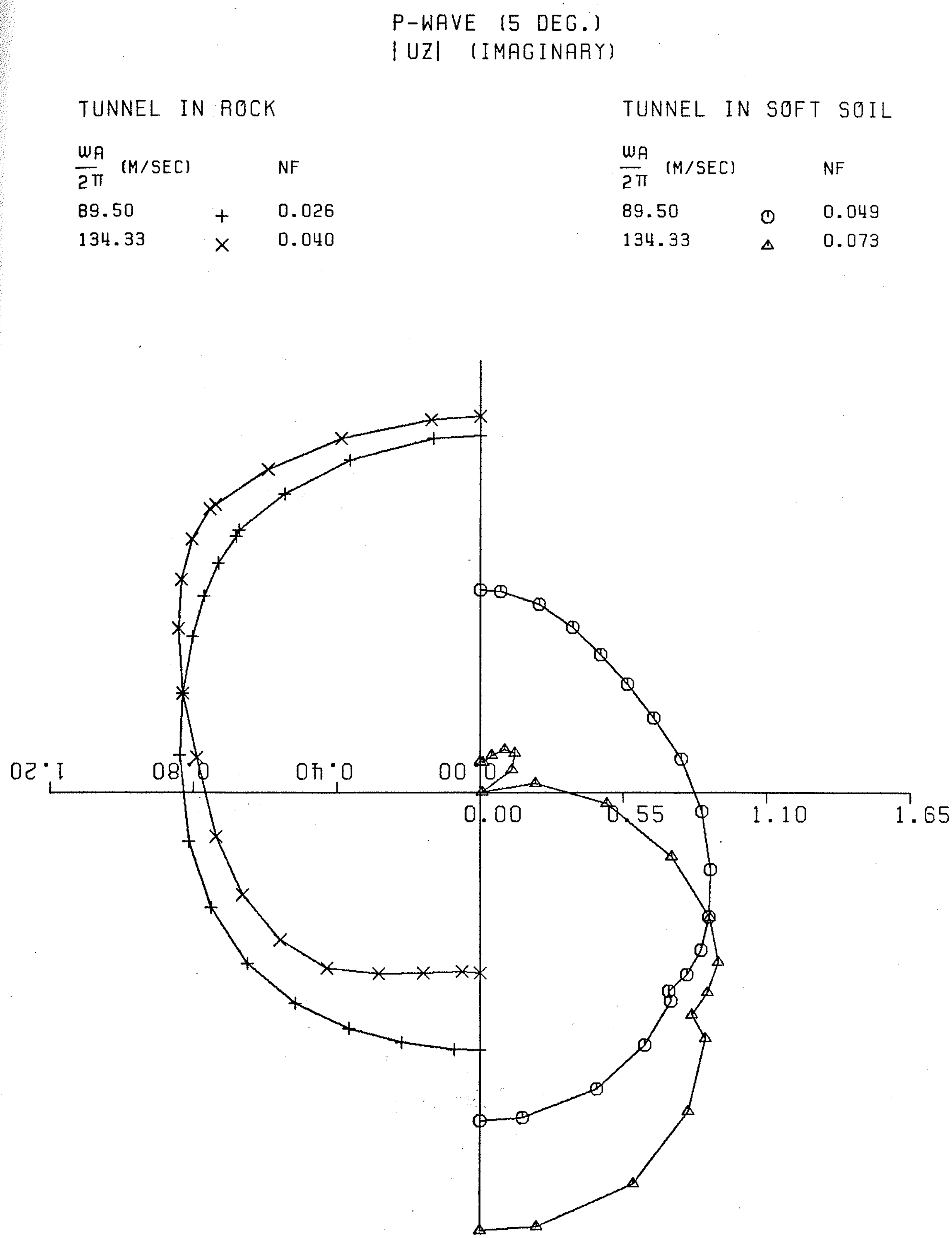

Fig. 40 Comparison between Case I and Case II for normalized imaginary part of axial displacement for P-Wave, incident angle = 5°

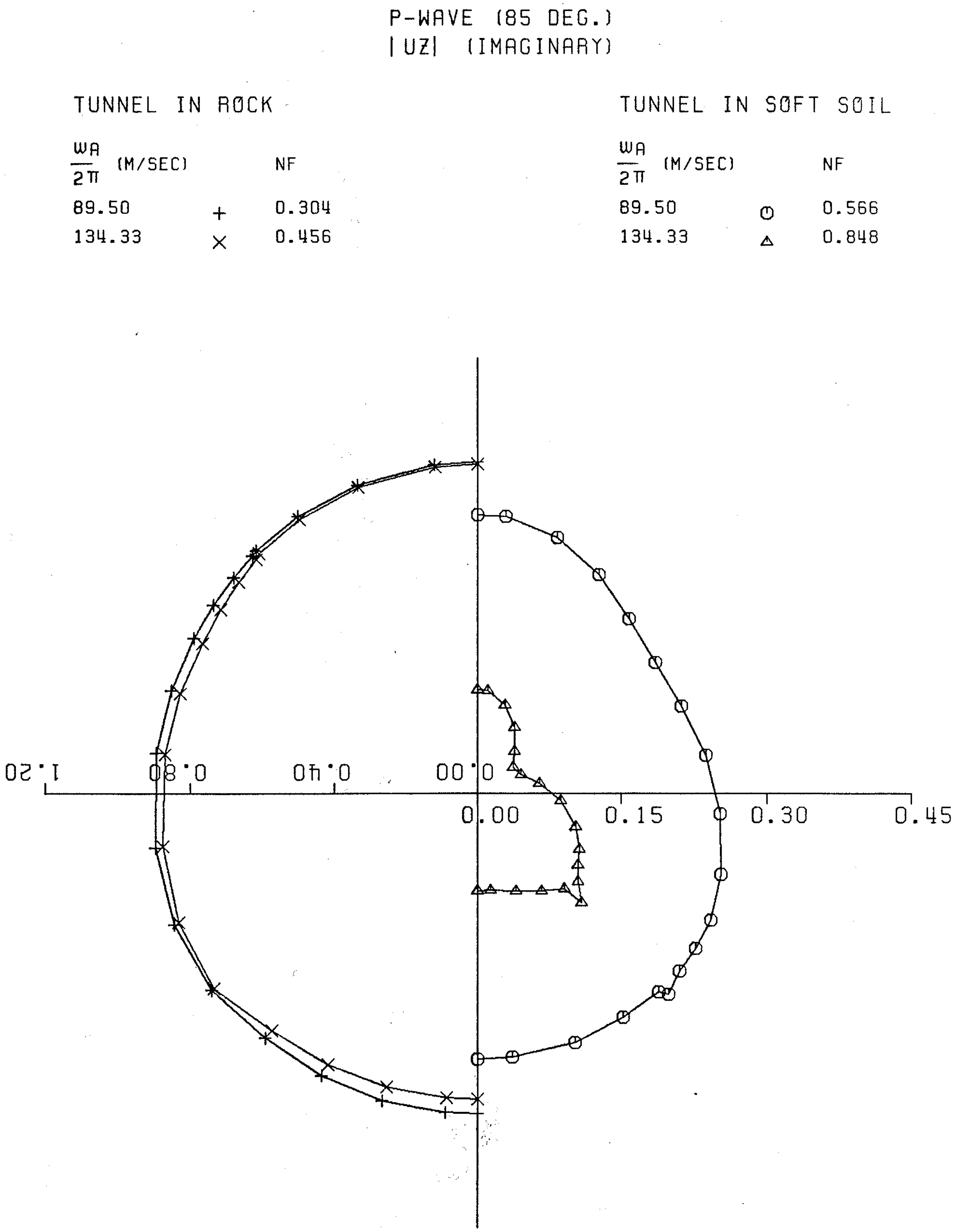

Fig. 41 Comparison between Case I and Case II for normalized imaginary part of axial displacement for P-Wave, incident angle = 85°

P-WAVE (5 DEG.)
|SRZ| (SOIL)
REAL

TUNNEL IN ROCK

$\frac{WA}{2\pi}$ (M/SEC)		NF
89.50	+	0.015
134.33	×	0.033

TUNNEL IN SOFT SOIL

$\frac{WA}{2\pi}$ (M/SEC)		NF
89.50	⊖	0.048
134.33	△	0.088

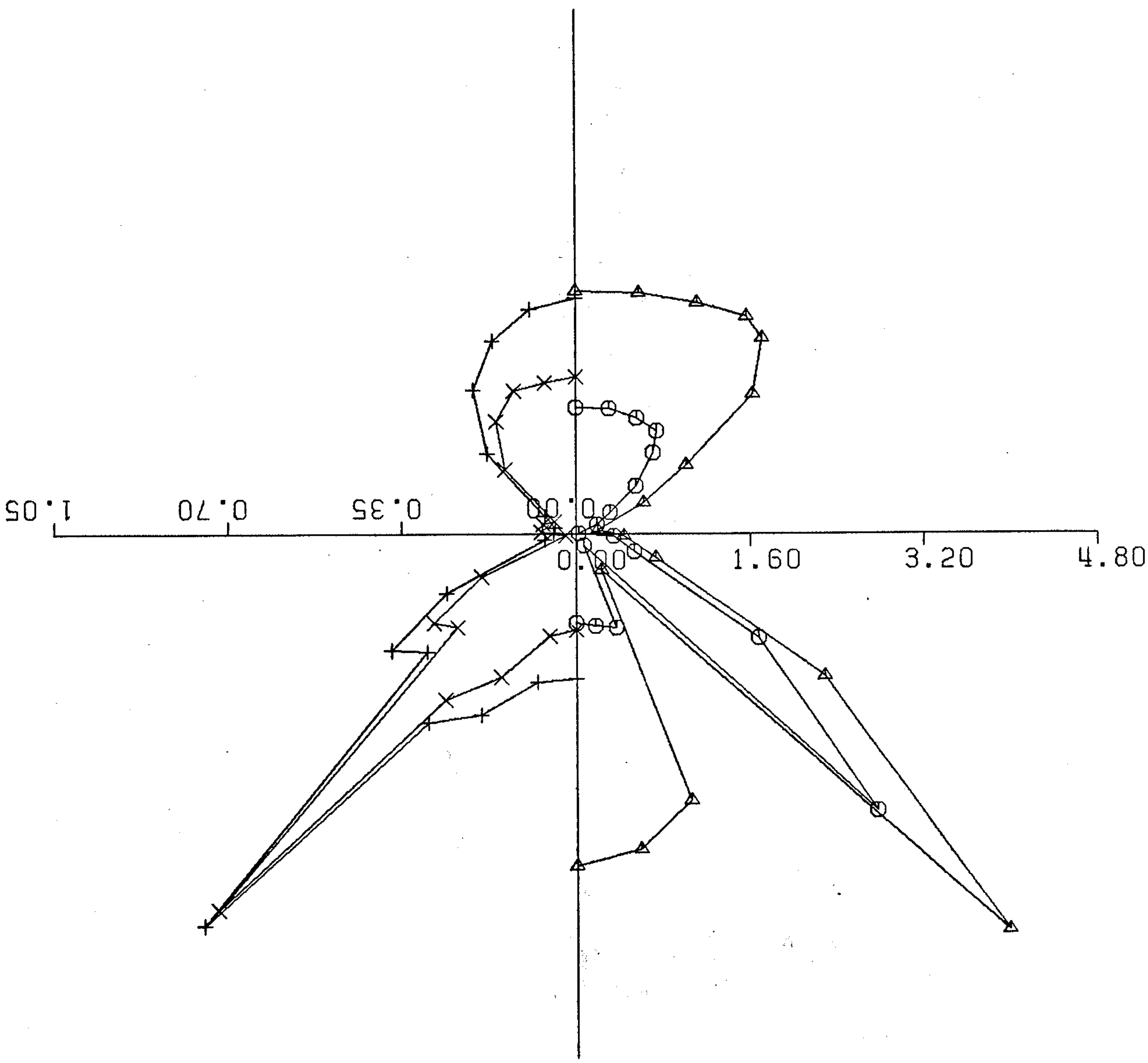

Fig. 42 Comparison between Case I and Case II for normalized real part of shear stress SRZ in soil for P-Wave, incident angle = 5°

P-WAVE (85 DEG.)
|SRZ| (SOIL)
REAL

TUNNEL IN ROCK			TUNNEL IN SOFT SOIL		
$\frac{WA}{2\pi}$ (M/SEC)		NF	$\frac{WA}{2\pi}$ (M/SEC)		NF
89.50	+	0.016	89.50	○	0.056
134.33	×	0.036	134.33	△	0.126

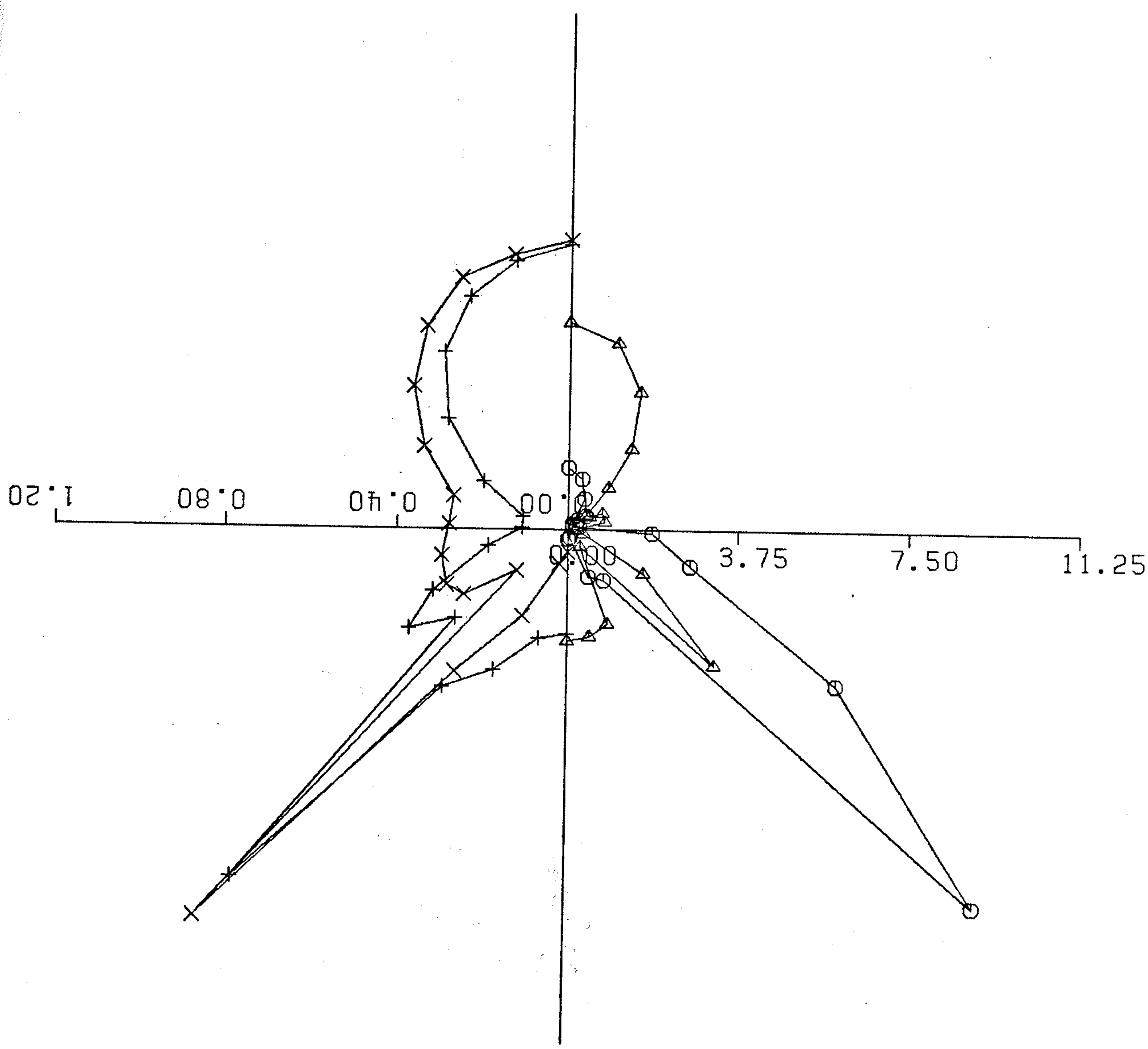

Fig. 43 Comparison between Case I and Case II for normalized real part of shear stress SRZ in soil for P-Wave, incident angle = 85°

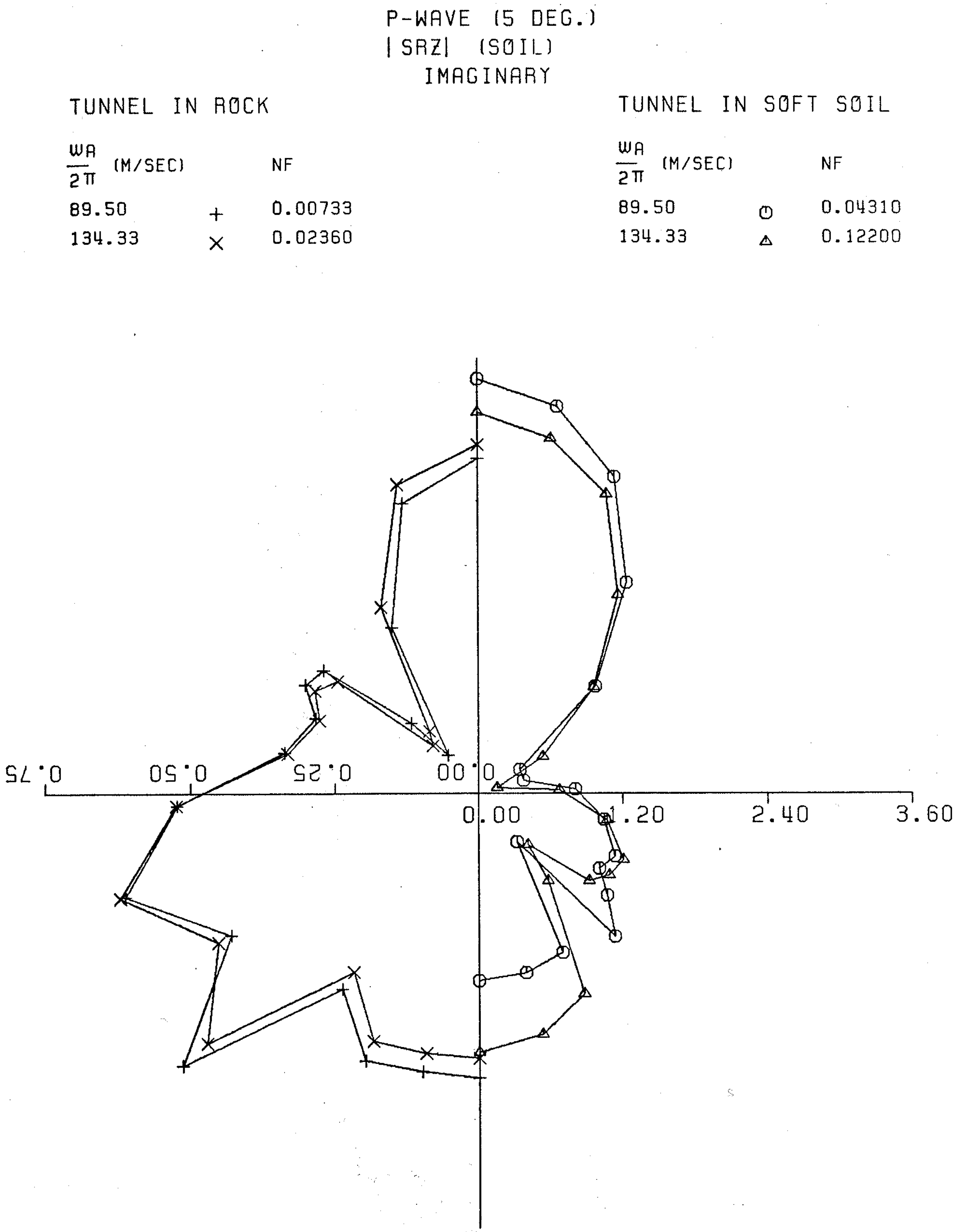

Fig. 44 Comparison between Case I and Case II for normalized imaginary part of shear stress SRZ in soil for P-Wave, incident angle = 5°

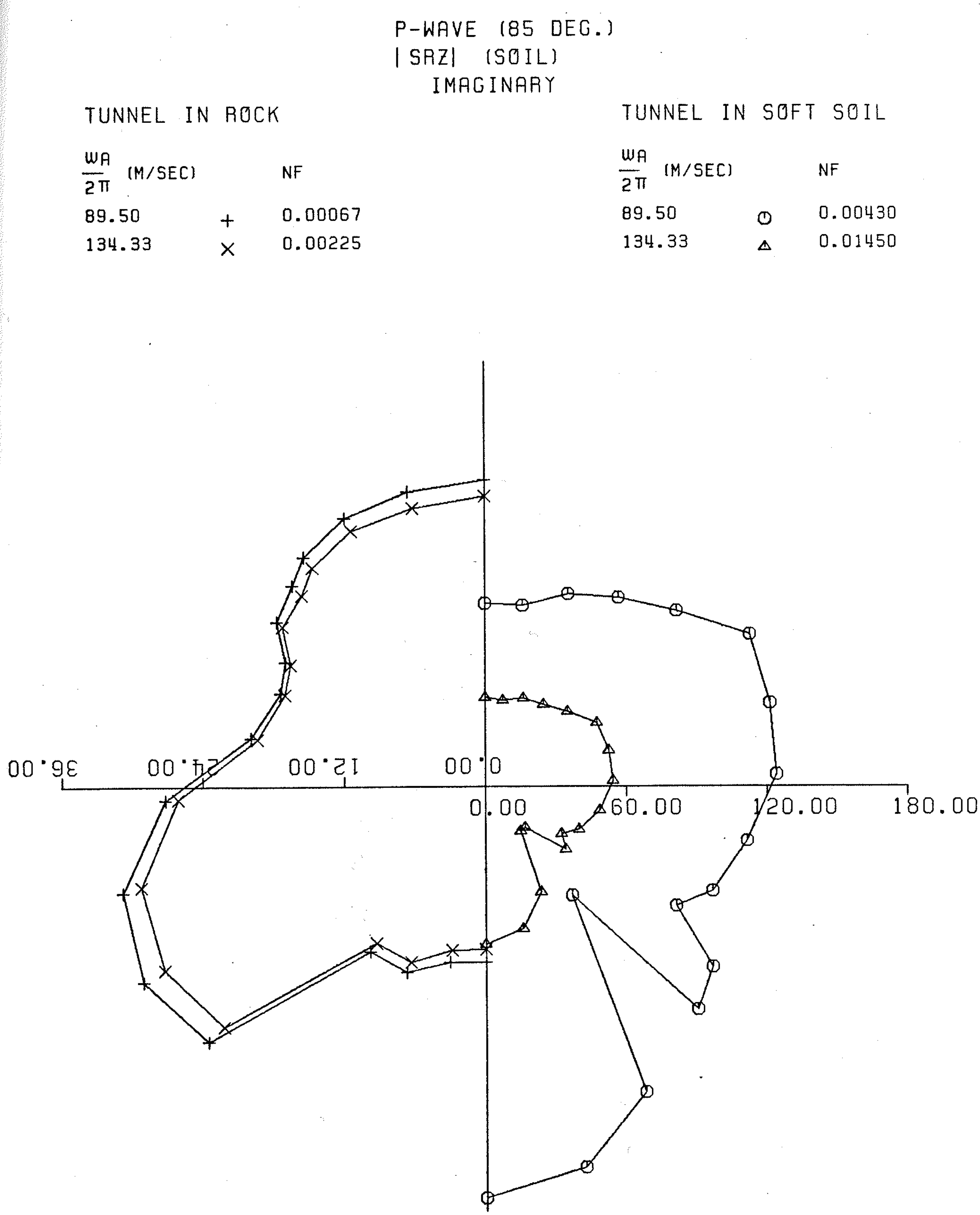

Fig. 45 Comparison between Case I and Case II for normalized imaginary part of shear stress SRZ in soil for P-Wave, incident angle = 85°

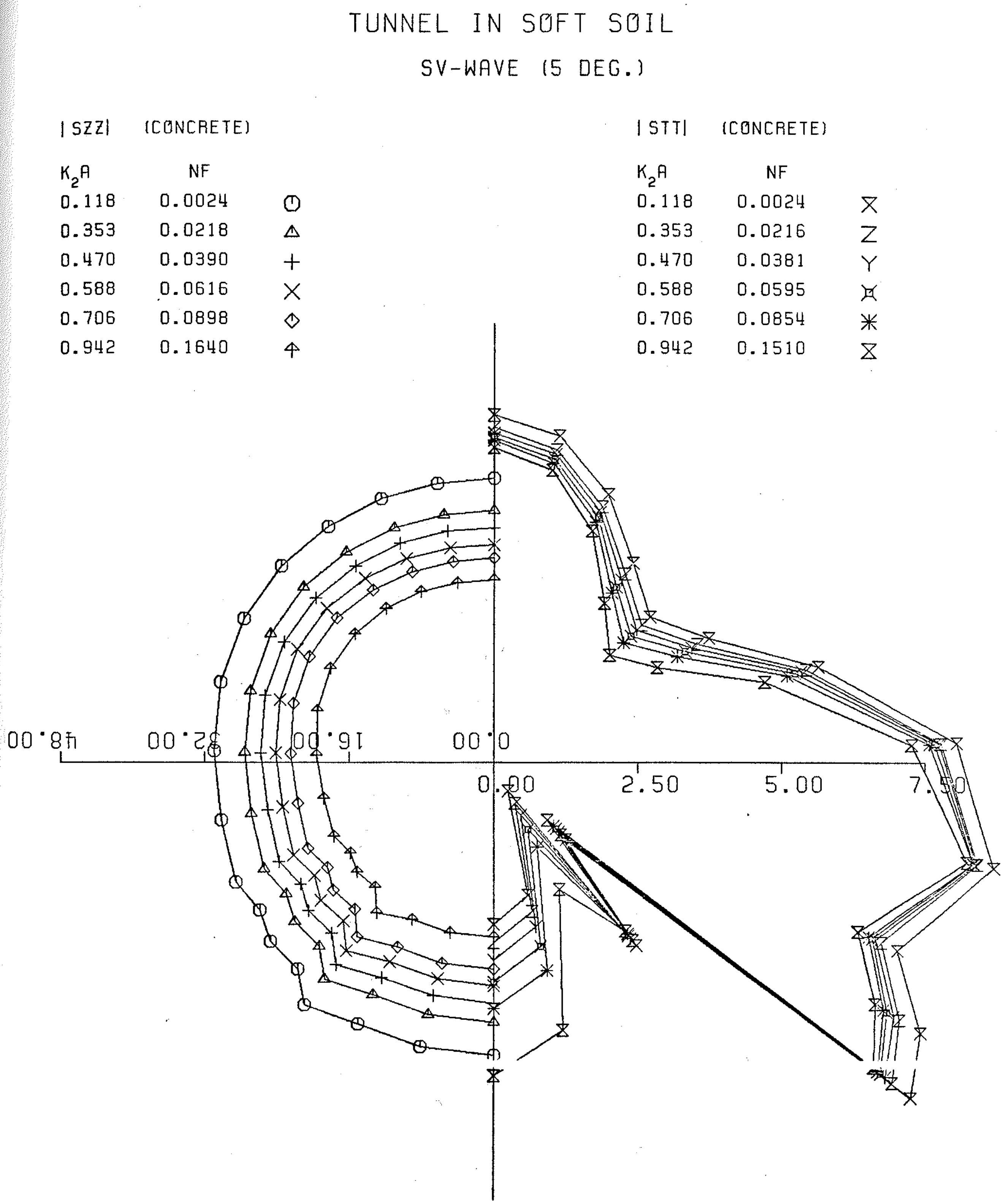

Fig. 46 Normalized axial stress and hoop stress in tunnel wall vs frequency for SV-Wave when the incident angle = 5° (Case I)

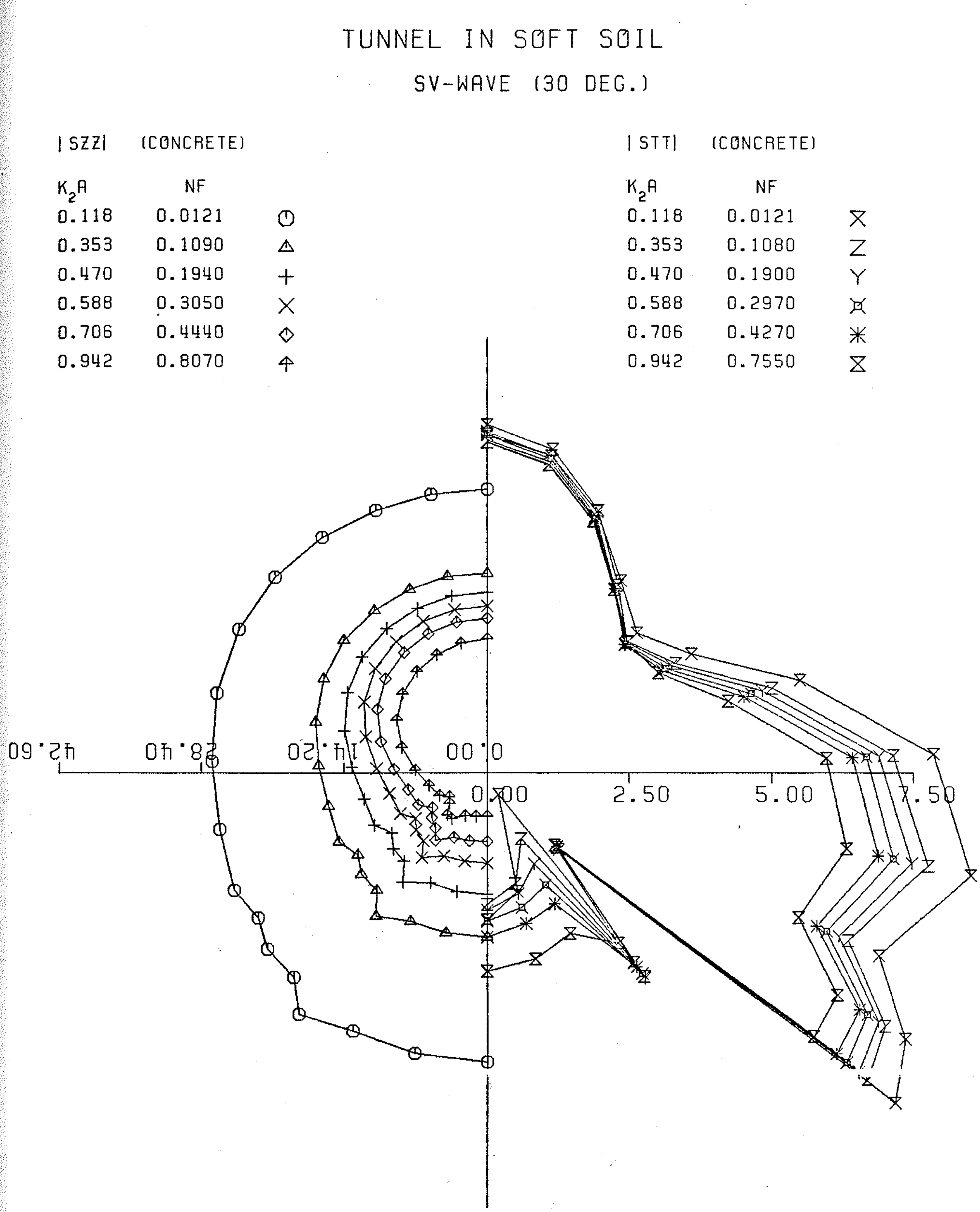

Fig. 47 Normalized axial stress and hoop stress in tunnel wall vs frequency for SV-Wave when the incident angle = 30° (Case I)

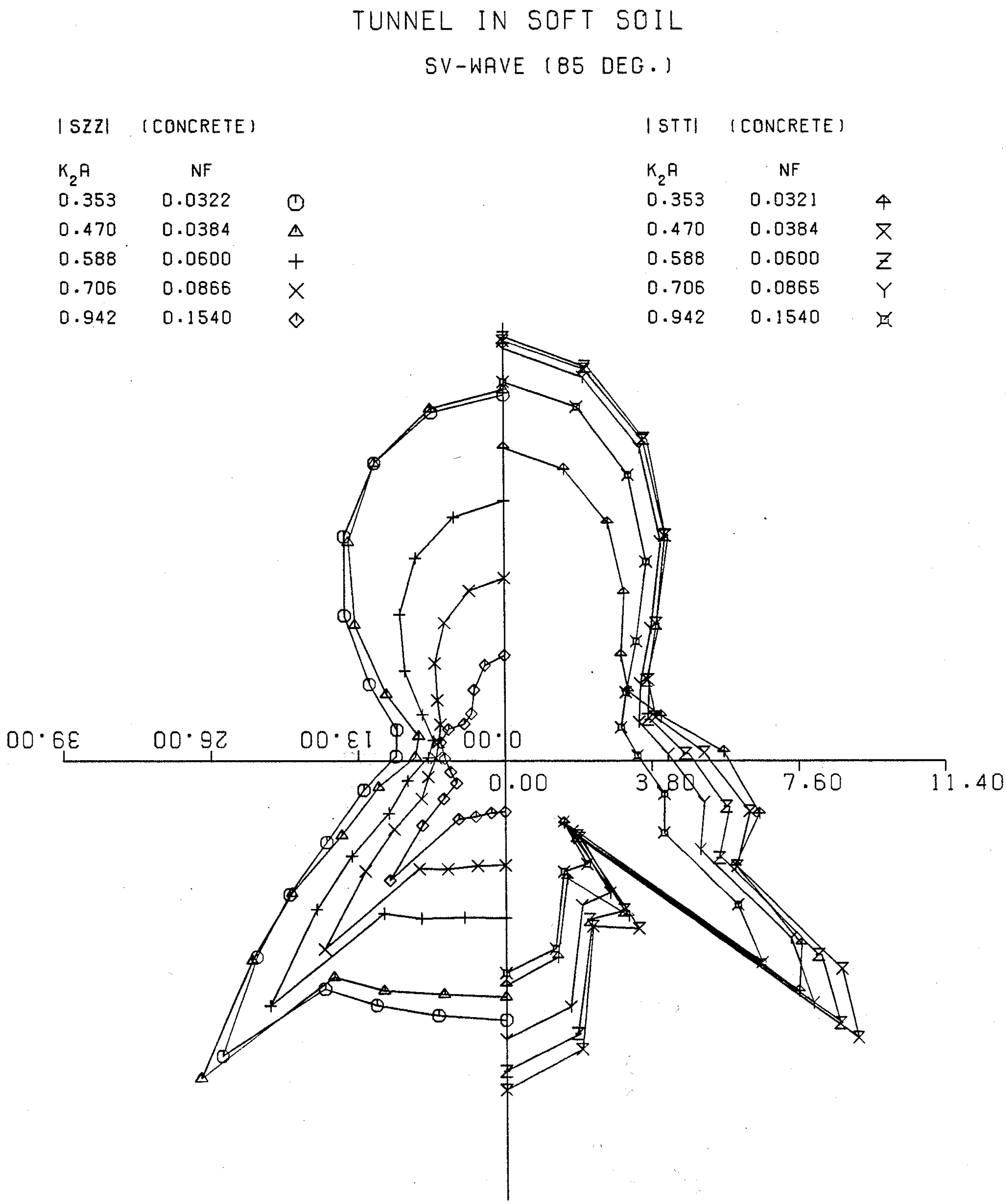

Fig. 48 Normalized axial stress and hoop stress in tunnel wall vs frequency for SV-Wave when the incident angle = 85° (Case I)

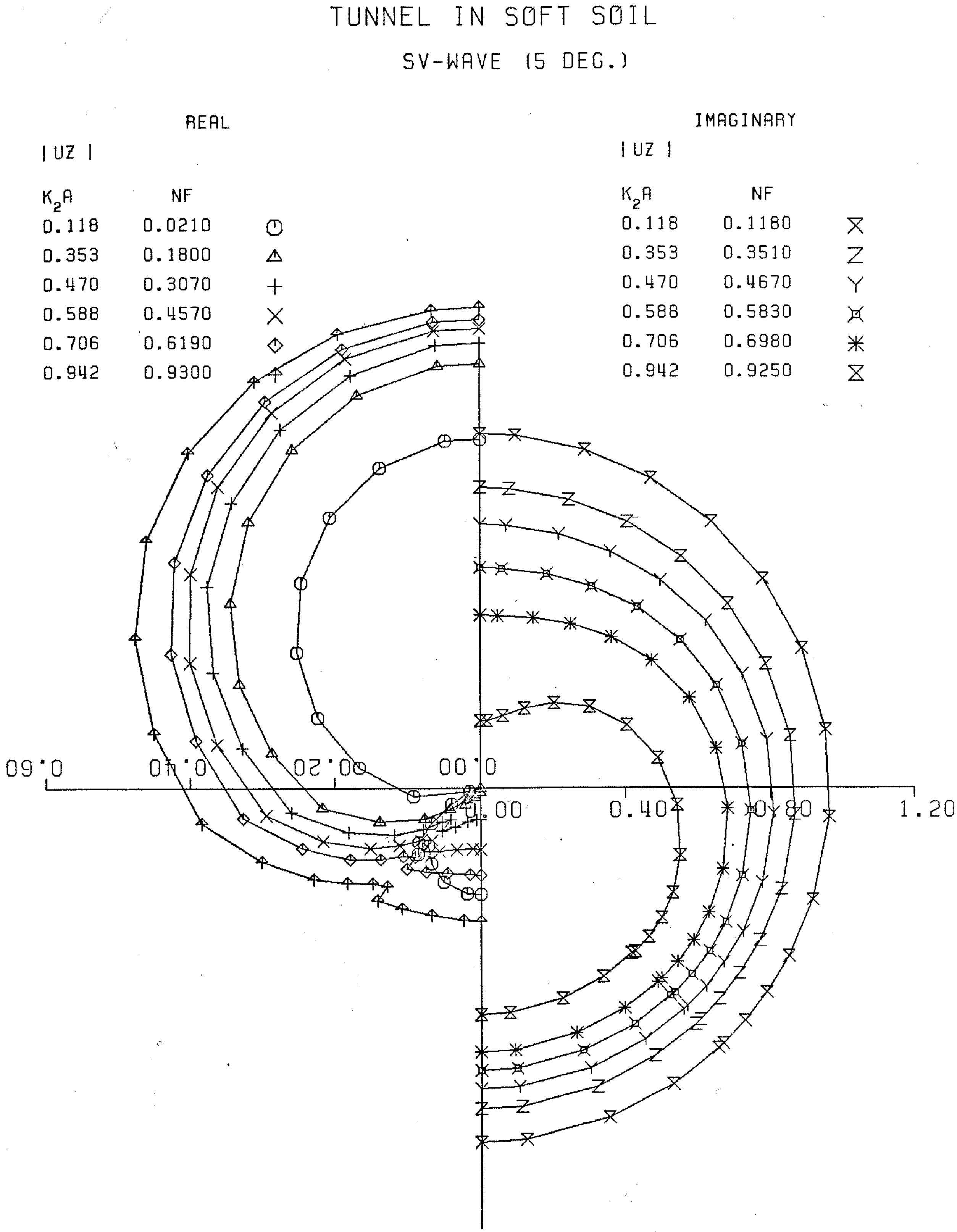

Fig. 49 Normalized real and imaginary part of axial displacement vs frequency for SV-Wave when the incident angle = 5°(Case I)

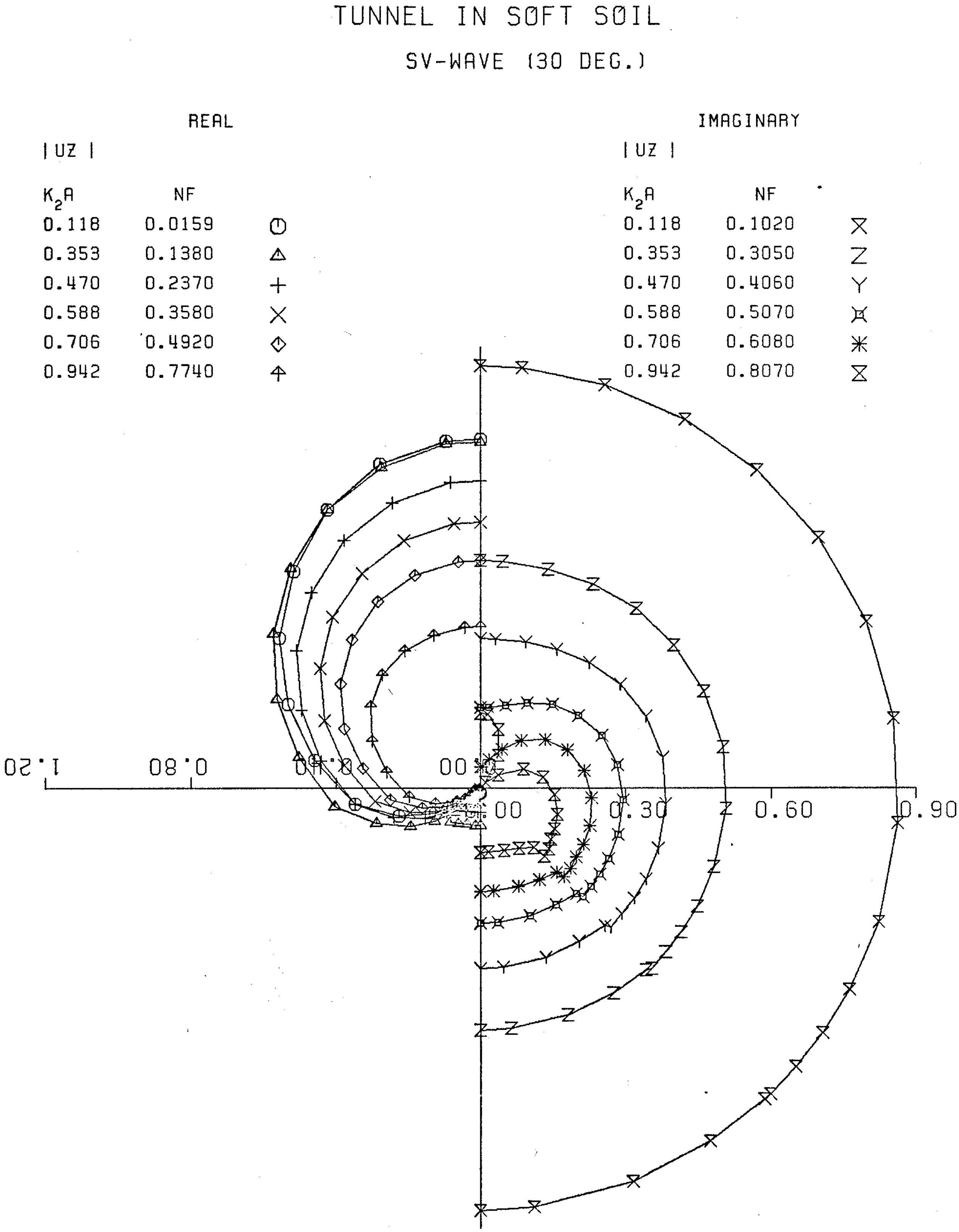

Fig. 50 Normalized real and imaginary part of axial displacement vs frequency for SV-Wave when the incident angle = 30° (Case I)

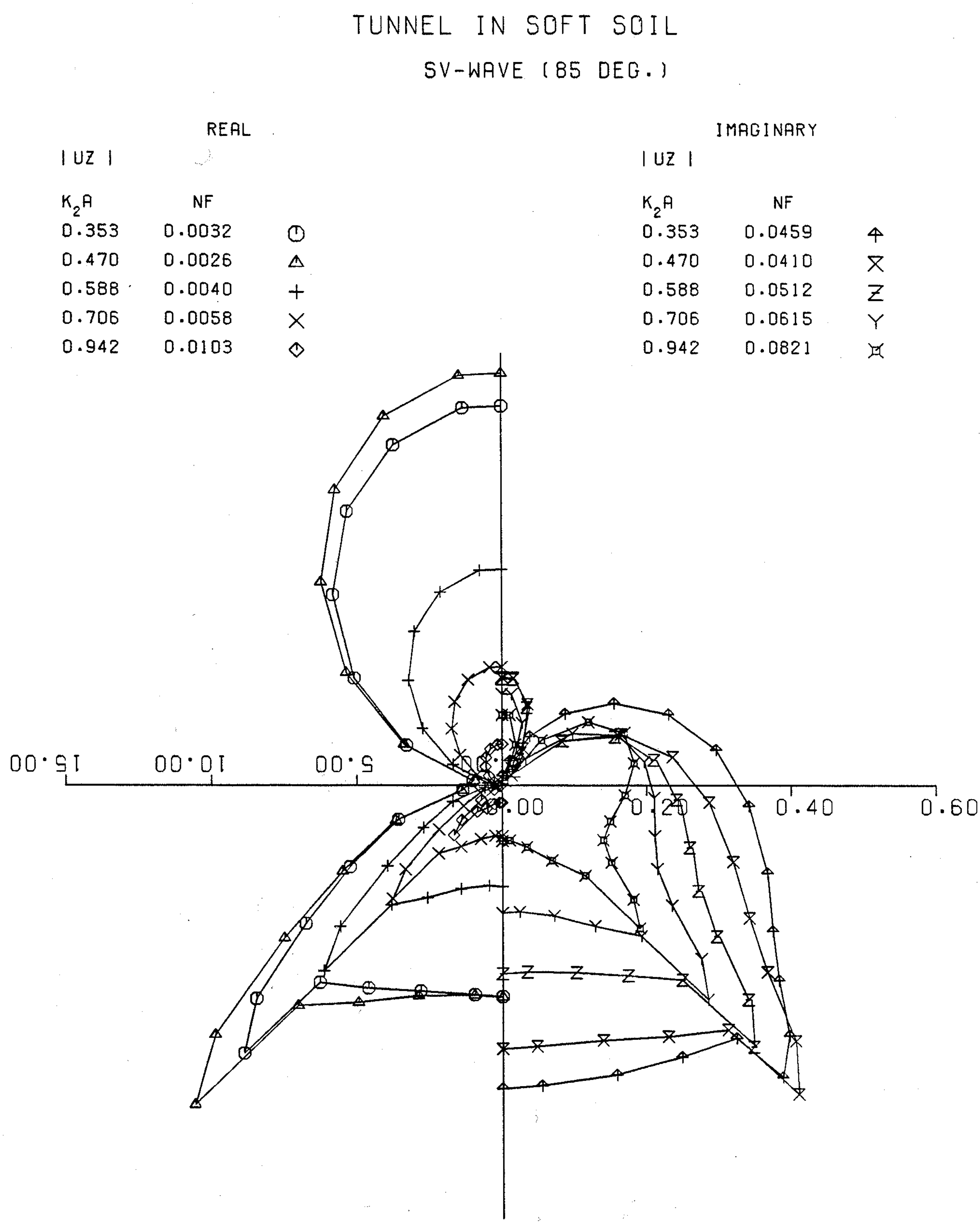

Fig. 51 Normalized real and imaginary part of axial displacement vs frequency for SV-Wave when the incident angle = 85° (Case I)

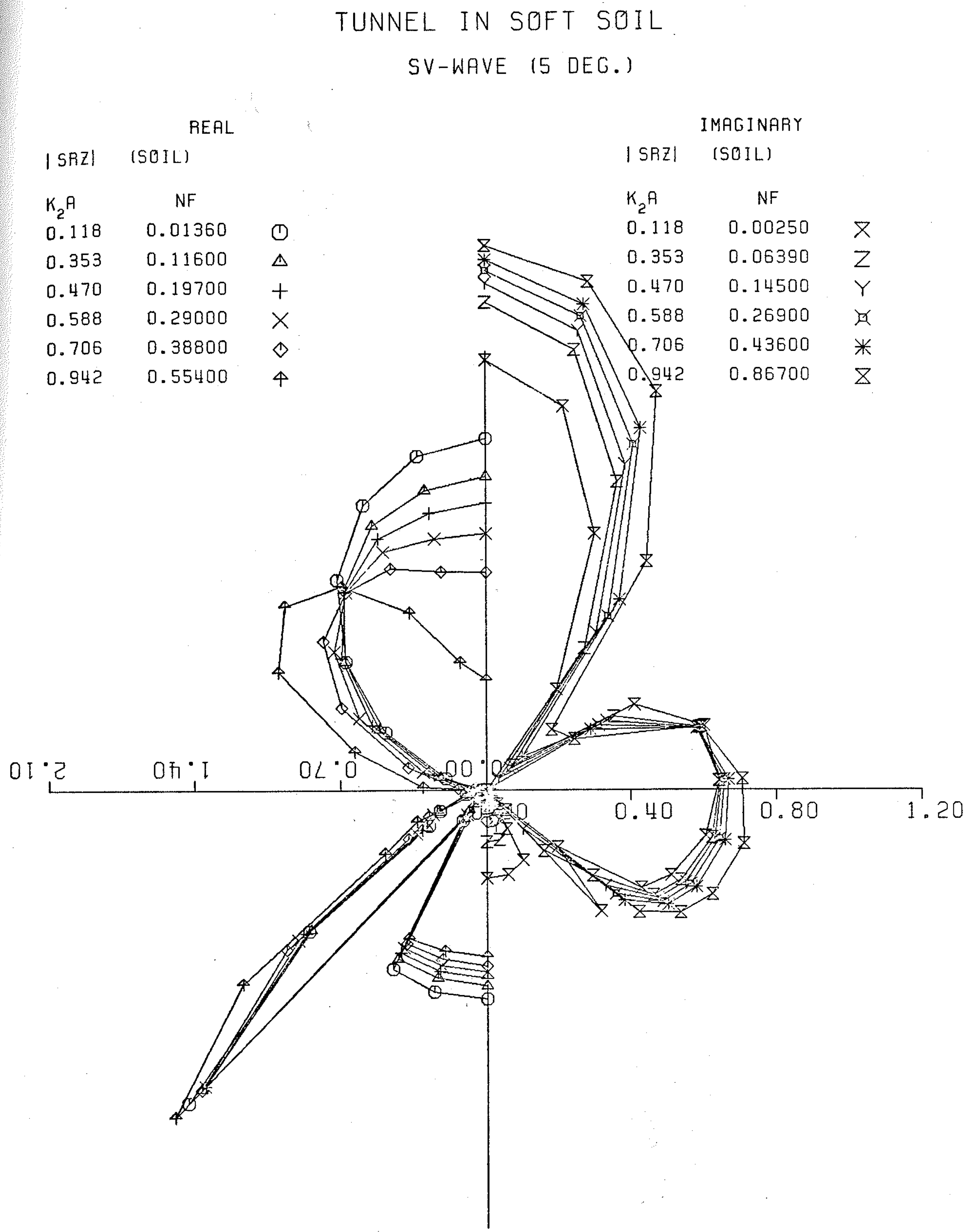

Fig. 52 Normalized real and imaginary part of shear stress SRZ in soil vs frequency for SV-Wave when the incident angle = 5° (Case I)

TUNNEL IN SØFT SØIL

SV-WAVE (30 DEG.)

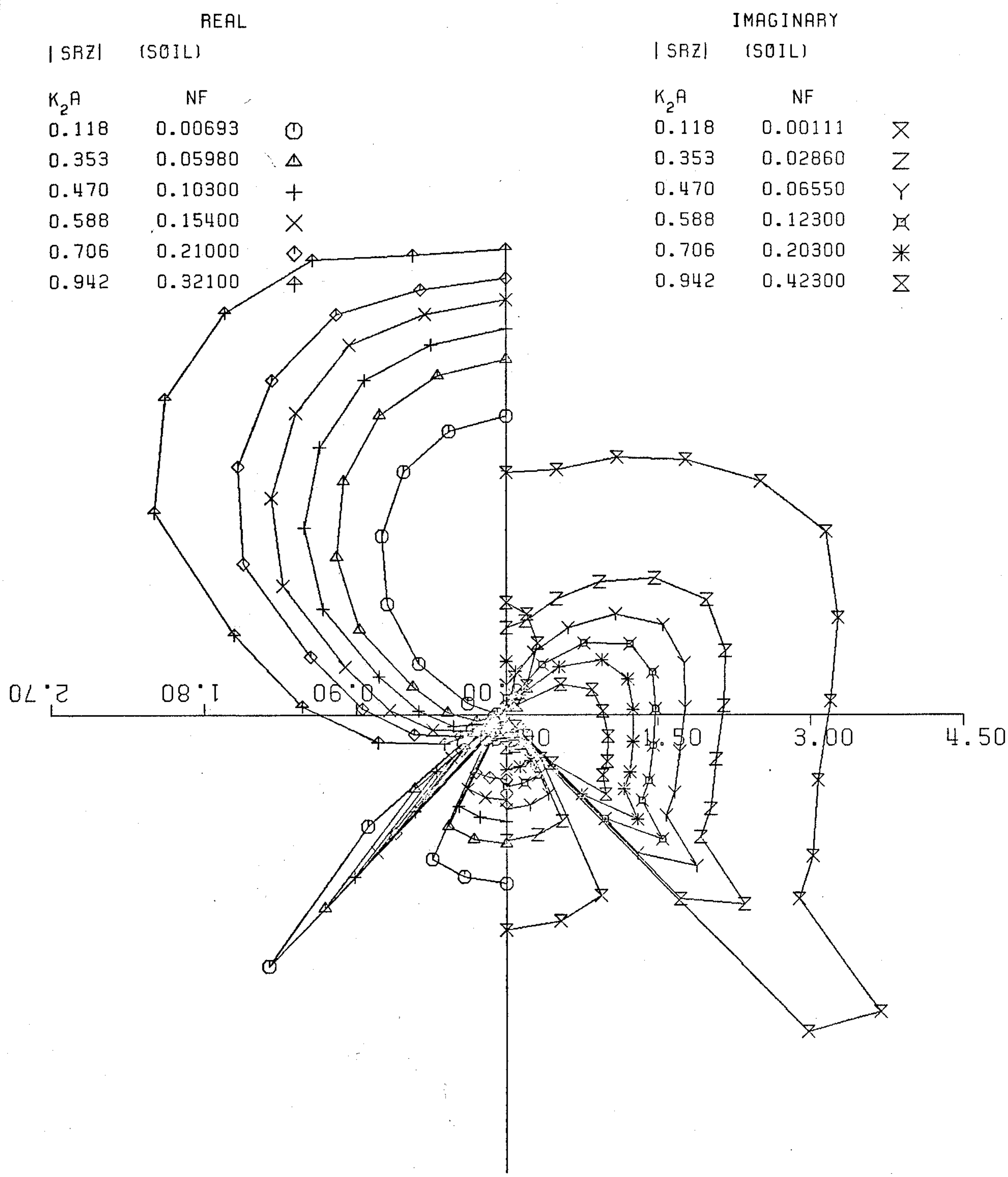

Fig. 53 Normalized real and imaginary part of shear stress SRZ in soil vs frequency for SV-Wave when the incident angle = 30° (Case I)

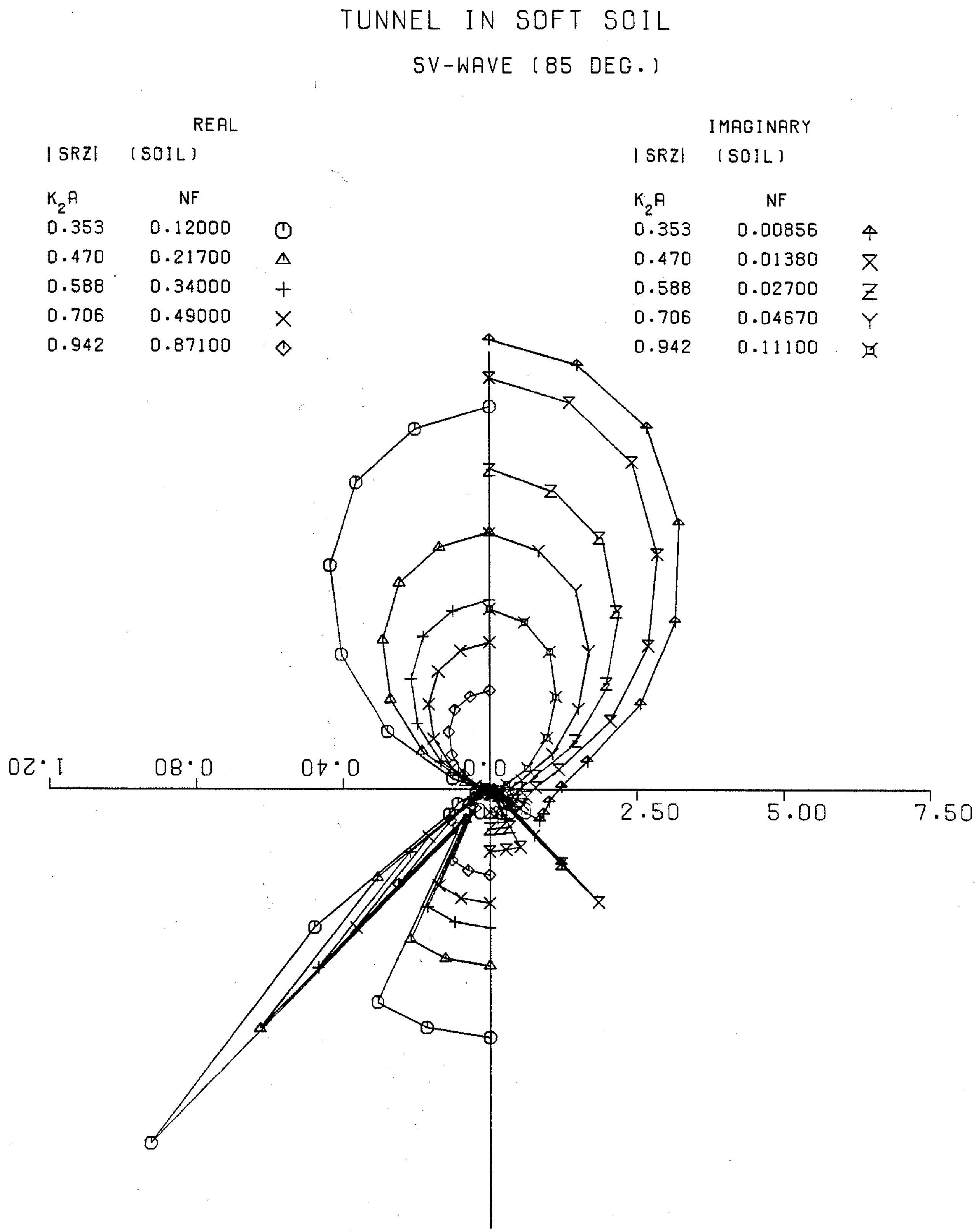

Fig. 54 Normalized real and imaginary part of shear stress SRZ in soil vs frequency for SV-Wave when the incident angle = 85°(Case I)

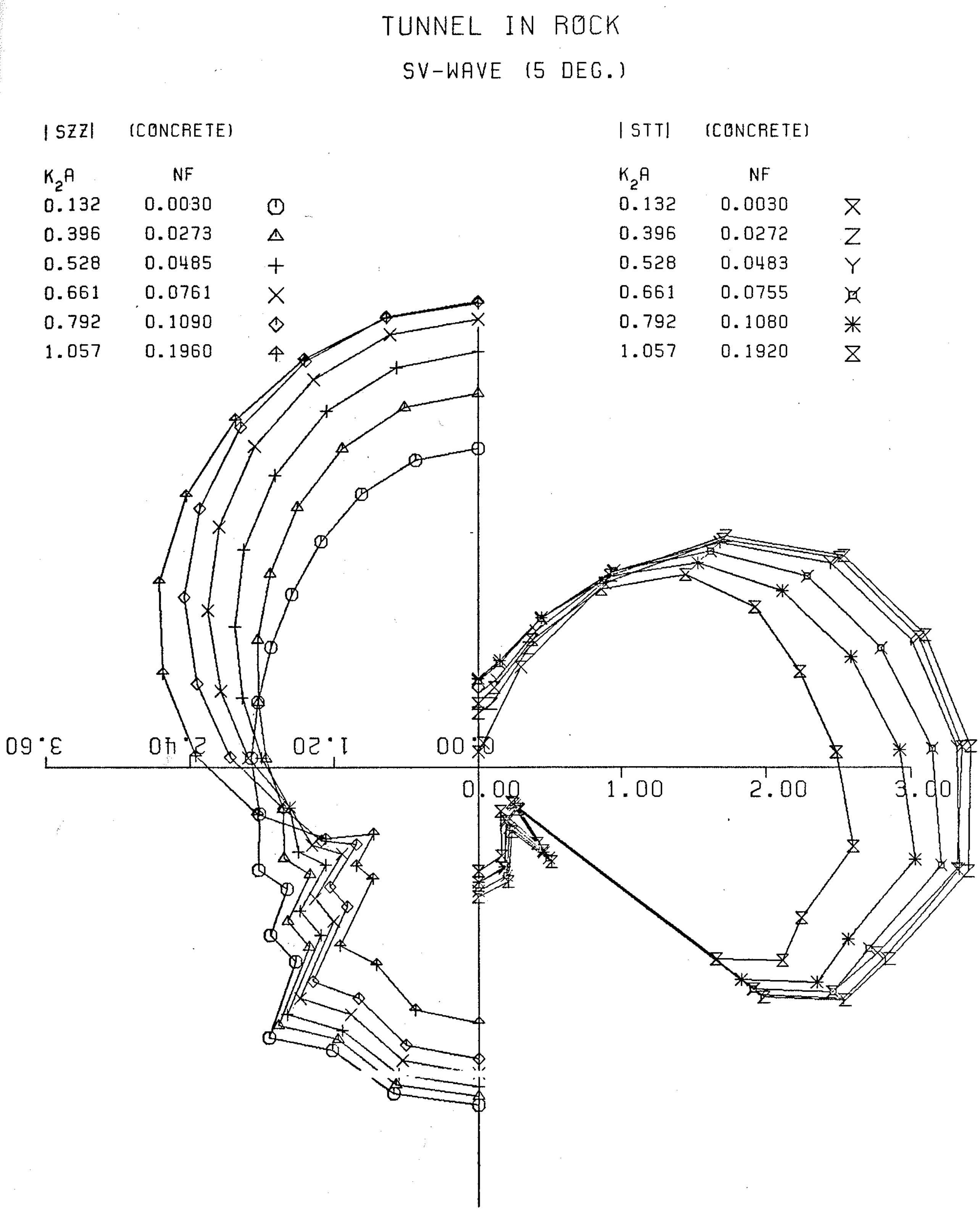

Fig. 55 Normalized axial stress and hoop stress in tunnel wall vs frequency for SV-Wave when the incident angle = 5°(Case II)

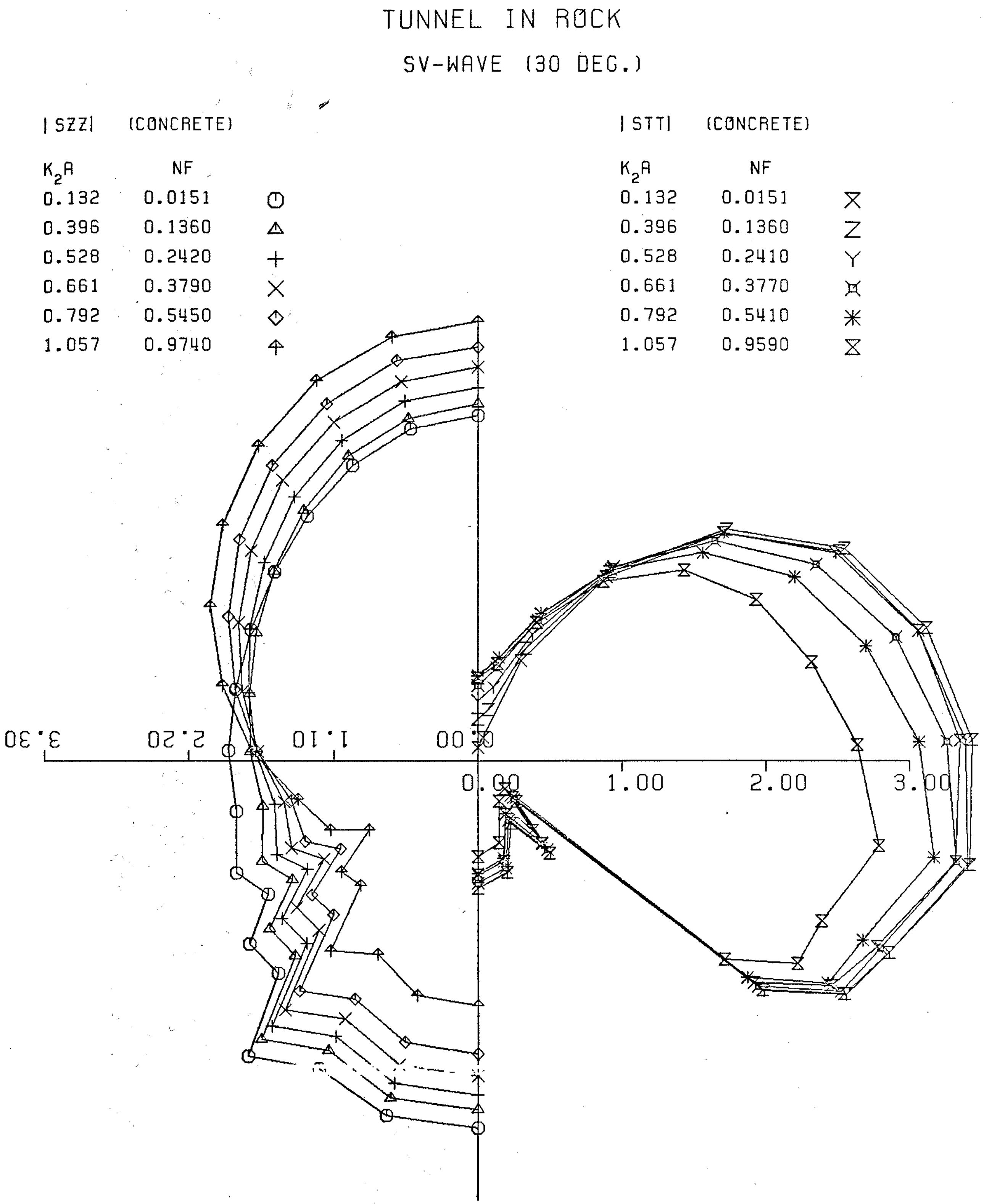

Fig. 56 Normalized axial stress and hoop stress in tunnel wall vs frequency for SV-Wave when the incident angle = 30° (Case II)

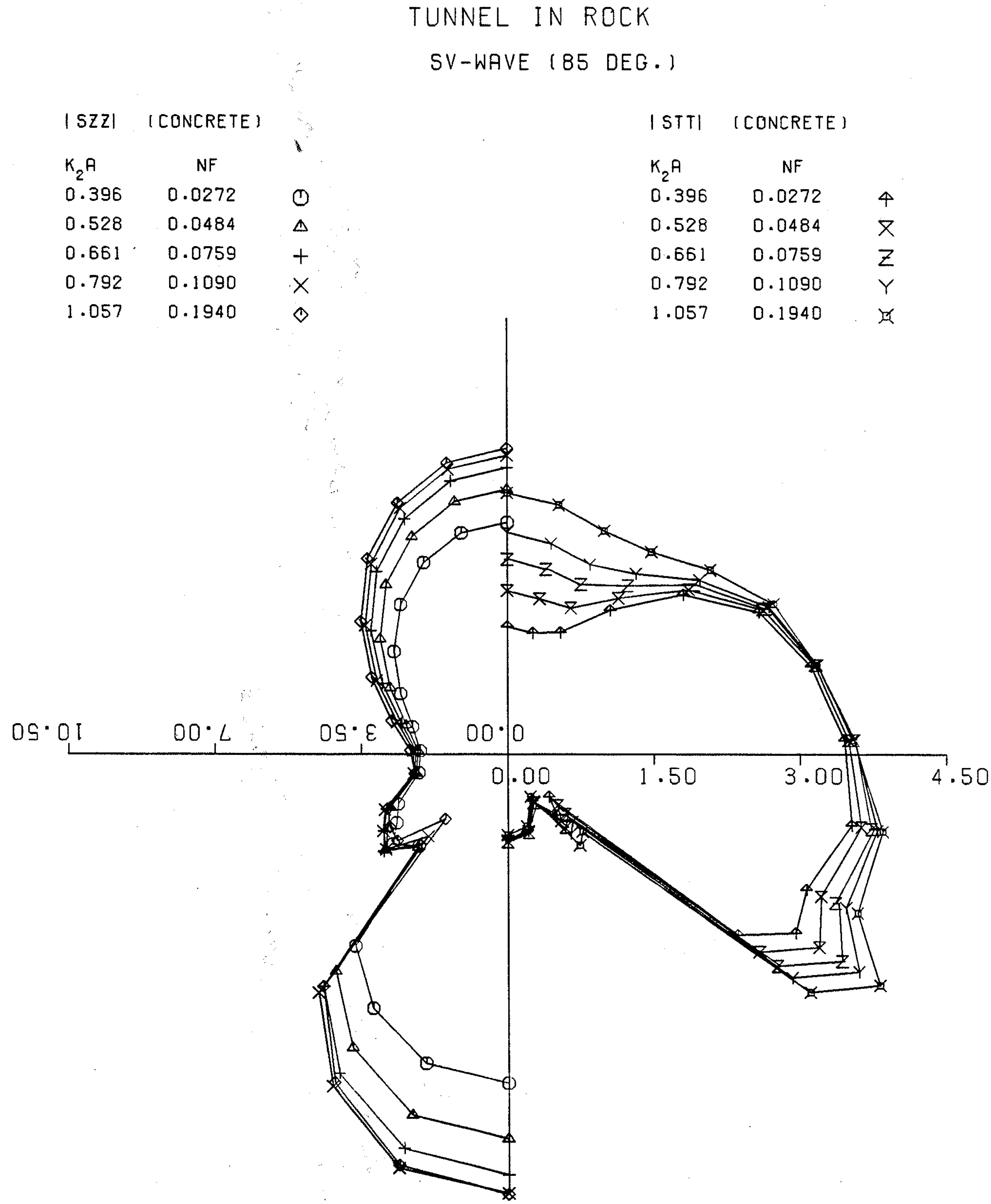

Fig. 57 Normalized axial stress and hoop stress in tunnel wall vs frequency for SV-Wave when the incident angle = 85° (Case II)

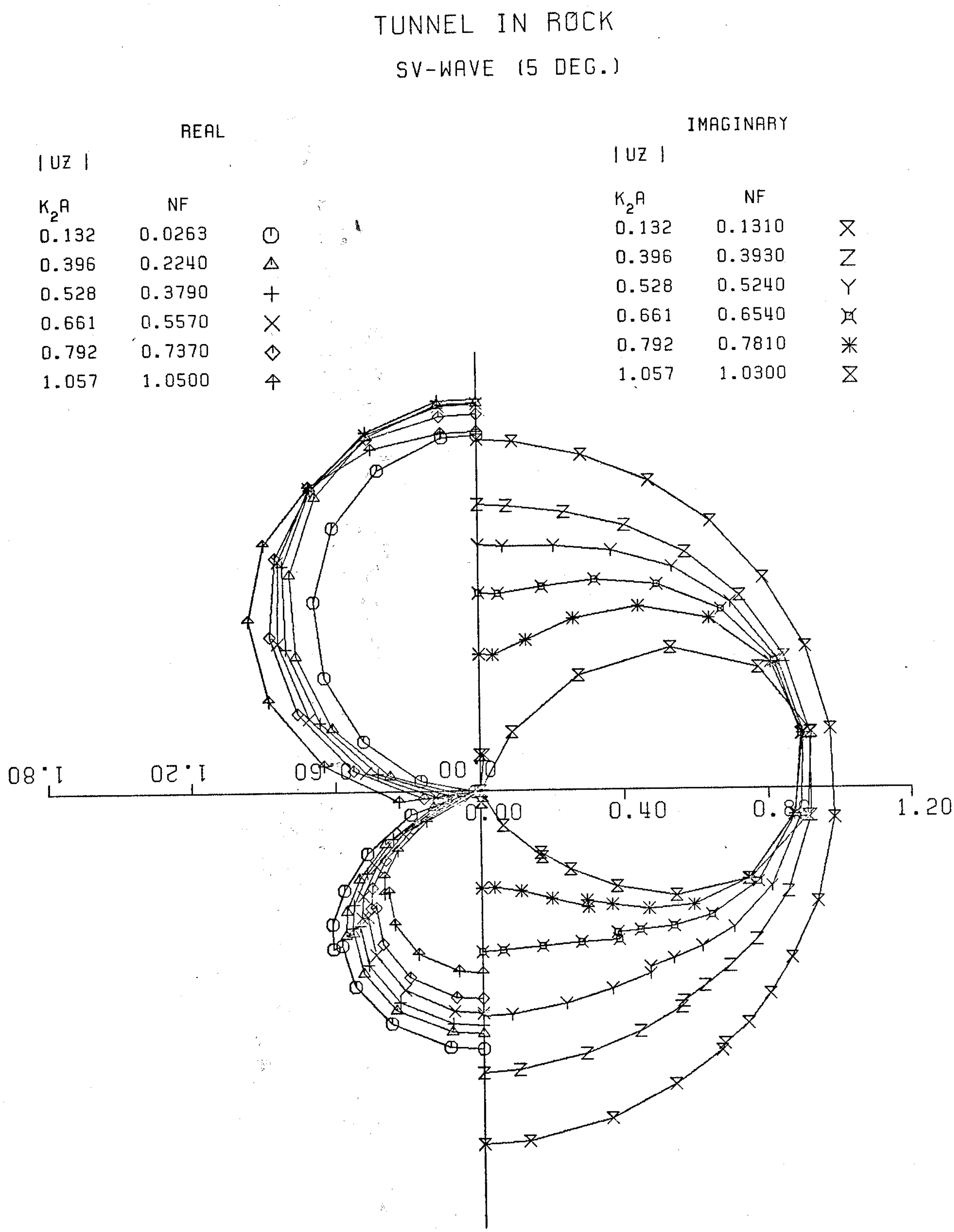

Fig. 58 Normalized real and imaginary part of axial displacement vs frequency for SV-Wave when the incident angle = 5° (Case II)

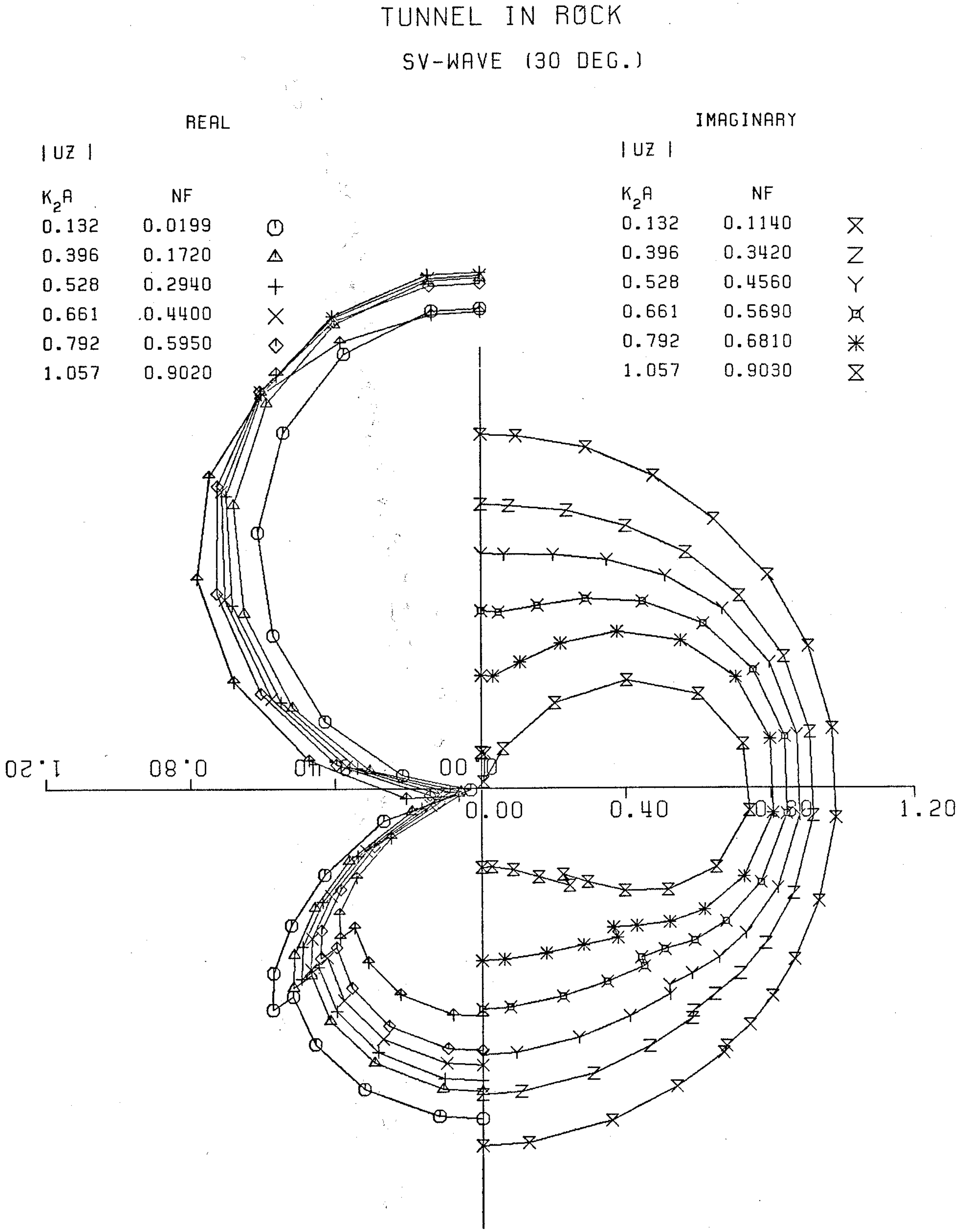

Fig. 59 Normalized real and imaginary part of axial displacement vs frequency for SV-Wave when the incident angle = 30° (Case II)

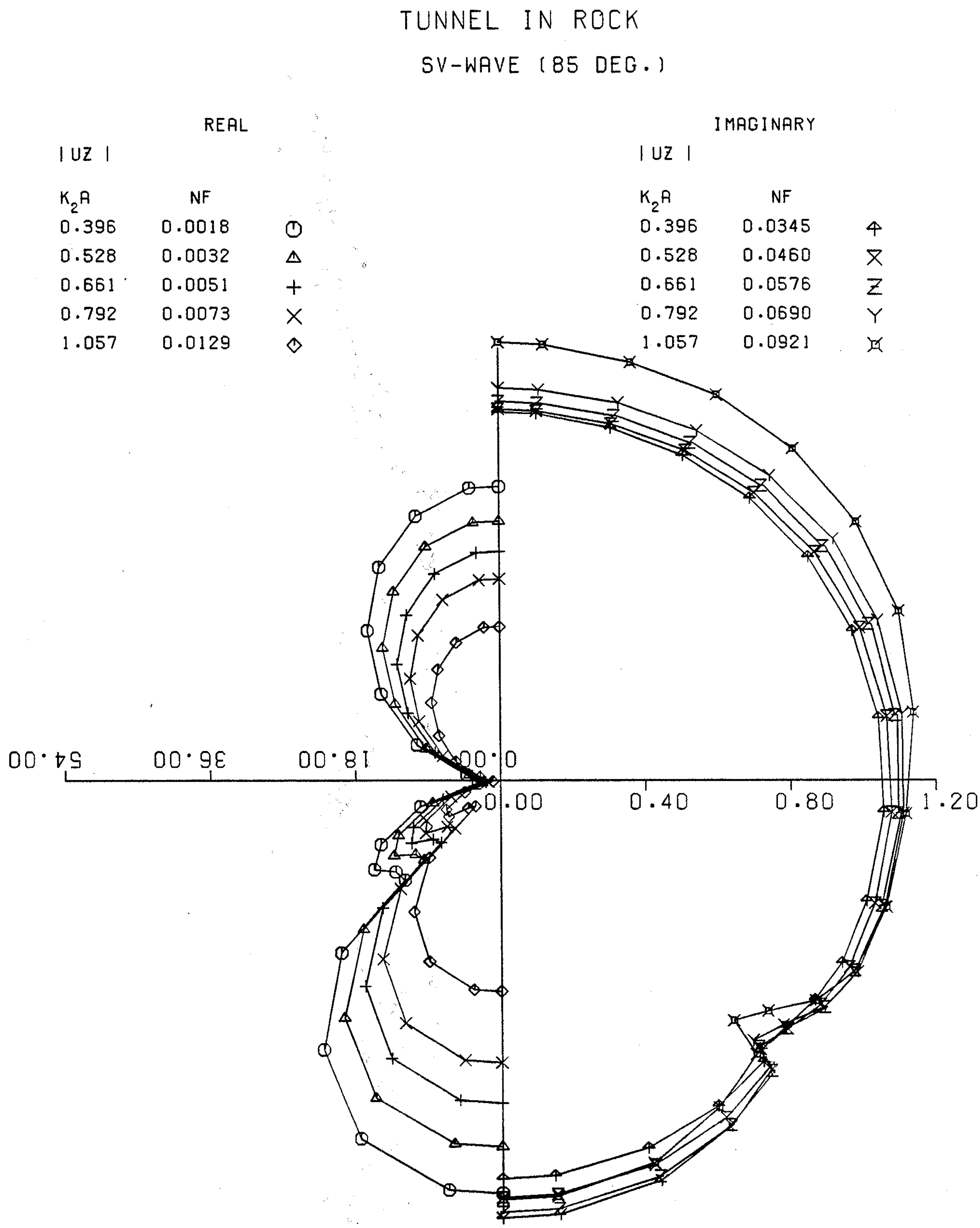

Fig. 60 Normalized real and imaginary part of axial displacement vs frequency for SV-Wave when the incident angle = 85° (Case II)

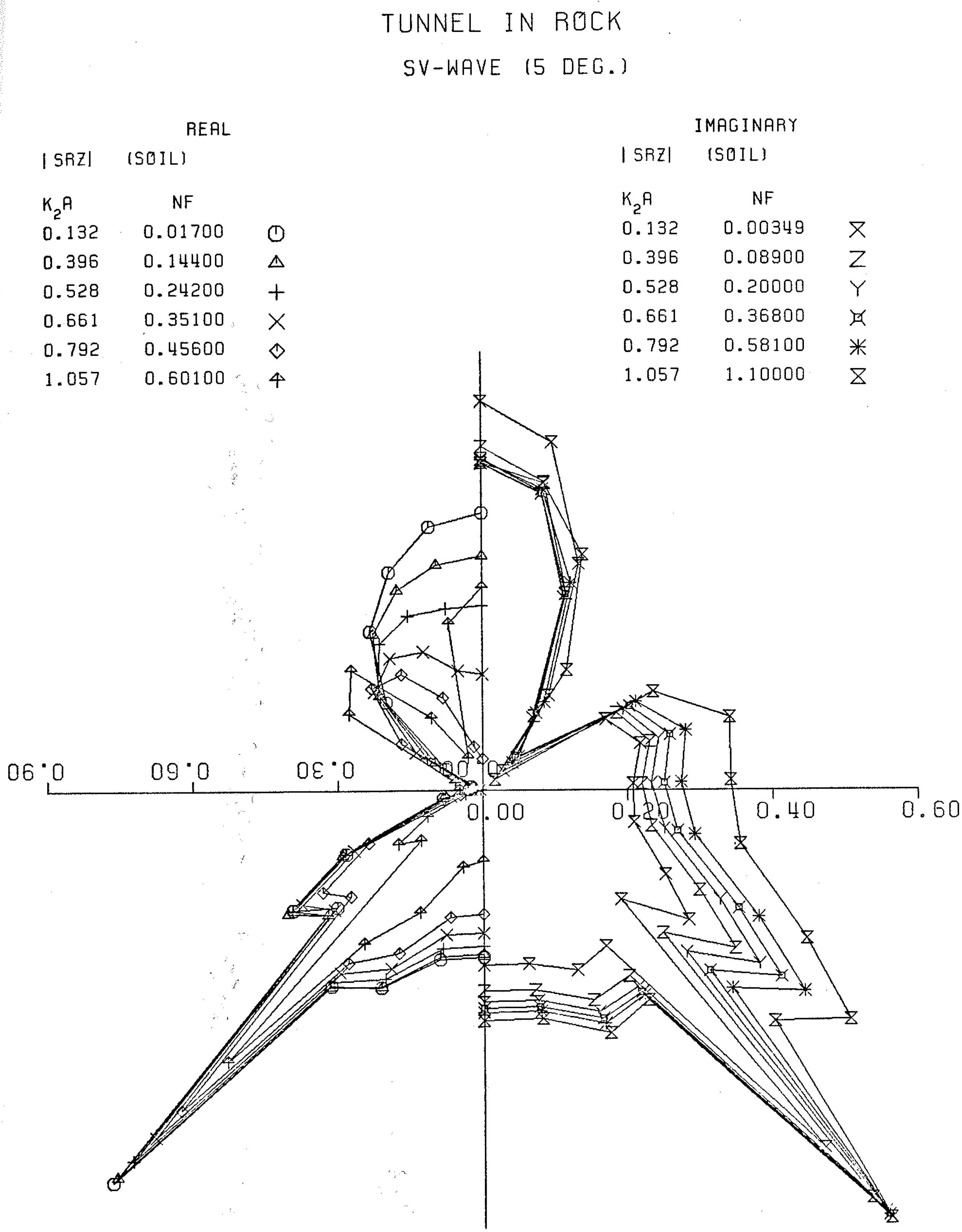

Fig. 61 Normalized real and imaginary part of shear stress SRZ in soil vs frequency for SV-Wave when the incident angle = 5° (Case II)

TUNNEL IN RØCK

SV-WAVE (30 DEG.)

REAL

|SRZ| (SØIL)

K_2A	NF
0.132	0.00866
0.396	0.07450
0.528	0.12700
0.661	0.18800
0.792	0.25200
1.057	0.36500

IMAGINARY

|SRZ| (SØIL)

K_2A	NF
0.132	0.00155
0.396	0.04000
0.528	0.09120
0.661	0.17000
0.792	0.27500
1.057	0.55200

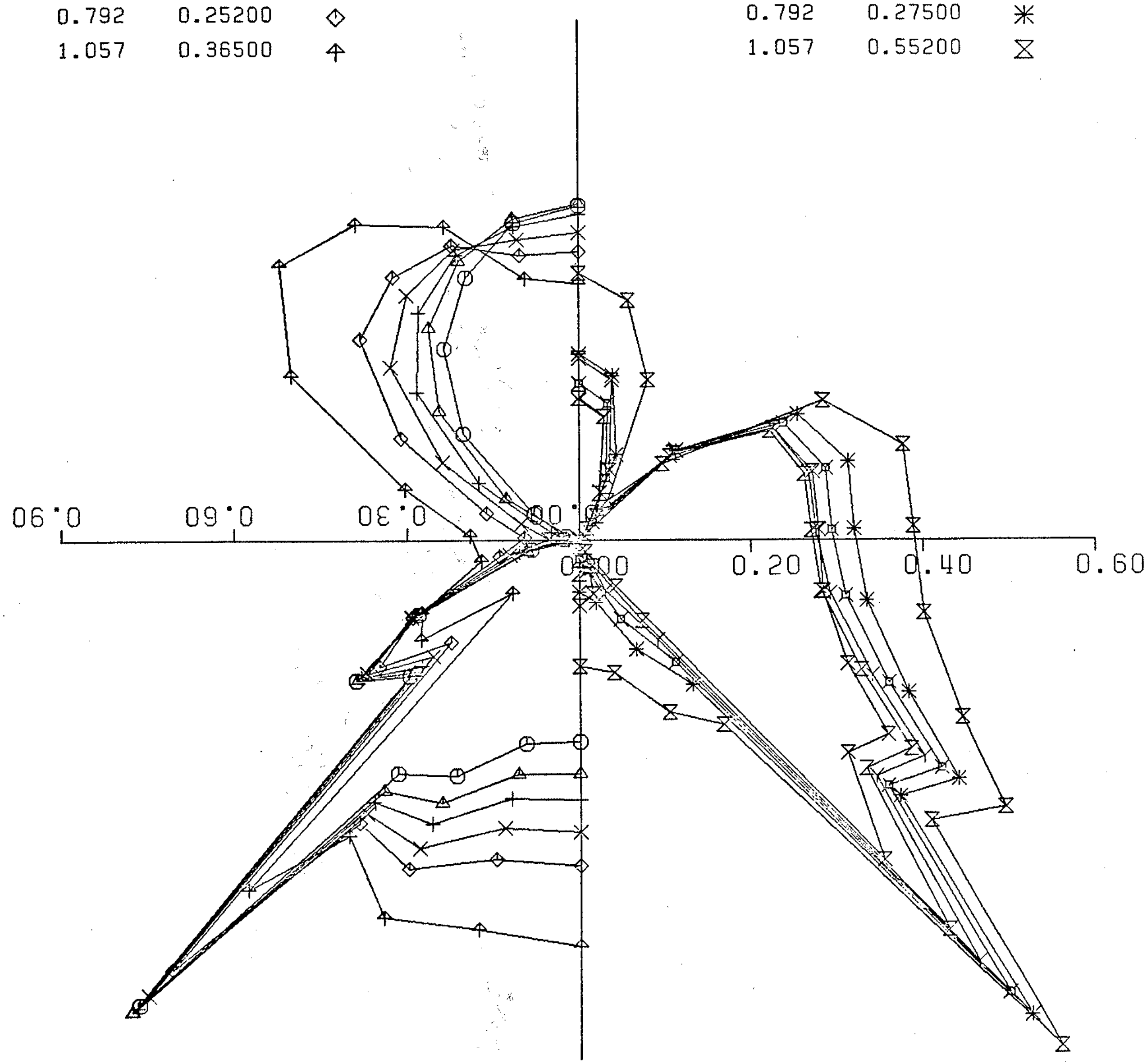

Fig. 62 Normalized real and imaginary part of shear stress SRZ in soil vs frequency for SV-Wave when the incident angle = 30°(Case II)

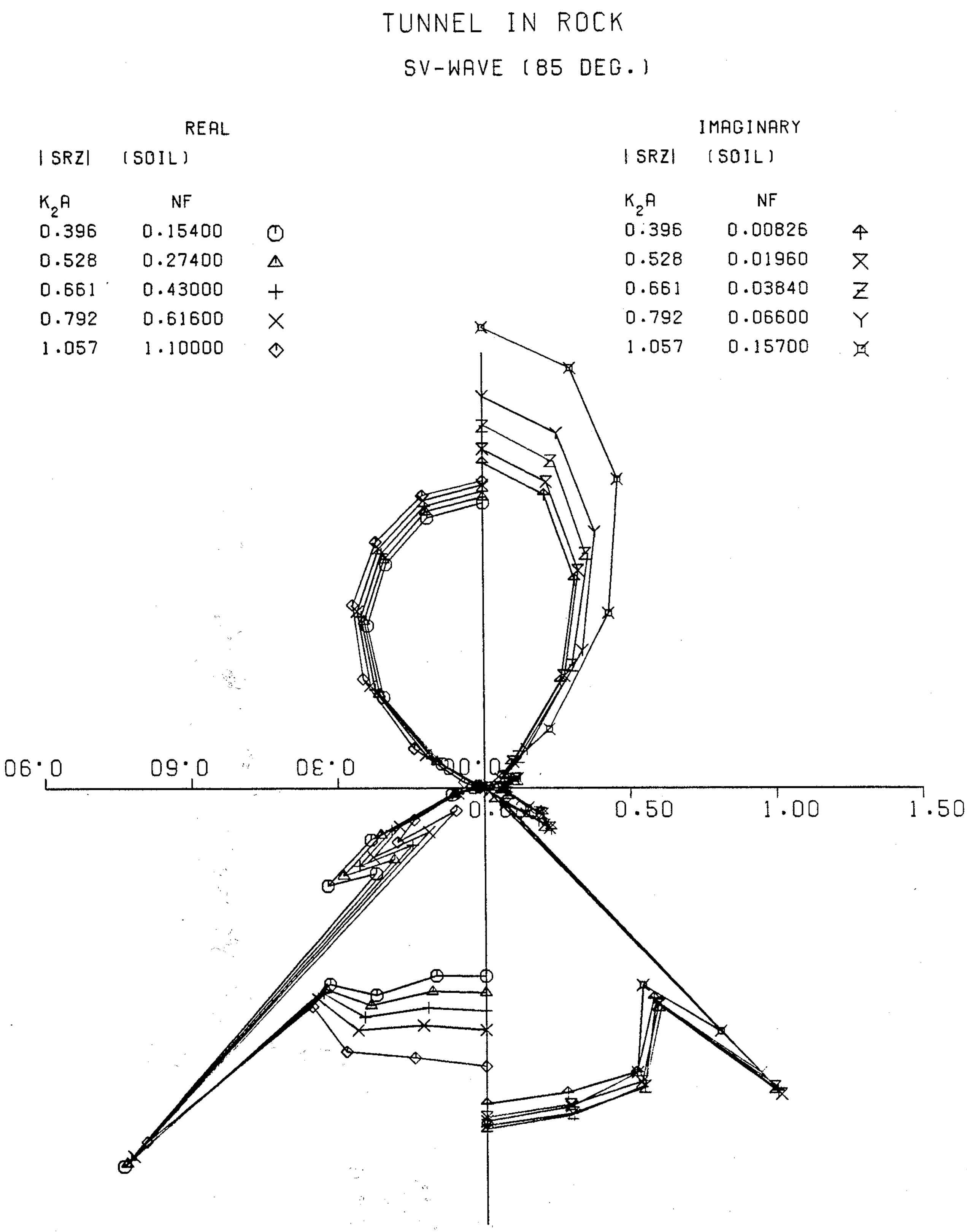

Fig. 63 Normalized real and imaginary part of shear stress SRZ in soil vs frequency for SV-Wave when the incident angle = 85° (Case II)

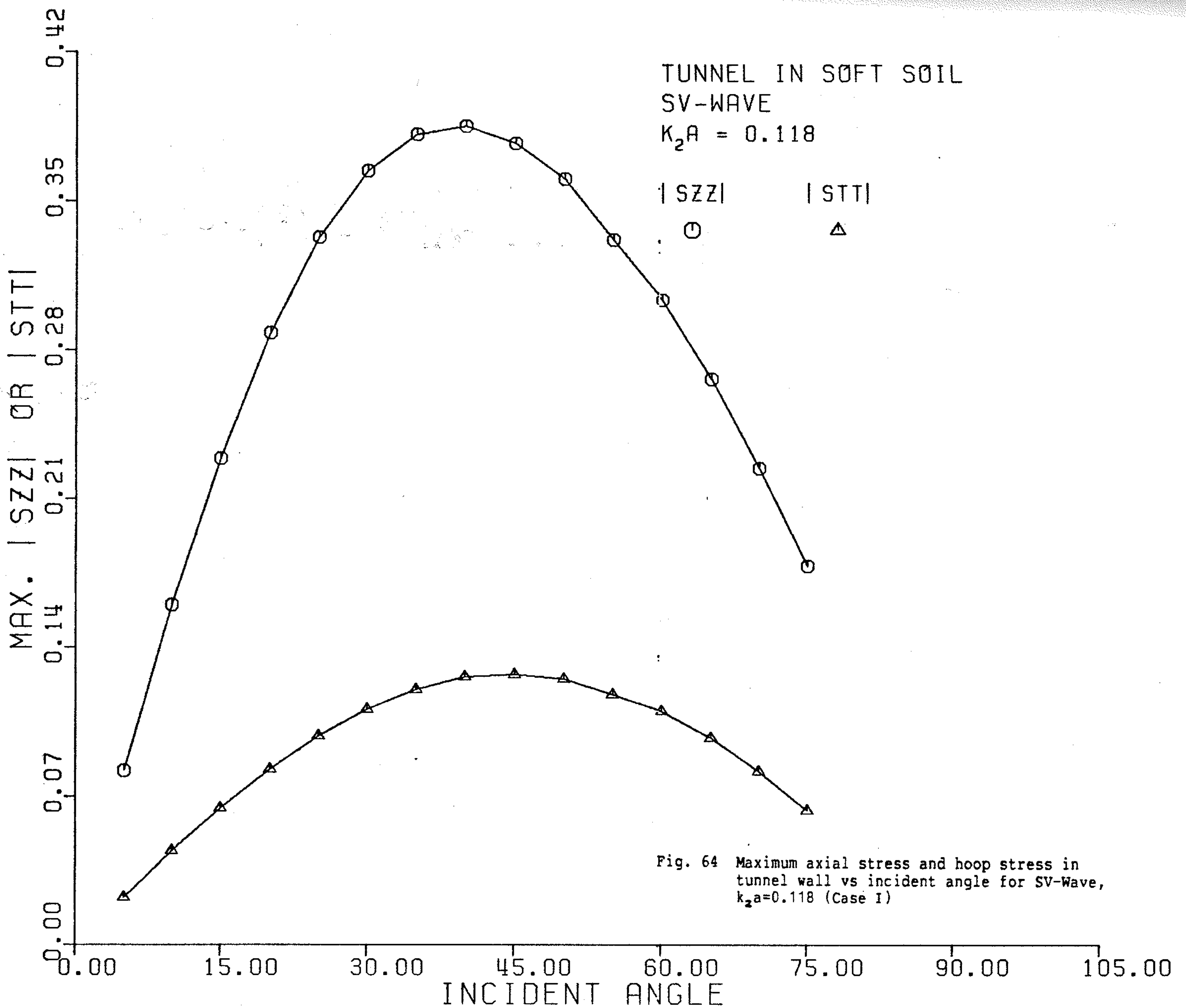

Fig. 64 Maximum axial stress and hoop stress in tunnel wall vs incident angle for SV-Wave, $k_2a=0.118$ (Case I)

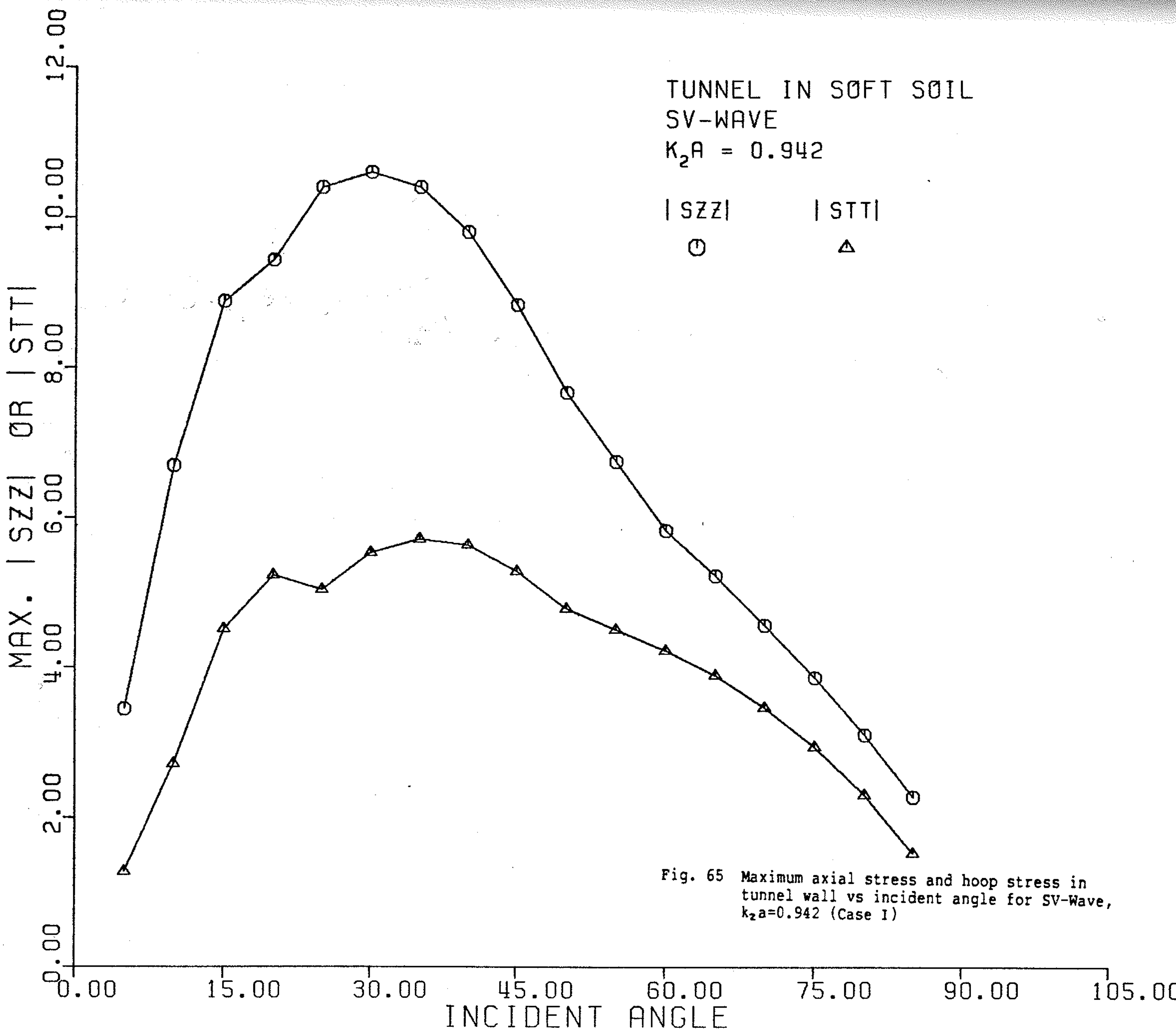

Fig. 65 Maximum axial stress and hoop stress in tunnel wall vs incident angle for SV-Wave, k_2a=0.942 (Case I)

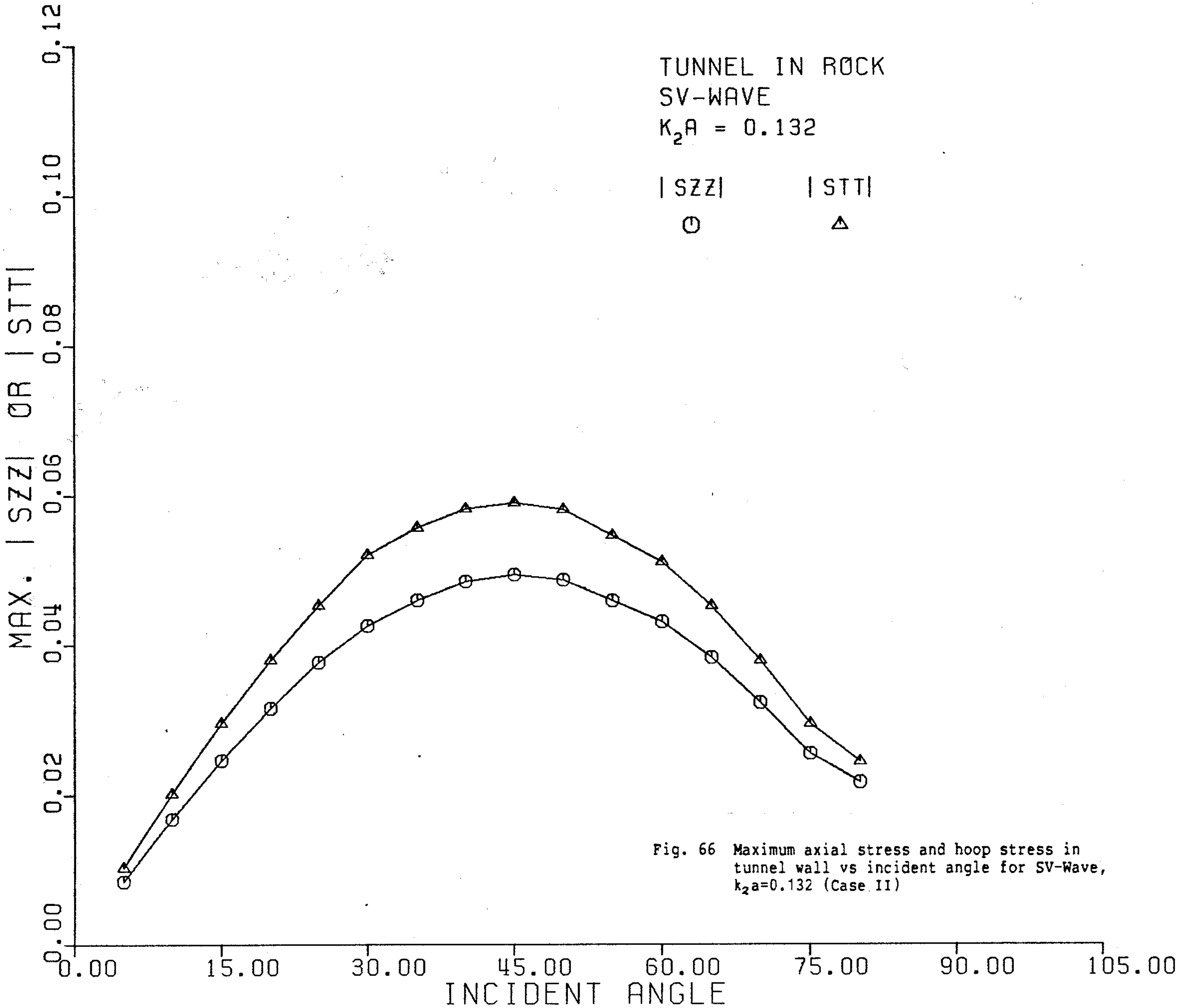

Fig. 66 Maximum axial stress and hoop stress in tunnel wall vs incident angle for SV-Wave, $k_2a=0.132$ (Case II)

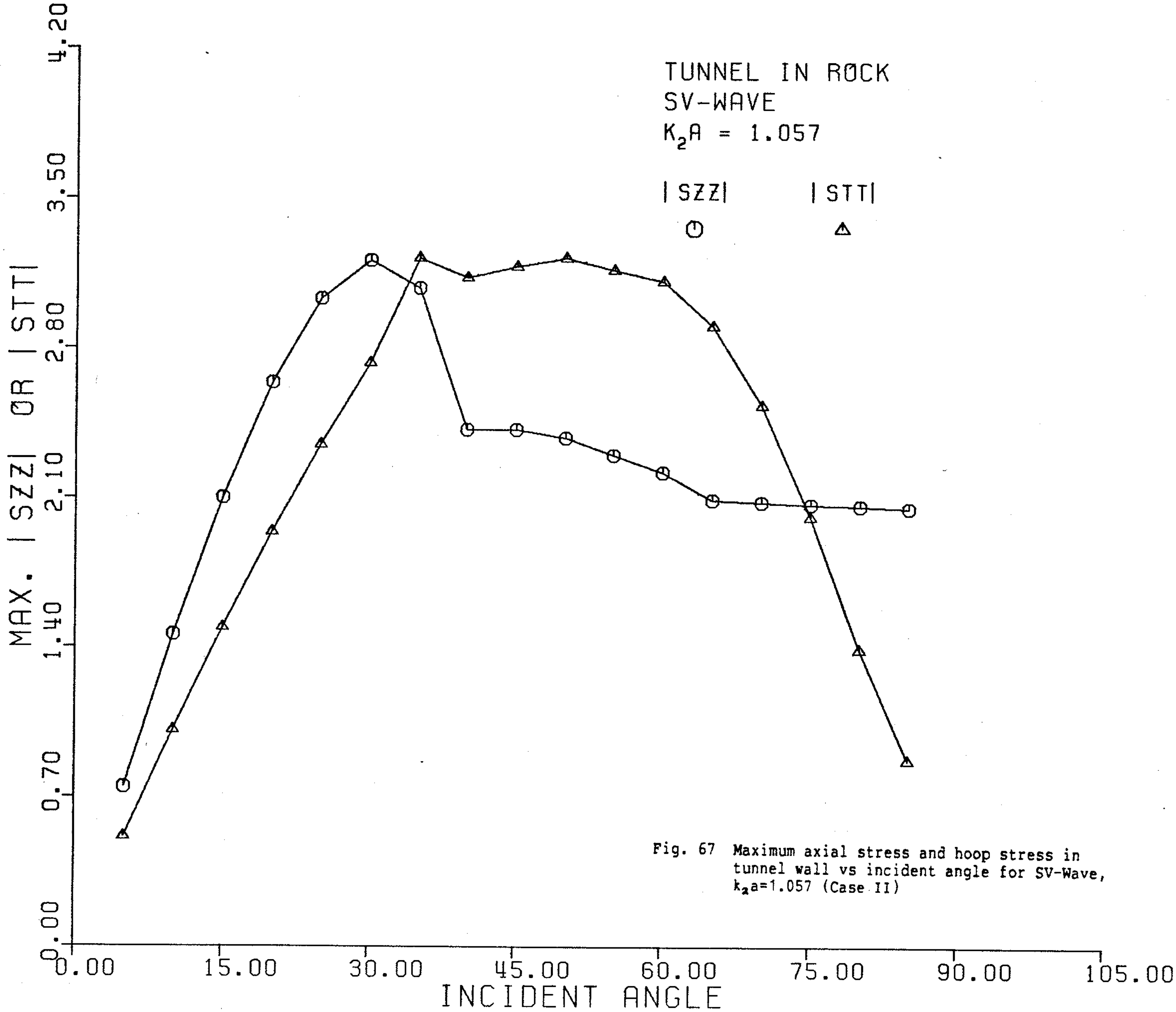

Fig. 67 Maximum axial stress and hoop stress in tunnel wall vs incident angle for SV-Wave, k_2a=1.057 (Case II)

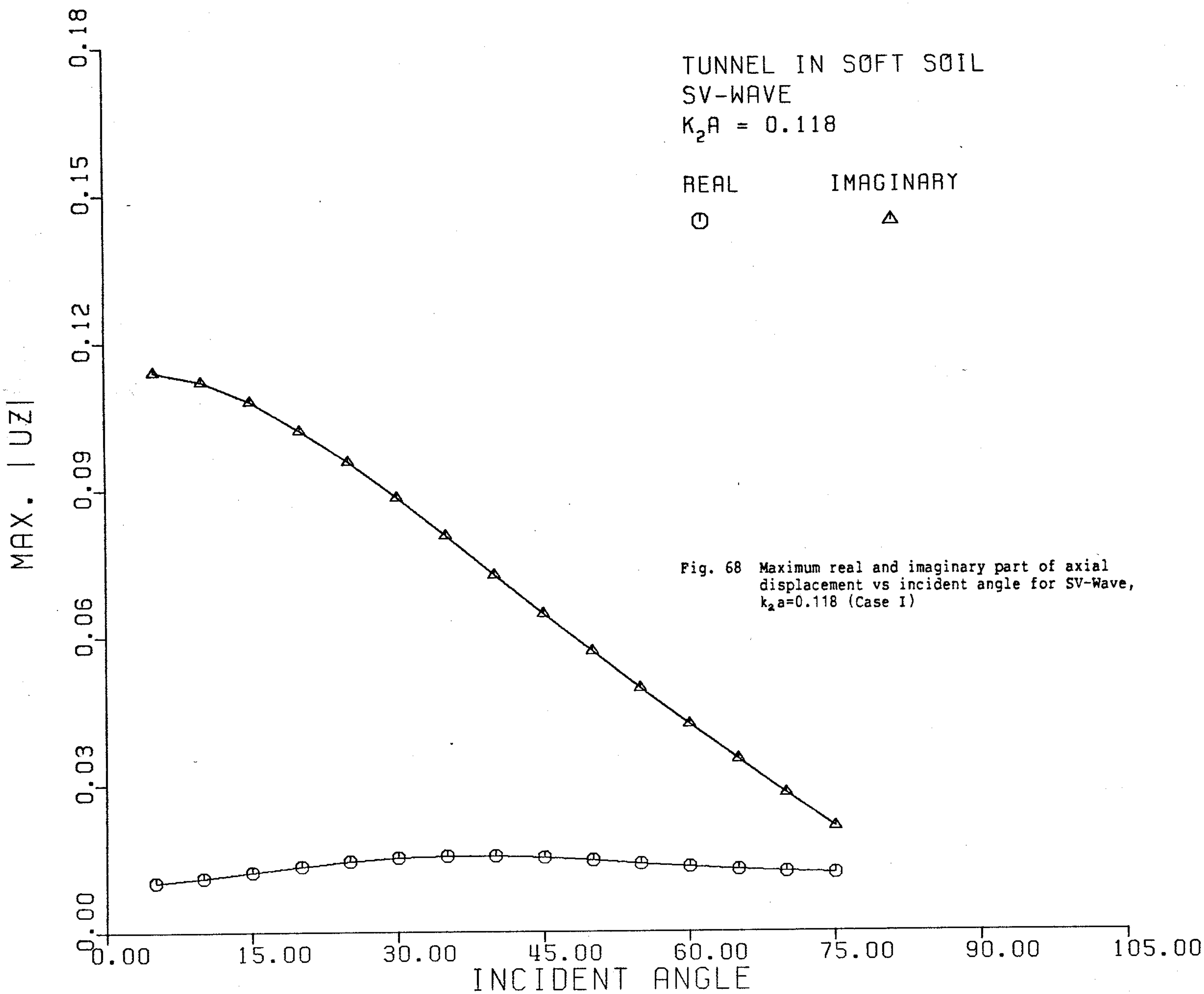

Fig. 68 Maximum real and imaginary part of axial displacement vs incident angle for SV-Wave, $k_2a=0.118$ (Case I)

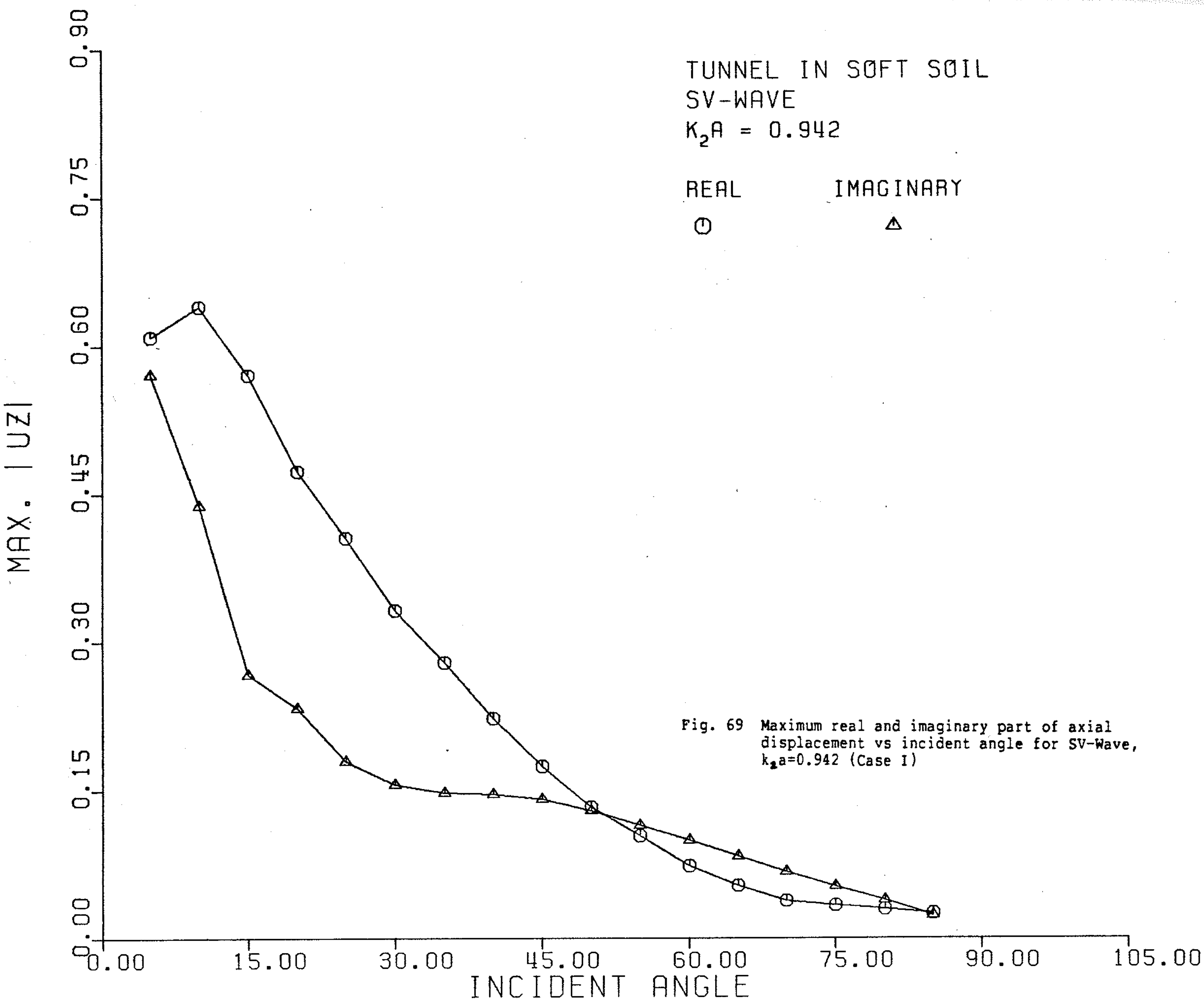

Fig. 69 Maximum real and imaginary part of axial displacement vs incident angle for SV-Wave, k_2a=0.942 (Case I)

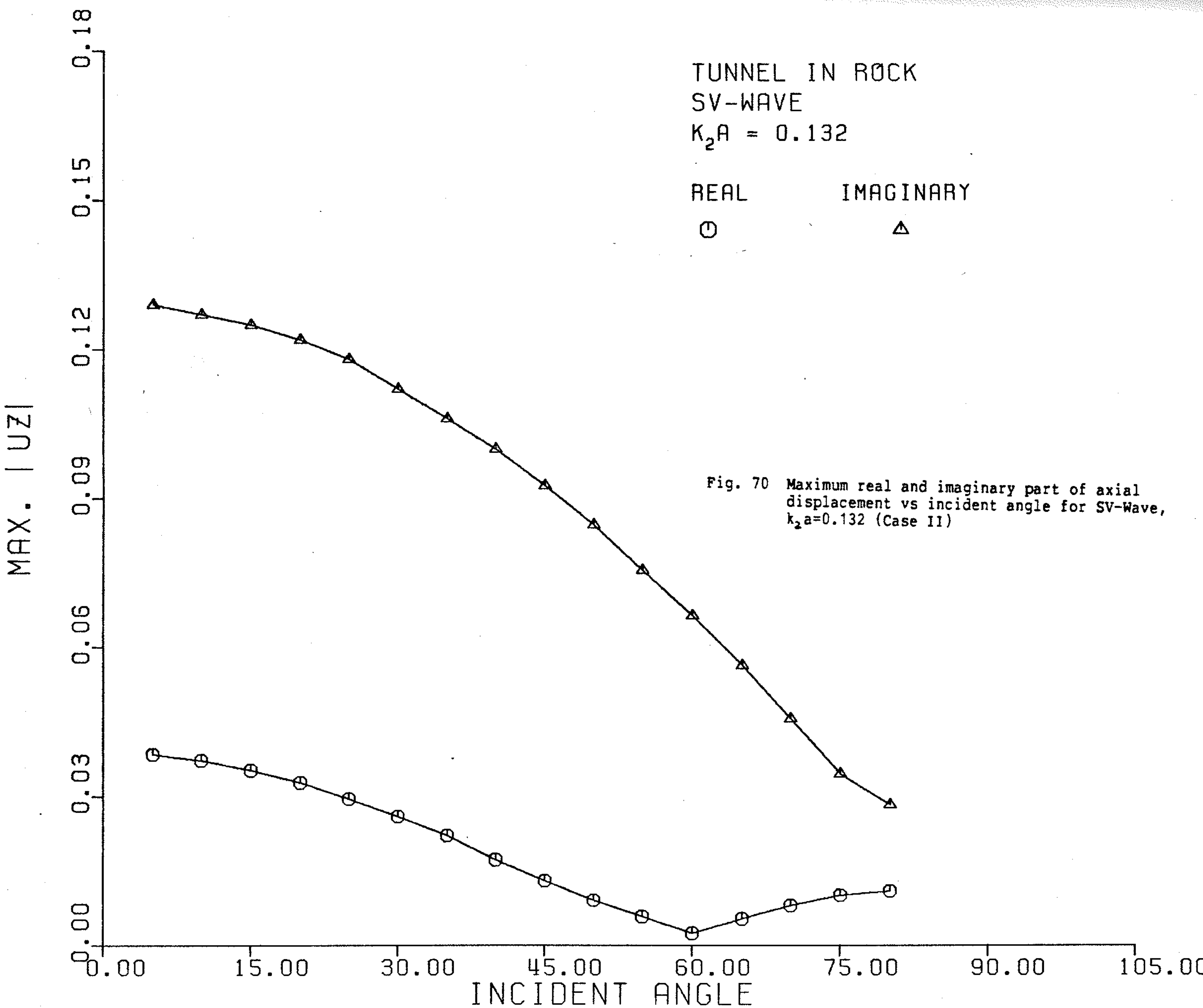

Fig. 70 Maximum real and imaginary part of axial displacement vs incident angle for SV-Wave, $k_2a=0.132$ (Case II)

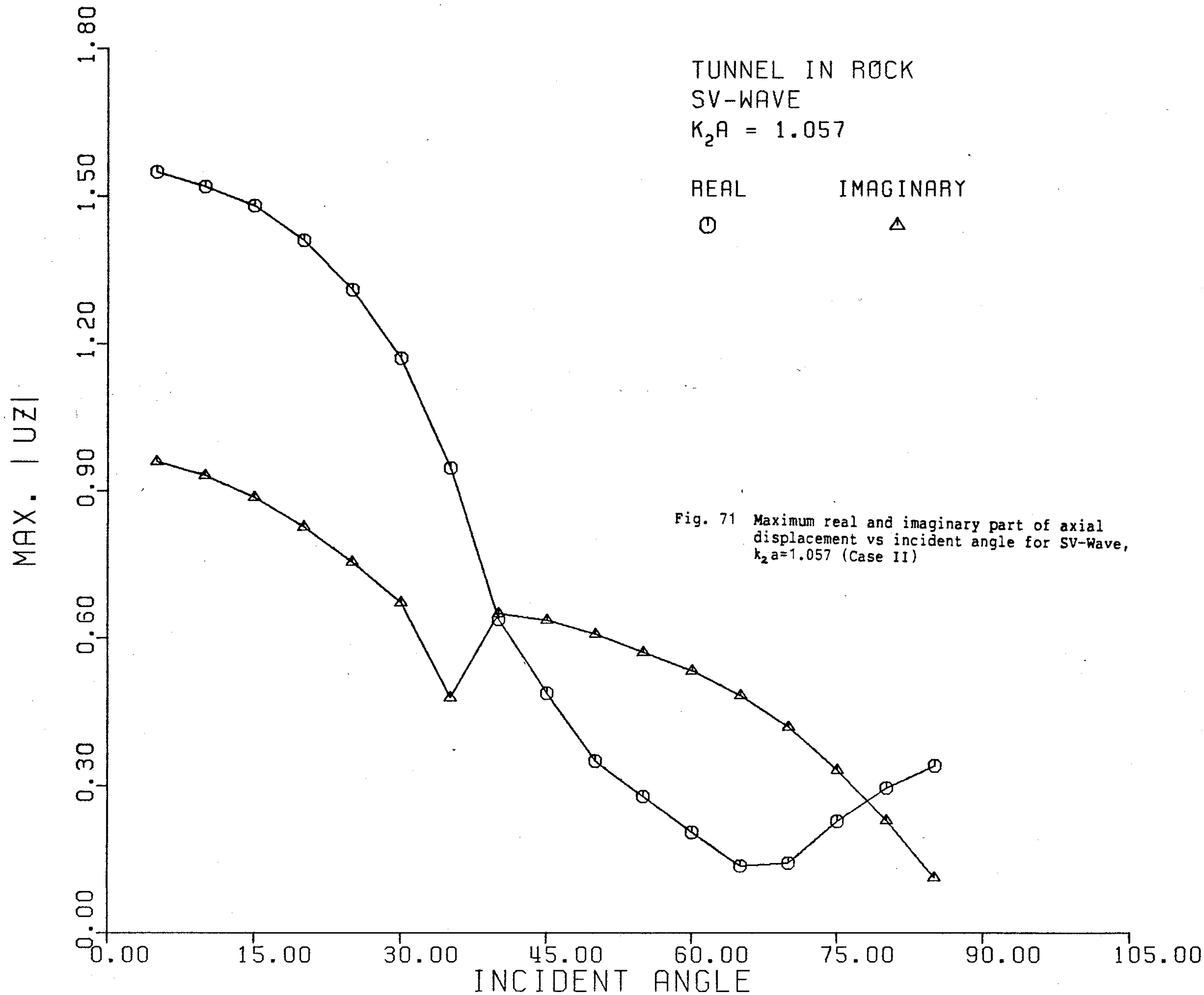

Fig. 71 Maximum real and imaginary part of axial displacement vs incident angle for SV-Wave, k_2a=1.057 (Case II)

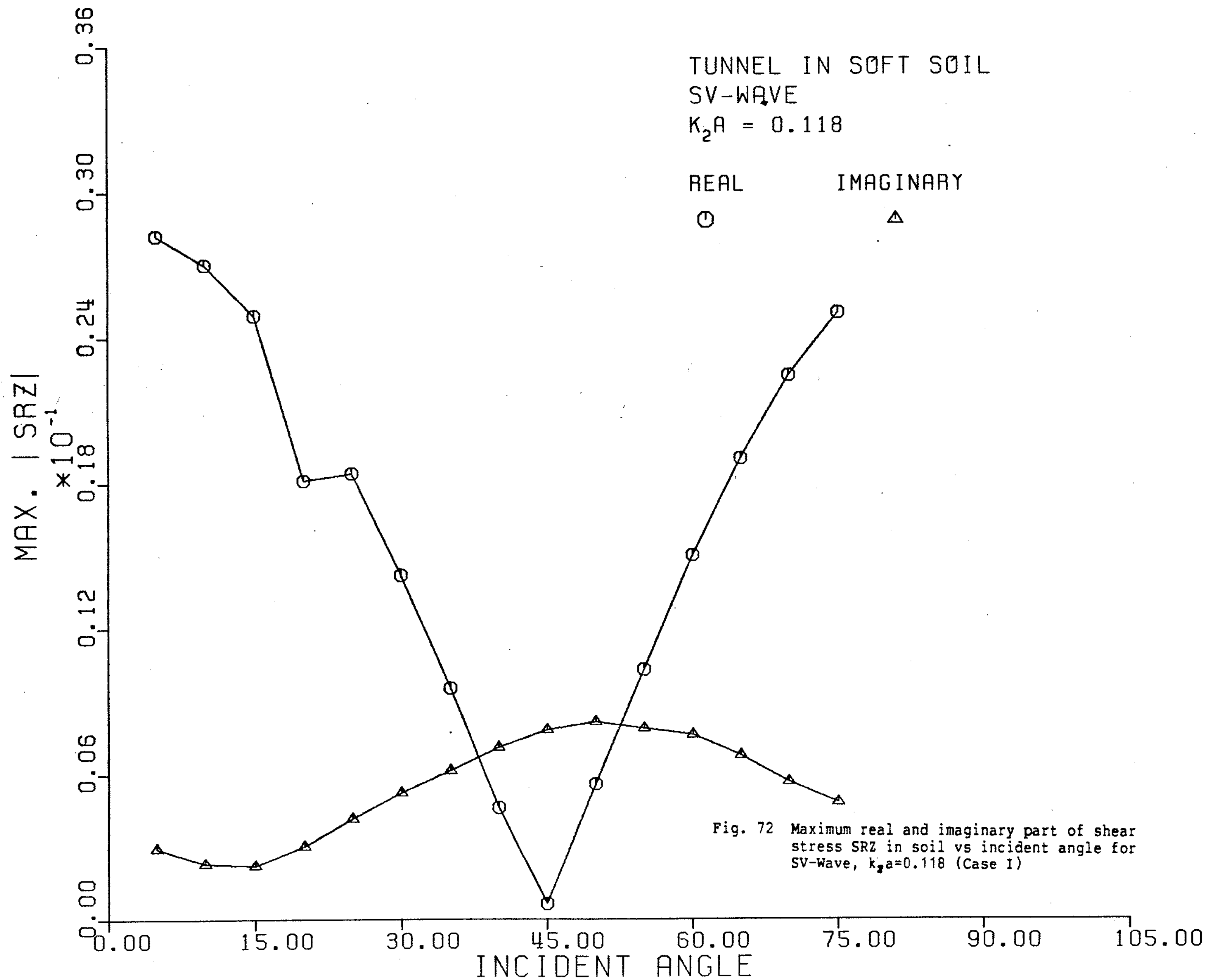

Fig. 72 Maximum real and imaginary part of shear stress SRZ in soil vs incident angle for SV-Wave, $k_2a=0.118$ (Case I)

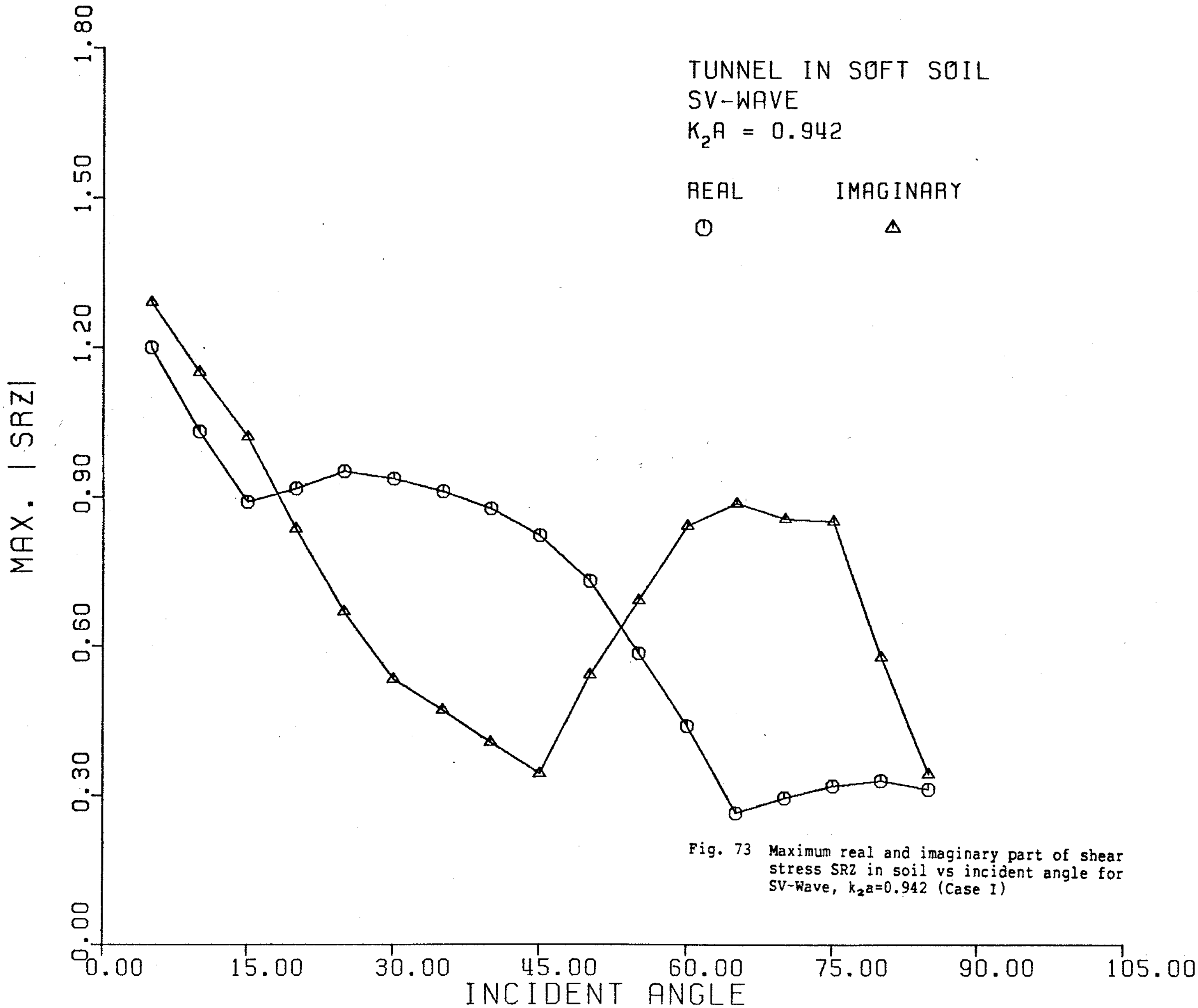

Fig. 73 Maximum real and imaginary part of shear stress SRZ in soil vs incident angle for SV-Wave, $k_2a=0.942$ (Case I)

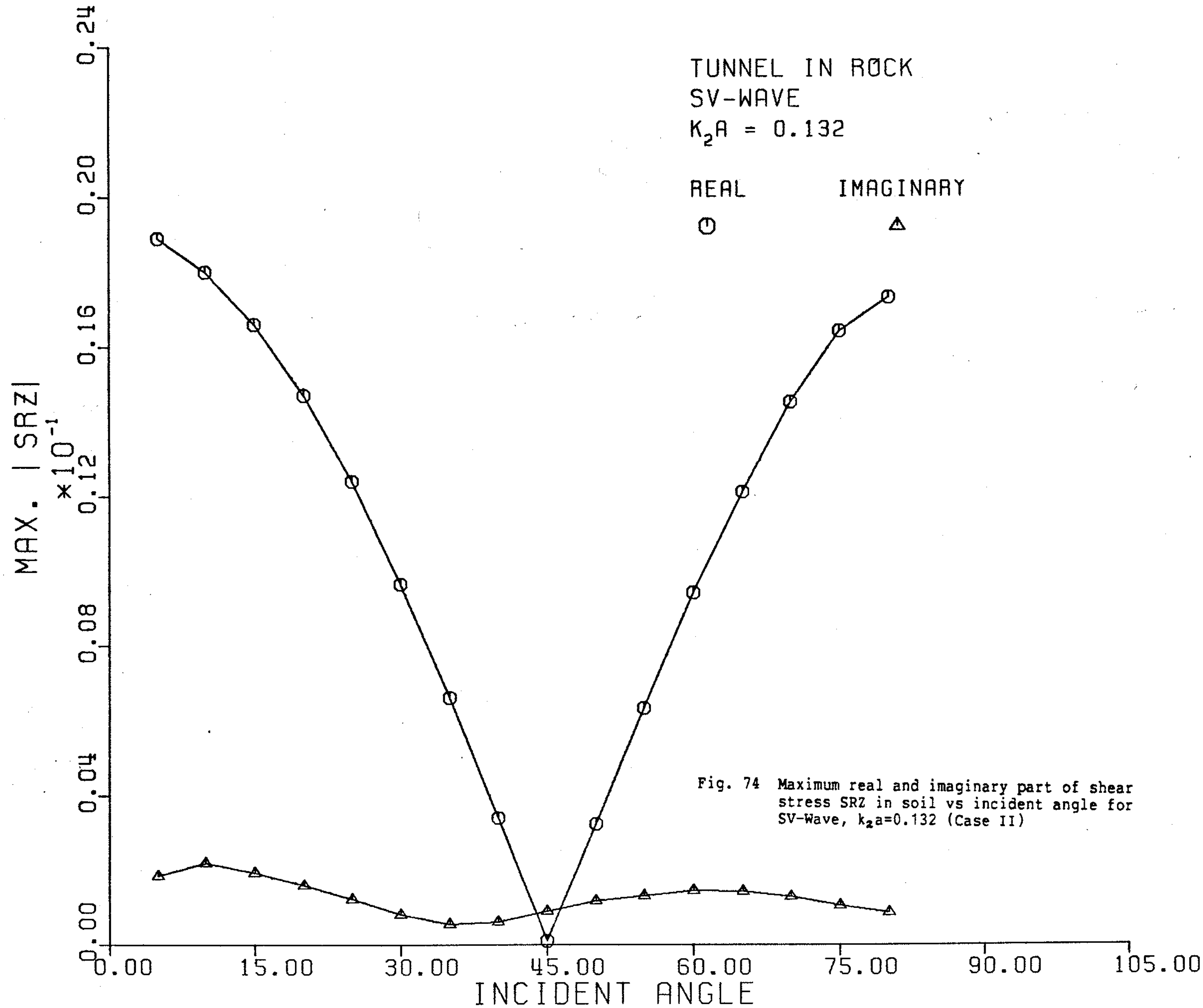

Fig. 74 Maximum real and imaginary part of shear stress SRZ in soil vs incident angle for SV-Wave, $k_2a=0.132$ (Case II)

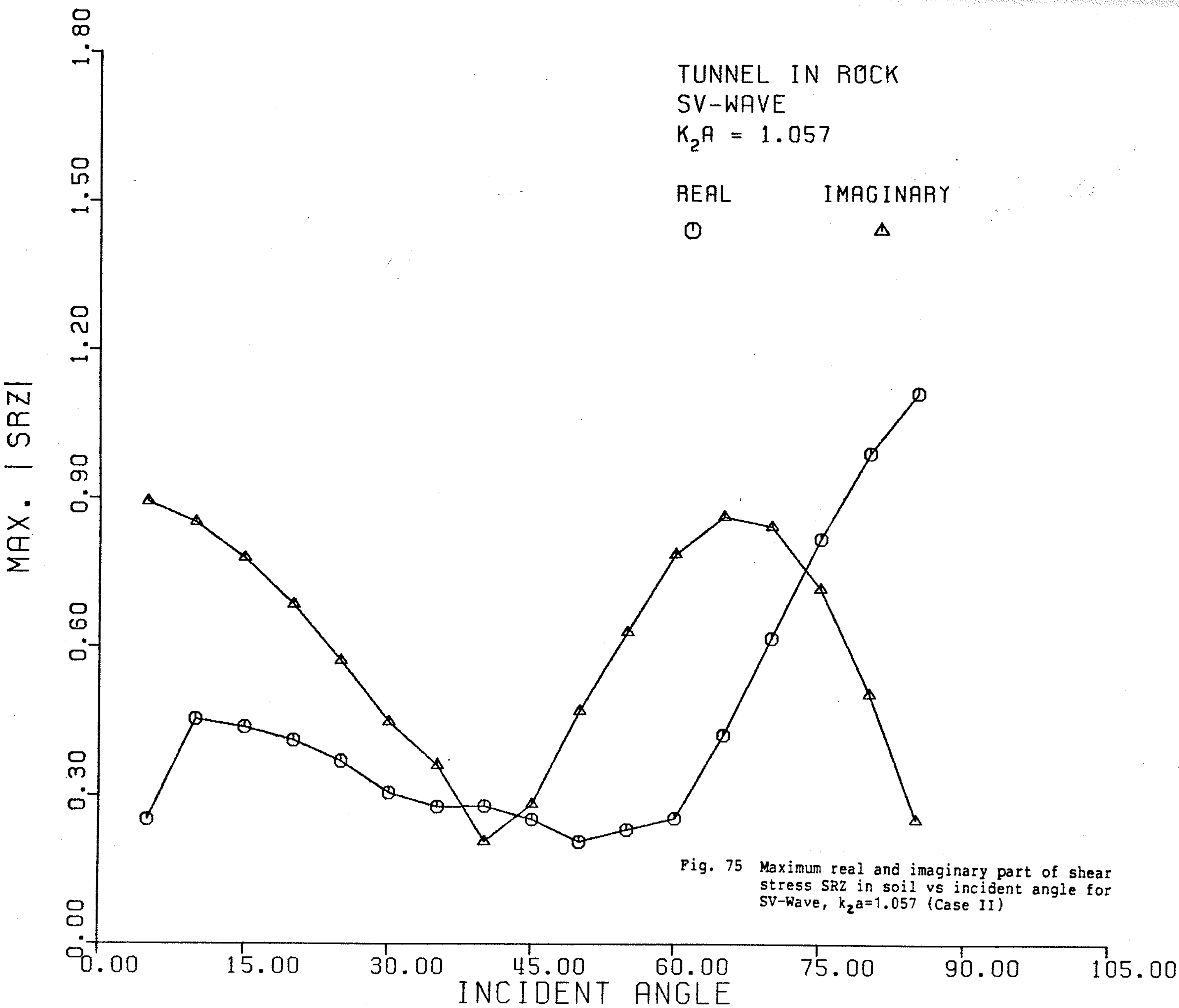

Fig. 75 Maximum real and imaginary part of shear stress SRZ in soil vs incident angle for SV-Wave, $k_2a=1.057$ (Case II)

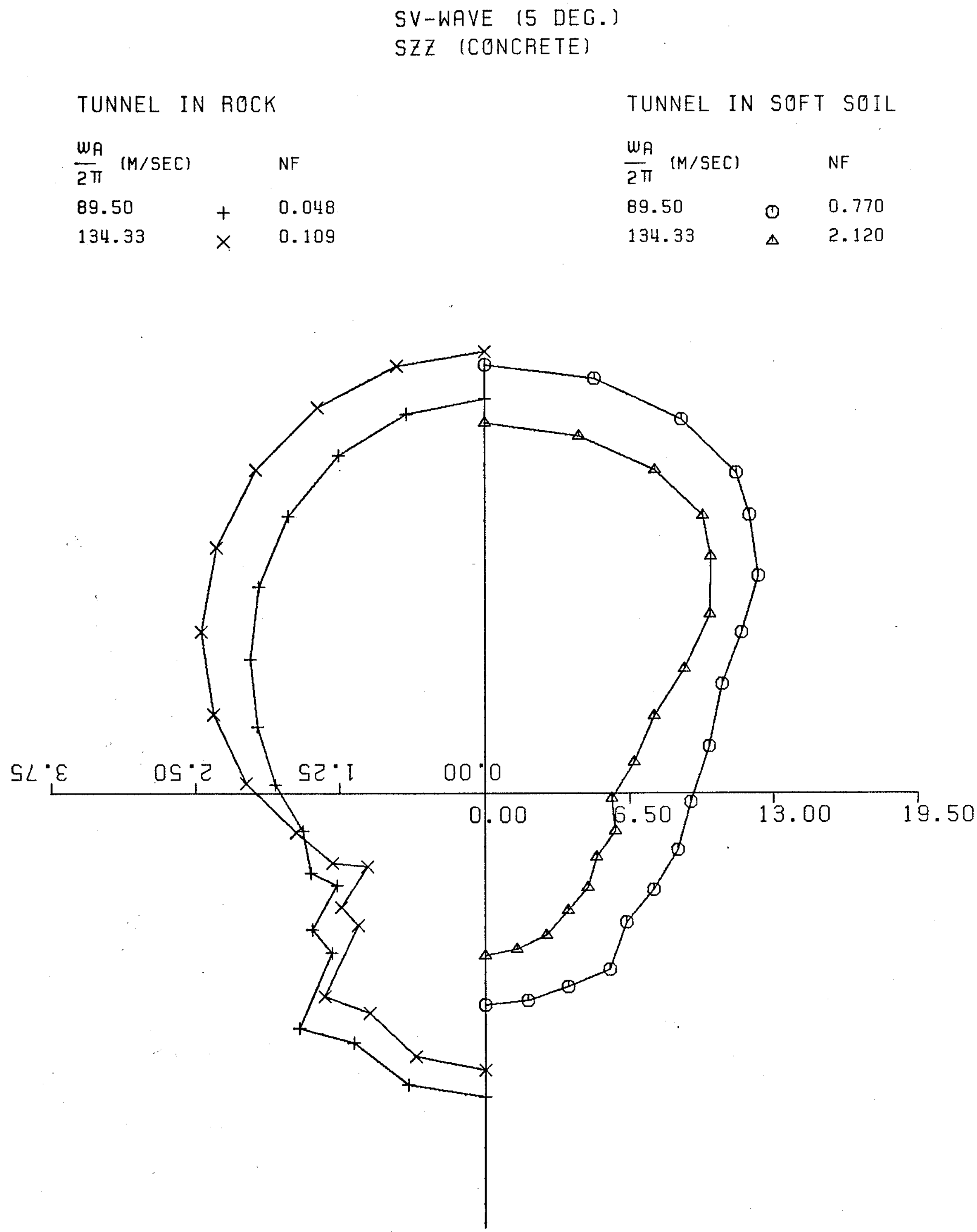

Fig. 76 Comparison between Case I and Case II for normalized axial stress in tunnel wall for SV-Wave, incident angle = 5°

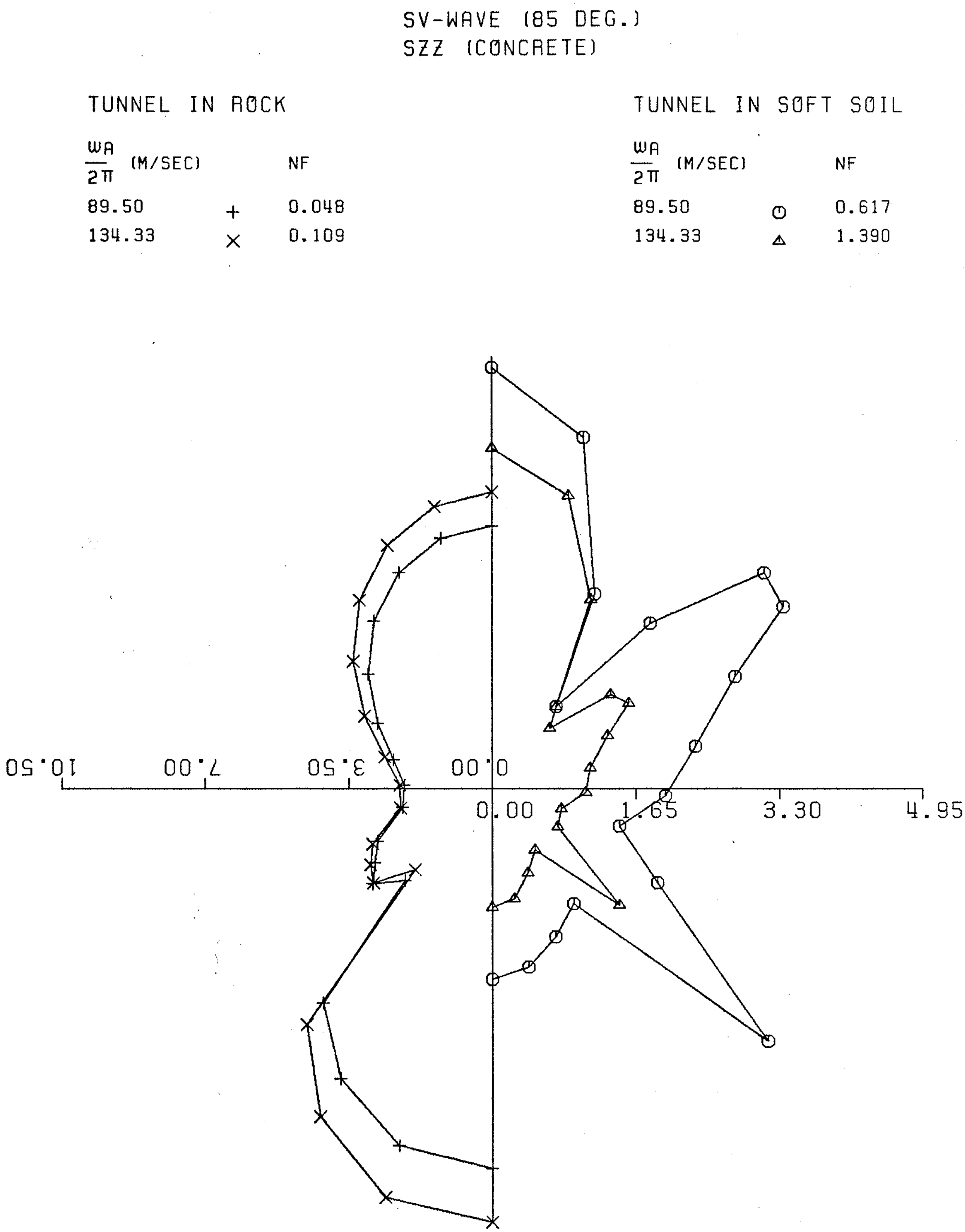

Fig. 77 Comparison between Case I and Case II for normalized axial stress in tunnel wall for SV-Wave, incident angle = 85°

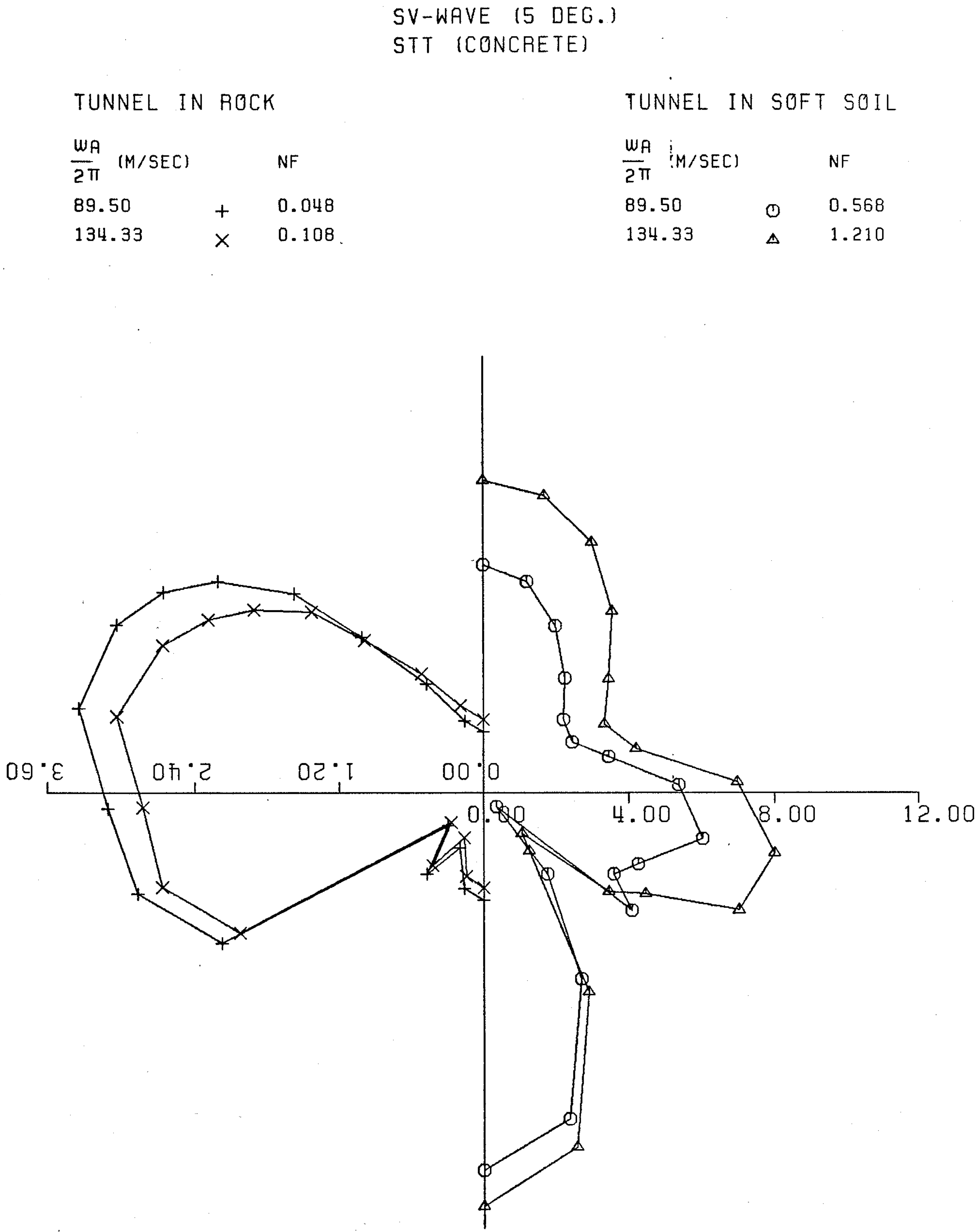

Fig. 78 Comparison between Case I and Case II for normalized hoop stress in tunnel wall for SV-Wave, incident angle = 5°

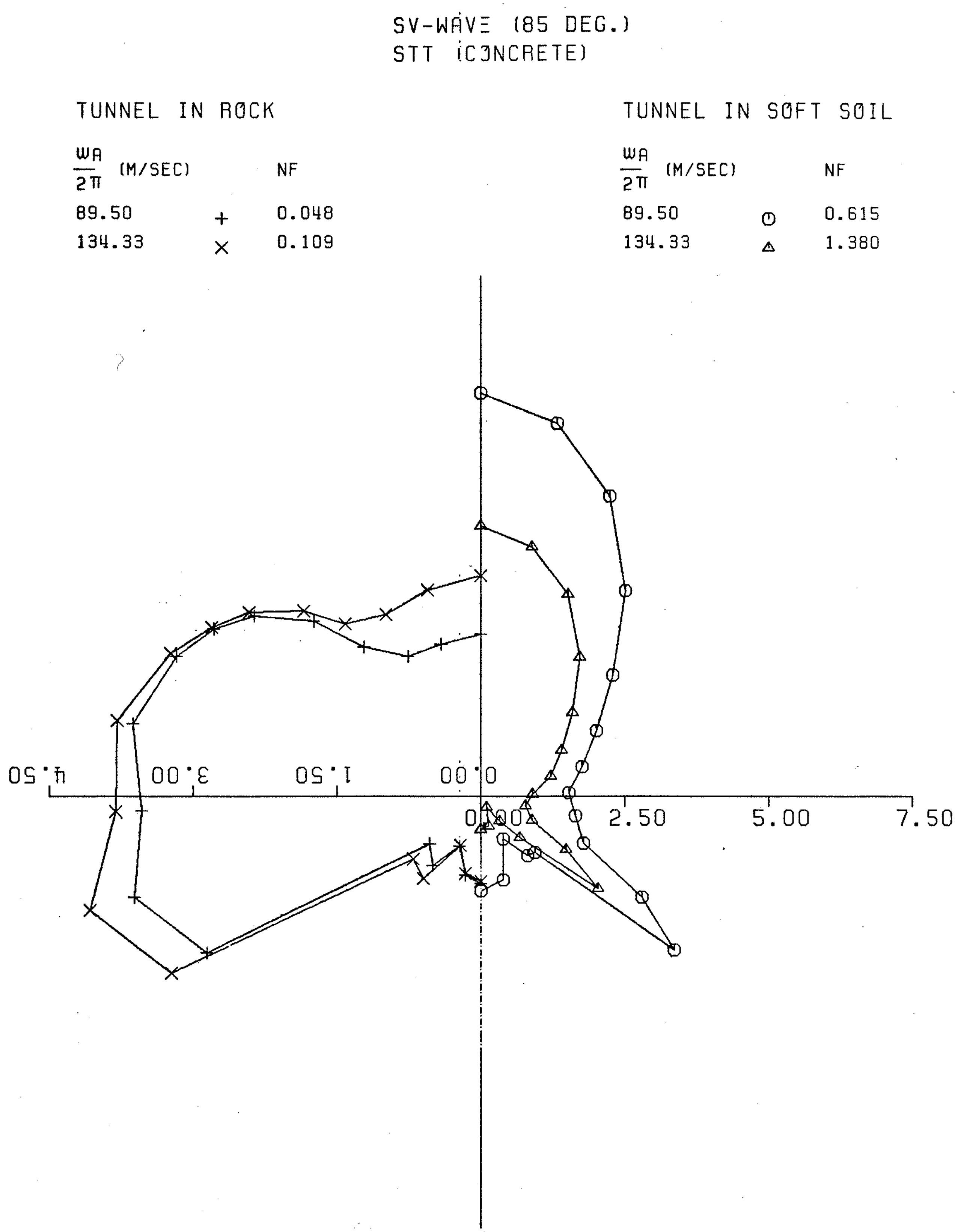

Fig. 79 Comparison between Case I and Case II for normalized hoop stress in tunnel wall for SV-Wave, incident angle = 85°

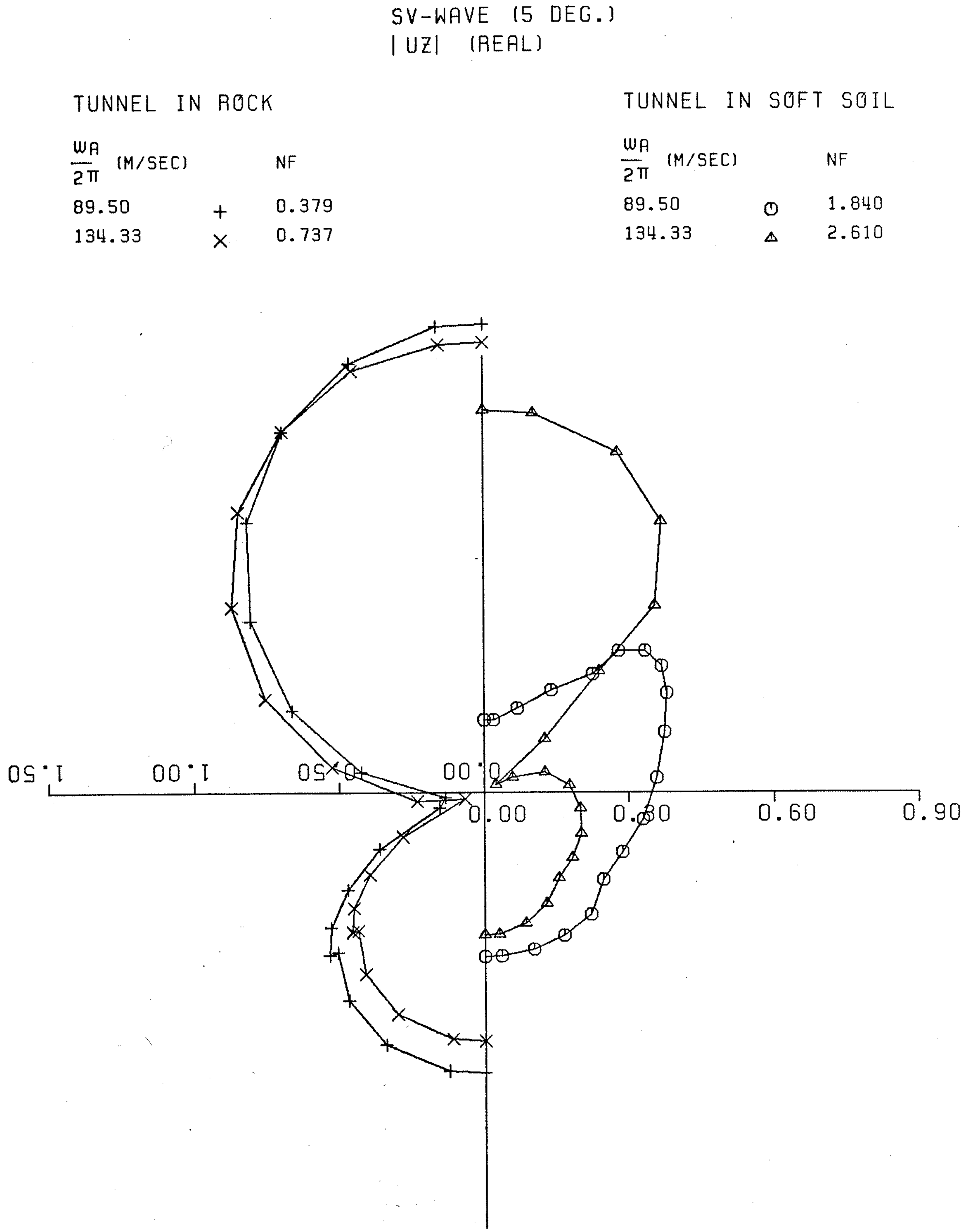

Fig. 80 Comparison between Case I and Case II for normalized real part of axial displacement for SV-Wave, incident angle = 5°

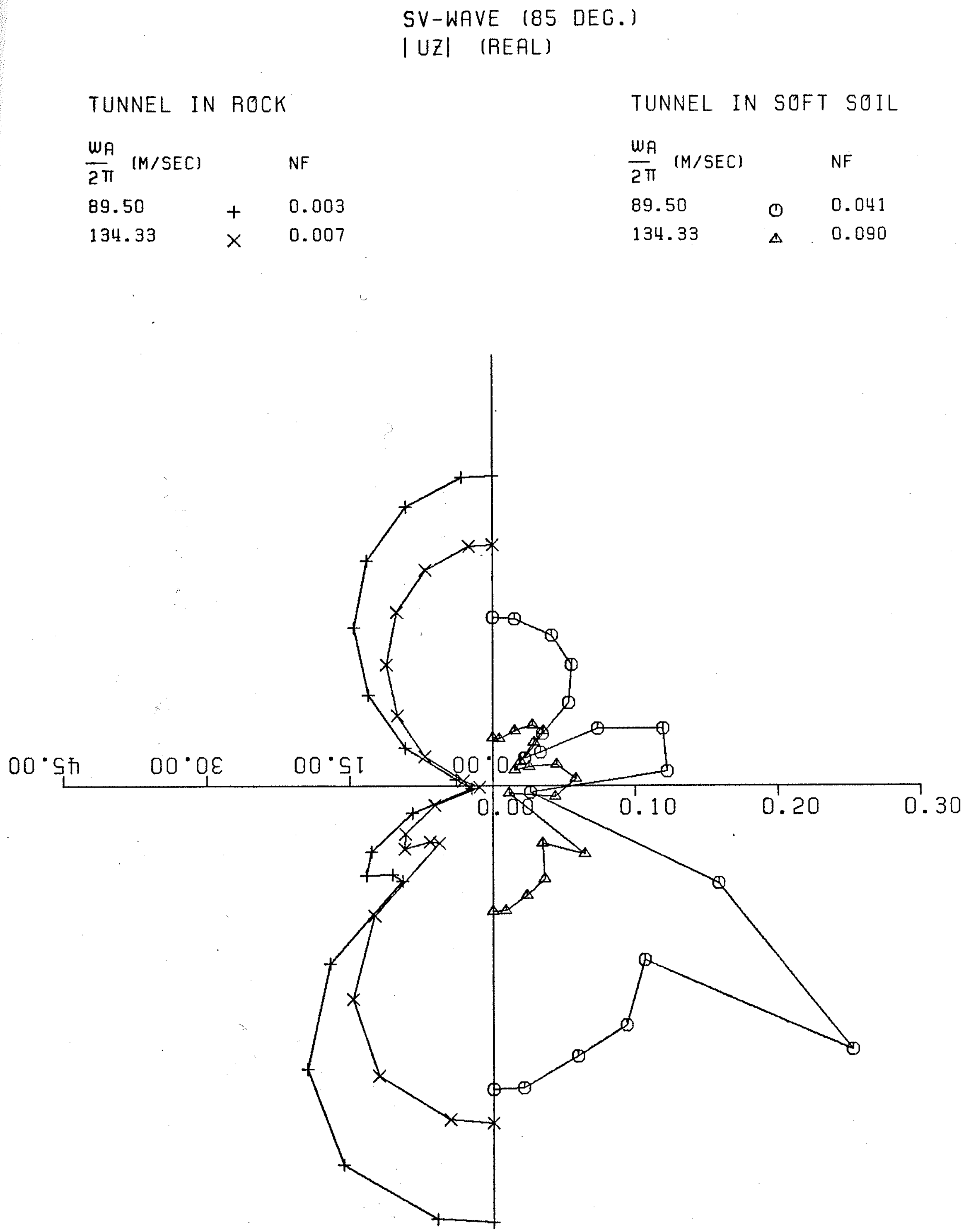

Fig. 81 Comparison between Case I and Case II for normalized real part of axial displacement for SV-Wave, incident angle = 85°

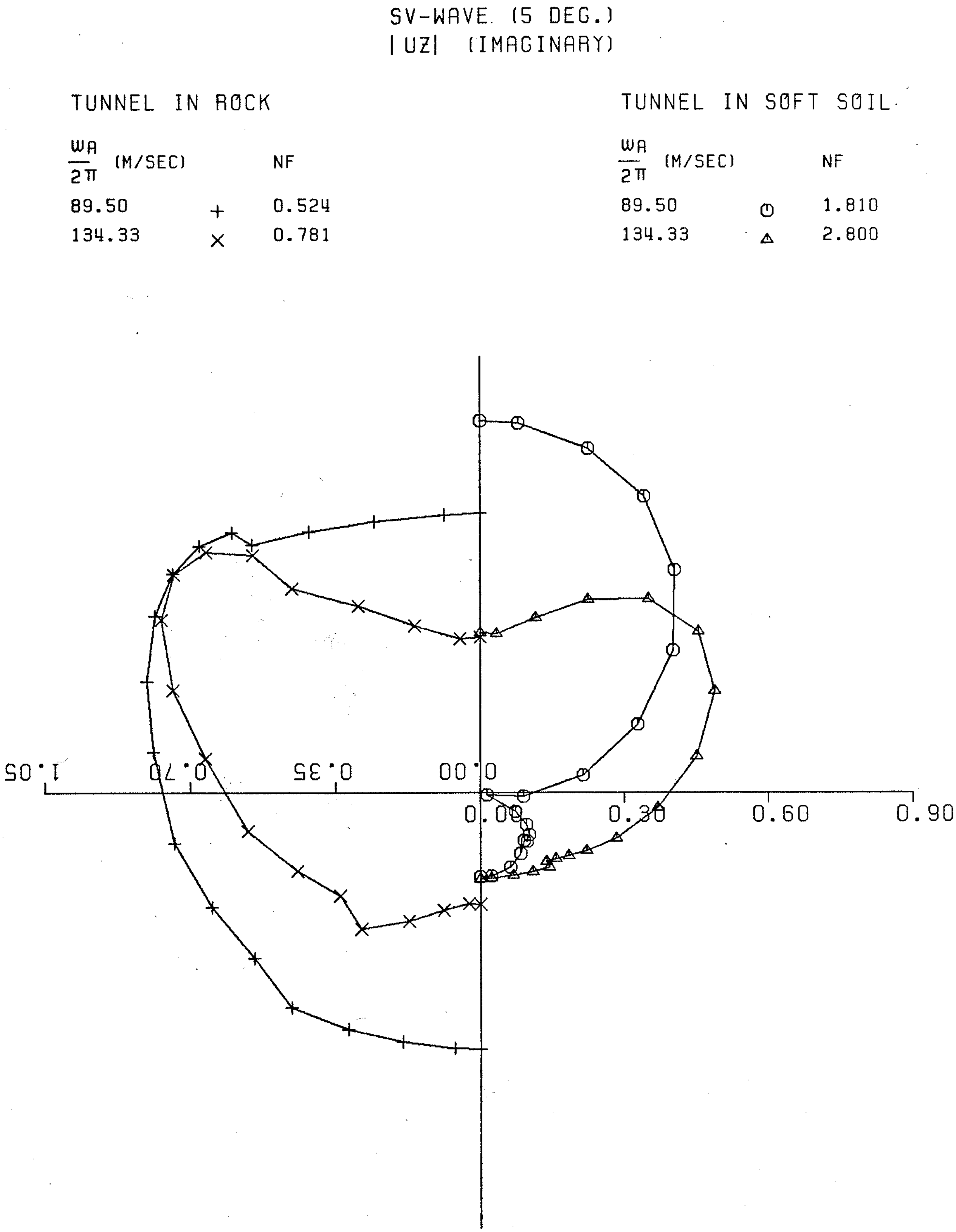

Fig. 82 Comparison between Case I and Case II for normalized imaginary part of axial displacement for SV-Wave, incident angle = 5°

SV-WAVE (85 DEG.)
|UZ| (IMAGINARY)

TUNNEL IN ROCK			TUNNEL IN SOFT SOIL		
$\frac{\omega a}{2\pi}$ (M/SEC)		NF	$\frac{\omega a}{2\pi}$ (M/SEC)		NF
89.50	+	0.046	89.50	⊕	0.164
134.33	×	0.069	134.33	△	0.246

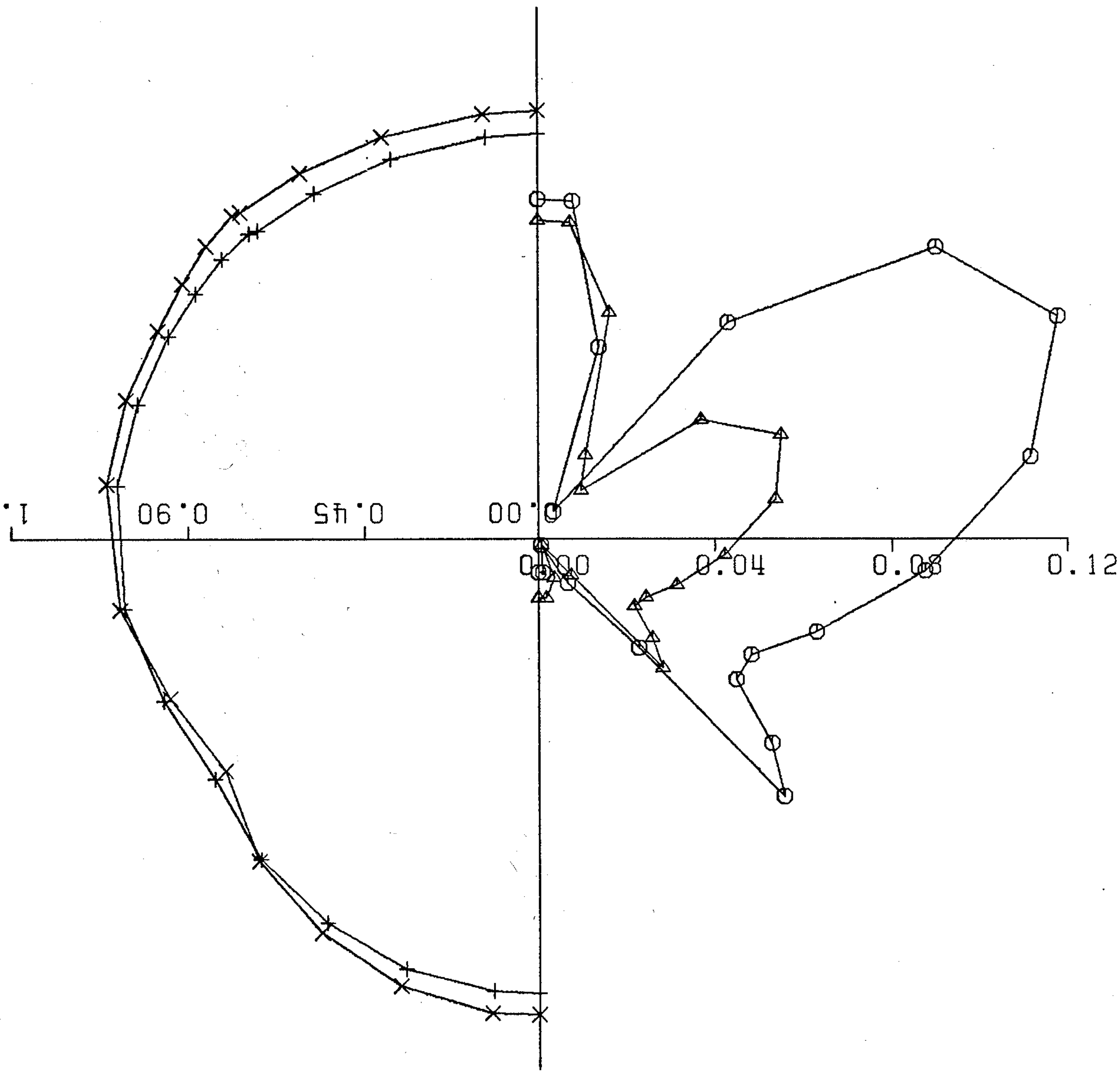

Fig. 83 Comparison between Case I and Case II for normalized imaginary part of axial displacement for SV-Wave, incident angle = 85°

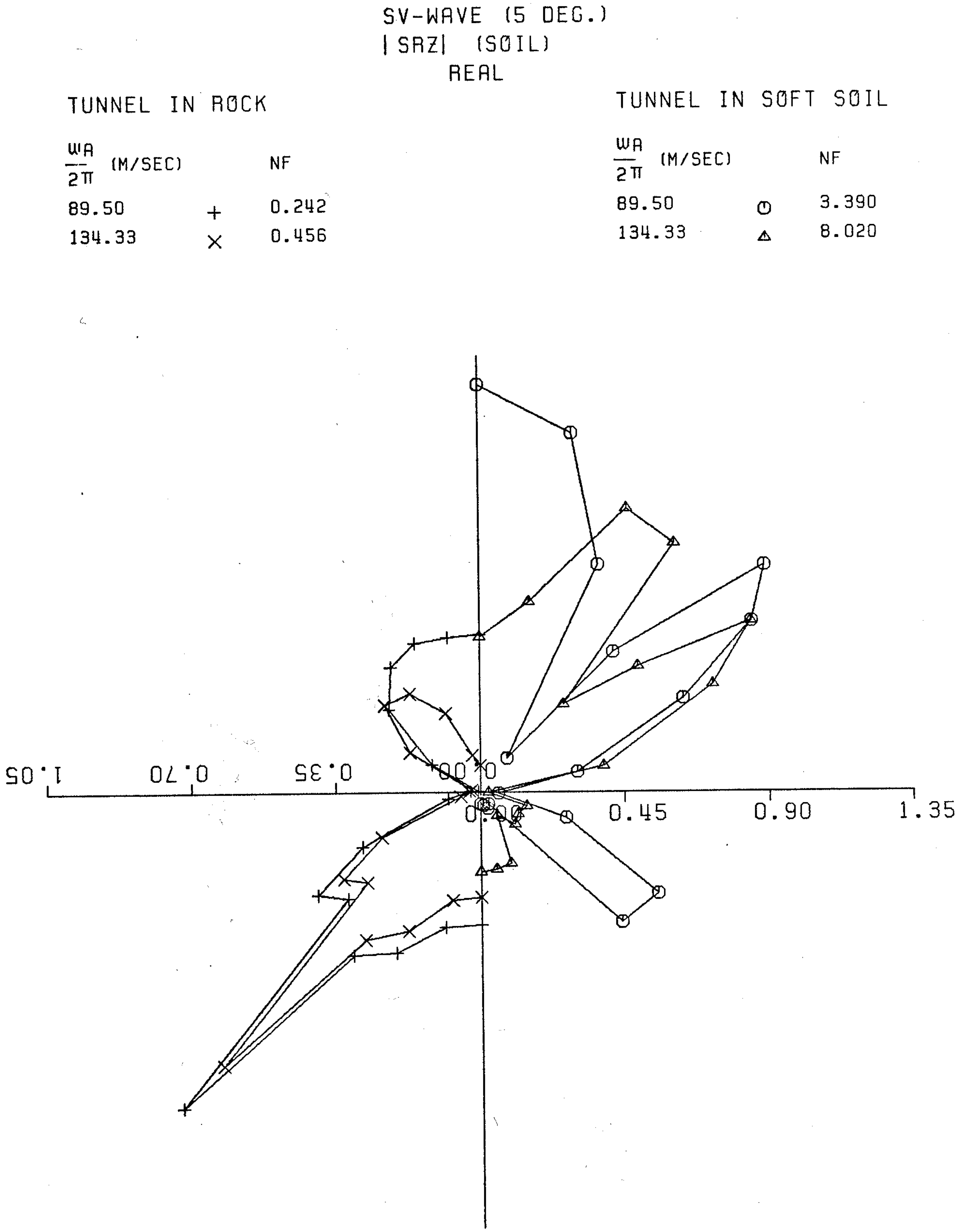

Fig. 84 Comparison between Case I and Case II for normalized real part of shear stress SRZ in soil for SV-Wave, incident angle = 5°

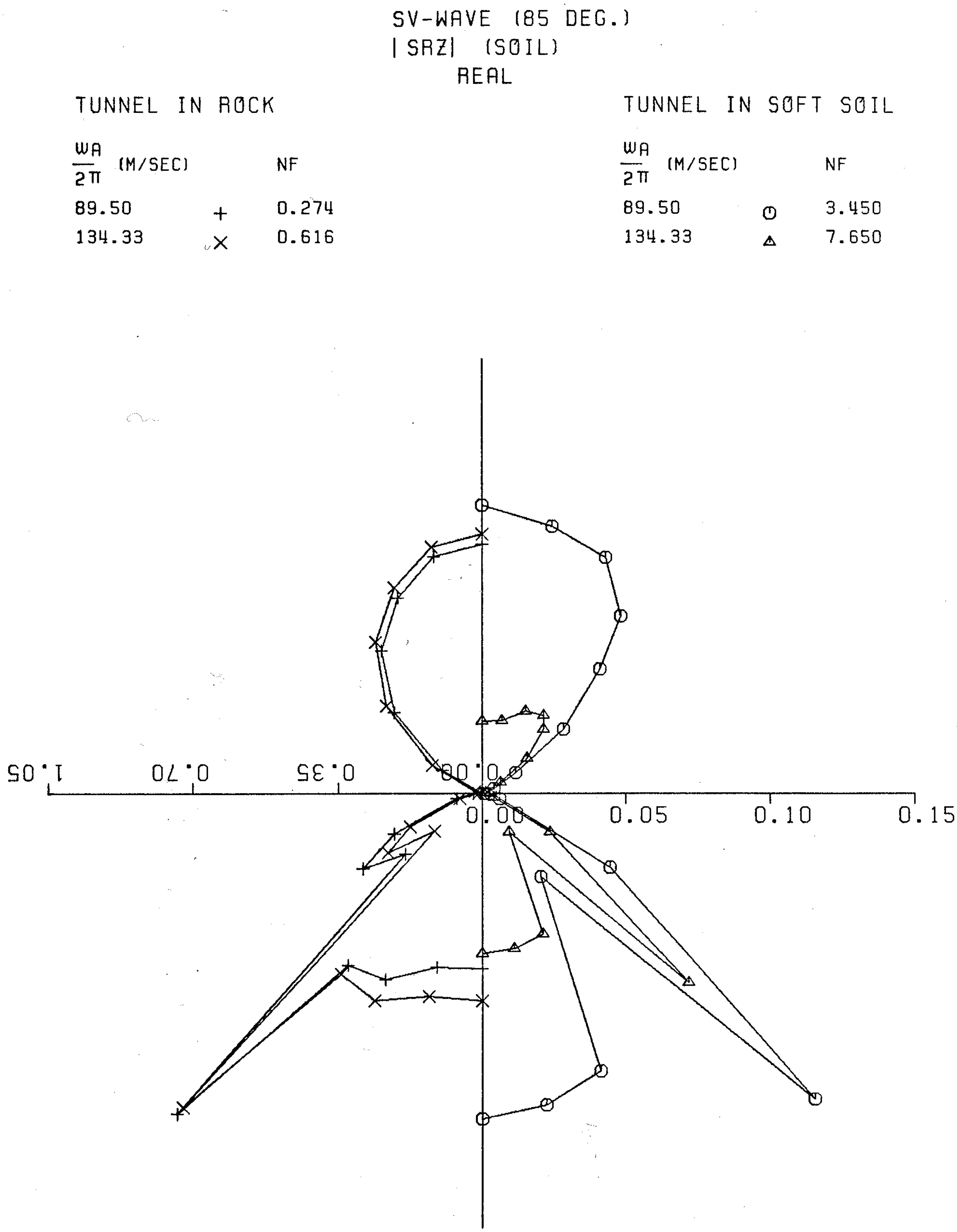

Fig. 85 Comparison between Case I and Case II for normalized real part of shear stress SRZ in soil for SV-Wave, incident angle = 85°

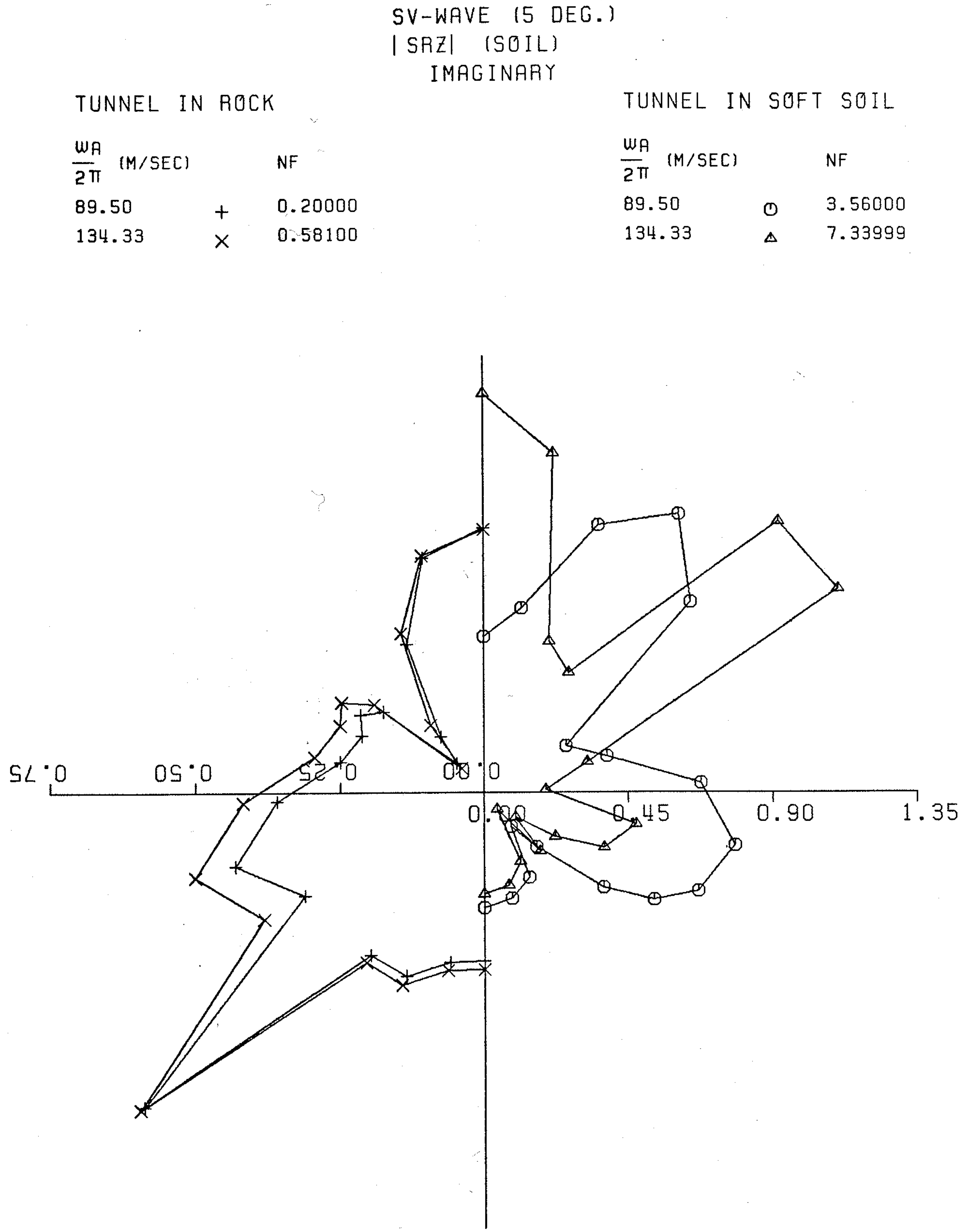

Fig. 86 Comparison between Case I and Case II for normalized imaginary part of shear stress SRZ in soil for SV-Wave, incident angle = 5°

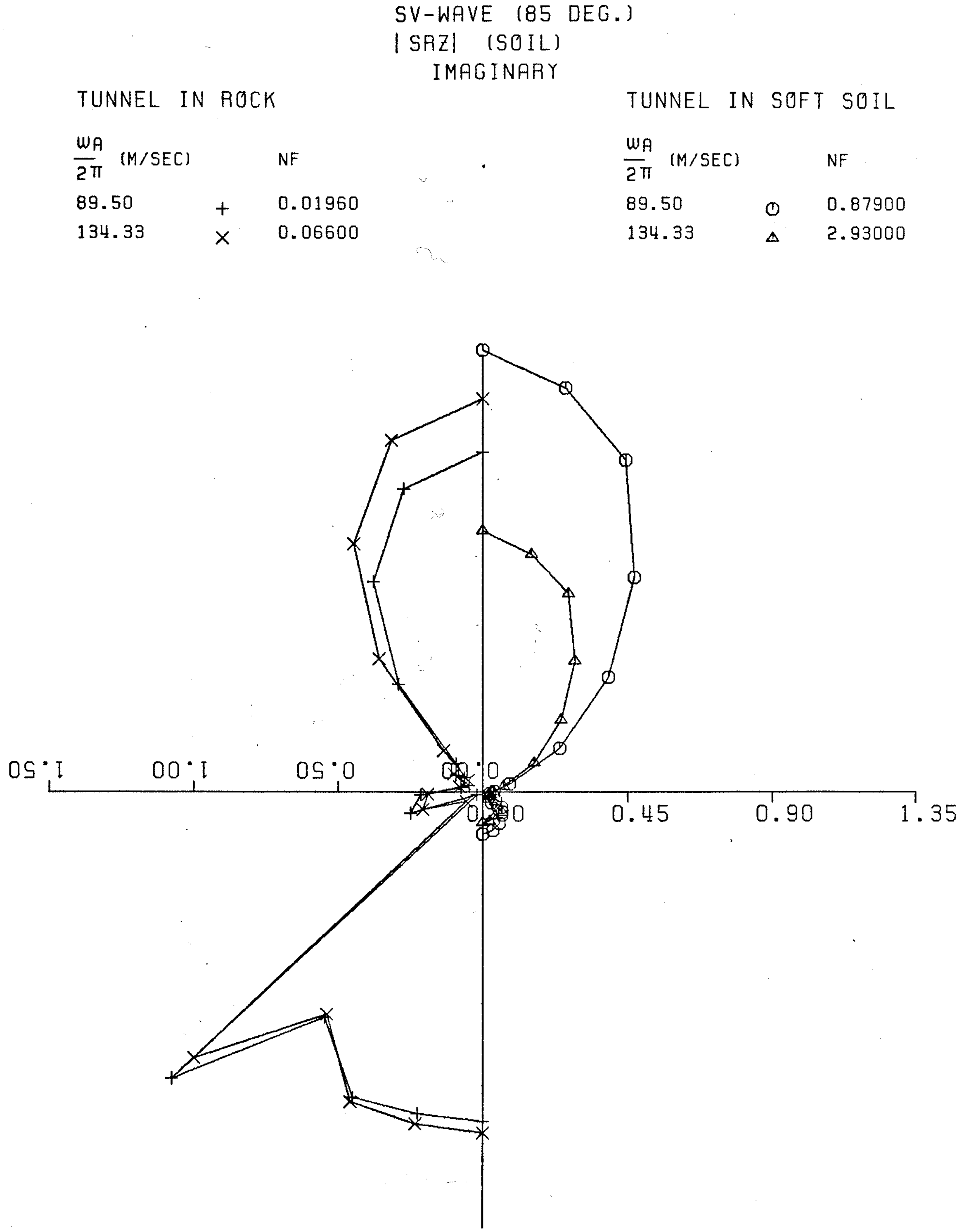

Fig. 87 Comparison between Case I and Case II for normalized imaginary part of shear stress SRZ in soil for SV-Wave, incident angle = 85°

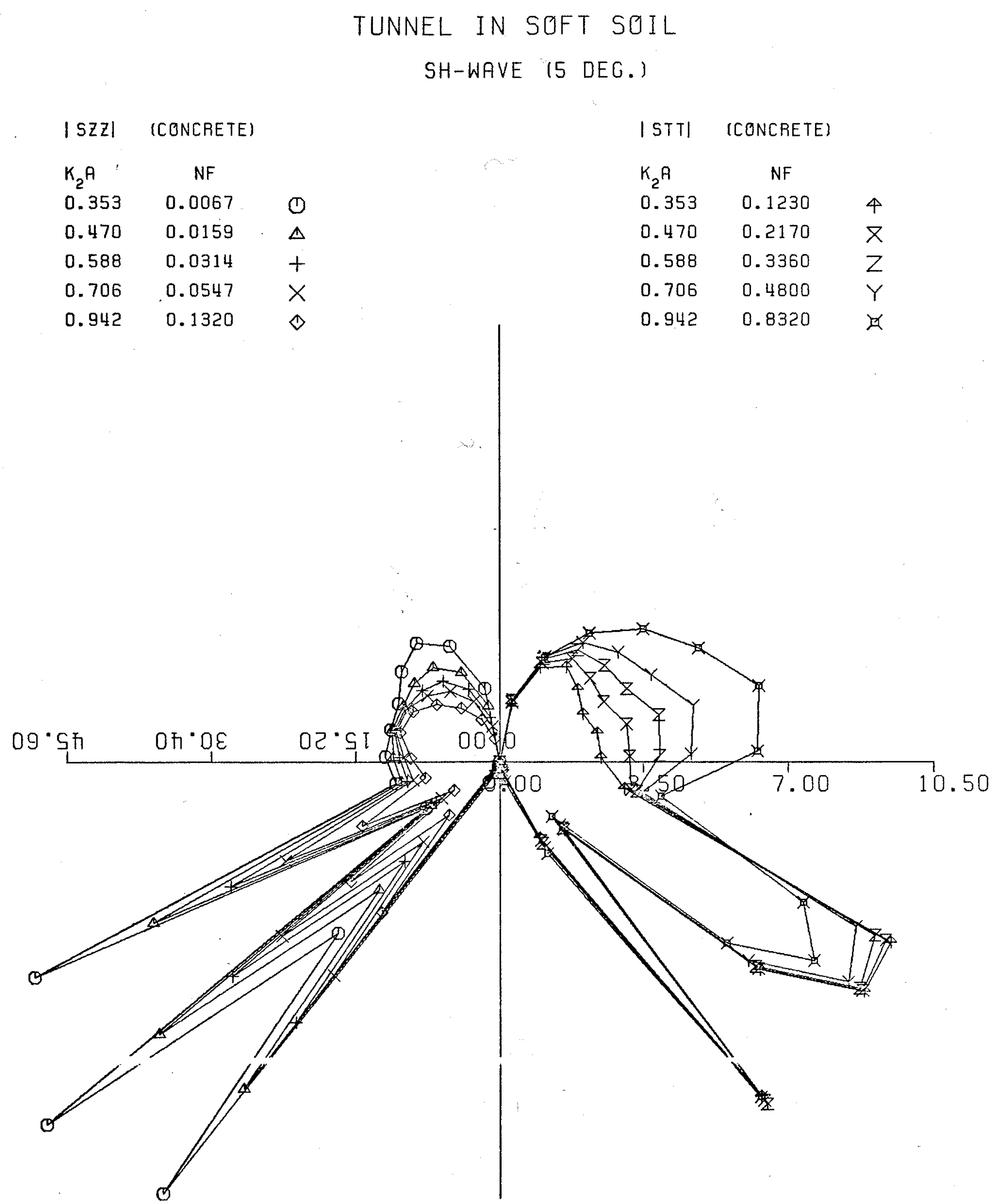

Fig. 88 Normalized axial stress and hoop stress in tunnel wall vs frequency for SH-Wave when the incident angle = 5° (Case I)

TUNNEL IN SOFT SOIL

SH-WAVE (30 DEG.)

|SZZ| (CONCRETE)

K_2A	NF	
0.353	0.0051	⊕
0.470	0.0120	△
0.588	0.0236	+
0.706	0.0411	×
0.942	0.0991	◇

|STT| (CONCRETE)

K_2A	NF	
0.353	0.1070	↑
0.470	0.1890	⧖
0.588	0.2940	Z
0.706	0.4210	Y
0.942	0.7550	⌑

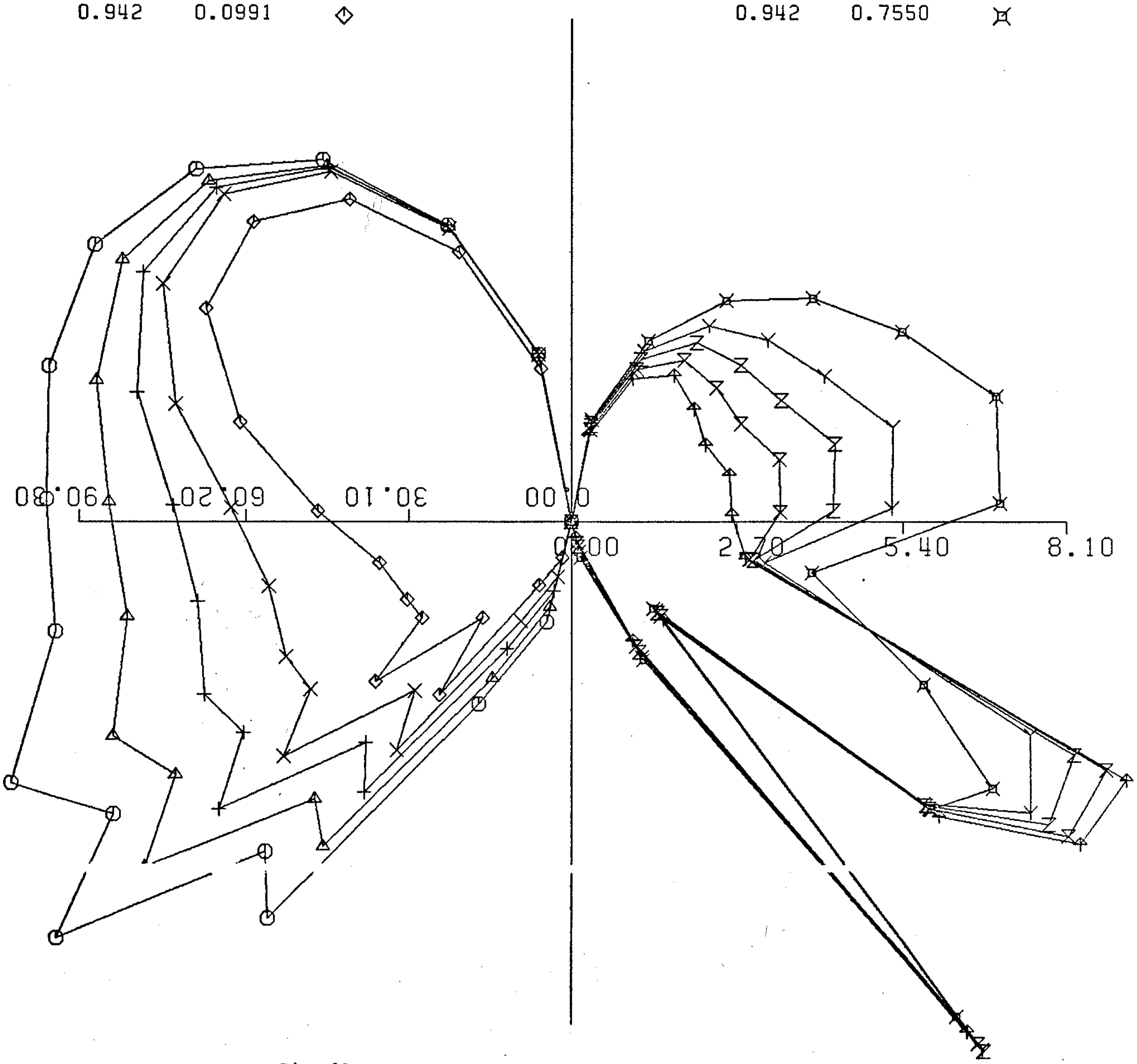

Fig. 89 Normalized axial stress and hoop stress in tunnel wall vs frequency for SH-Wave when the incident angle = 30° (Case I)

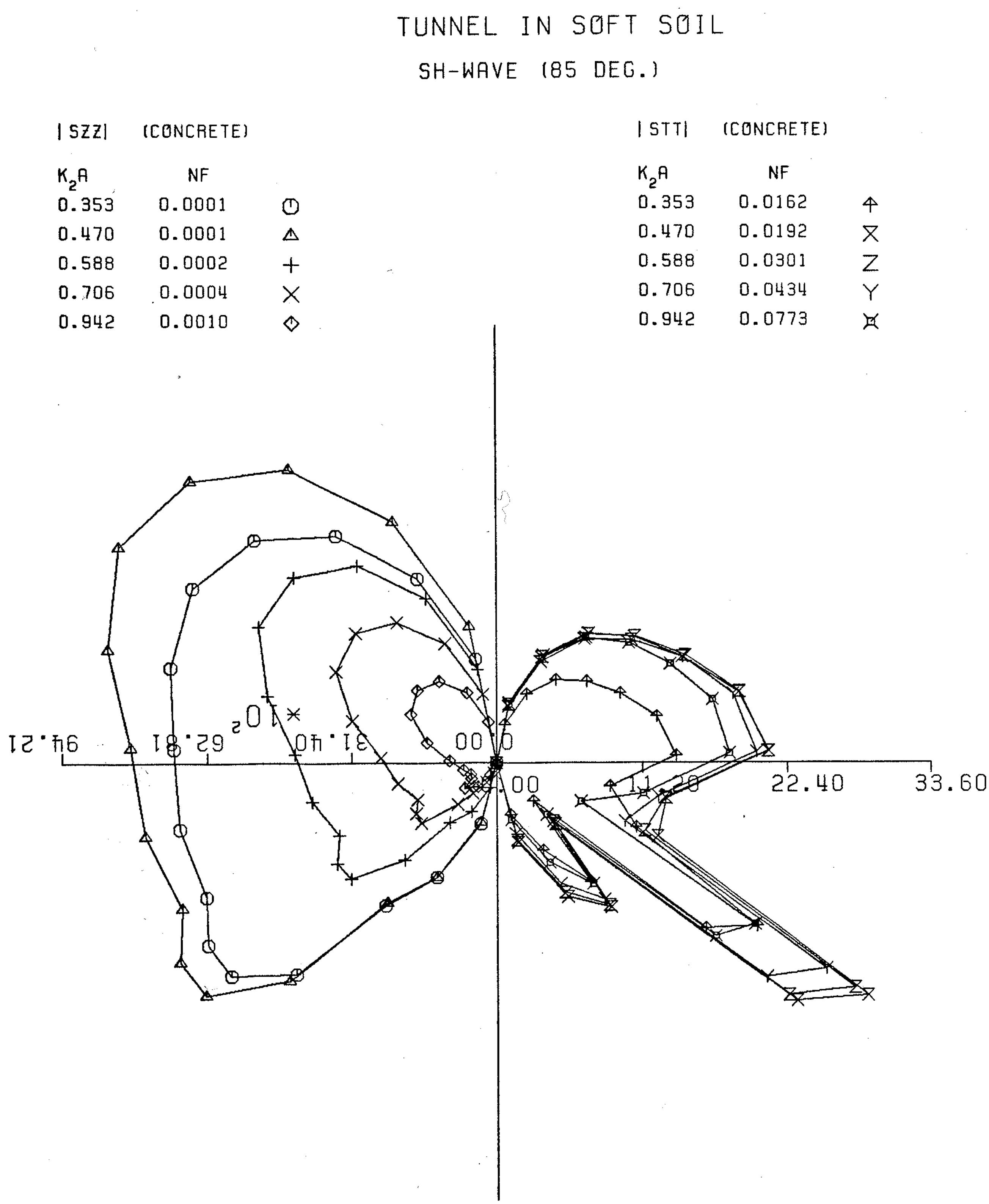

Fig. 90 Normalized axial stress and hoop stress in tunnel wall vs frequency for SH-Wave when the incident angle = 85°(Case I)

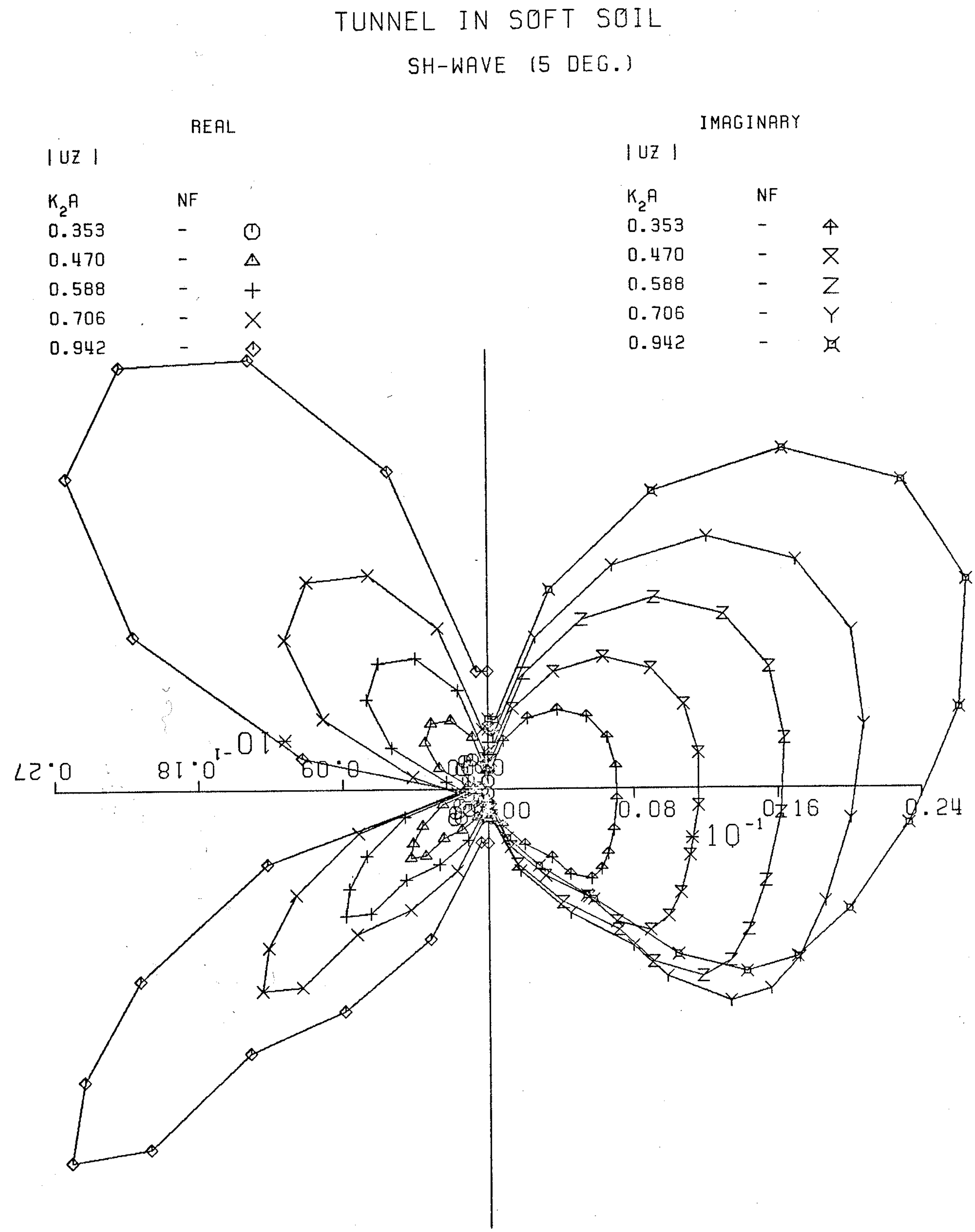

Fig. 91 Real and imaginary part of axial displacement vs frequency for SH-Wave when the incident angle = 5° (Case I)

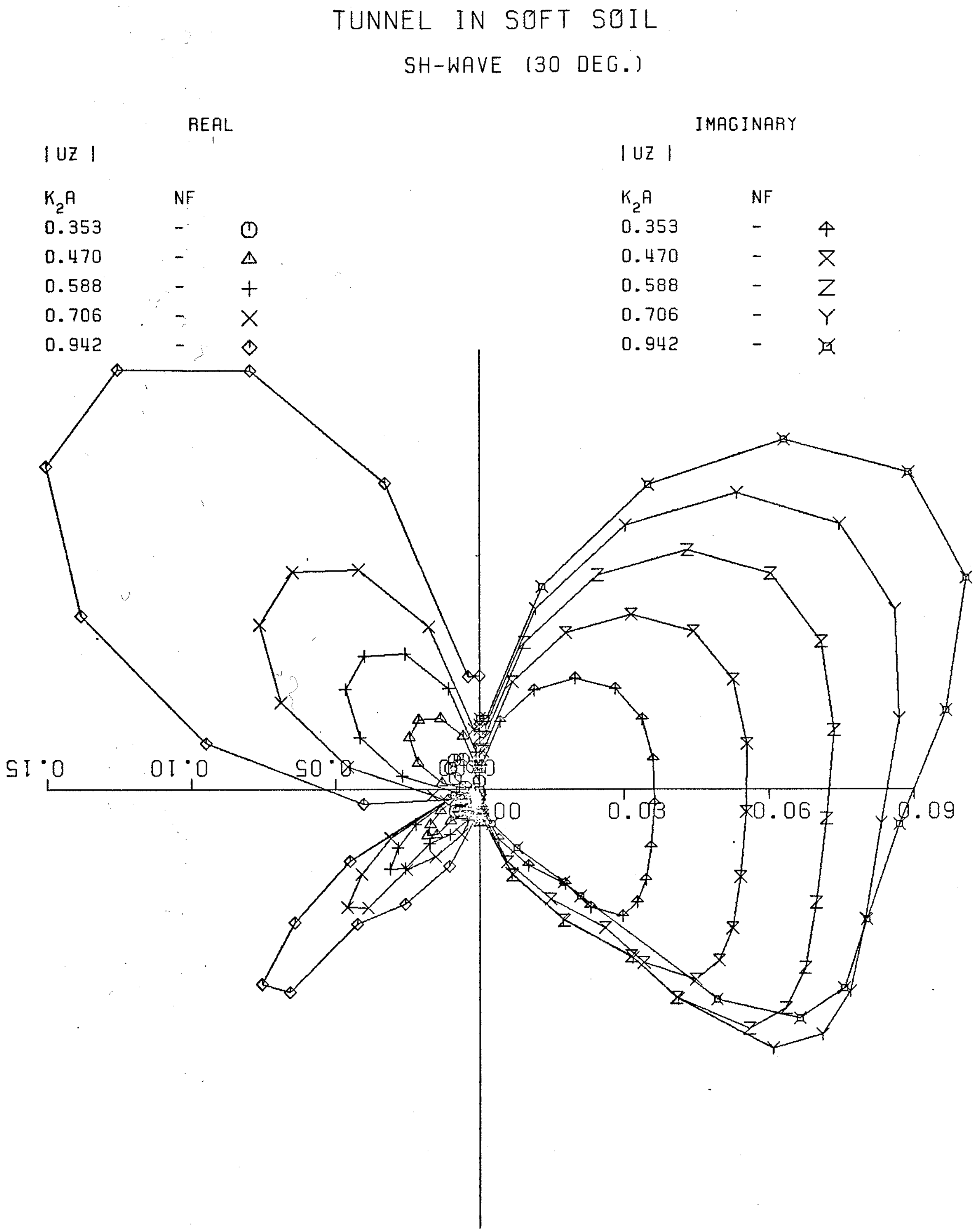

Fig. 92 Real and imaginary part of axial displacement vs frequency for SH-Wave when the incident angle = 30° (Case I)

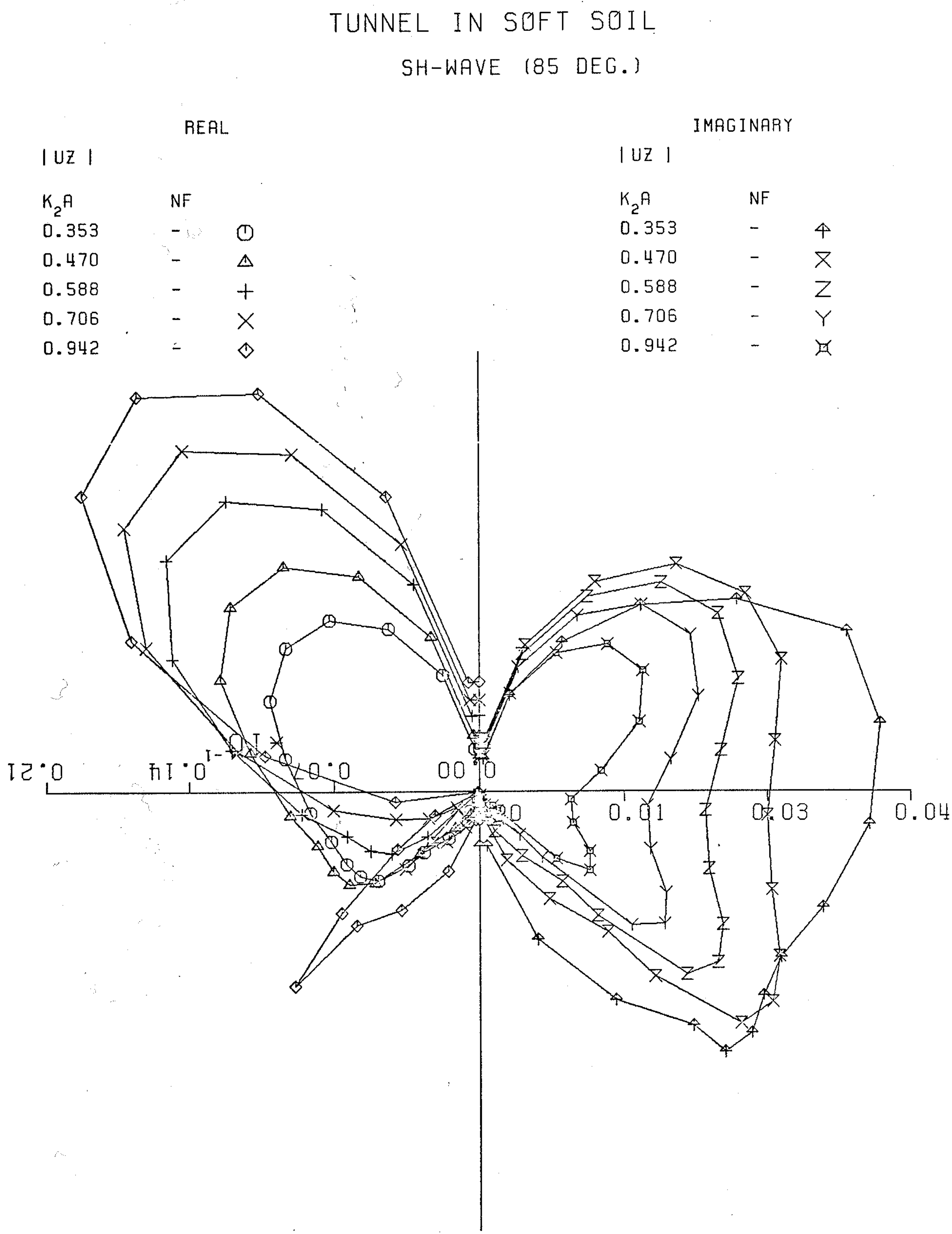

Fig. 93 Real and imaginary part of axial displacement vs frequency for SH-Wave when the incident angle = 85°(Case I)

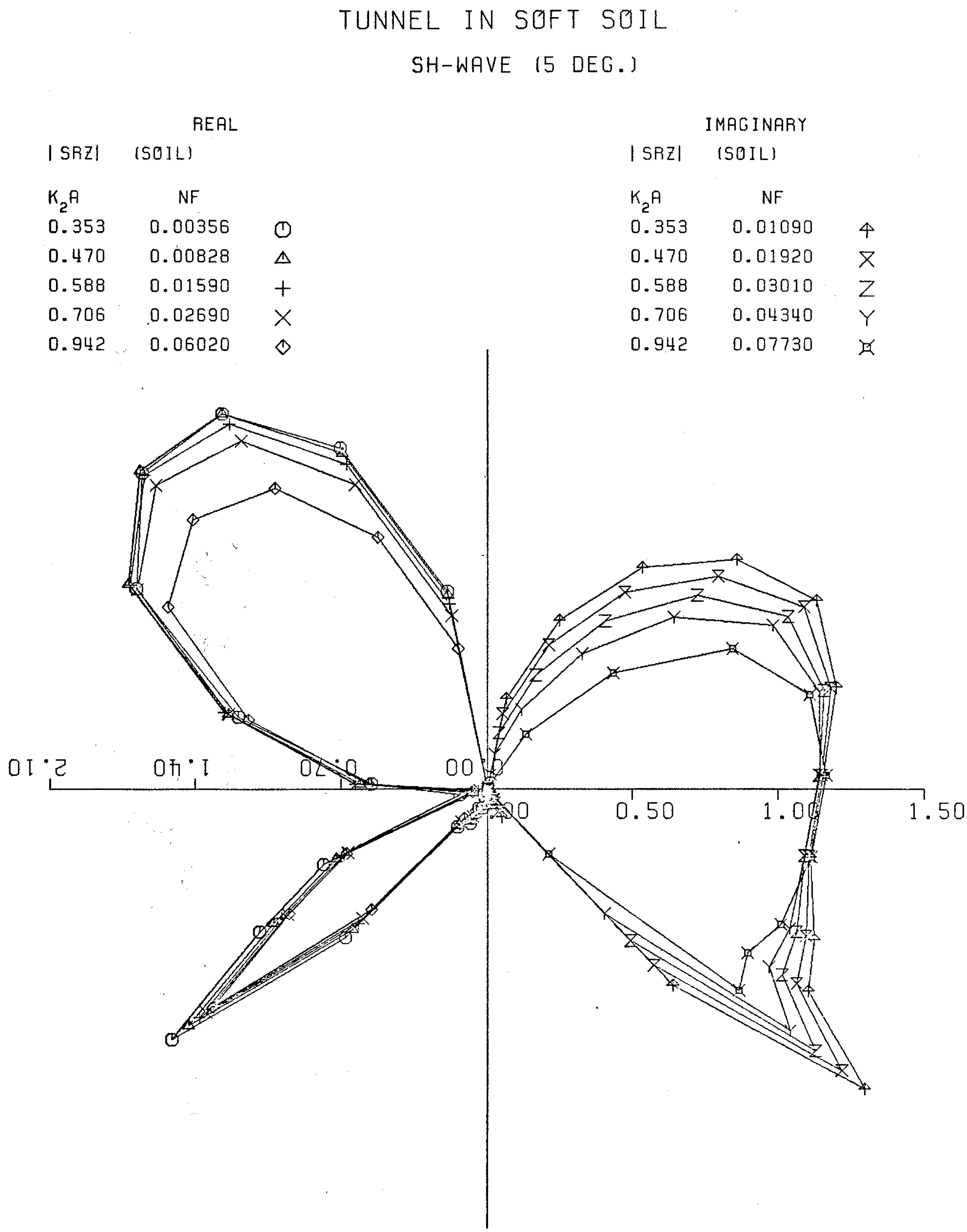

Fig. 94 Normalized real and imaginary part of shear stress SRZ in soil vs frequency for SH-Wave when the incident angle = 5° (Case I)

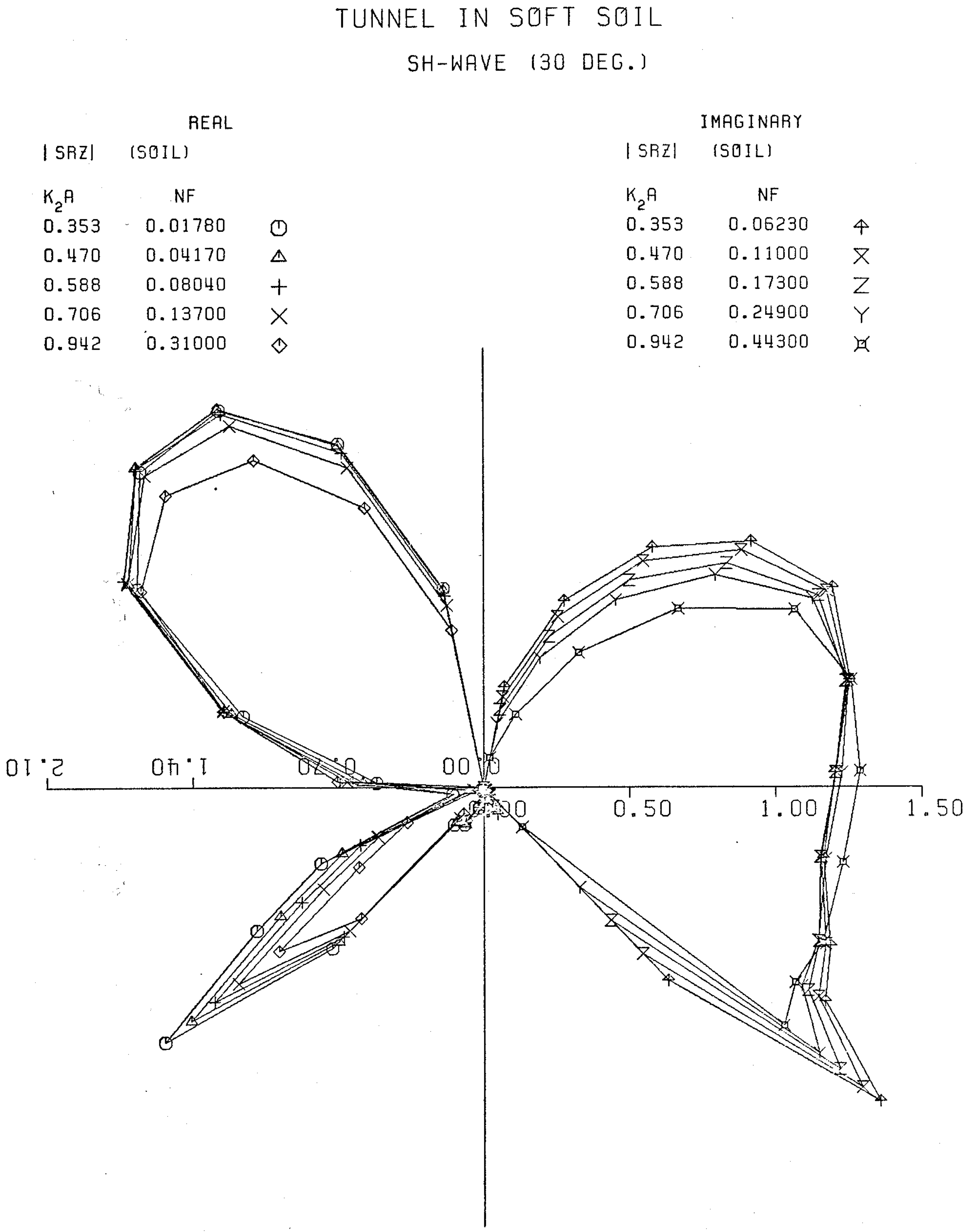

Fig. 95 Normalized real and imaginary part of shear stress SRZ in soil vs frequency for SH-Wave when the incident angle = 30° (Case I)

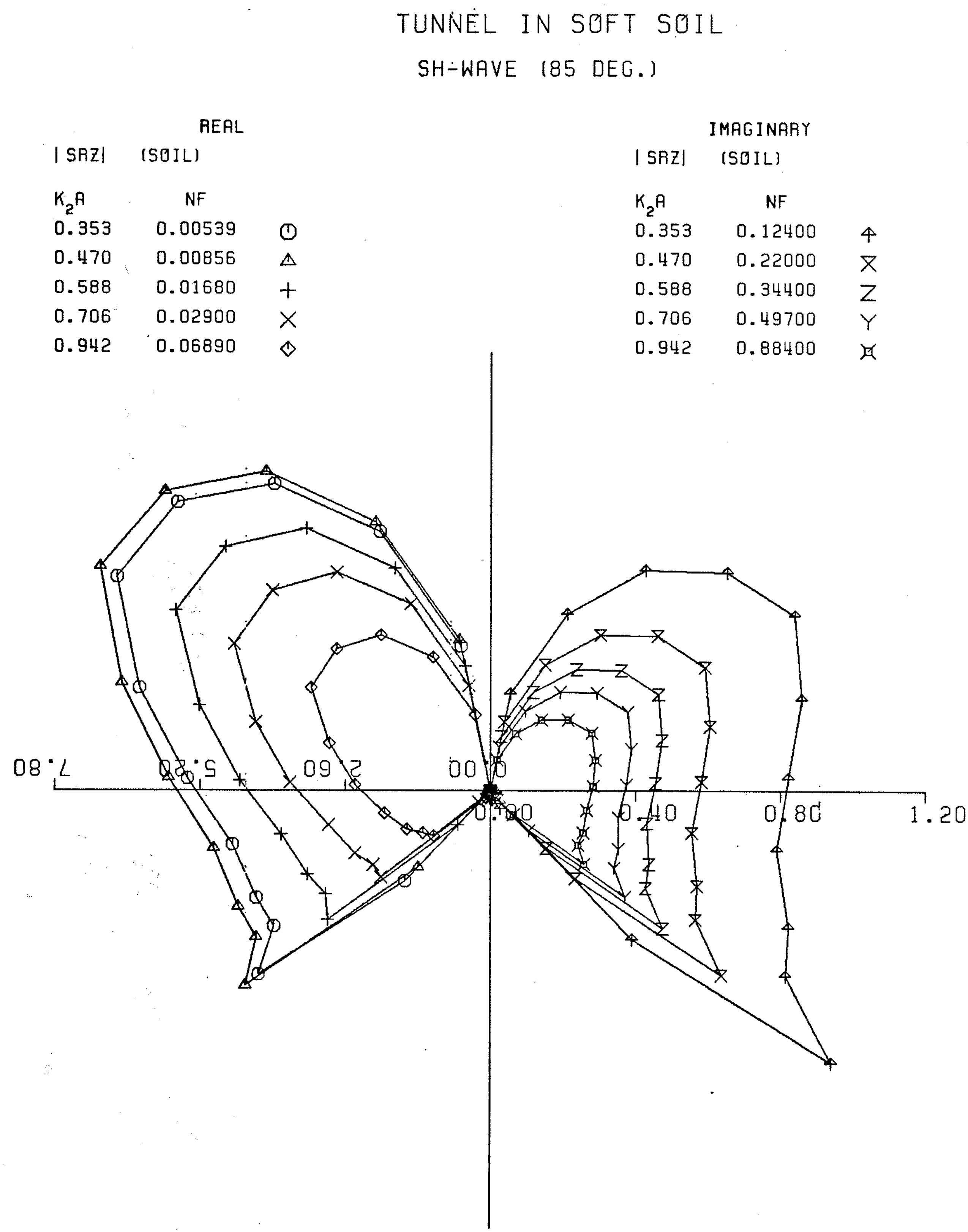

Fig. 96 Normalized real and imaginary part of shear stress SRZ in soil vs frequency for SH-Wave when the incident angle = 85° (Case I)

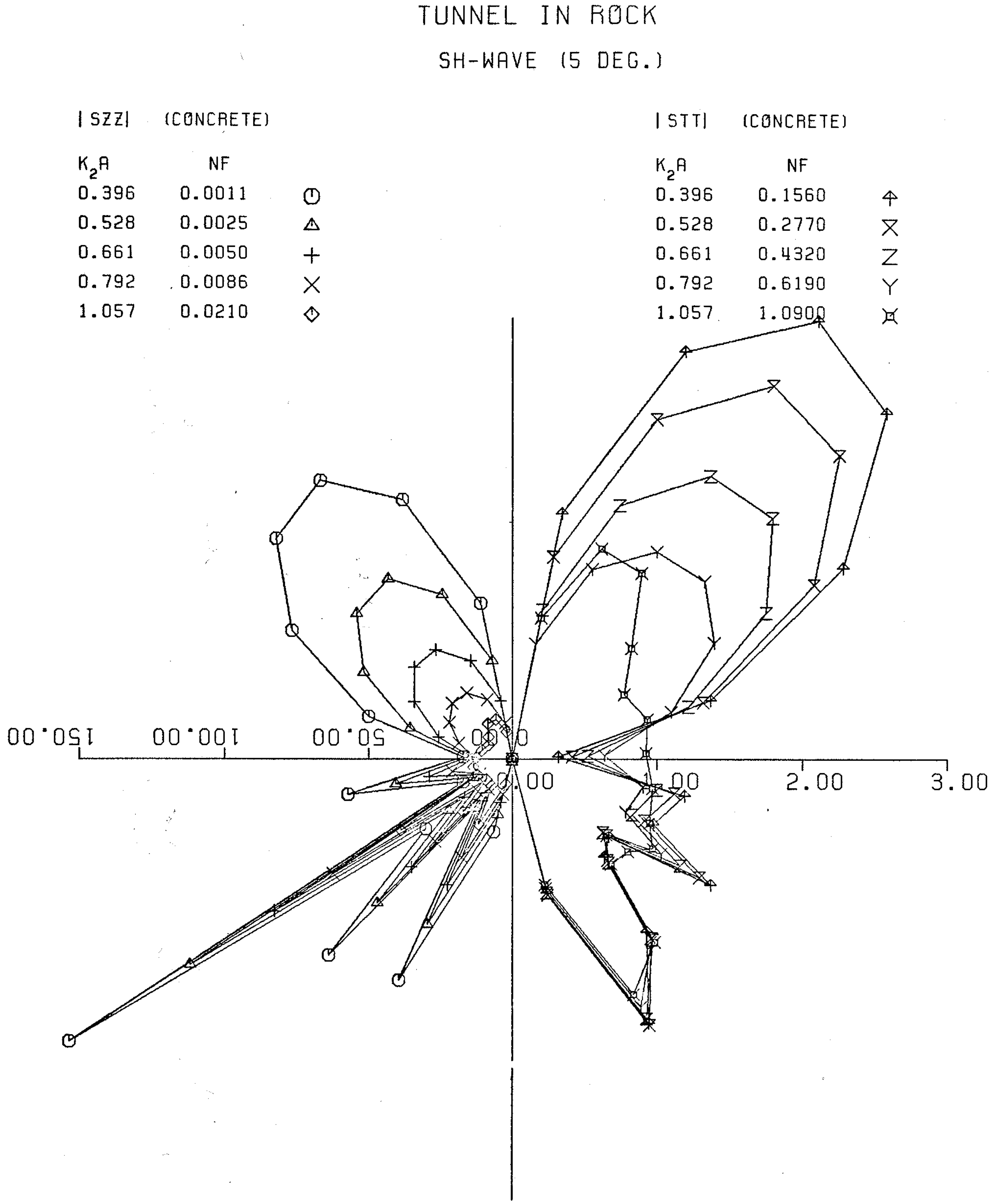

Fig. 97 Normalized axial stress and hoop stress in tunnel wall vs frequency for SH-Wave when the incident angle = 5° (Case II)

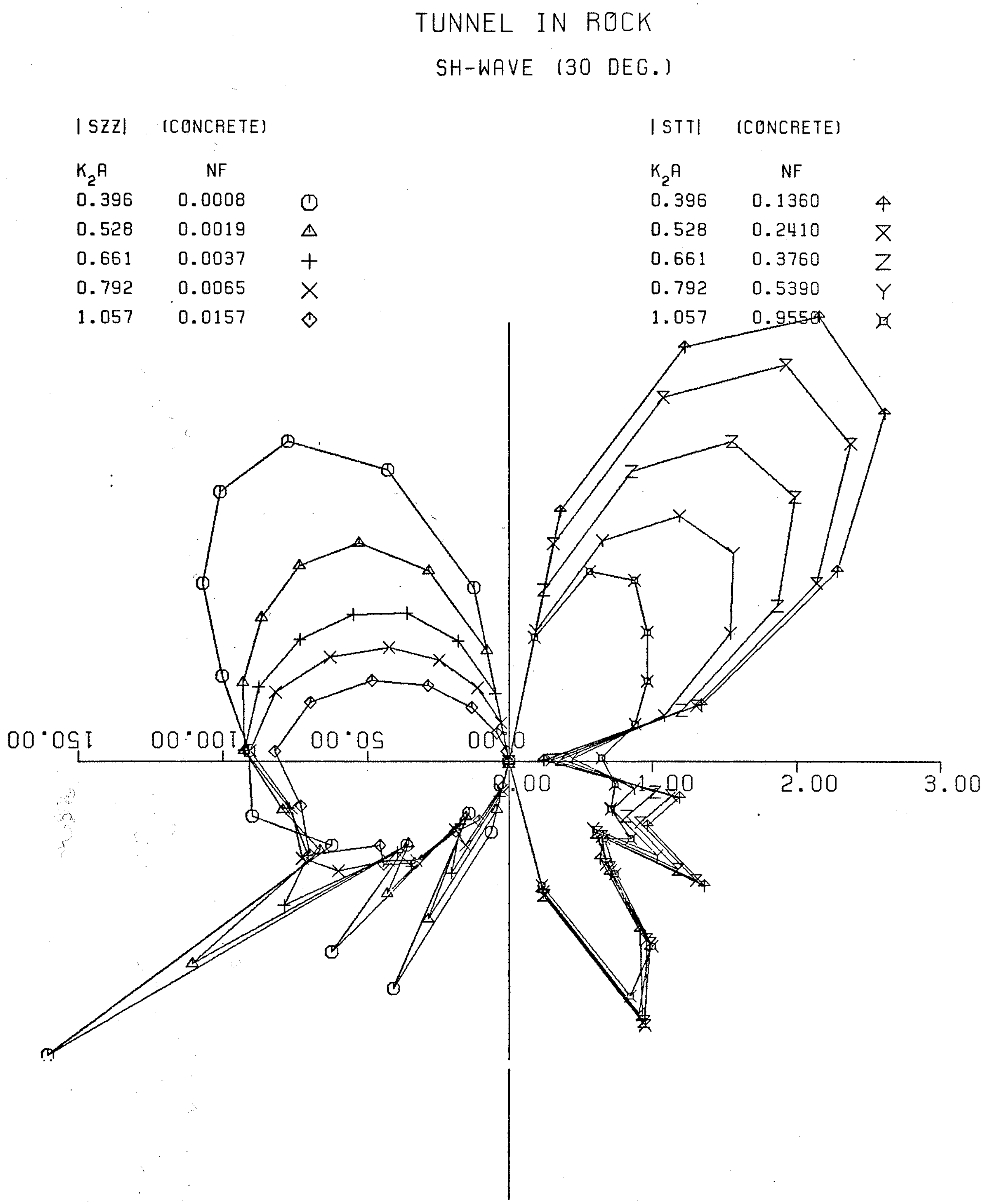

Fig. 98 Normalized axial stress and hoop stress in tunnel wall vs frequency for SH-Wave when the incident angle = 30° (Case II)

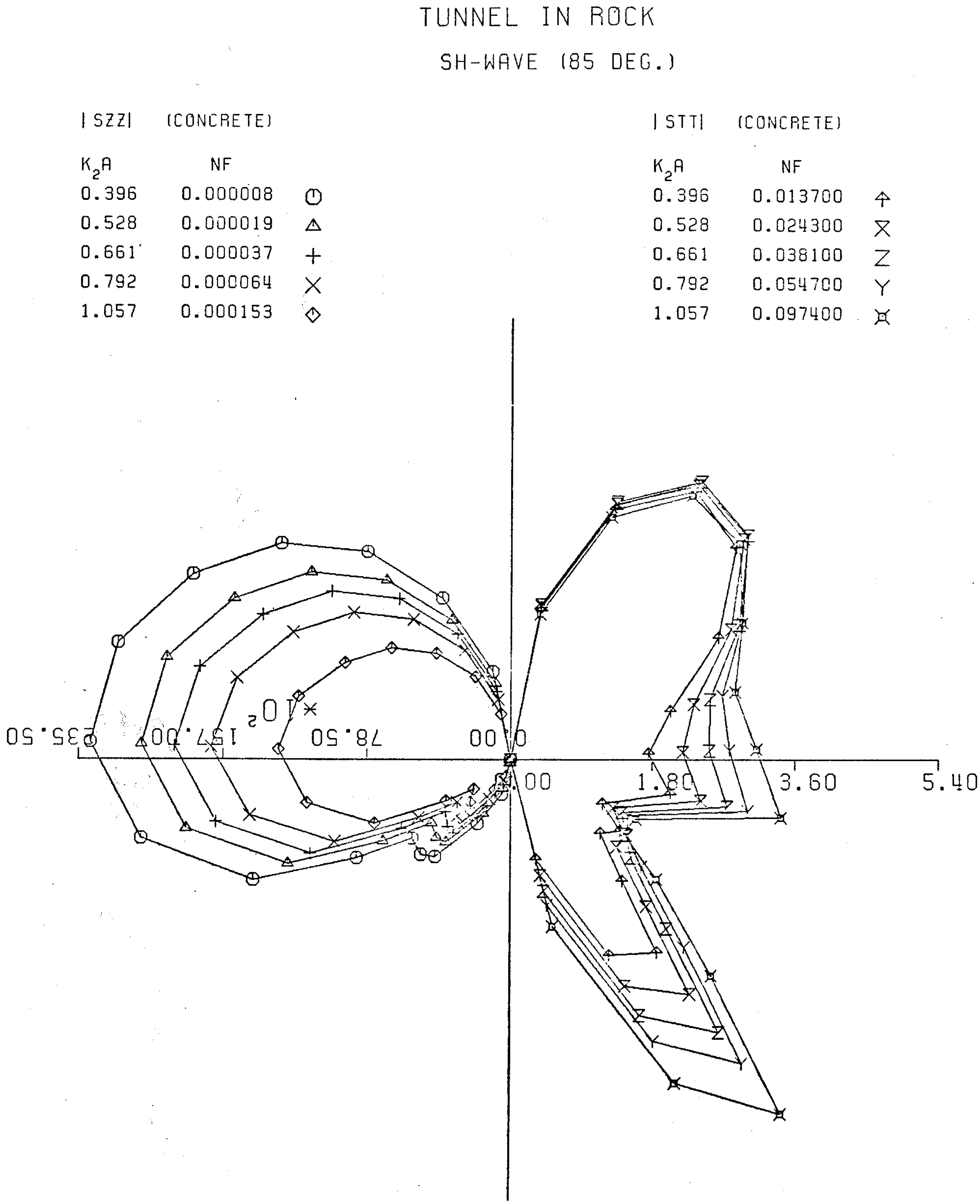

Fig. 99 Normalized axial stress and hoop stress in tunnel wall vs frequency for SH-Wave when the incident angle = 85° (Case II)

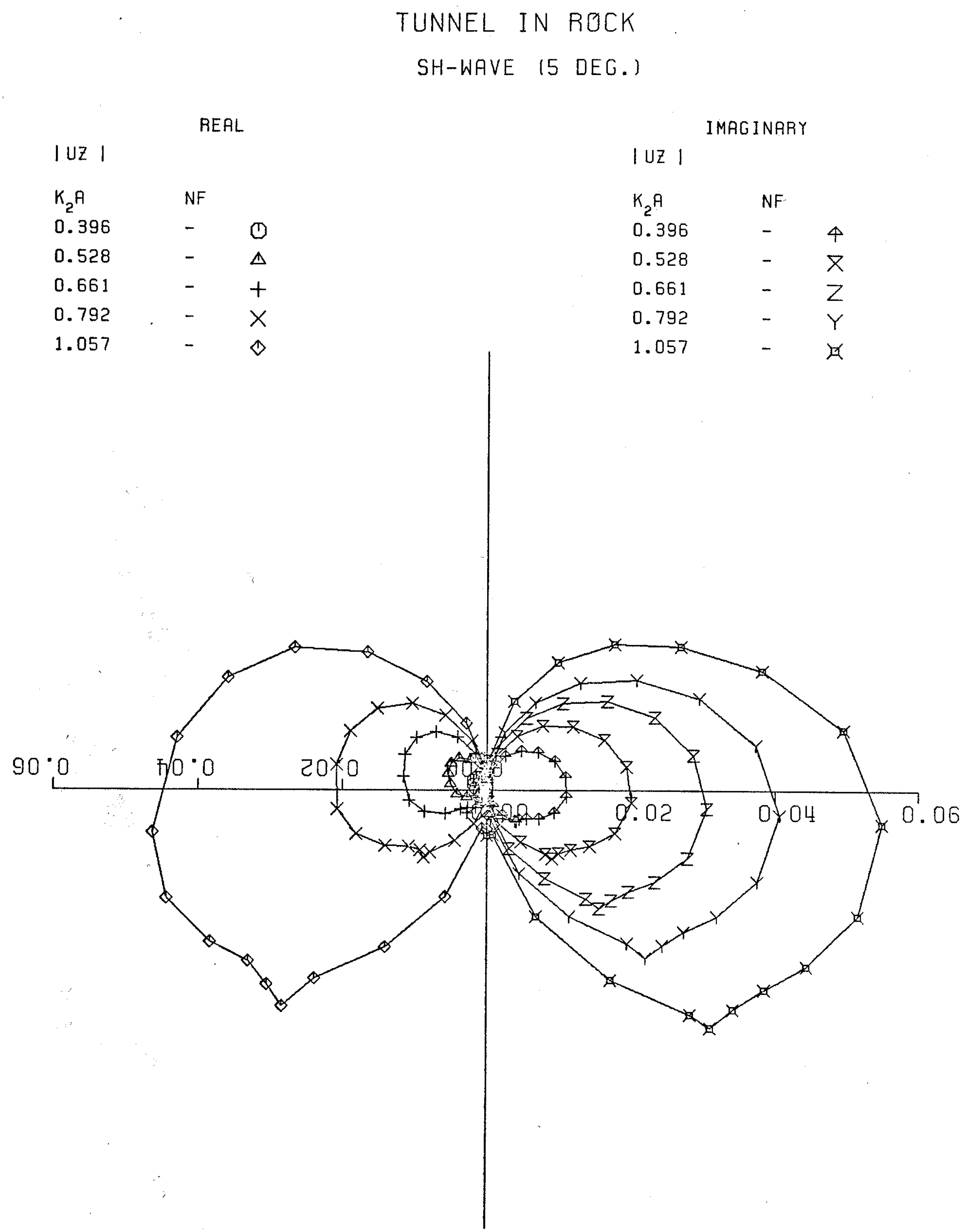

Fig. 100 Real and imaginary part of axial displacement vs frequency for SH-Wave when the incident angle = 5° (Case II)

TUNNEL IN RØCK

SH-WAVE (30 DEG.)

REAL			IMAGINARY		
|UZ|			|UZ|		
K_2A	NF		K_2A	NF	
0.396	-	⌽	0.396	-	⌖
0.528	-	△	0.528	-	⌛
0.661	-	+	0.661	-	Z
0.792	-	×	0.792	-	Y
1.057	-	◇	1.057	-	⌘

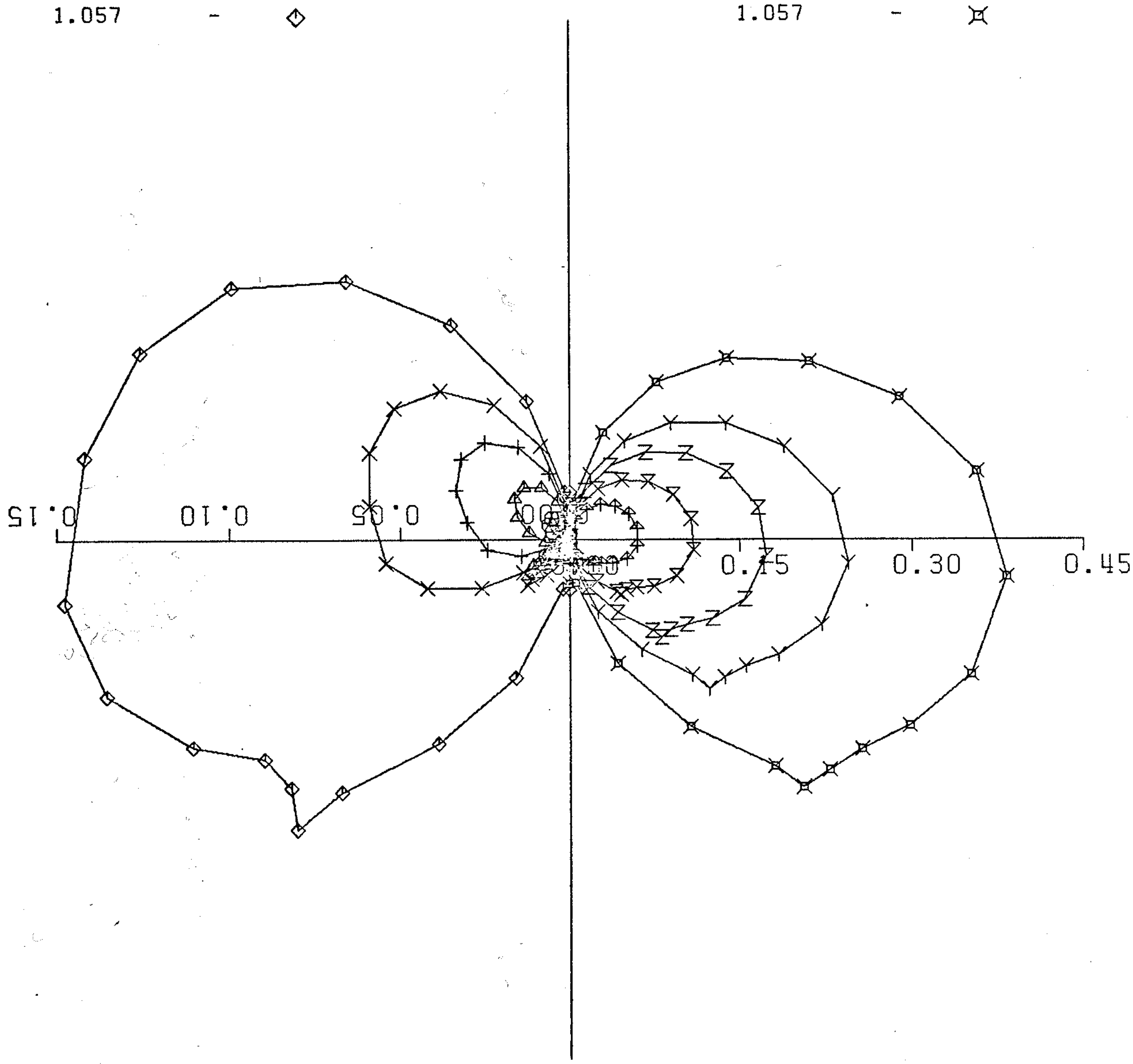

Fig. 101 Real and imaginary part of axial displacement vs frequency for SH-Wave when the incident angle = 30° (Case II)

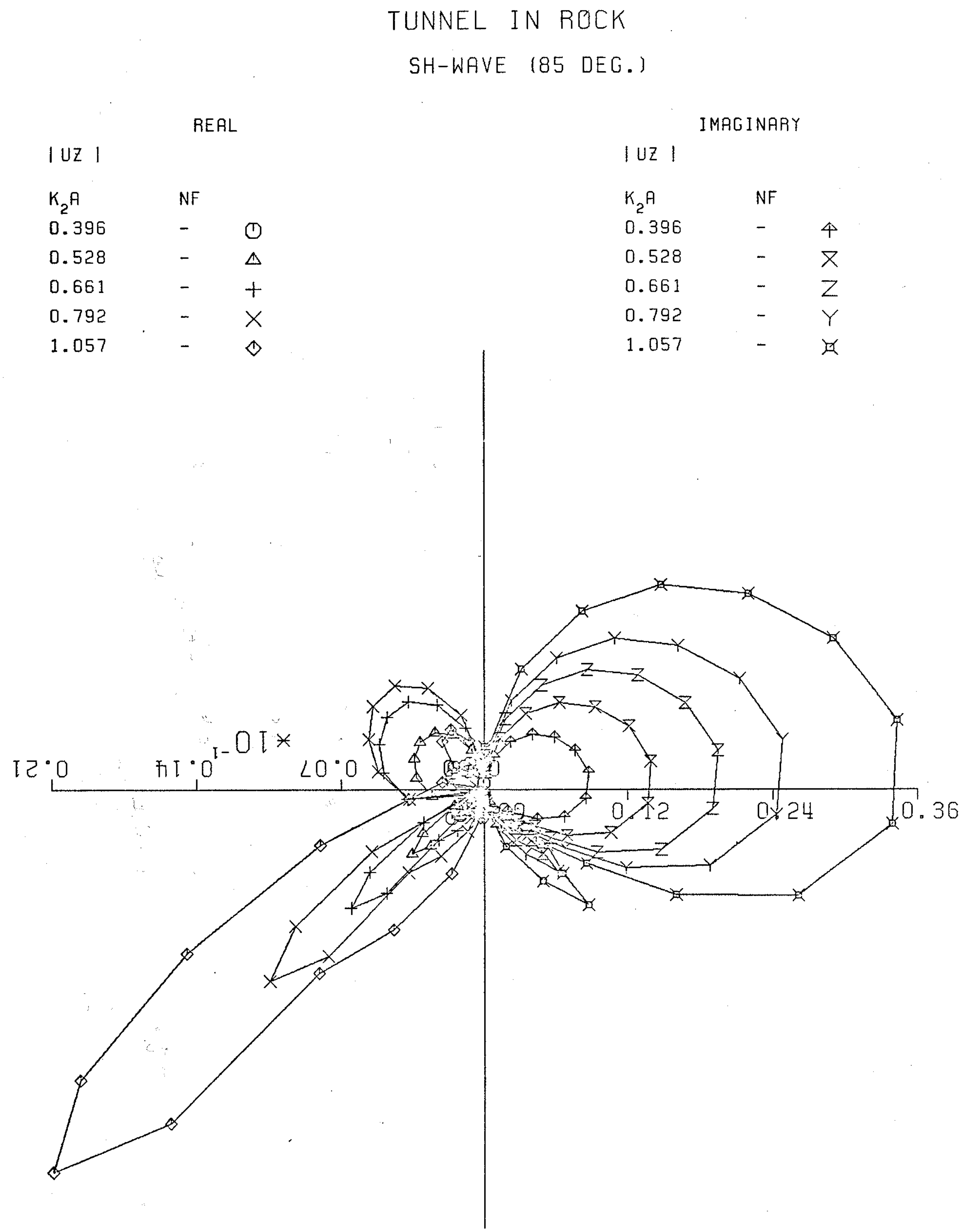

Fig. 102 Real and imaginary part of axial displacement vs frequency for SH-Wave when the incident angle = 85° (Case II)

TUNNEL IN RØCK

SH-WAVE (5 DEG.)

REAL

| SRZ | (SØIL)

K_2A	NF	
0.396	0.00500	⦶
0.528	0.01160	△
0.661	0.02230	+
0.792	0.03720	×
1.057	0.08200	◇

IMAGINARY

| SRZ | (SØIL)

K_2A	NF	
0.396	0.01370	✢
0.528	0.02430	⧖
0.661	0.03810	Z
0.792	0.05460	Y
1.057	0.09720	⌑

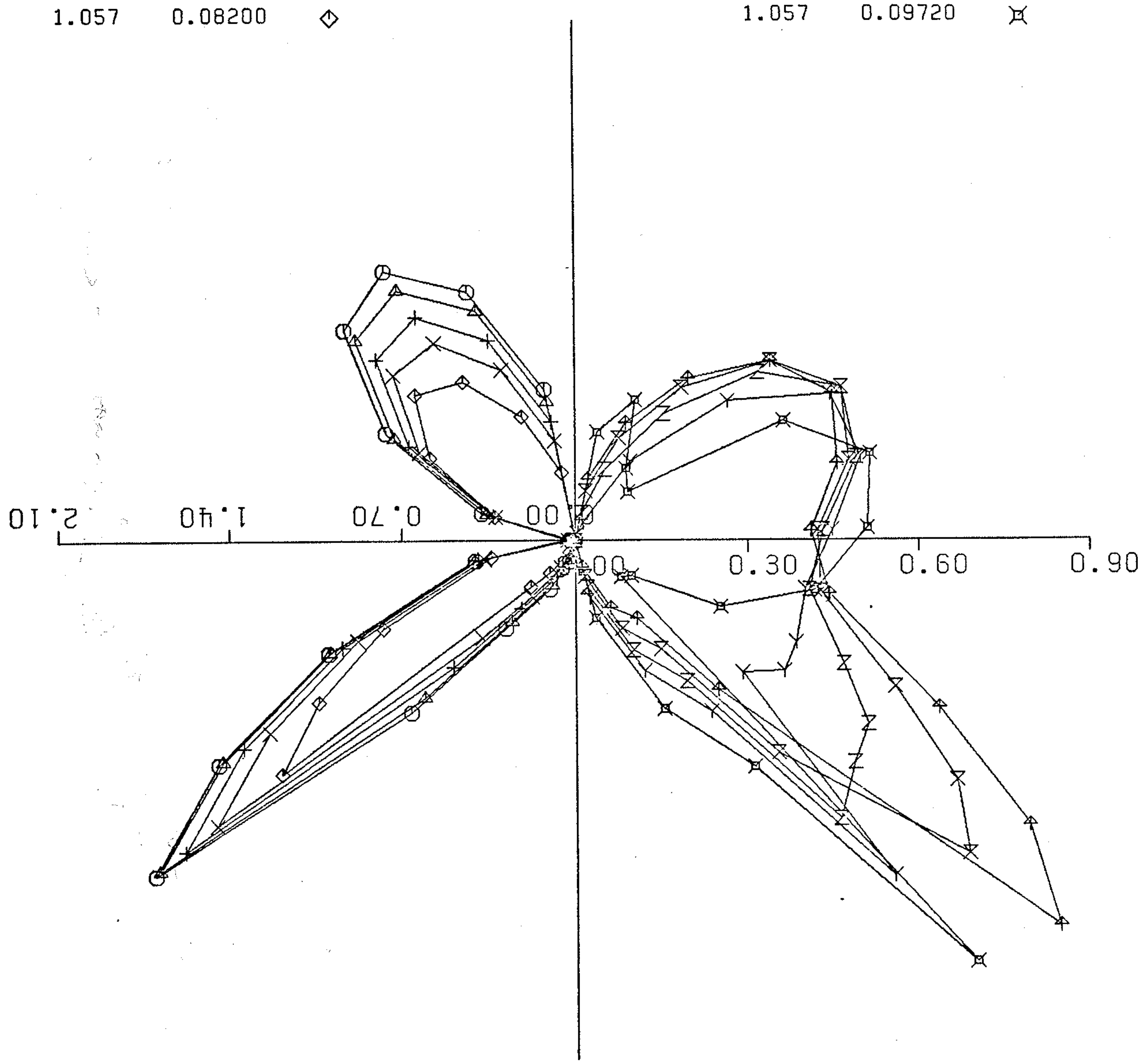

Fig. 103 Normalized real and imaginary part of shear stress SRZ in soil vs frequency for SH-Wave when the incident angle = 5° (Case II)

TUNNEL IN ROCK

SH-WAVE (30 DEG.)

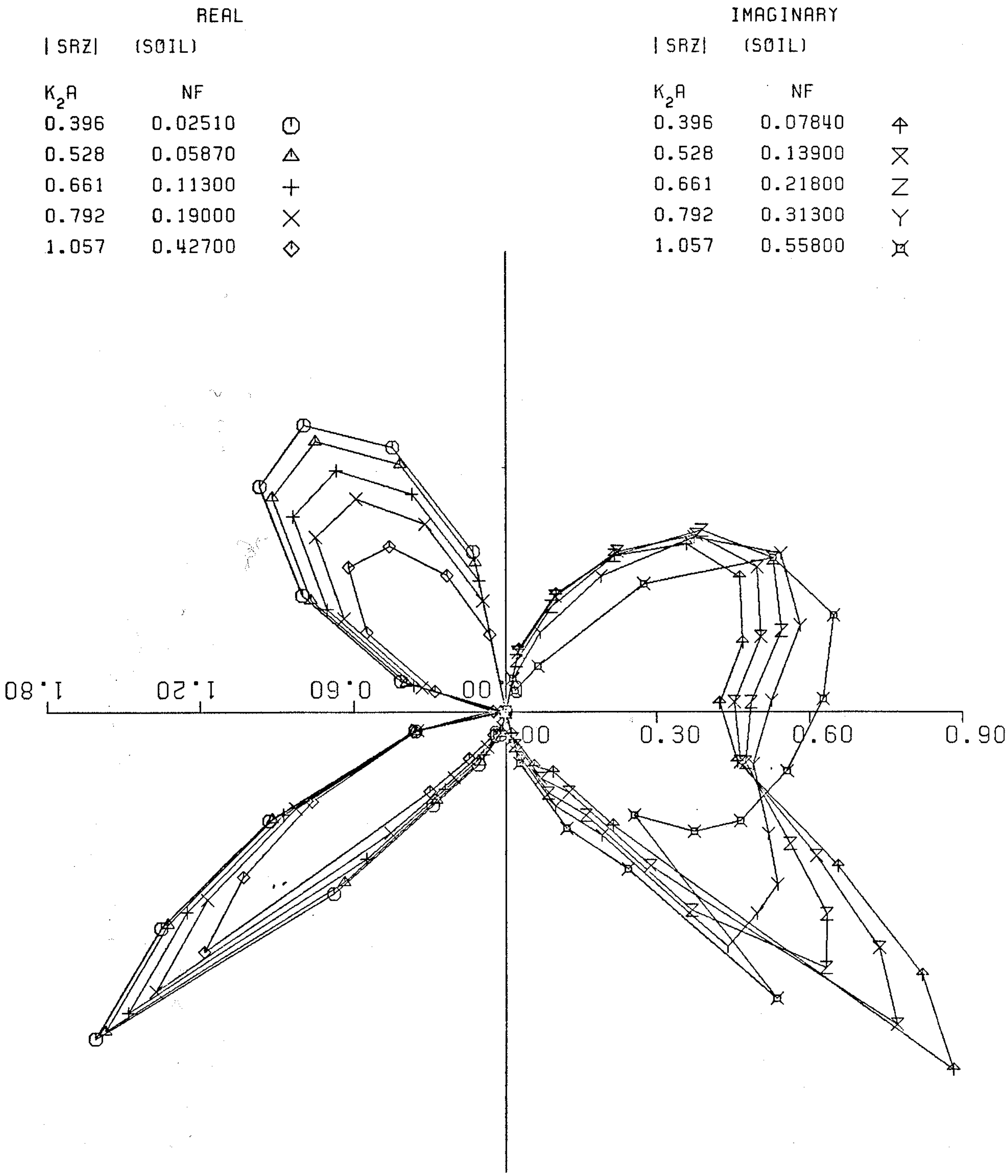

Fig. 104 Normalized real and imaginary part of shear stress SRZ in soil vs frequency for SH-Wave when the incident angle = 30° (Case II)

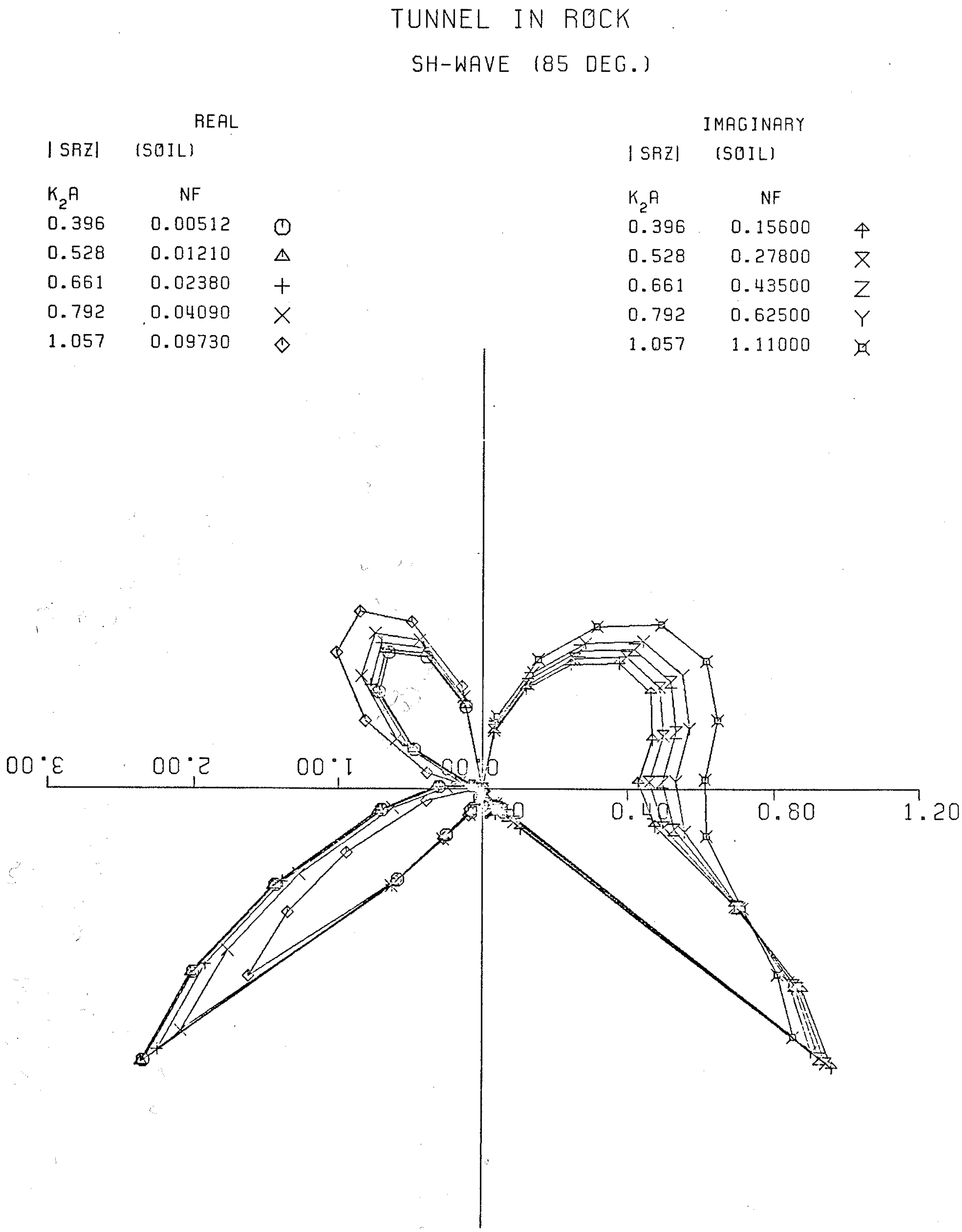

Fig. 105 Normalized real and imaginary part of shear stress SRZ in soil vs frequency for SH-Wave when the incident angle = 85° (Case II)

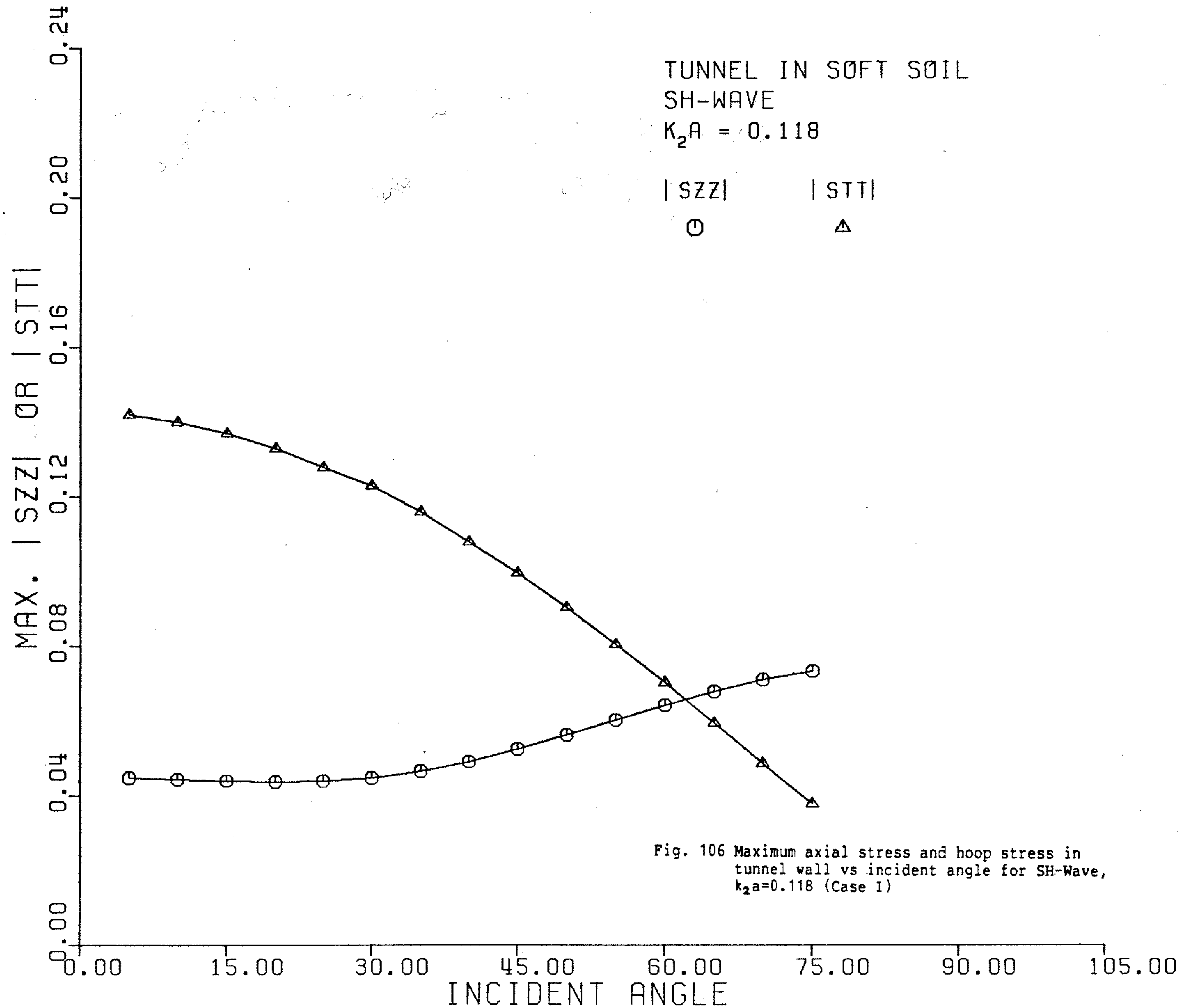

Fig. 106 Maximum axial stress and hoop stress in tunnel wall vs incident angle for SH-Wave, $k_2a=0.118$ (Case I)

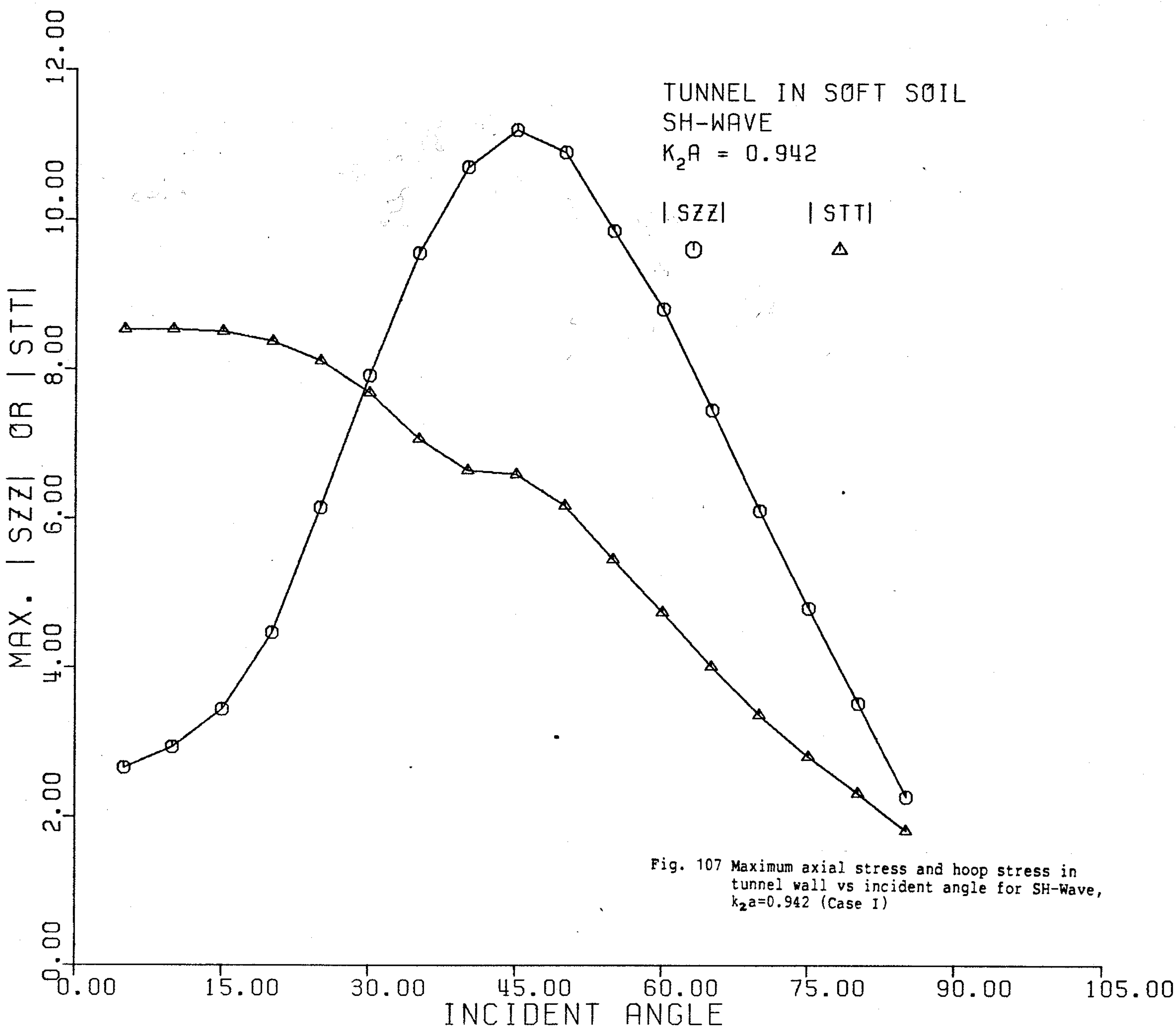

Fig. 107 Maximum axial stress and hoop stress in tunnel wall vs incident angle for SH-Wave, k_2a=0.942 (Case I)

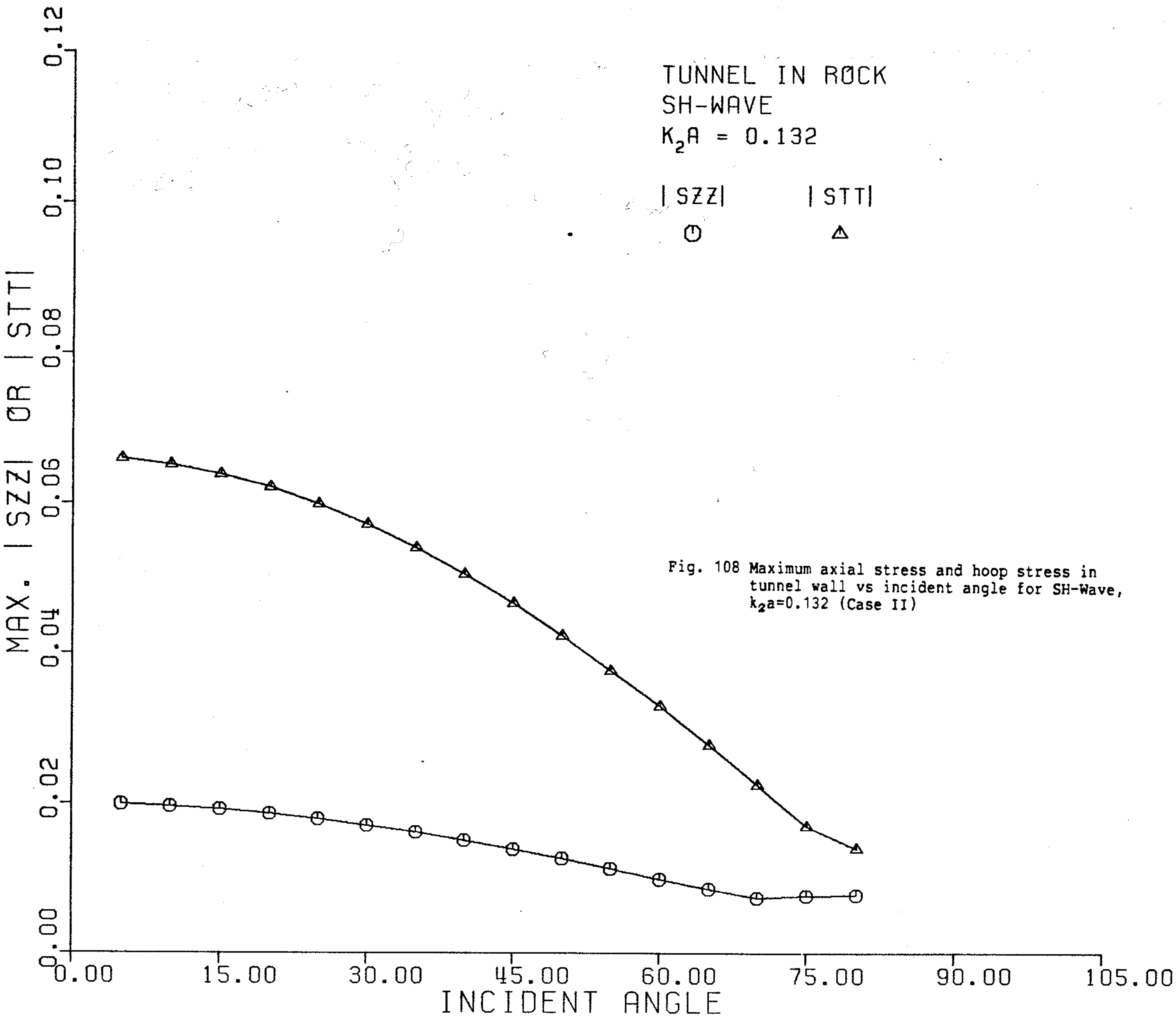

Fig. 108 Maximum axial stress and hoop stress in tunnel wall vs incident angle for SH-Wave, $k_2a=0.132$ (Case II)

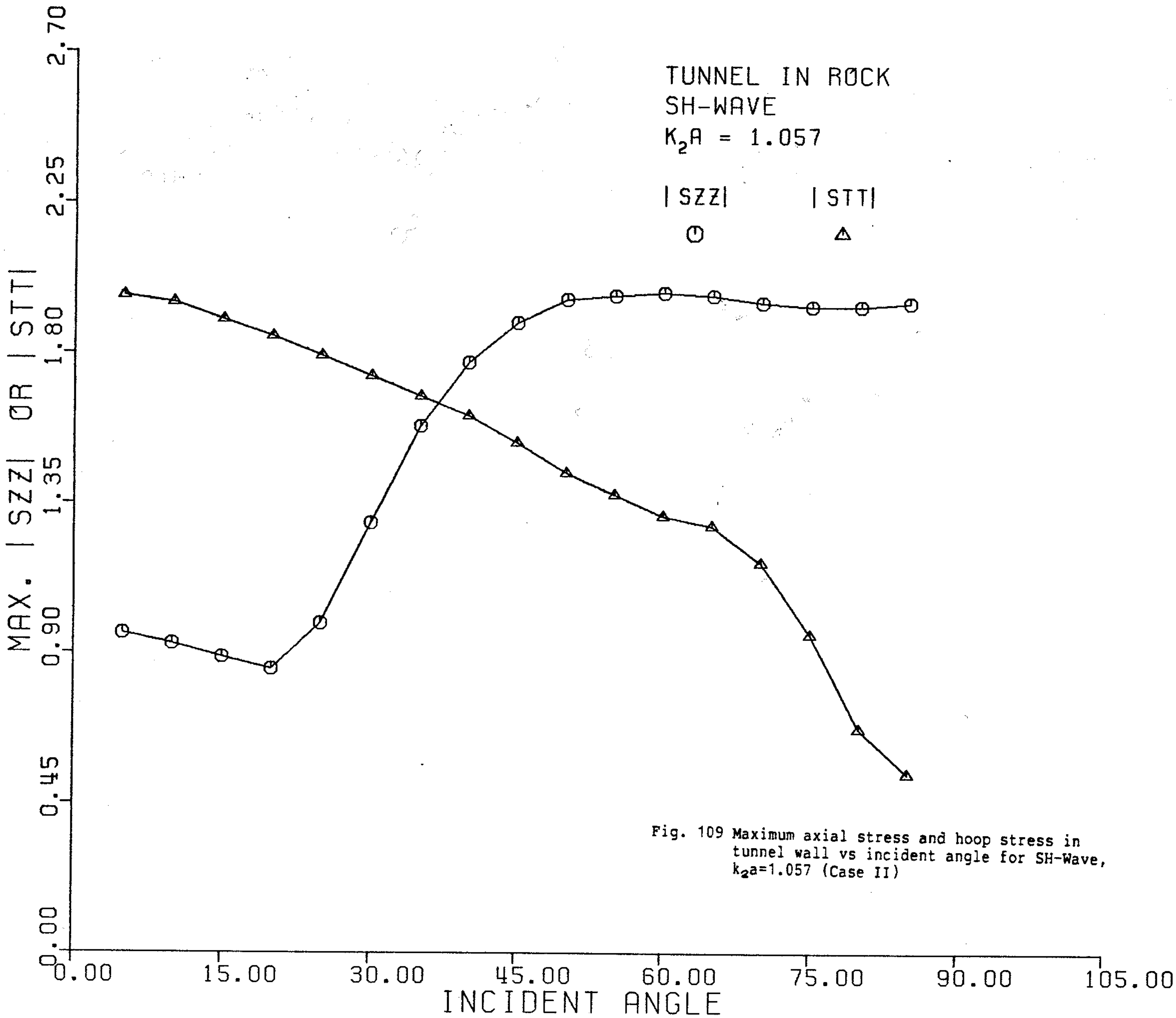

Fig. 109 Maximum axial stress and hoop stress in tunnel wall vs incident angle for SH-Wave, $k_2a=1.057$ (Case II)

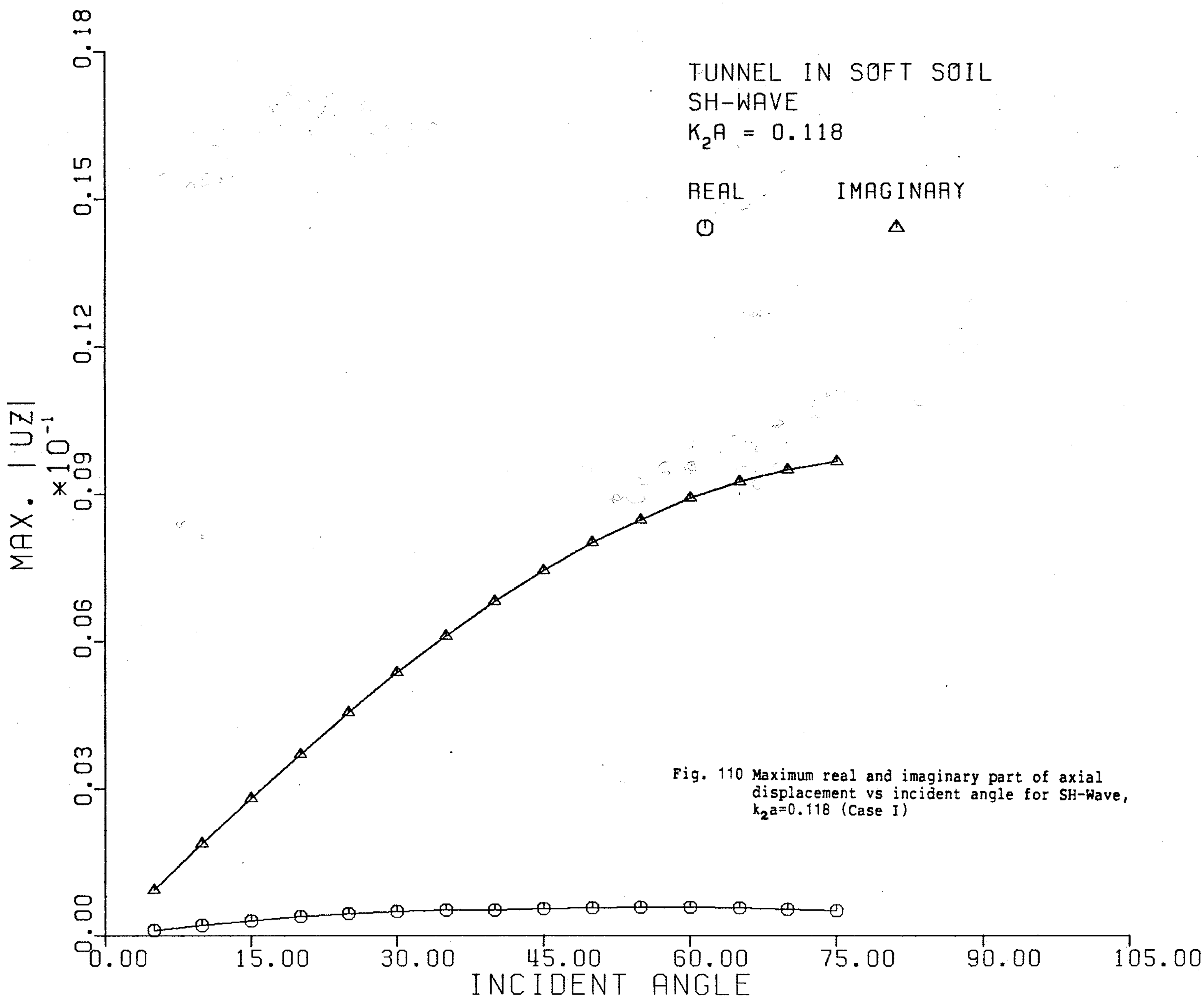

Fig. 110 Maximum real and imaginary part of axial displacement vs incident angle for SH-Wave, $k_2a=0.118$ (Case I)

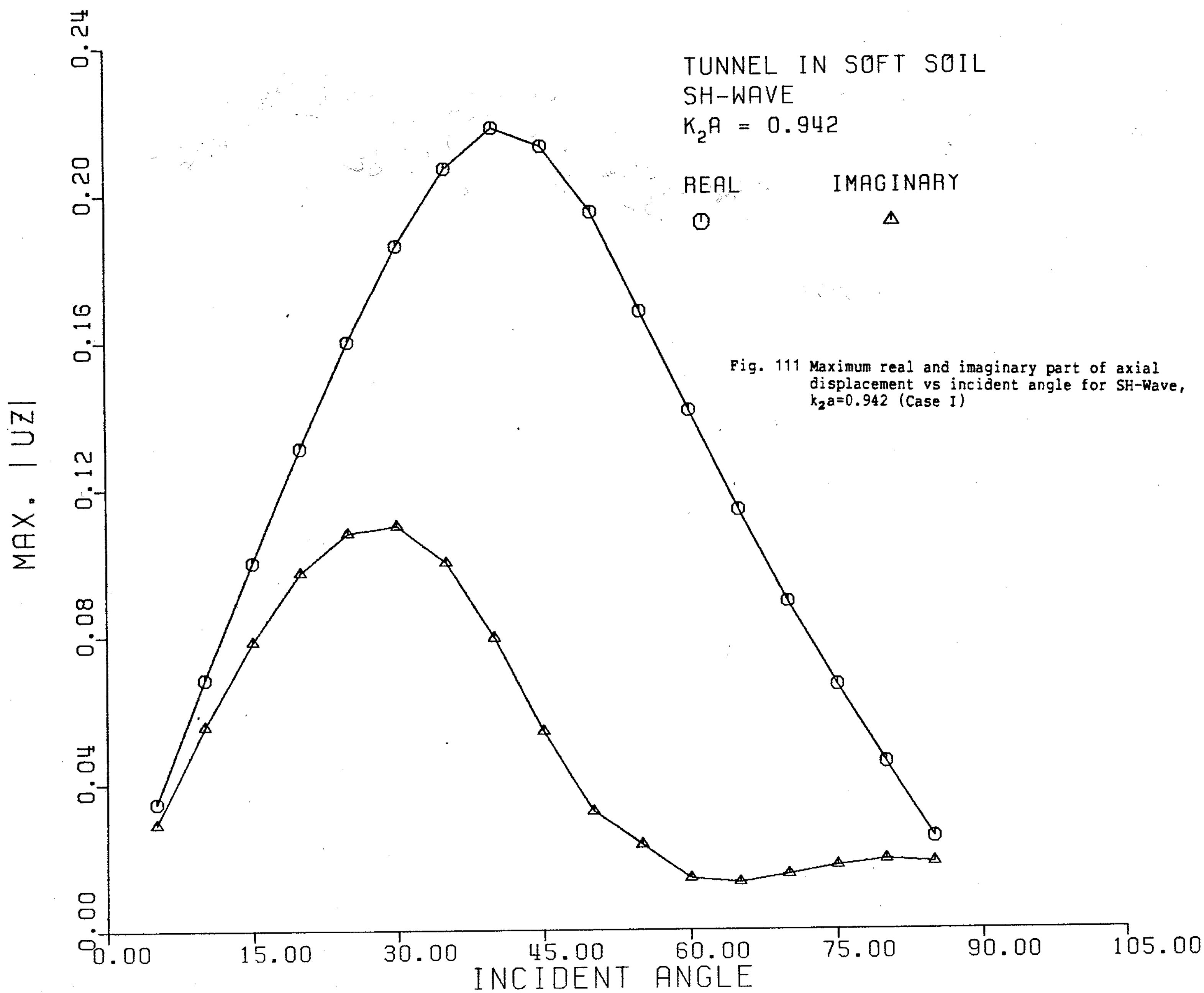

Fig. 111 Maximum real and imaginary part of axial displacement vs incident angle for SH-Wave, $k_2a=0.942$ (Case I)

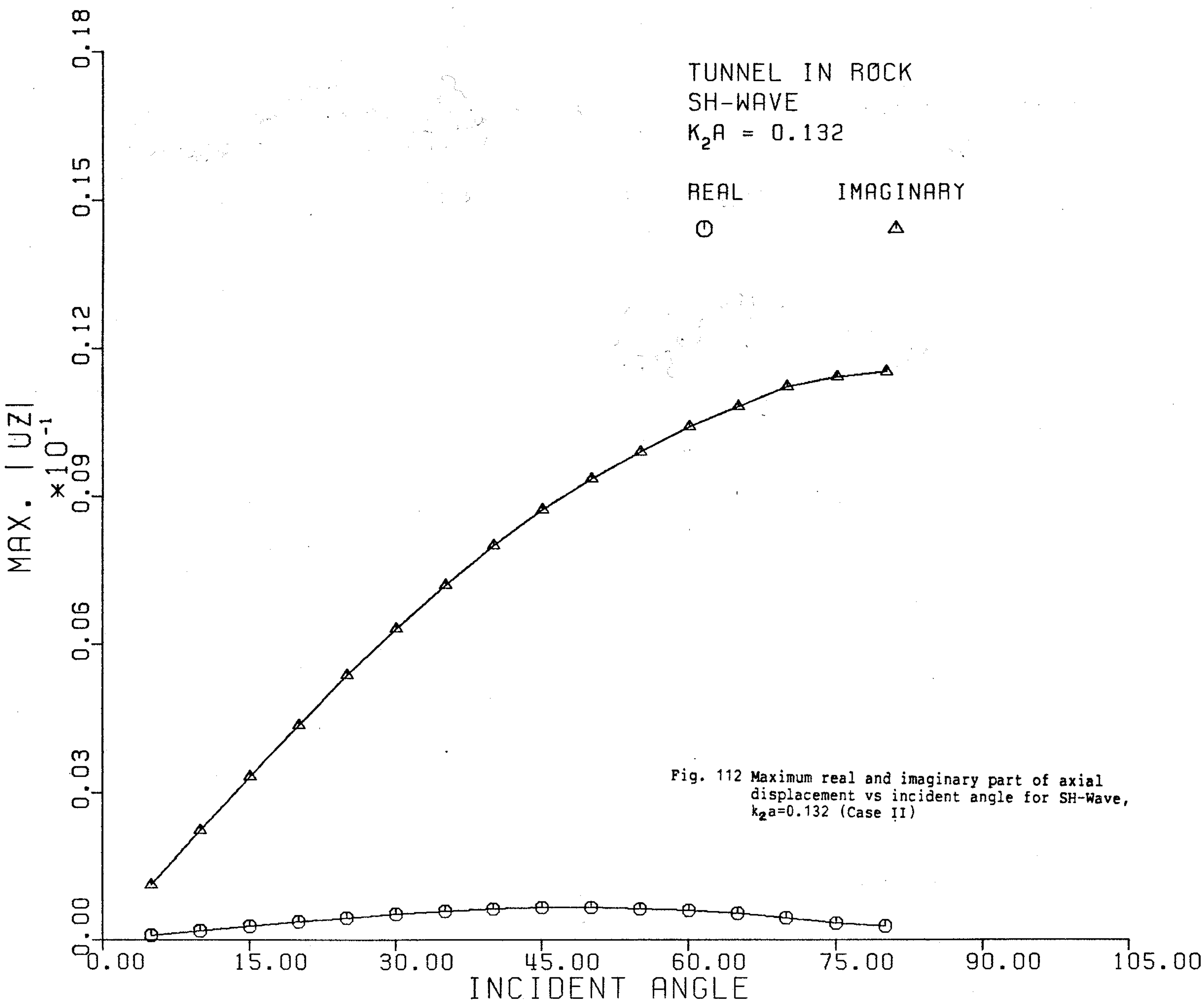

Fig. 112 Maximum real and imaginary part of axial displacement vs incident angle for SH-Wave, $k_2a=0.132$ (Case II)

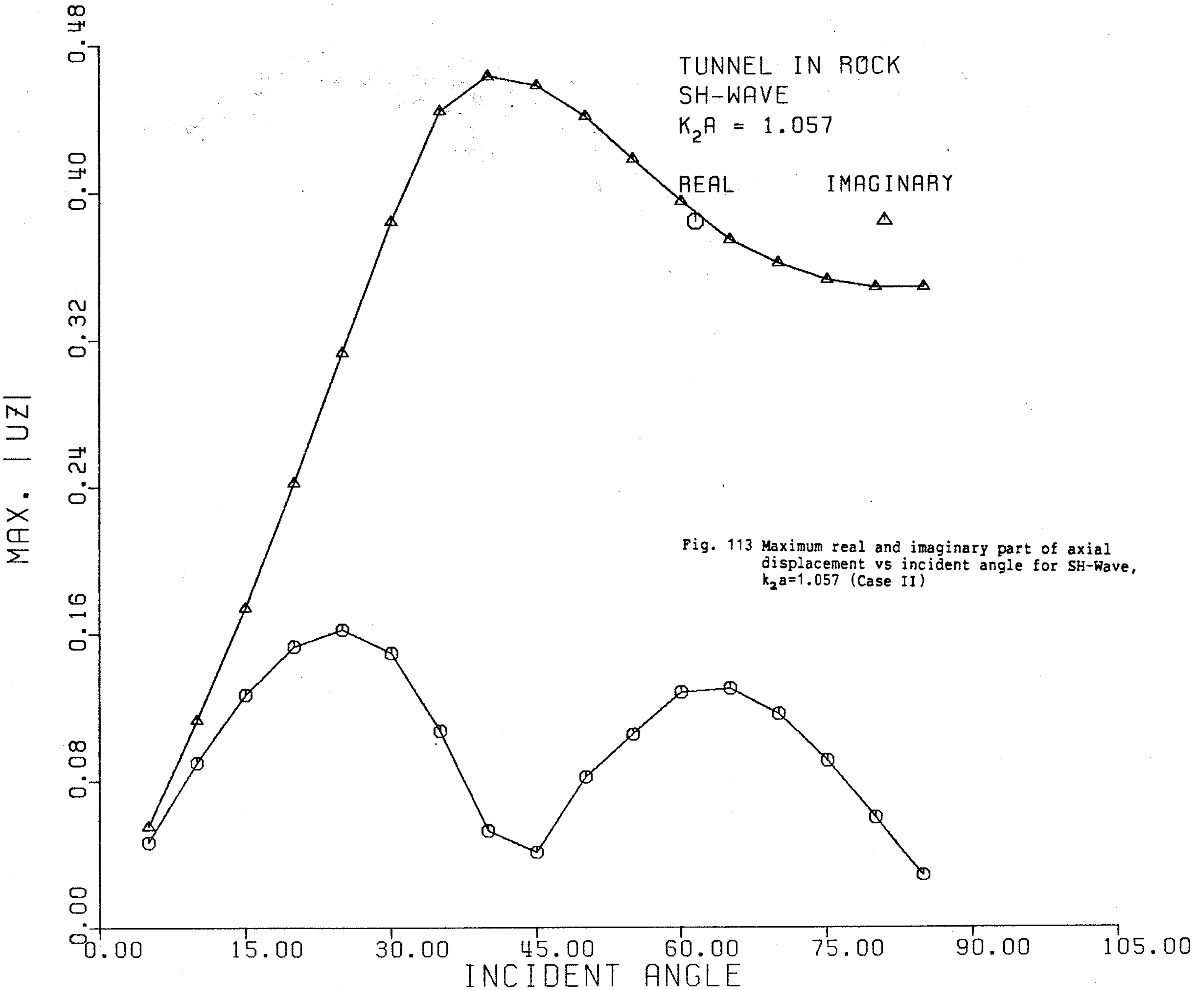

Fig. 113 Maximum real and imaginary part of axial displacement vs incident angle for SH-Wave, $k_2a=1.057$ (Case II)

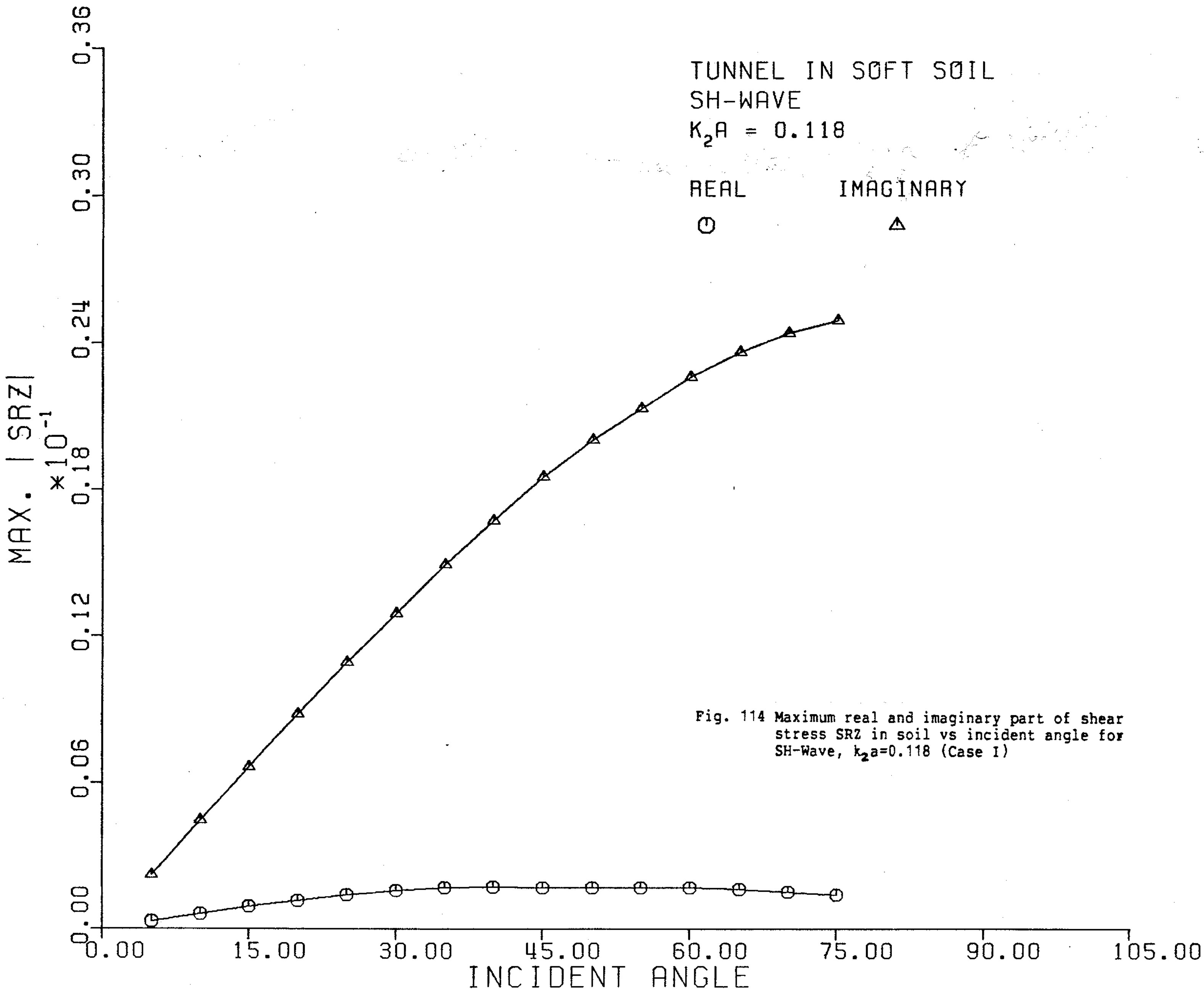

Fig. 114 Maximum real and imaginary part of shear stress SRZ in soil vs incident angle for SH-Wave, k_2a=0.118 (Case I)

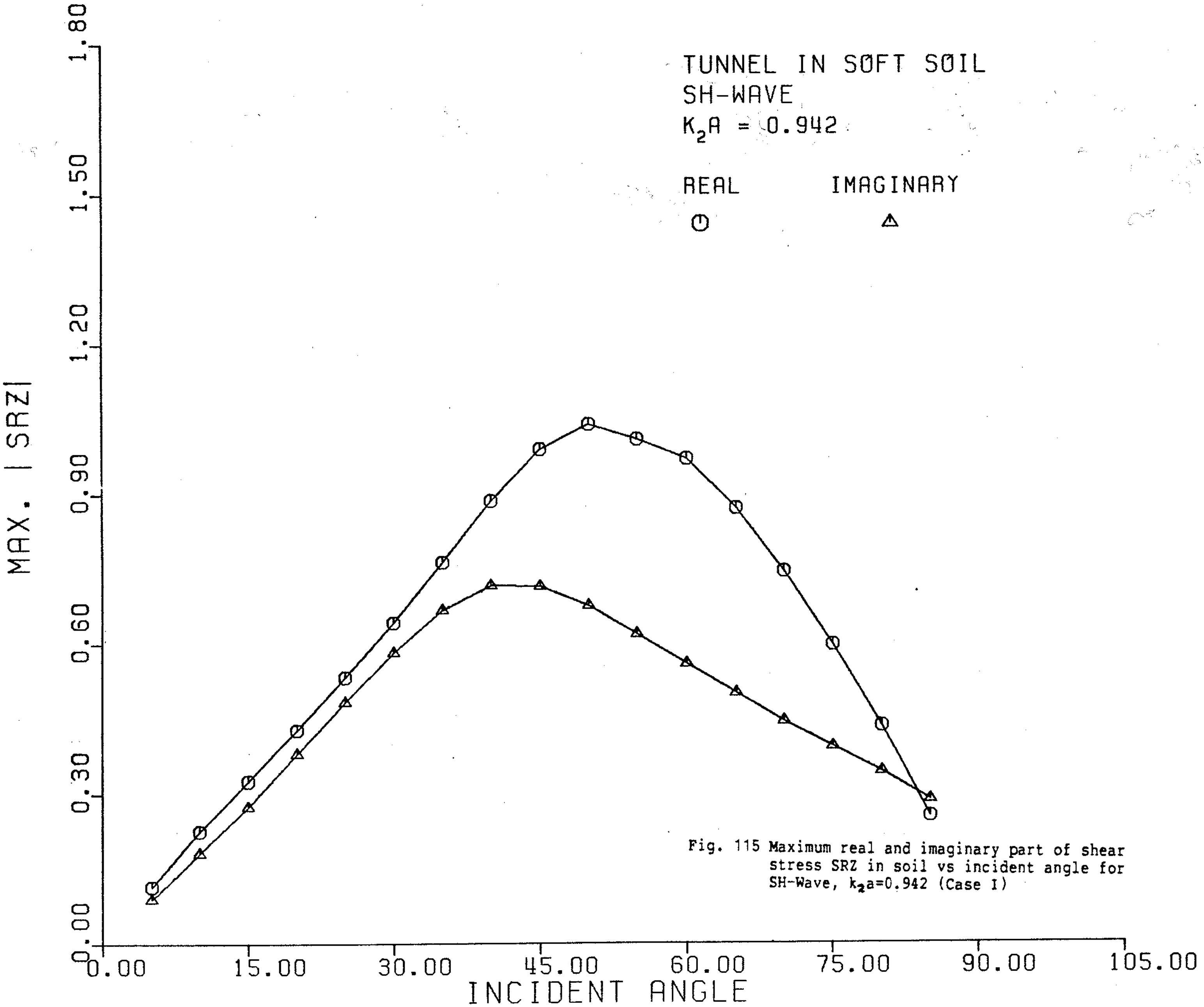

Fig. 115 Maximum real and imaginary part of shear stress SRZ in soil vs incident angle for SH-Wave, k_2a=0.942 (Case I)

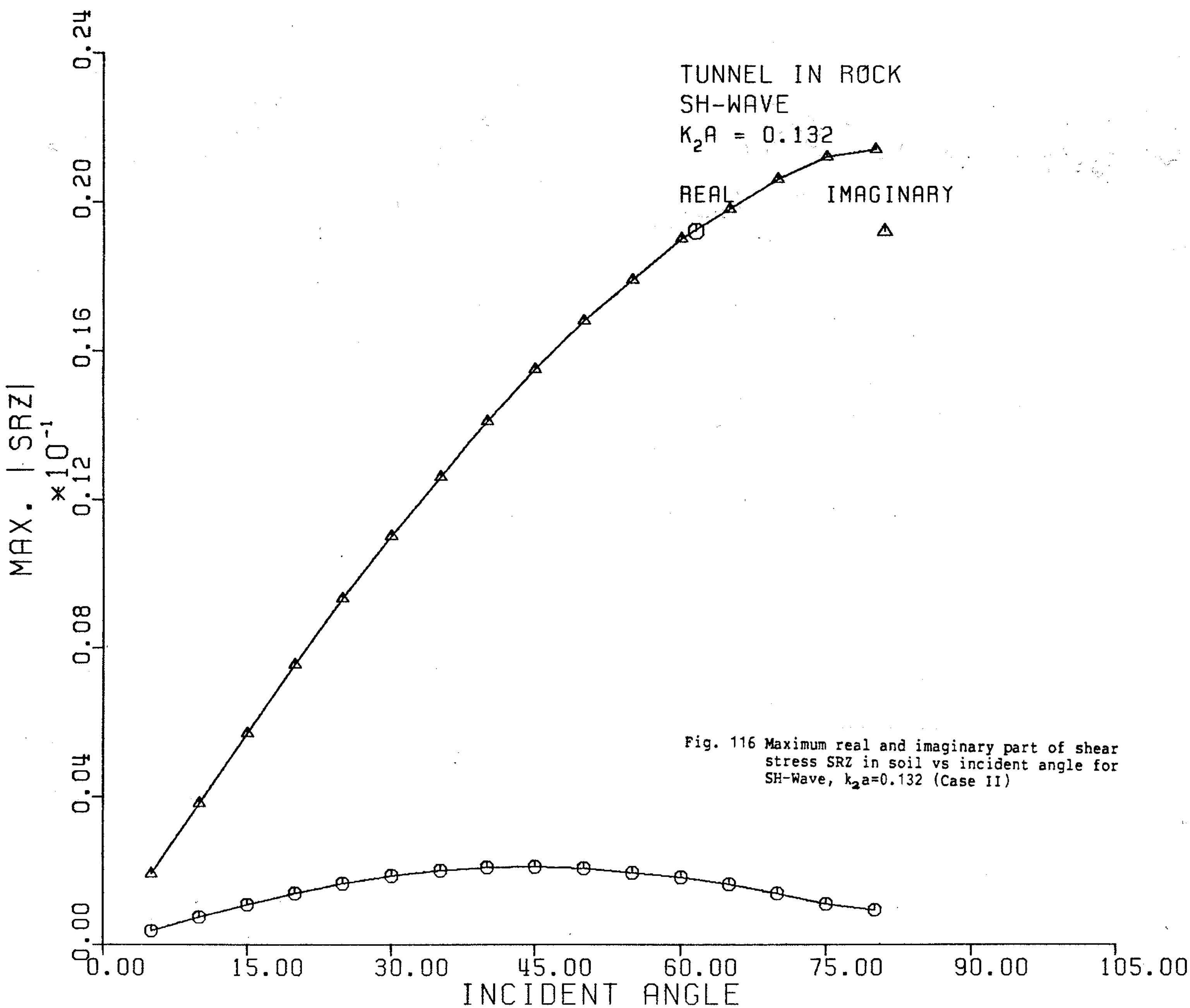

Fig. 116 Maximum real and imaginary part of shear stress SRZ in soil vs incident angle for SH-Wave, $k_2a=0.132$ (Case II)

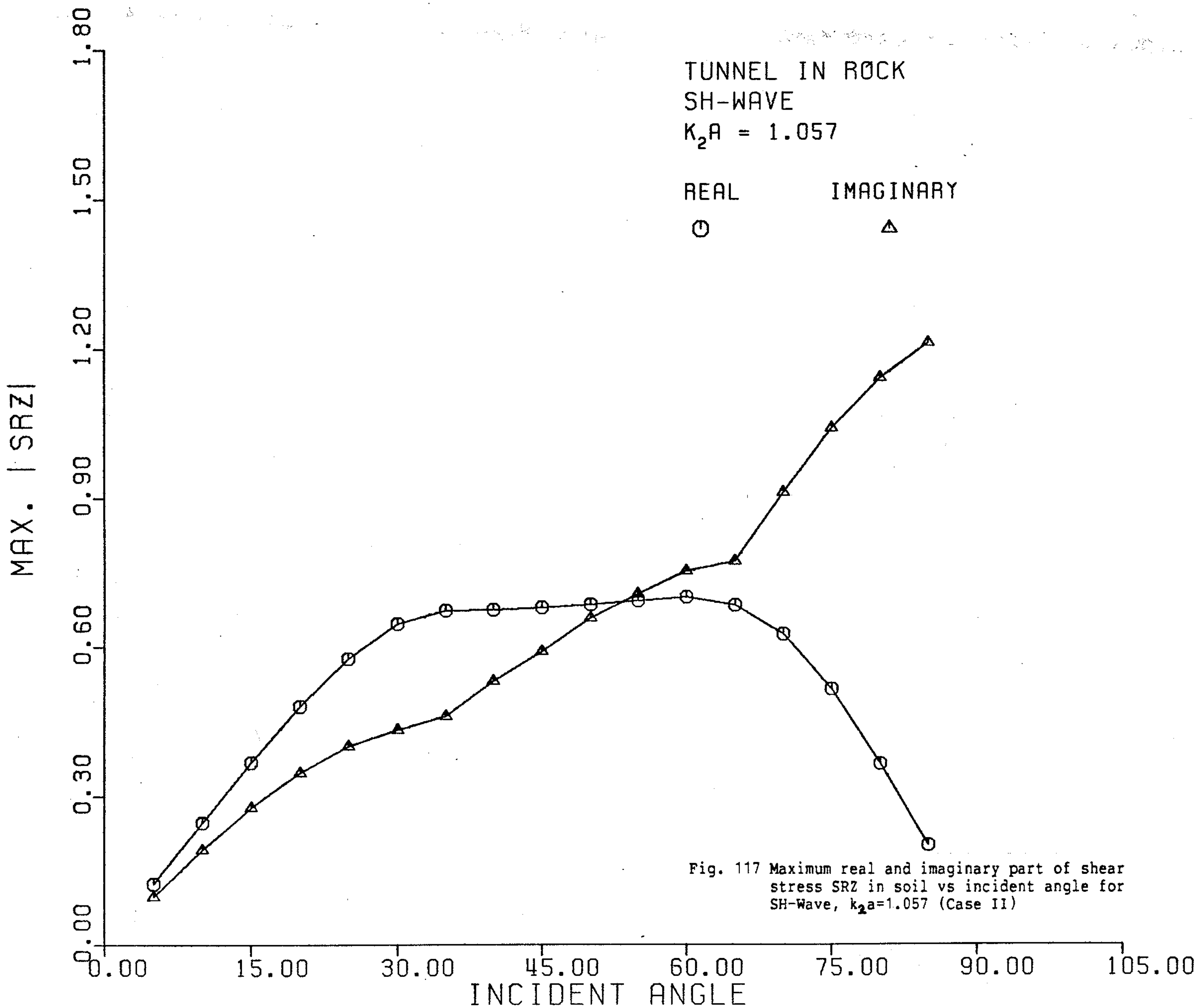

Fig. 117 Maximum real and imaginary part of shear stress SRZ in soil vs incident angle for SH-Wave, k_2a=1.057 (Case II)

SH-WAVE (5 DEG.)
SZZ (CONCRETE)

TUNNEL IN ROCK			TUNNEL IN SOFT SOIL		
$\frac{WA}{2\pi}$ (M/SEC)		NF	$\frac{WA}{2\pi}$ (M/SEC)		NF
89.50	+	0.00252	89.50	O	1.39000
134.33	×	0.00864	134.33	△	6.19000

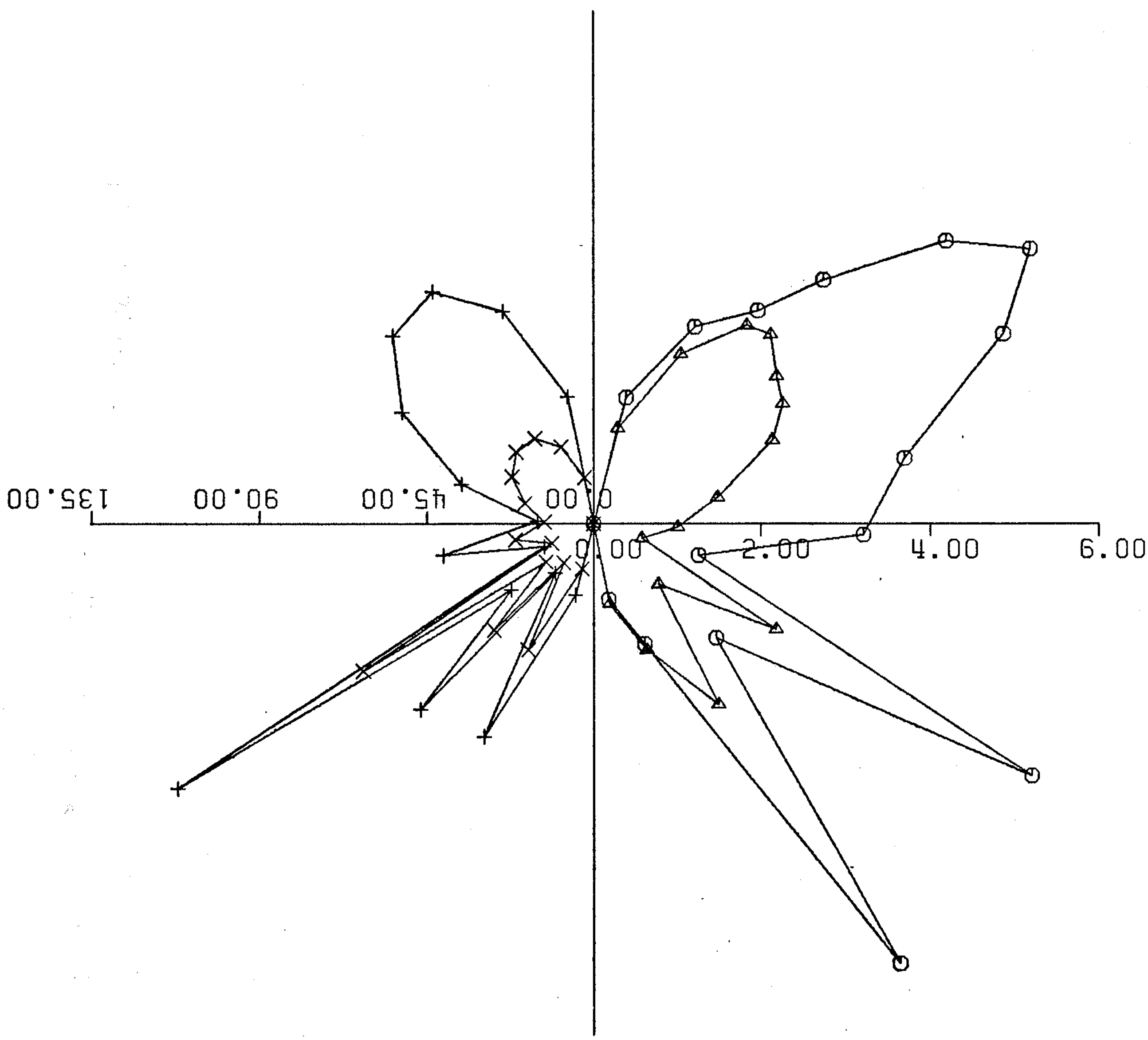

Fig. 118 Comparison between Case I and Case II for normalized axial stress in tunnel wall for SH-Wave, incident angle = 5°

SH-WAVE (85 DEG.)
SZZ (CONCRETE)

TUNNEL IN ROCK			TUNNEL IN SOFT SOIL		
$\frac{WA}{2\pi}$ (M/SEC)		NF	$\frac{WA}{2\pi}$ (M/SEC)		NF
89.50	+	0.00002	89.50	O	0.00777
134.33	×	0.00006	134.33	△	0.02630

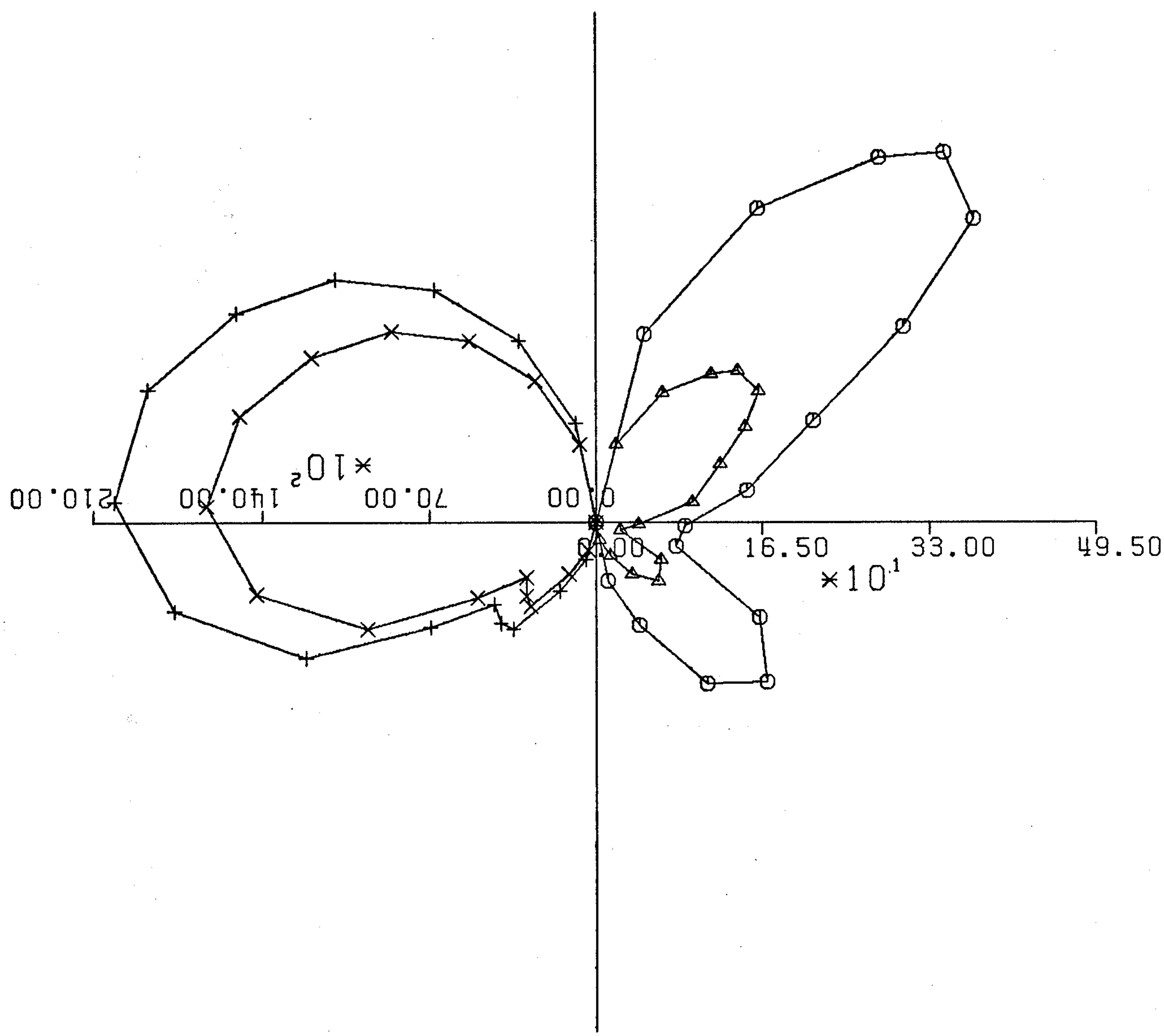

Fig. 119 Comparison between Case I and Case II for normalized axial stress in tunnel wall for SH-Wave, incident angle = 85°

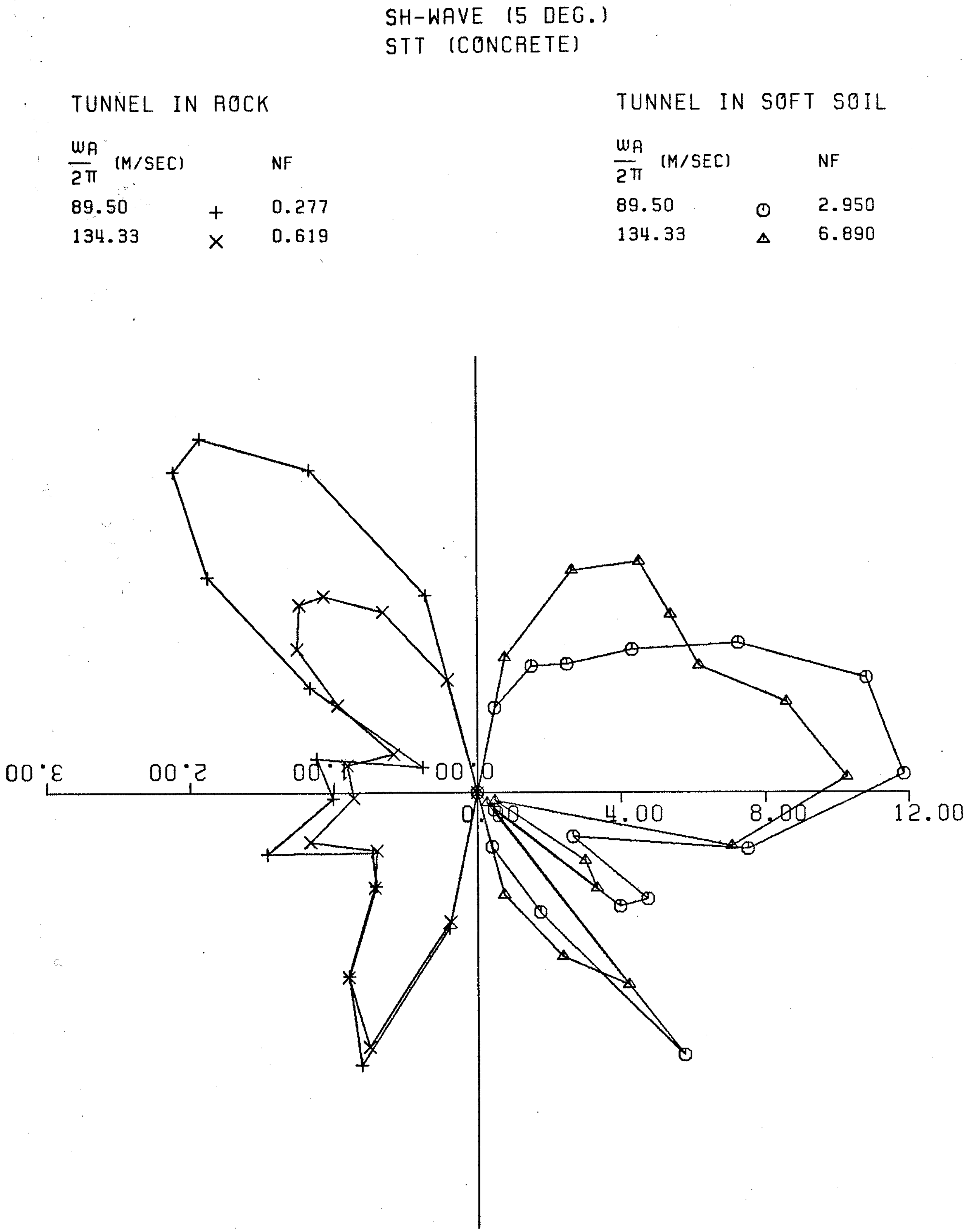

Fig. 120 Comparison between Case I and Case II for normalized hoop stress in tunnel wall for SH-Wave, incident angle = 5°

SH-WAVE (85 DEG.)
STT (CONCRETE)

TUNNEL IN ROCK			TUNNEL IN SOFT SOIL		
$\frac{\omega a}{2\pi}$ (M/SEC)		NF	$\frac{\omega a}{2\pi}$ (M/SEC)		NF
89.50	+	0.024	89.50	⊙	0.308
134.33	×	0.055	134.33	△	0.693

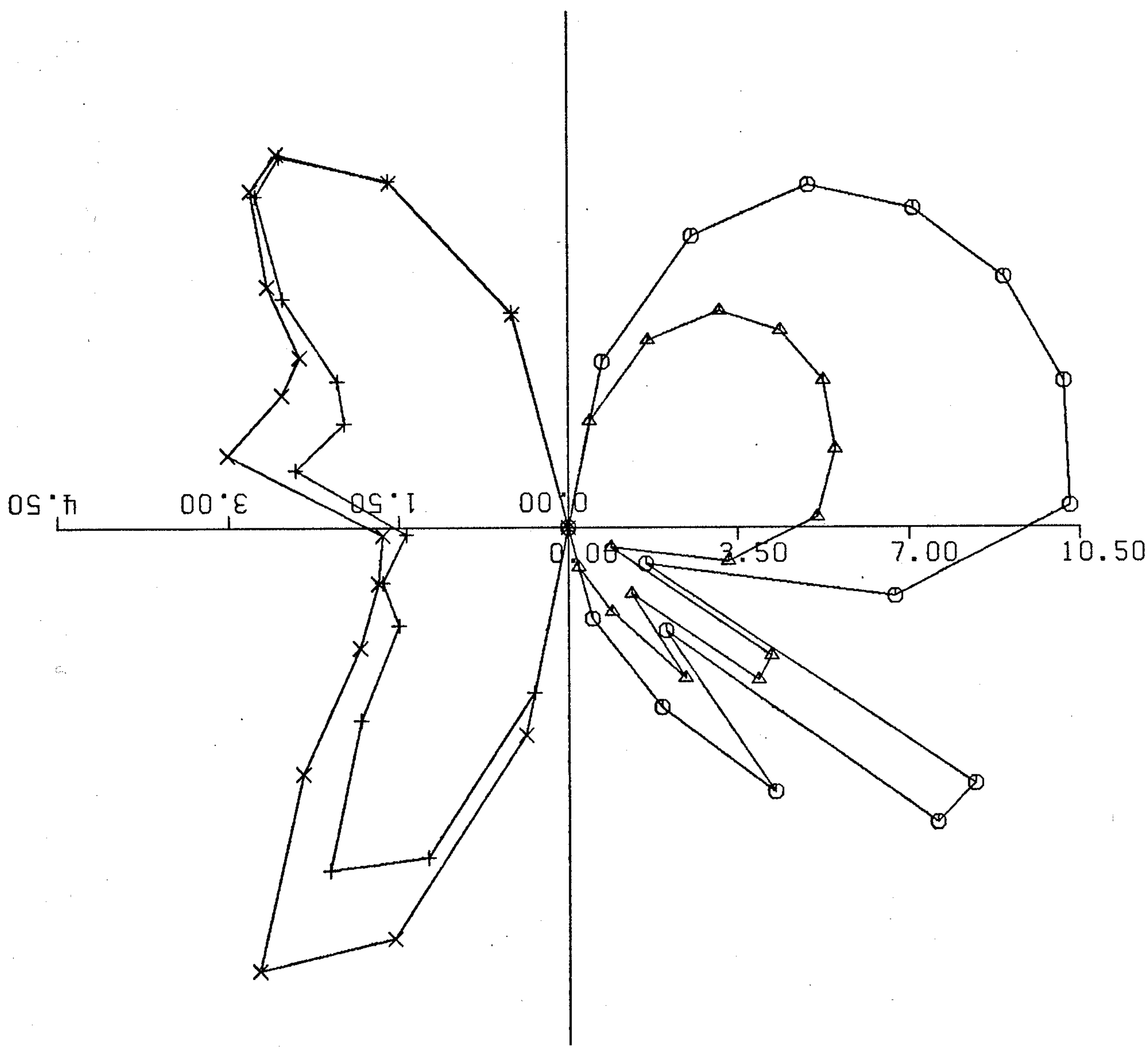

Fig. 121 Comparison between Case I and Case II for normalized hoop stress in tunnel wall for SH-Wave, incident angle = 85°

SH-WAVE (5 DEG.)
|UZ| (REAL)

TUNNEL IN ROCK			TUNNEL IN SOFT SOIL		
$\frac{WA}{2\pi}$ (M/SEC)		NF	$\frac{WA}{2\pi}$ (M/SEC)		NF
89.50	+	--	89.50	O	--
134.33	×	--	134.33	△	--

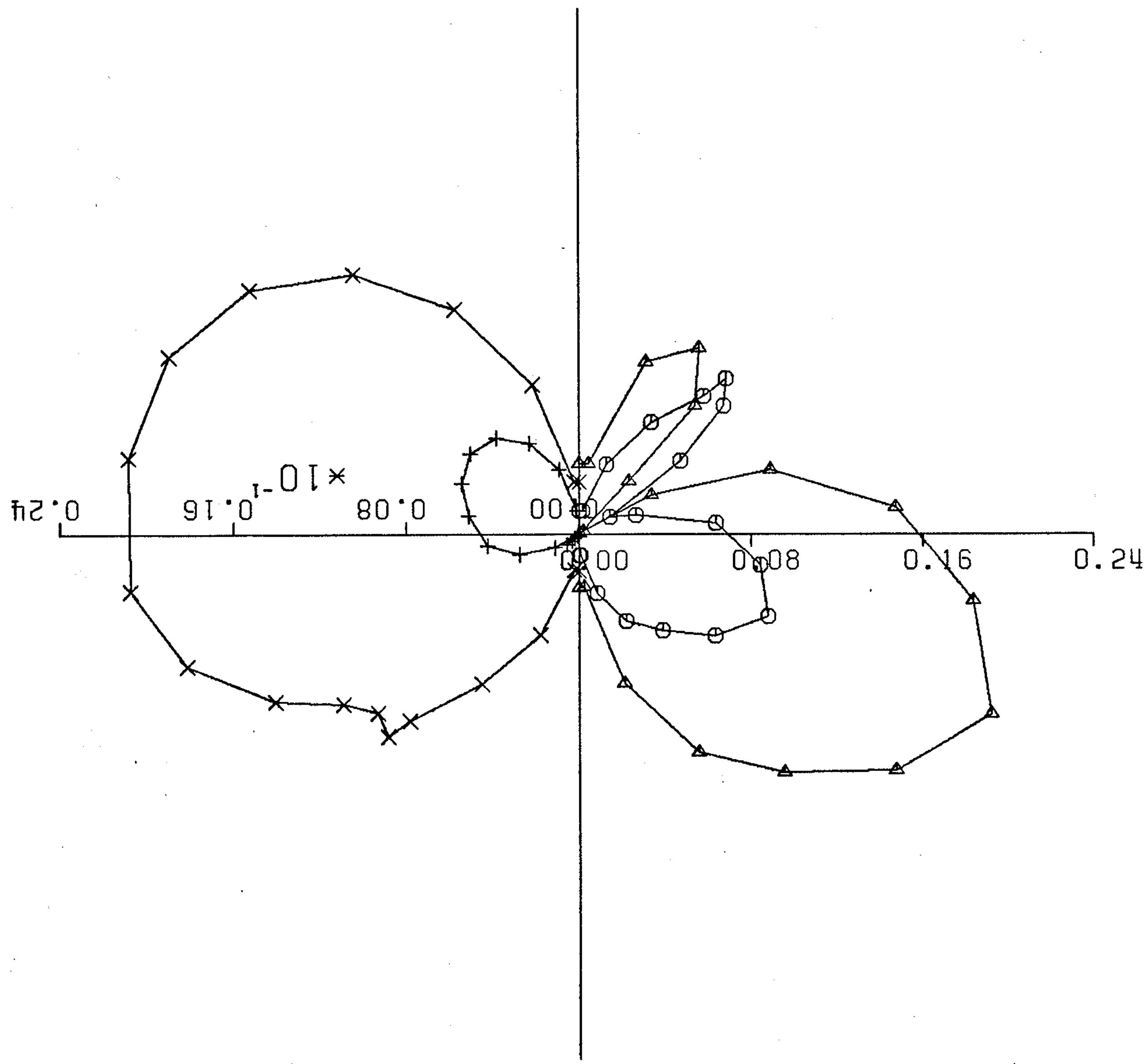

Fig. 122 Comparison between Case I and Case II for real part of axial displacement for SH-Wave, incident angle = 5°

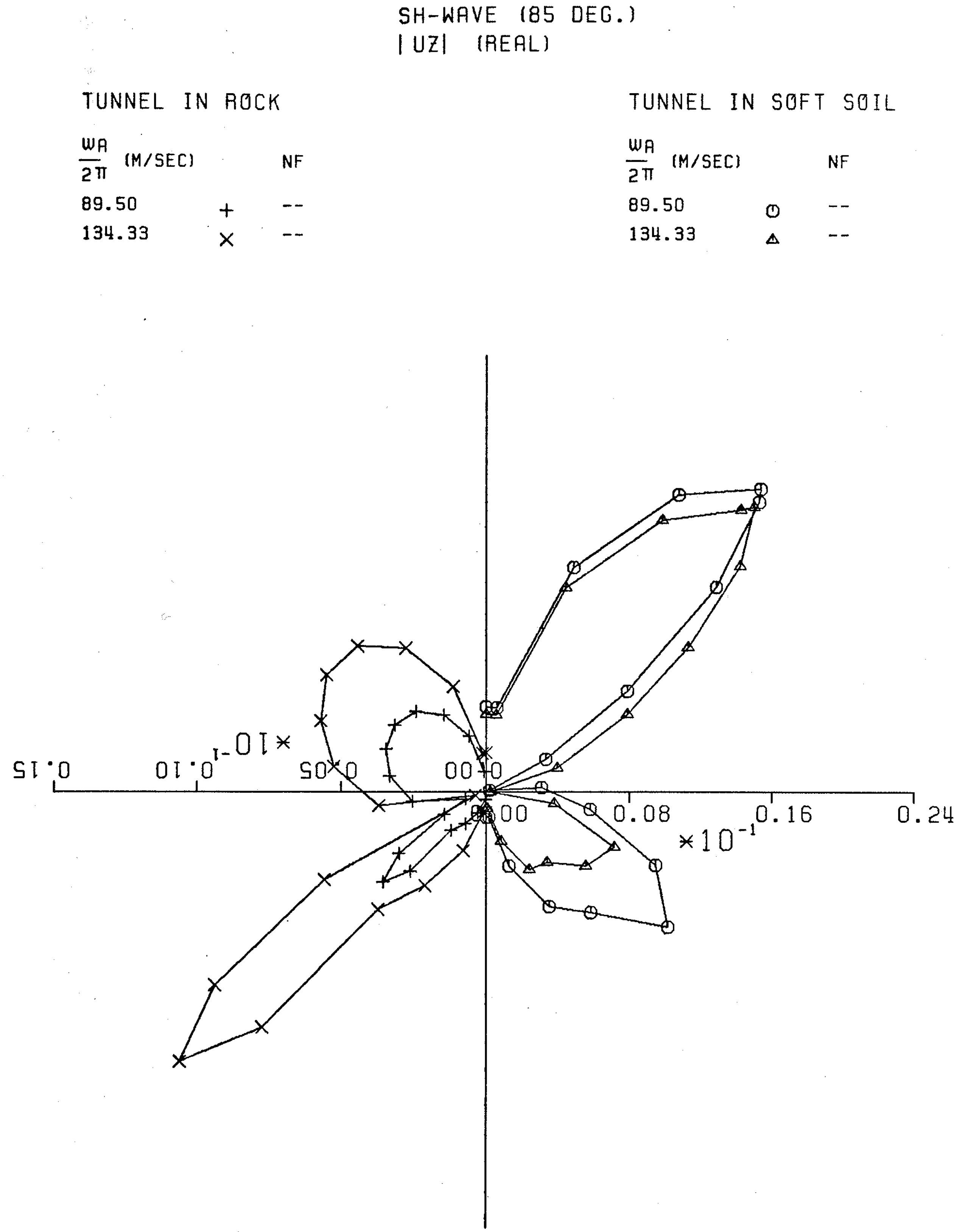

Fig. 123 Comparison between Case I and Case II for real part of axial displacement for SH-Wave, incident angle = 85°

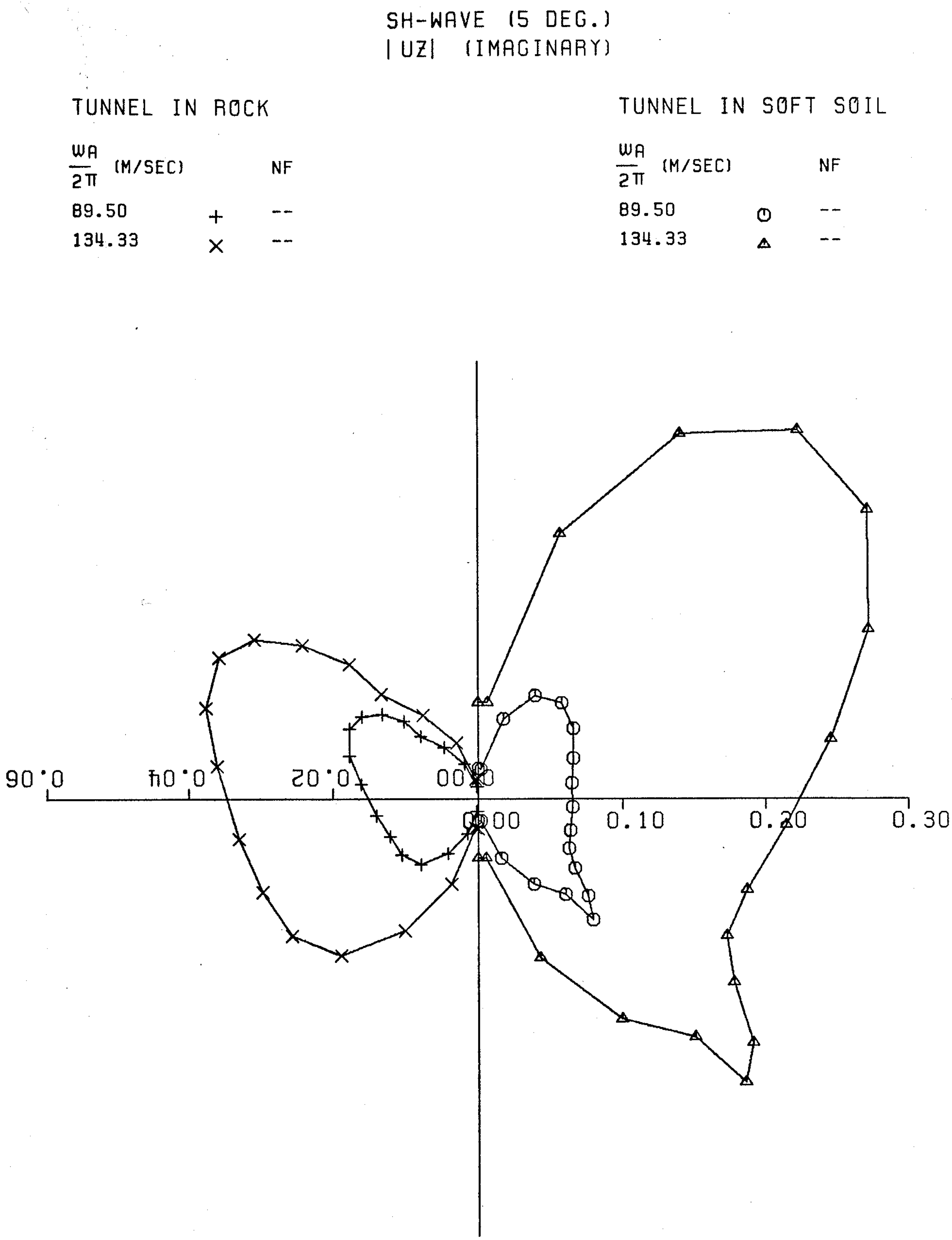

Fig. 124 Comparison between Case I and Case II for imaginary part of axial displacement for SH-Wave, incident angle = 5°

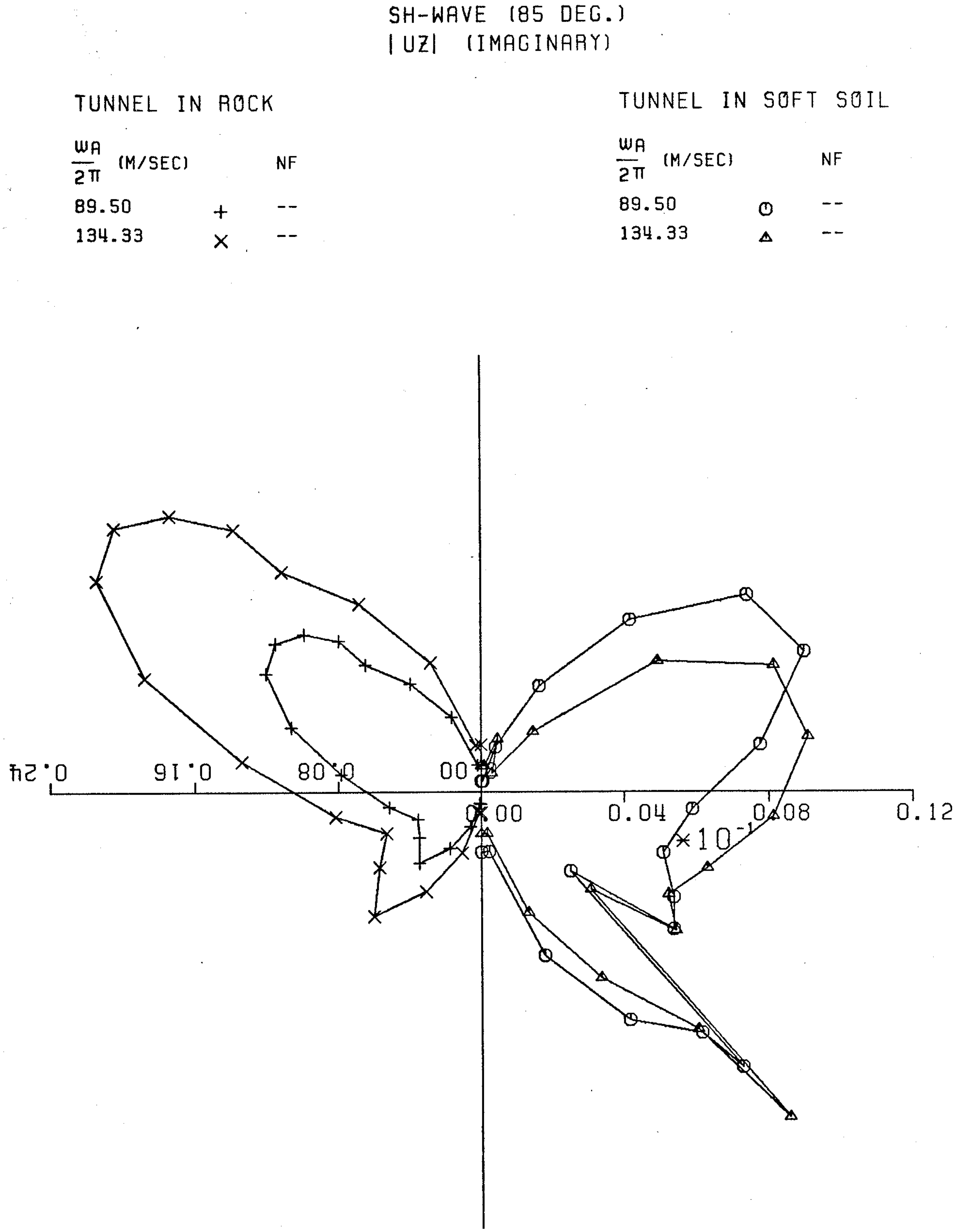

Fig. 125 Comparison between Case I and Case II for imaginary part of axial displacement for SH-Wave, incident angle = 85°

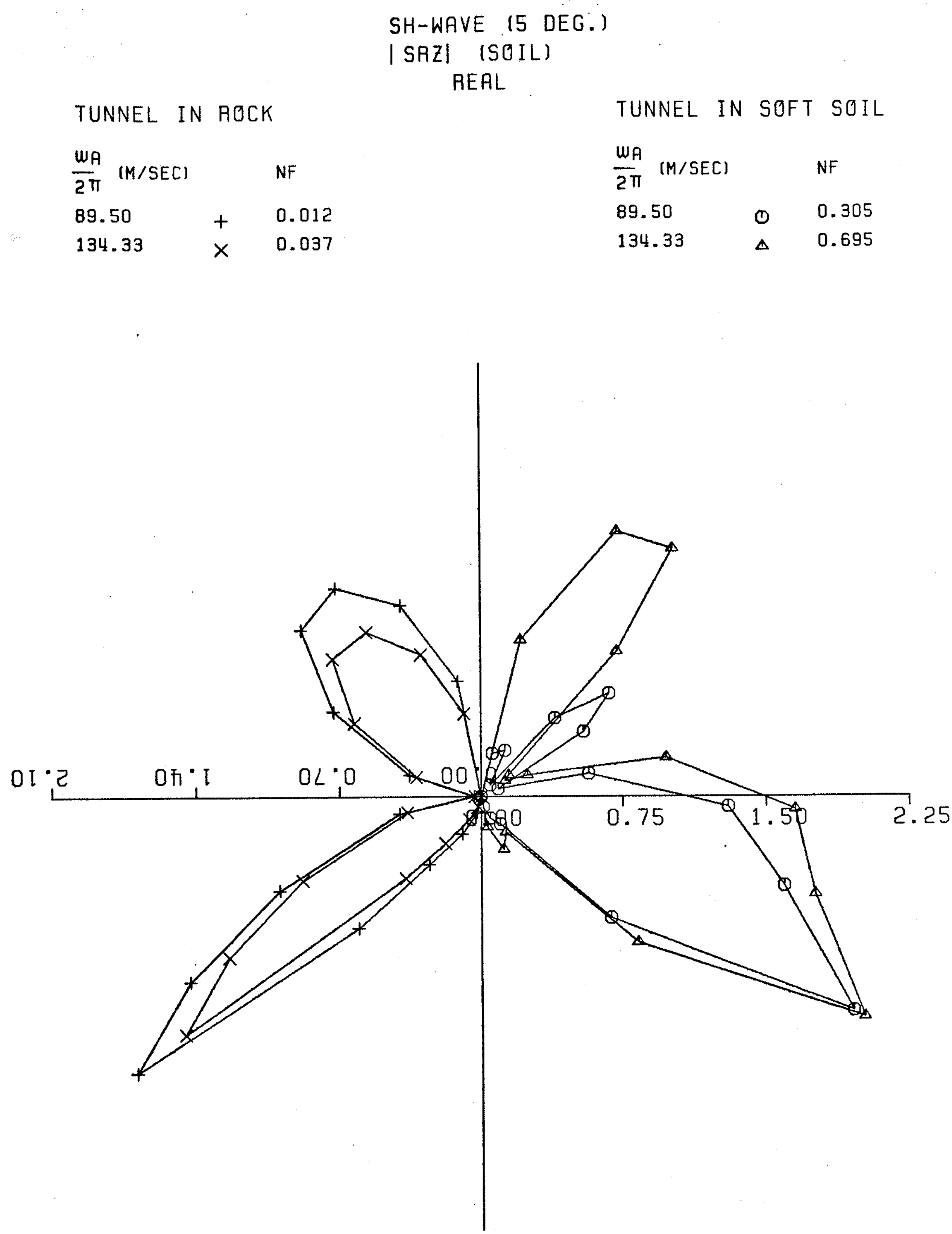

Fig. 126 Comparison between Case I and Case II for normalized real part of shear stress SRZ in soil for SH-Wave, incident angle = 5°

SH-WAVE (85 DEG.)
|SRZ| (SOIL)
REAL

TUNNEL IN ROCK			TUNNEL IN SOFT SOIL		
$\frac{WA}{2\pi}$ (M/SEC)		NF	$\frac{WA}{2\pi}$ (M/SEC)		NF
89.50	+	0.012	89.50	⊕	0.548
134.33	×	0.041	134.33	Δ	1.840

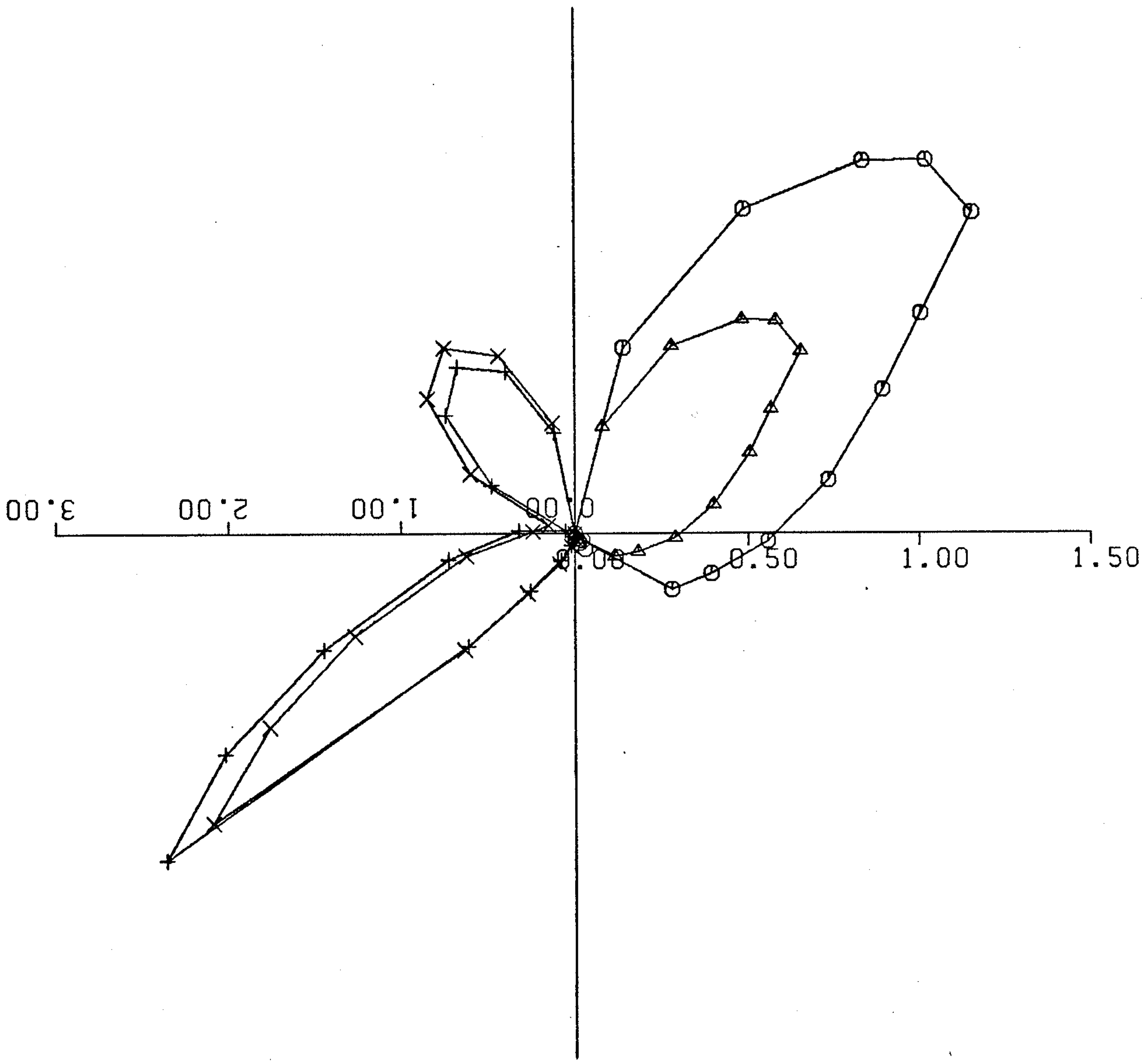

Fig. 127 Comparison between Case I and Case II for normalized real part of shear stress SRZ in soil for SH-Wave, incident angle = 85°

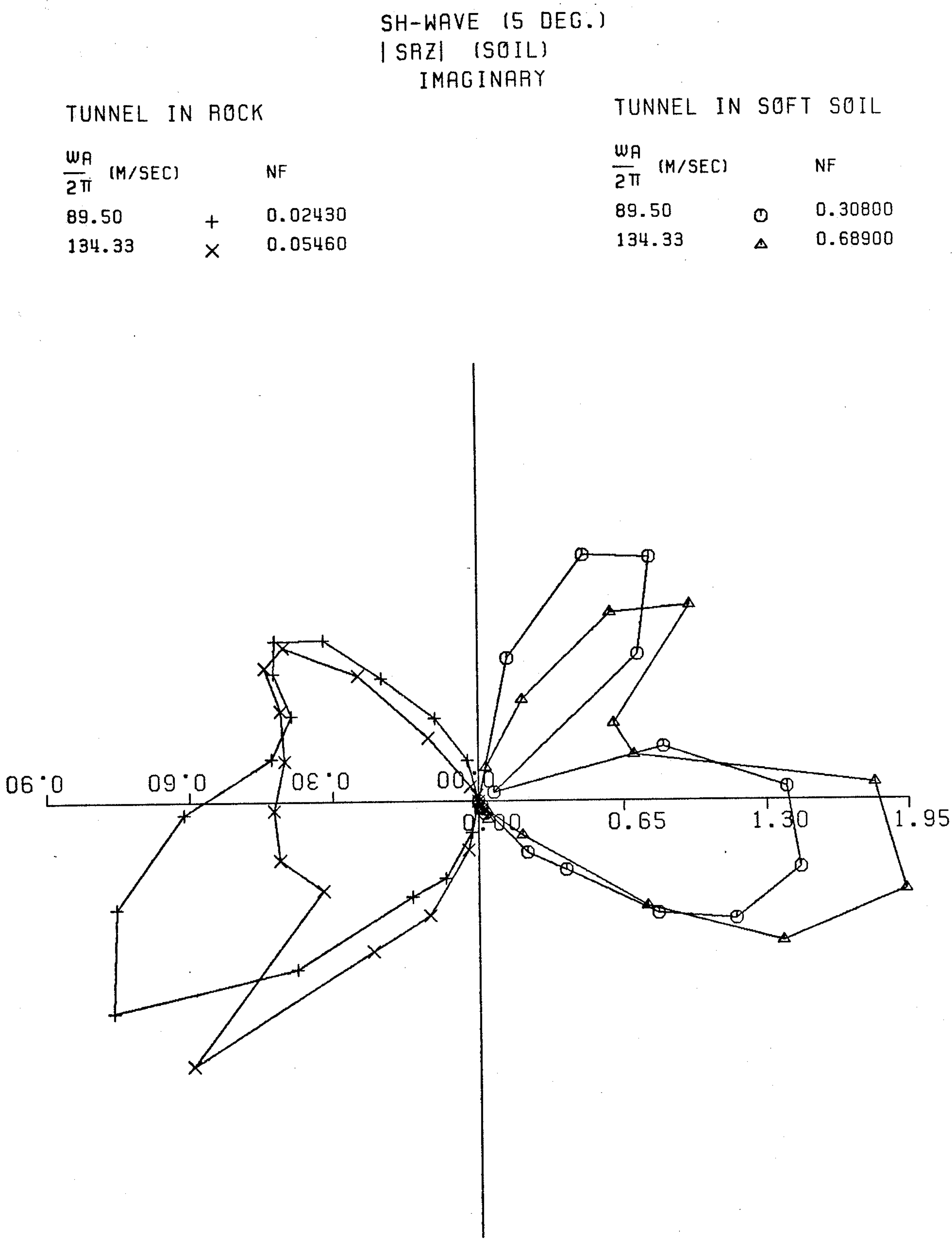

Fig. 128 Comparison between Case I and Case II for normalized imaginary part of shear stress SRZ in soil for SH-Wave, incident angle = 5°

SH-WAVE (85 DEG.)
|SRZ| (SOIL)
IMAGINARY

TUNNEL IN ROCK			TUNNEL IN SOFT SOIL		
$\frac{WA}{2\pi}$ (M/SEC)		NF	$\frac{WA}{2\pi}$ (M/SEC)		NF
89.50	+	0.27800	89.50	⊕	3.53000
134.33	×	0.62500	134.33	△	7.94999

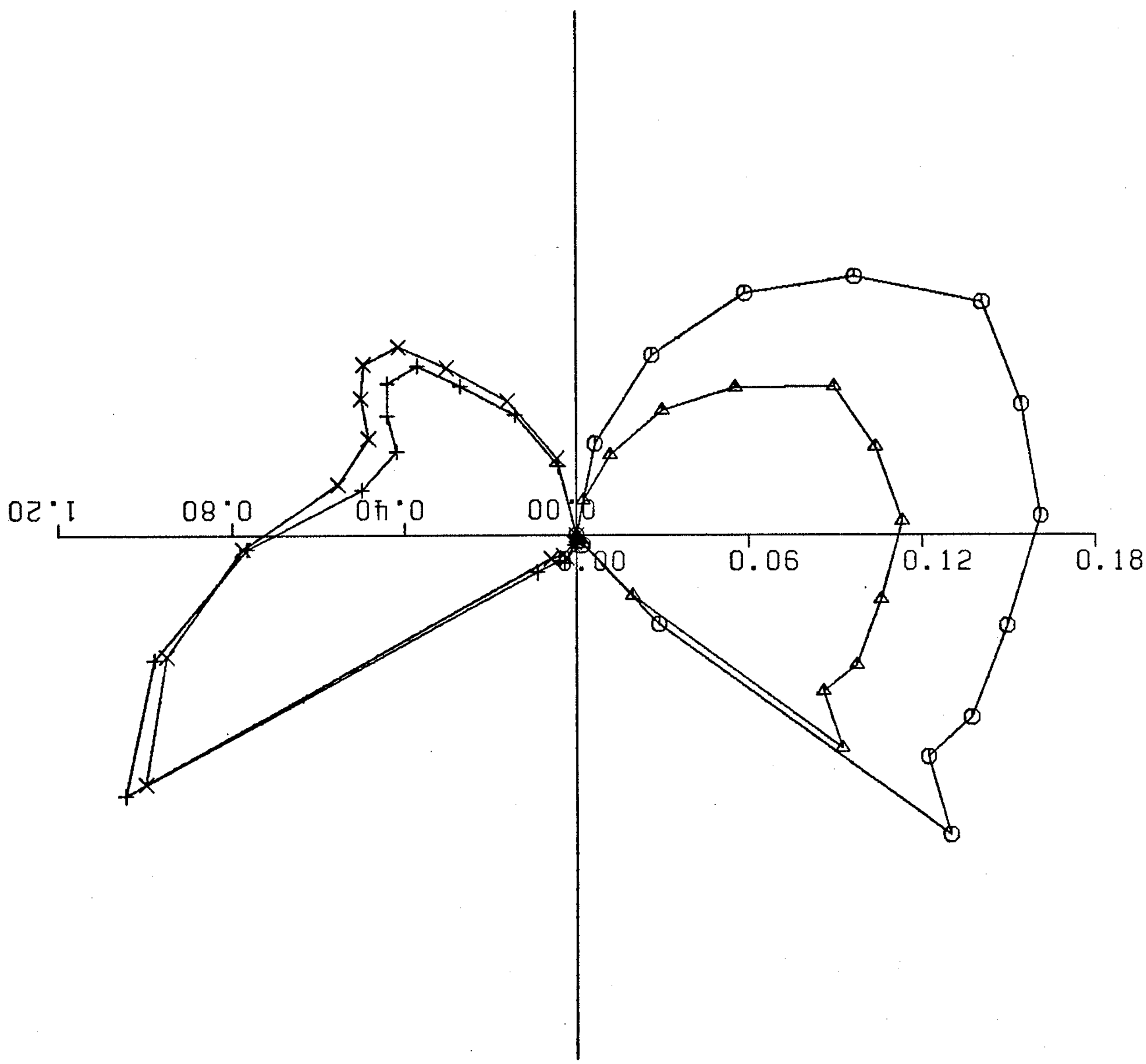

Fig. 129 Comparison between Case I and Case II for normalized imaginary part of shear stress SRZ in soil for SH-Wave, incident angle = 85°